DESIGN OF PHOTOMODIFIABLE MATERIAL SYSTEMS FOR MASKLESS PATTERNING OF FUNCTIONAL CERAMIC AND METALLIC MATERIALS AT MULTIPLE LENGTH SCALES.

A Thesis
Presented to
The Academic Faculty

by

Taiwo Raphael Alabi

In Partial Fulfillment
of the Requirements for the Degree
PhD in Polymer, Textile and Fiber Engineering in the
School of Materials Science and Engineering

Georgia Institute of Technology
May 2013

DESIGN OF PHOTOMODIFIABLE MATERIAL SYSTEMS FOR MASKLESS PATTERNING OF FUNCTIONAL CERAMIC AND METALLIC MATERIALS AT MULTIPLE LENGTH SCALES.

Approved by:

Dr.Suman Das, Advisor
School of Mechanical Engineering
Georgia Institute of Technology
School of Materials Science and Engineering
Georgia Institute of Technology

Dr. David Bucknall
School of Materials Science and Engineering
Georgia Institute of Technology

Dr. Anselm Griffin
School of Materials Science and Engineering
Georgia Institute of Technology

Dr. Haskell Beckham
School of Materials Science and Engineering
Georgia Institute of Technology

Dr. Karl Jacob
School of Materials Science and Engineering
Georgia Institute of Technology

Date Approved: [April 04, 2013]

To my Mum for keeping me sane and my Dad for letting me be.

ACKNOWLEDGEMENTS

I am thankful to God for giving me the privilege to be at the position I am in today, and for taking me through the thick and thin during my undergraduate and graduate studies across several continents. Furthermore, I would like to thank my mother, father and sisters for their support through the ups and downs of graduate school. Without their support through phone calls, texts, and actual visits I would not have put in the extra effort required to obtain this degree.

I would like to thank my advisor, Prof. Suman Das, for supporting me through my graduate school program and providing guidance. I would also like to thank my committee, Prof. David Bucknall, Prof. Karl Jacob, Prof. Anselm Griffin, and Prof. Haskell Beckham for assistance and guidance during the PhD program. I want to thank Professor Thadhani, for financial support during my final semester. I would like to thank Prof. Meisha Shoefner, Prof. Kiryaki Kalaitzidou, Prof. John Colton, Yolande Berta, Dr. Dajun Yuan for assistance with the use of several characterization equipments for my thesis work. More importantly, I would like to thank the School of Materials Science and Engineering at Georgia Tech, Center for Education Teaching and Learning at Georgia Tech for providing me with the technical-know-how, knowledge, and support, during my short, eventful and interesting stay at Georgia Tech.

TABLE OF CONTENTS

LIST OF TABLES

Page

LIST OF FIGURES

Page

LIST OF SYMBOLS AND ABBREVIATIONS

SEM	Scanning Electron Microscope
AFM	Atomic Force Microscope
TEM	Transmission Electron Microscope
XPS	X-ray Photoelectron Spectroscopy
MOSFET	Metal Organic Semiconductor Field Effect Transistor
FTIR	Fourier Transformed Infrared Spectroscopy
ATR	Attenuated Total Internal Reflection
LAMP	Large Area Maskless Photopolymerization
CAD	Computer Aided Design
HOMO	Higher Occupied Molecular Orbital
LUMO	Lowest Unoccupied Molecular Orbital
PAG	Photoacid Generator
THF	Tetrahydrofuran
DPE	Diphenylethylene
PS-b-PI	Polystyrene-b-Polyisoprene
PS-b-P4VP	Polystyrene-b-Poly-4-Vinylpyridine
PS-b-PMMA	Polystyrene-b-Polymethylmethacrylate
PS-b-PEO	Polystyrene-b-Polyethylene oxide
PS-b-PCL	Polystyrene-b-Polycaprolactone
DMSB	1,1-dimethylsilacyclobutane
PS-PBd-PS	Polystyrene-b-Polybutylene-b-Polystyrene
PαMeS-PIB	Polyαmethylstyrene-b-Polyisobutylene
PαMeS-PIB-PαMeS	Polyαmethylstyrene-b-Polyisobutylene-b-Polyαmethylstyrene

TEMPO	2,2,6,6-tetramethylpiperidin-1-yl)oxidanyl
BPO	Biphenyl peroxide
ATRP	Atom transfer free radical polymerization
PS-PFx-14	Polystyrene-b-Polyfluoropolymer
ULSI	Ultra Large Surface Integration
VLSI	Very Large Surface Integration
Nd:YAG	Neodynium doped Yttrium Alluminum Garnet
RIE	Reactive Ion Etching
PS-b-PFS	Polystyrene-b-Polyferrocenyldimethylsilane
PS-b-PDMS	Polystyrene-b-Polydimethylsilane
DMF	Dimethyl formamide
PI-b-PS-b-PDMS	Polyisoprene-Polystyrene-Polydimethylsiloxane
P2VP-PDMS	Poly-2-vinylpyridine-Polydimethylsiloxane
PS-b-PMMA	Polystyrene-b-Polymethylmethacrylate
CVD	Chemical Vapor Deposition
RT-FTIR	Real Time Fourier Transformed Infrared Spectroscopy
E_c	Critical energy Dose
D_p	Depth of Penetration
HF:H_2O_2	Hydrofloric Acid Solution: Hydrogen Peroxide Solution
H_2SO_4:H_2O_2	Sulfuric Acid Solution: Hydrogen Peroxide Solution
SCFT	Self Consistent Field Theory
SSL	Strong Segregation Limit
WSL	Weak Segregation Limit
LIP	Laser Interference Patterning
PDI	Poly Dispersity Index

Si (100)	Single Crystal silicon with a crystallographic orientation of (100)
M_w	Weight Average Molecular Weight
M_n	Number Average Molecular Weight
VLS	Vapor Liquid Solid
BCPS	Block Copolymer Phase Separation
TGA	Thermo Gravimetric Analysis
DMD	Digital Micromirror Device
DMA	Dynamic Mechanical Analysis
HDDA	Hexane dioldiacrylate
Variquat CC-55	Diethyl Polypropoxy-2-hydroxyethyl Ammonium Acetate
Irgacure 250	(4-methylphenyl)[4-(2-methylpropyl)phenyl]-hexafluorophosphate(1-)
Curcumin	(E,E)-1,7-bis(4-hydroxy-3-methoxyphenyl)-1,6-heptadiene-3,5-dione
Irgacure 184	1-hydroxy-cyclohexyl-phenylketone
ALD	Atomic Layer Deposition

SUMMARY

Silicon and silicon-based materials have been investigated over the years for the fabrication of electronic, optoelectronic, solar, and other structural/mechanical devices. The properties and applications of these silicon-based materials to a large extent depend on the length scale at which the material is being utilized. To enable the continuous use of silicon-based materials for next generation electronic, optoelectronic and structural device applications, new and inexpensive ways of fabricating features of silicon, silica and silica-based materials are needed. This dissertation investigates: 1) novel techniques for the fabrication of silicon oxide and silicon nanofeatures with potential application in the electronics, optoelectronics and industry; 2) new designs of photomodifiable material systems (resists) for maskless patterning of silica filled composites for structural and mechanical applications.

Sub-micron and nano-scaled features were fabricated onto silicon and silicon oxide substrates using a novel technique combining block copolymers and laser interference ablation. The sacrificial block copolymers, serving as both a positive tone resist and as a template for generating nanofeatures, are loaded with metallic salt precursors and patterned with a UV laser to generate device-oriented nanofeatures. New photopolymerizable material systems (negative tone resists) were developed based on a curcumin photosensitizer and an epoxy-acrylate, vinylether, and vinylether-acrylate silica-loaded material systems. The cationic and radical mechanisms employed by the monomeric systems under a high vapor pressure mercury lamp source were investigated with several materials characterization techniques.

CHAPTER 1

INTRODUCTION

The objective of this chapter is to introduce the areas of concentration of this dissertation which are: (a) nanoscale fabrication with organic materials and UV light sources and (b) materials system design for large area maskless photopolymerization (LAMP). This section also includes a motivation for this research as well as literature review on existing technologies and techniques for the fabrication of nanoscaled features. The literature review section also covers additive manufacturing technologies as well as laser interference ablation techniques. Section 1.5 provides a general outline of this dissertation.

1.1.Monomeric, Oligomeric and Organic Materials for Lithography[1]

Lithography, a Greek word, invented in 1798 by Artist Alois Senefelder describes the unique art of applying paint- *Graphein* to stones- *Lithos* using an hydrophobic ink. However, over the years, the word lithography has also been associated with the use of light for feature generation on various substrates—photolithography, the use of electron beams for the generation of features on various substrates—e-beam lithography, the use of stamps for feature transfer to substrates- soft lithography, direct writing of features on substrates using nano-precise tips- dip pen lithography, the use of laser interference at various wavelengths for generating periodic features—laser interference lithography, the direct writing of features with laser on substrates— projection optical lithography, and layer by layer writing of ceramic polymer composite features—stereo-lithography. Although the word lithography now has different connotations, the fundamental concept of lithography has remained the same, i.e.the patterning of surfaces with monomers, oligomers, polymers or other functional materials aided by optical and/or mechanical instruments.

This section will focus on introducing existing techniques for the fabrication of features, with various dimensions, from organic materials and UV light sources. The disadvantages of these existing techniques will serve as a motivation for the design of new techniques and material systems that have been investigated in this thesis.

Photolithography, a fabrication technique without which the past and current generations of electronic computing devices may not have been developed, is the most important fabrication process used in the electronics industry for the fabrication of processors, metal oxide semiconductor field-effect transistors (MOSFETs), and other logic devices. Continued miniaturization of electronic devices coupled with the increased efficiency of such devices has largely been due to the ability to increase the density of structures in a given space. Increased feature density is a direct result of the ability to pattern photosensitive materials at smaller and smaller length scales through the careful manipulation of light; particularly at UV wavelengths. This ability, in conjunction with the rational design of photosensitive materials that can effectively replicate the light exposure pattern, has revolutionized the electronics industry and resulted in the age of nanotechnology.

The need for rational design of radiation-sensitive material systems for application in the electronics industry is due to the fact that silicon, silicon-oxide, and other semiconducting substrates do not absorb at the UV wavelengths. Thus direct exposure of these materials to light will not generate features capable of use in the fabrication of logic devices, gates, transistors etc.

Advances in photolithography have broadened the application of lithography to other areas of manufacturing including additive manufacturing. Stereo-lithography is a form of additive manufacturing that applies photolithography to fabricate parts using photocurable resins in a layer-by-layer approach. Each layer of patterns registered on the radiation sensitive material system corresponds to a sequential layer through a stack of

thin slices of the digital rendition of an object in real time. Because conventional stereo-lithography employs a single laser for direct writing on a photocurable resin, the process is not only tedious but also very expensive and non-flexible to changes in part design or product. To curb some of the short-falls of stereo-lithography, an advanced patterning technique that allows direct image exposure without the requirement of a mask has been developed at Georgia Tech. The process called large area maskless polymerization (LAMP) employs the concepts of photolithography and stereo-lithography for the fabrication of integrally-cored ceramic molds for investment casting of turbine blade airfoil designs.

LAMP inherits problems associated with materials design and formulation from photolithography. For LAMP, photoactive monomeric materials systems have to be developed that have optimal absorbance and fast polymerization kinetics for a perfect registry of the image from a UV light source. Furthermore, these photopolymerized materials should have good mechanical properties in the cured state, in addition to retaining those properties after exposure to harsh developer solvents.

Because the LAMP process is used for the fabrication of ceramic molds that would be used to cast single-crystal airfoil blades, with casting temperatures approaching and exceeding 1700ºC, photopolymerized monomeric material systems cannot withstand such high temperatures. Therefore, the monomeric material system used in LAMP is loaded with silica ceramic micro-particles upto 60 vol% concentration. Silica is the ceramic material of choice because of its current use in investment casting foundries to produce superalloy castings, its high thermal stability, low refractive index, and relatively lowcost. The monomeric/organic component of the material system is then removed via a binder burn-out sequence to leaving behind a green ceramic mold.

The resolution of features in the final single-crystal airfoil blade is determined by the photo-absorptive properties of the ceramic-loaded monomeric material system. For

this reason the design of novel material systems, on the basis of readily available resists, tailored to the LAMP fabrication process is necessary for the successful commercialization of the technology. The current material system in use for LAMP fabrication is a ceramic-loaded acrylate system. Acrylate material systems are known to have a high rate of polymerization and a low intrinsic viscosity. A downside to acrylate material systems for photoinduced curing is the high volumetric shrinkage in photocured acrylates coupled with ambient oxygen inhibition effects. These effects can lead to delamination of parts built from acrylates and a failure of the LAMP-fabricated mold during binder burnout and casting processes.

The following subsections introduce the two main research foci of this dissertation: (i) non-conventional facile nanofabrication with techniques like block-copolymer phase separation and laser interference ablation, and (ii) photopolymerizable material systems design for additive manufacturing technologies. Literature review pertinent to the thesis is also provided in this section as well as the research motivation and objectives. The first subsection introduces non-conventional facile nanofabrication with block copolymers and laser interference ablation. This is followed by literature review on the subject and the motivation for pursuing a technique combining block copolymer phase separation and laser interference ablation. The next subsection introduces additive manufacturing technologies involving the use of photomodifiable material systems. The LAMP technology is introduced followed by literature review on additive manufacturing. The motivation for developing epoxy-acrylate, vinylether, vinylether-acrylate ceramic-loaded material systems for LAMP fabrication is also introduced.

1.1.1 Nanoscale Fabrication with Organic Materials and UV Light Sources.

Commercially available photoresists used for lithography suffer from a number of draw backs. These draw-backs can increase the time required for the fabrication of features, and sometimes lead to loss in resolution of the fabricated features. The loss in

resolution is usually from the different processing parameters used while developing the photoresist during the fabrication process.

Processing of conventional photoresists for the fabrication of sub-micron, and nano-scaled features involves several steps. Shown in scheme 1.1.1 are the typical steps that are involved while processing a photoresist. The first step involves the substrate preparation, which varies from substrate to substrate, and from application to application. The removal of organic residues from the surface of a substrate is the first preparatory step in any lithography fabrication technique. A piranha solution is used in most cases during this step, as it attacks all organic residues on the surface of various semiconductor and insulator type substrates. The next step is usually but not necessarily substrate modification. Substrates can be modified via the introduction of a primer layer spin-coated unto the substrate. The primer layer serves as an adhesion promoter between the substrate and photoresist. Improved adhesion between the substrate and photoresist is essential for high resolution nanoscale fabrication. A substrate like silicon or silicon oxide can have its surface modified to promote adhesion by an H_2SO_4:H_2O_2 rinse followed by an HF:H_2O_2 rinse. The rinse generates dangling oxygen and hydroxyl bonds on the surface of the substrate. Substrates that can be modified using solvents like those highlighted above primarily do not require a primer layer to promote photoresist adhesion.

After surface modification, a uniform layer of photoresist is deposited on the substrate using a spin coater. This is followed by exposure of the resist to a light source through a photomask. Masks are usually made via e-beam lithography of chromium on quartz wafers with manufacturing costs scaling exponentially with density and resolution of features to be fabricated. The exposure of some parts of the resist to light, through a mask, leads to a photochemical process in the exposed region. The photochemical process is sped up by a catalyst present in the resists, and then amplified through heating.

The next step is solvent rinsing. The solvent differentially attacks either the photoexposed region, i.e a positive tone resist, or the non-photoexposed region- negative tone resist and leaves behind insoluble regions that generate the sub-micron or nanoscale features.

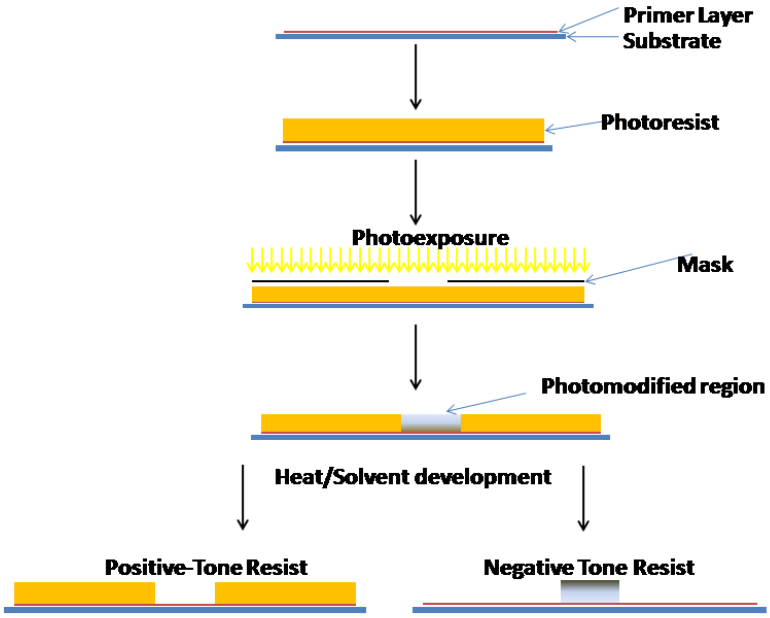

Scheme 1.1.1. A figure showing the steps used in a conventional lithography process for the generation of micro and nanoscale features

One of the main limitations of the conventional photolithography process as is apparent from the discussion above is the requirement for photomask production to fabricate features. Although e-beam lithography is one of the few techniques that does not require a mask, it is a very slow process, and it is also an expensive technique to set-up and maintain on an industrial scale. Conventional lithography processes are also solvent intensive. Harsh solvents like aqueous bases, xylene, acetone, and toluene are required during the development stage for removal of uncured and soluble portions of the resists. Apart from the potential toxic nature of some of these solvents, the as-fabricated

features can sometimes absorb these solvents and swell, thus resulting in loss of resolution.

The ideal photoresist for a lithography process will require minimal processing steps that do not require solvents and photomasks. The photoresist should be able to withstand plasma etch and enable the transfer of high-aspect-ratio submicron and nanoscale features to underlying substrates. An additional function that would be desirable in a photoresist would be its ability to yield improved resolution, which translates to increased feature density at UV wavelength range.

Block copolymers are potential candidates for a low-ablation threshold photoresist. The ability of block copolymers to phase separate into nanodomains in combination with laser interference ablation can be utilized for the generation of hierarchical features on different substrates. This is discussed in more details in chapter 3 of this dissertation. Moreover, the differential chemistry between the two components of the block copolymer can be utilized, as will be discussed in chapter 4, to replicate the hierarchical features on various substrates using metallic and ceramic nanomaterials.

1.1.2. Additive Manufacturing with Photopolymerizable Composite Organic Systems

Additive manufacturing or freeform fabrication is a manufacturing technique that allows the fabrication of 3D parts via a layer-by-layer approach. This manufacturing procedure eliminates the need for making molds thereby cutting cost and effectively reducing production time. Early reports on additive manufacturing started in the 1980's with the first commercialized system built by 3D systems in Valencia, California.

In additive manufacturing, 3D solids are fabricated using an energy deposition source or a material deposition source that moves in a defined path determined by information from

the specific section of the part, in real life, as represented in computer aided design (CAD) data. The resolution capability of an additive manufacturing process is dependent on several parameters including: sensitivity of the material system, the composition of the material system, and the smallest feature resolution of the energy or material sources for instance the focal spot size of the UV light source. There are several variations of additive manufacturing that have been reported including: stereolithography, LAMP, selective laser sintering, and fused deposition modeling and extrusion forming. In stereolithography a laser beam from an He-Cd or Ar-ion laser is scanned across a photocurable material system in a defined pattern to generate features representing a cross-sectional layer of the real part. LAMP improves over stereolithography by orders of magnitude, by projecting over 1 million beams from individual micro mirrors onto a photocurable ceramic matrix. An advantage of the LAMP process is increased throughput, since a larger area can be patterned in a shorter time. The increased throughput from the LAMP process also makes it attractive for incorporation into industrial scale manufacturing processes. LAMP also provides a much finer resolution of 17μm compared to stereolithography which has a minimum feature resolution > 100μm. Selective laser sintering, another form of additive manufacturing, was developed by DTM corporation Austin, Texas. In selective laser sintering, a heated bed of powder material is selectively sintered using light from a CO_2 or YAG laser. After sintering a layer of powder, a piston lowers the layer followed by the deposition of another heated layer of powder. The process repeats itself till the desired geometry is built. The piston then raises the fused, porous geometry from the powder bed.

Fused deposition modeling and extrusion forming was developed by Stratasys Corporation and involves the use of a write head having x-y degree of motion. The write head is fitted with a glue gun that extrudes molten plastic materials to precise locations to generate 3D objects. Fused deposition modeling and extrusion forming, although interesting, is yet to find industrial application and will not be discussed further in this dissertation.

However, the next sub-chapter introduces the LAMP technology, an improvement on stereolithography.

1.1.2.1. The LAMP Fabrication Technology

Large area maskless polymerization (LAMP) is an advanced form of additive manufacturing for layer-by-layer fabrication of complex shapes and geometries. Layer-by-layer fabrication, with ~20 μm resolution, is aided by a UV light source incident on a photocurable ceramic resin. Unlike stereolithography that uses a single laser beam for the layer-by-layer fabrication using photocurable materials, the LAMP technique uses a 1024 × 768 micromirror array to project images unto a photocurable material system. The micromirrors are 17μm squares representing one pixel in a 1500 dots per inch (dpi) bitmap image. During a LAMP fabrication process, bitmap images representing ~100 μm sections of the desired object are projected sequentially from the DMD chip onto the surface of a photocurable material system. After each successive exposure, a build platform is lowered automatically and a new layer of photocurable material system is deposited on the previously fabricated layer. This process is repeated until a full height 3D replica of the desired object is fabricated. After photofabrication, the uncured resin can be removed using benign solvents such as isopropyl alcohol. A binder burn-out step

is then used to convert the polymer-ceramic composite geometry into a “green” ceramic part. The binder burn-out temperature depends on the chemical nature of the organic material used as the monomer. After binder burn-out, the green ceramic parts are fired at temperatures above 1000ºC to sinter the ceramic particles to the desired density, crystallinity and mechanical property suitable for investment casting. This is followed by the molten metal casting and the subsequent generation of single crystal airfoil blades from the ceramic molds.

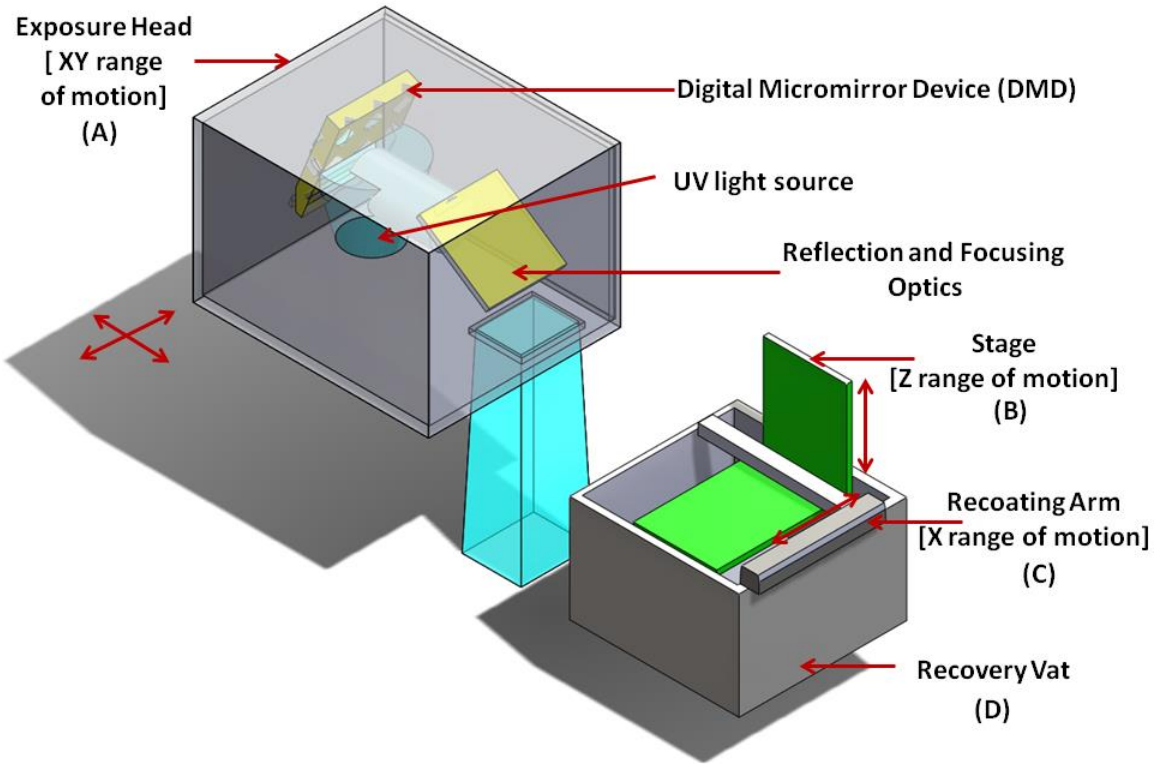

Scheme 1.1.2.1.1 A figure showing the (A) exposure head, (B) stage, (C) recoating arm, and (D) recovery vat: The major components of the LAMP fabrication process

The main components of LAMP are: the exposure head, stage, recovery vat and a recoating arm. The exposure head, shown in scheme 1.1.2.1.1 consists of the high pressure UV mercury light source, a digital micromirror device (DMD), reflecting, and

focusing optics. The exposure head has a range of motion in the x and y directions, that allows a serpentine motion of the focusing optics and DMD chip over a large area. The high pressure mercury lamp is the light source used for LAMP fabrication, and it has emission maxima at ~405 and 437 nm.

Further discussion on the LAMP fabrication technique will be provided in chapter 6 of this dissertation.

A liquid photocurable material system for LAMP fabrication must possess certain characteristics for it to serve as a good ceramic composite in the cured solid state. The most important property is photosensitivity. The material system must be sensitive/photomodifiable at the emission maxima of the high pressure mercury light source. A high pressure mercury light source however consists of several emission maxima corresponding to the i-line atomic transitions—365nm, h-line atomic transitions—404.7nm, and g-line atomic transitions—435.8nm. Most conventional high pressure lamp sources have an emission maximum corresponding to the i-line atomic transition i.e. 365nm. However, the LAMP UV light source is red-shifted with emission maxima occurring at 404 and 435 nm. Thus most conventional photoinitiators would either not work or work inefficiently with the LAMP process. This further emphasizes the need for rational design of materials for use in the LAMP fabrication process. Another important property a material system must possess for use in the LAMP process is low-to-medium range viscosity. Any material system designed for LAMP fabrication should have a viscosity in the range of 200-400 mPas based on requirements for ease of dispense, stability of recoated layers, and stability of fabricated features. The viscosity restraint rules out the use of aromatic epoxy resins in LAMP. However, low-viscosity

resins including: acrylates, urethane acrylates, ether acrylates, vinylethers, can be designed for use with the LAMP. The design of resins for use with LAMP involves the rational selection of photoinitiators and photosensitizers with absorption properties matching the emission characteristics of the high pressure mercury light source.

1.1.3. Literature Survey

Current scientific literatures pertinent to the area of concentration of this doctoral dissertation are large. While the introductory section has provided general background information about the new area of research this doctoral thesis expounds upon, the literature review section will be tailored towards key research areas investigated: block copolymer lithography, laser interference ablation, and UV curable material systems. The chapter 2 of this thesis, however, provides in-depth fundamental knowledge on the physics behind phase separating block copolymers. Information is also provided on the photophysics and photochemistry in light-initiated polymerization processes used in various industrial scale photolithographic processes. The photophysics of lasers and laser interference ablation is also covered in details.

1.1.3.1 Block copolymer lithography

There have been numerous reports on the use of block copolymers for the fabrication of features with dimensions in the nanodomain using several methods and processes [2-6]. This subsection will discuss several of the more recent techniques.

Park et al. fabricated periodic dense arrays of holes and dots on silicon nitride using diblock copolymers consisting of assymetric polystyrene-b-polybutadiene and polystyrene-b-polyisoprene [7]. Polybutadiene and polyisoprene are the minor components of the block copolymers. The block copolymer after annealing at 125ºC for

24 hours phase-separated forming hexagonally ordered domains with 40 nm periodicity. Periodic hole arrays were fabricated on silicon nitride substrates via a sequential O_2 and CF_4:O_2 reactive ion etching (RIE), of phase-separated block copolymers, in a plasma chamber. Periodic dot arrays were fabricated after exposure of the phase-separated block copolymer to osmium tetroxide vapor. This was followed by RIE in a CF_4:O_2 plasma chamber.

Cheng et al. fabricated cobalt magnetic nanodot arrays on a silicon substrate using an asymmetric polystyrene (PS)-b-polyferrocenyldimethylsilane (PFS) block copolymer[8]. The minor component of the block copolymer, the PFS block, upon annealing forms ordered spherical domains within the PS matrix. An O_2 RIE plasma etch was first used to remove the PS matrix, thus generating the template nanodots. The template nanodots were used to etch into underlying silicon oxide substrate with a CHF_3 RIE, to generate nanopillars. The nanopillars, consisting of PFS, Polymer, and SiOx, were used as masks to etch into a tungsten underlying substrate with CF_4+O_2 RIE. This generated nanopillars having a basal section made up of tungsten. Tungsten nanodots, obtained after the removal of top layers of polymer, silicon oxide and PFS, were used to etch into a cobalt underlying substrate with ion beam etching.

Cheng et al. also employed an assymetric PS-b-PFS block copolymer to fabricate patterned ceramic nanofeatures with long range ordering [9]. Patterned array of ceramic nanoparticles was obtained via O_2 RIE of phase-separated PS-b-PFS block copolymer on lithographically patterned silica substrates.

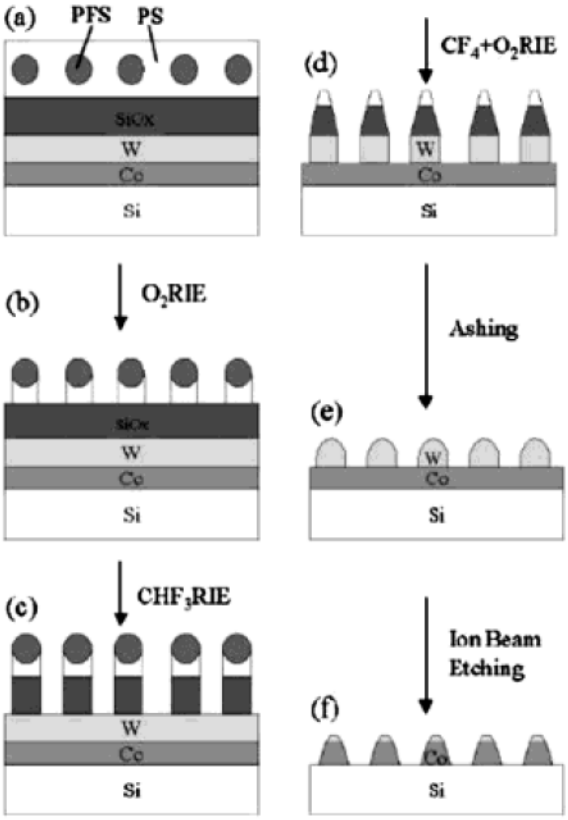

Figure 1.1.3.1.1. Scheme showing the steps for fabrication of cobalt nanodot arrays via PS-b-PFS phase separation, RIE and ion beam etching [8].

Long-range ordering, 4μm×4μm, with minimal defects, was achieved using graphoepitaxy enabled by the lithographically patterned silica substrates. Similar reports by Lammertink et al. have generated large area PFS ceramic nanofeatures from a PI-b-PFS block copolymer [10].

Chang et al. reported the fabrication of high aspect ratio silicon nanowires using PS-b-PFS block copolymer combined with metal-assisted etching [11]. The PS-b-PFS block copolymer after phase separation on an Si:SiO_2 bi-layered substrate is etched in a plasma chamber with O_2 gas. This generates PFS spheres in conformal contact with the SiO_2 layer of the Si:SiO_2 bi-layered substrate. Acting as masks, the PFS spheres upon

exposure to a plasma chamber containing CF_4 gas resulted in the generation of SiO_2 nanopillars. Gold was evaporated onto the nanopillars. Gold capped PFS:SiO_2 nanopillars were then removed via rinse in HF, and gold mediated etching of silicon was subsequently performed via substrate immersion in an HF:H_2O_2 mixture.

Jung et al. reported the fabrication of PDMS cylinder patterns on a silicon substrate from phase-separated PS-b-PDMS block copolymer [12]. The asymmetric PS-PDMS block copolymer with a PDMS minor component, phase separates upon temperature annealing at 150ºC, to give parallel cylinders with a PDMS layer at the air-film interface. After phase separation of the PS-b-PDMS block copolymer on a PDS brush treated substrate, the substrate was first etched in a plasma chamber with CF_4 to expose parallel cylindrical patterns. This was then followed by etching in a plasma chamber with O_2 gas to remove the PS layer and generated the silica nano cylindrical arrays.

An interesting report by Gon Son et al. described the fabrication of PDMS cylindrical and spherical morphologies on the same substrate using a combination of solvent annealing and ion-beam polymerization techniques [13]. Spherical morphologies were obtained from solvent annealing PS-b-PDMS diblock copolymer in dimethyl formamide (DMF) vapor, while cylindrical morphologies were obtained from solvent annealing PS-b-PDMS diblock copolymer in acetone vapor. Mixed morphologies having cylindrical and spherical domains were fabricated by solvent annealing in either a DMF or acetone vapor. This was then followed by exposure to ion beam in order to crosslink the PDMS block. Exposure of the sample to a different vapor results in the generation of mixed morphologies on the substrate.

In a separate report by Jeong Won et al., diblock copolymers of polyvinylpyridine (P2VP)-b-polydimethylsiloxane (PDMS) were demonstrated to give various morphologies from lamellar, perforated lamellar, cylinder, and sphere after phase separation and etch in a CF_4 and O_2 plasma. These morphologies were obtained by selecting different solvents to anneal the diblock copolymer, and also by varying the vapor pressure within the annealing chamber. These factors were used to vary the swelling ratio of each block in the diblock copolymer, as well as the thickness of the block copolymer film. The substrates were modified with a PDMS brush prior to the sin coat of the P2VP-PDMS block copolymer.

Most reports have focused on block copolymers phase separating into spherical, cylindrical or gyriodic morphologies, however, Gon Son et al. reported the formation of square arrays of PDMS from a phase-separated polyisoprene (PI)-b-polystyrene (PS)-b-polydimethyl siloxane (PDMS) terpolymer [14]. Square arrays were obtained using various techniques including solvent annealing with swelling, and substrate modification via the use of polymer brushes. Solvent annealing of PI-PS-PDMS triblock terpolymer, in chloroform vapor with 152% swelling, was reported to generate square arrays on the substrate. Square arrays were also reported to form on substrates that have been modified with P2VP, PEO and P4VP brushes.

The chemical incompatibility of block copolymers can also be utilized during the dissolution of the blocks. Micelles that form during during the dissolution of chemically incompatible block copolymer in a solution compatible to one of the blocks, can be used for the directed assembly of metallic nanoparticles. Glass et al. fabricated patterned arrays of gold metallic nanoparticles using PS-b-P2VP micelles obtained from a toluene

solution [15]. Gold was introduced into the micelle solution by the addition of $HAuCl_4$ salt solution. The P4VP block forms the core of the micelles due to unfavourable interaction with toluene, and they also complex with gold forming gold-core-loaded micelles. The gold-loaded micelles were transferred to silicon substrates by dipping and slow retraction of the substarte. Gold metallic particles were obtained after etching the gold-loaded micelles in an O_2 plasma.

Kang et al. also demonstrated the use of block copolymers for the generation of metal nanofeatures, including gold nanofeatures, on silicon substrates [16]. The method involved the use of an asymmetric PS-b-PMMA block copolymer spin coated from a 1 wt.% toluene solution onto a 3-(p-methoxyphenyl)propyltrichlorosilane (MPTS) treated Si substrate. After annealing the diblock copolymer, the PMMA component that formed vertical cylindrical domains, was removed via UV induced degradation. The resultant pattern consisting of periodic arrays of holes was then placed in an e-beam chamber. Gold, nickel and other metal films were evaporated onto the patterned substrate, and the PS was removed via lift-off in DMF. This generated arrays of metallic gold, nickel, aluminum and chrome on the silicon substrate.

Ok Shin et al. used an asymmetric PS-b-P4VP diblock copolymer to fabricate sub-nanometer iron oxide nanoparticles on a silicon substrate [17]. The block copolymer was spin-coated unto a silicon substrate from a 1wt.% concentration THF:Toluene (20:80) solvent. Solvent annealing the block copolymer in THF:Toluene (80:20) vapors resulted in the generation of hexagonally packed vertical cylinders of P4VP in a PS matrix. Iron was later introduced into the P4VP domains by immersion of the substrates into an iron salt solution in 1wt.% hydrochloric acid.

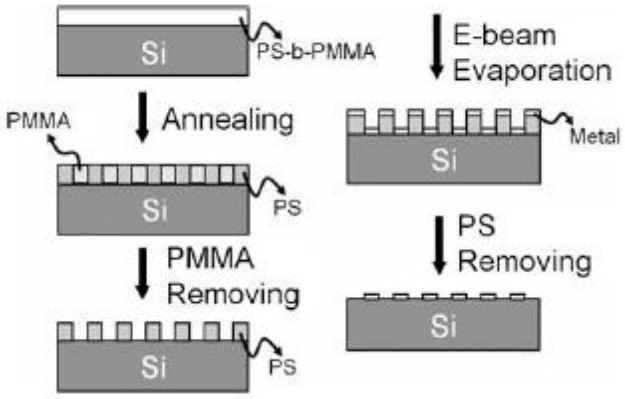

Figure 1.1.3.1.2. Scheme showing the steps for fabricating nanofeatures on silicon [16].

Iron metallic nanoparticles were generated on the substrate, replicating the hexagonal packing of the phase-separated diblock copolymer, via exposure to O_2 plasma. The iron nanoparticles were later used for plasma enhanced chemical vapor deposition (PECVD) growth of carbon nanotubes.

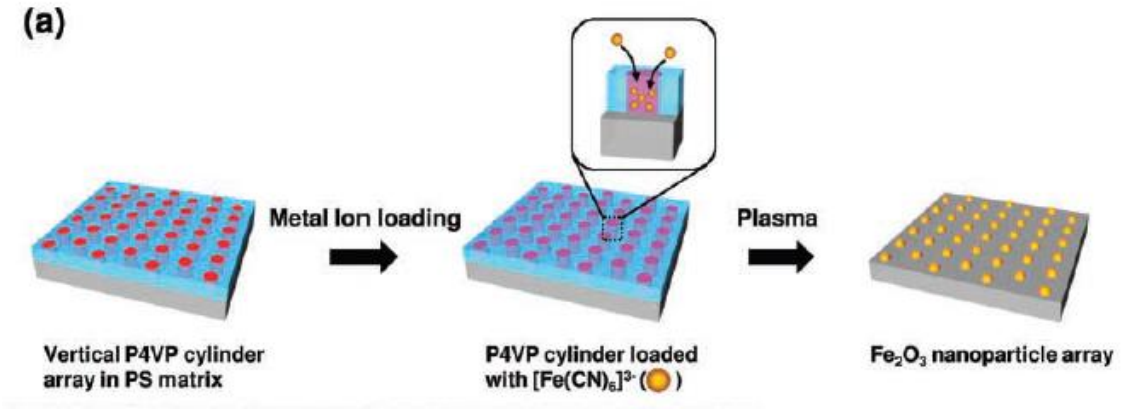

Figure 1.1.3.1.3. Scheme showing the steps used for obtaining sub-nanometer Fe_2O_3 nanoparticles [17].

Ruiz and Nealey et al. have also used PS-b-PMMA diblock copolymer on lithographically patterned substrates for density multiplication and generation of

chromium and silicon oxide arrays [18]. Silicon oxide substrates were modified with an hydroxyl terminated polystyrene brush. A negative resist sensitive to an e-beam is then used to create patterns on the substrate with periodicities equal to or twice that of the asymmetric PS-b-PMMA block copolymer. The patterned substrate is etched in an O_2 plasma to remove the rest of the photoresist as well as remove the PS brushes from regions that have been exposed to the e-beam. Regions where the PS brushes have been removed are preferentially wet by the PMMA block while regions with the PS brushes are preferentially wet by the PS block. Density rectification of PS-b-PMMA block copolymer occurred on substrates that were patterned with e-beam having periodicities commiserate with the domain spacing of the diblock copolymer, while density multiplication occurred on substrates patterned with e-beam having periodicities twice that the domain spacing of the diblock copolymer.

After removal of the PMMA blocks, chrome was evaporated on the PS patterned substrate. Silicon pillars were then fabricated on the substrate through a CF_4 RIE plasma etch.

Similar report by shin et al. also involved the use of PS-b-PMMA asymmetric block copolymers for the generation of gold and chromium nanodots as well as multilayered nanodots [19]. Silicon substrates were modified with polystyrene-random-methyl methacrylate P(S-r-MMA) to generate a substrate neutral to the PS and PMMA blocks.

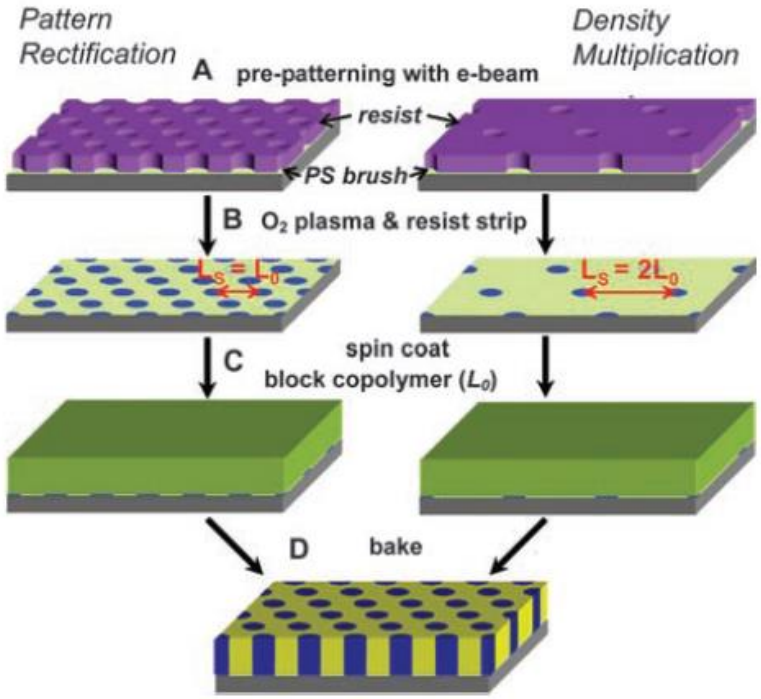

Figure 1.1.3.1.4. Scheme showing the steps for density multiplication and density rectification using e-beam lithography and PS-b-PMMA block copolymer.

PS-b-PMMA block copolymer was spincoated unto the neutralized substrate and then temperature annealed for two days. The PMMA vertical cylinders were removed via UV exposure and acetic acid rinse leading to the generation of hexagonally parked hole arrays on a PS matrix. Chromium or gold were then evaporated unto the substrate using an e-beam evaporator, followed by a lift off process in toluene solvent. Nanowires can also be grown in the pores generated after the removal of PMMA as demonstrated by Thurn-albrecht et al.[20] The underlying substrate in this case is conductive, because electric current is required for the electrochemical deposition and growth of the conducting nanowires. Nanowires made from nickel and cobalt were fabricated using this process.

Polystyrene (PS)-b-polyethylene oxide (PEO) diblock copolymer has also been utilized in the literature, as reported by Ha Kim et al., for the fabrication of nanofeatures such as titania and silica on silicon substrates [21]. A silicon substrate is spin coated with an assymetric PS-b-PEO block copolymer followed by solvent annealing in a benzene vapor. Vertical cylinders of PEO were formed in the phase-separated PS-b-PEO block copolymer. The substrate with phase-separated block copolymer is immersed in water swelling preferentially the PEO block. Silica or titania nanoparticles were formed on the swollen PEO domains via introduction of the substrate to either a silicon tetrachloride ($SiCl_4$) or a titanium tetrachloride ($TiCl_4$) vapors.

Polystyrene-b-polyisoprene (PS-b-PI) has been demonstrated for use in large area nanoscale patterning by Park et al [22]. PS-b-PI was spin-coated on a tri-layered substrate having silicon nitride, polyimide and silicon layers. After phase separation, the block copolymer is etched in O_2 RIE followed by CF_4 RIE. The CF_4 RIE is used to etch into the silicon nitride substrate with the PS layer serving as a mask. An O_2 RIE is then used to selectively etch into the polyimide substrate. The pores generated are then filled with Ti or Au by CVD evaporation.

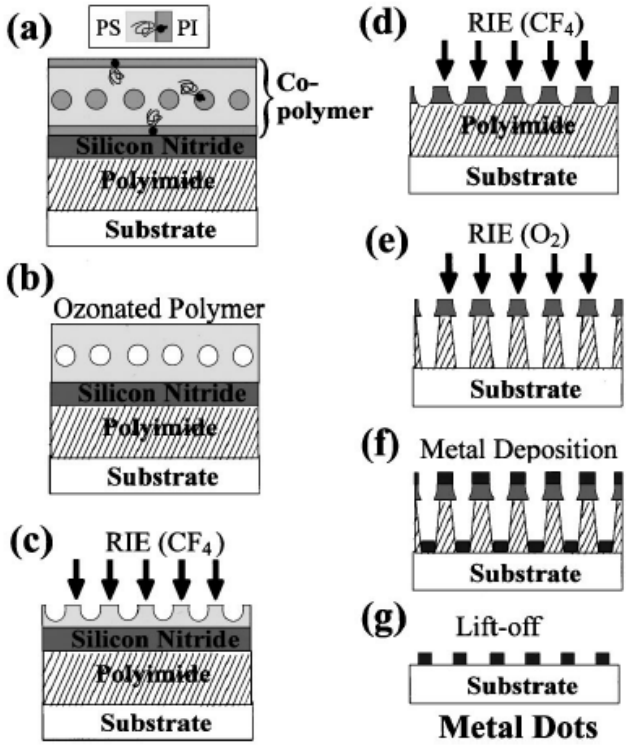

Figure 1.1.3.1.5. Schematic of the steps used to obtain metal dots on a substrate using PS-b-PI block copolymer and RIE.

1.1.3.2 UV Curable Material Systems

There have been several reviews on the design of photocurable material systems for additive manufacturing and also on the technique of solid free form fabrication (SFF) [23, 24]. This literature review will discuss about additive manufacturing and the design of material systems relevant to large area maskless photopolymerization (LAMP).

Some of the first reports in the literature about additive manufacturing came from Haertling et al.[25] In the report, polymeric composites having alumina, barium titanate, lead magnesium niobate, lead zirconate titanante and zinc oxide were fabricated through exposure of acrylic and urethane monomers, through a mask, to a UV light source.

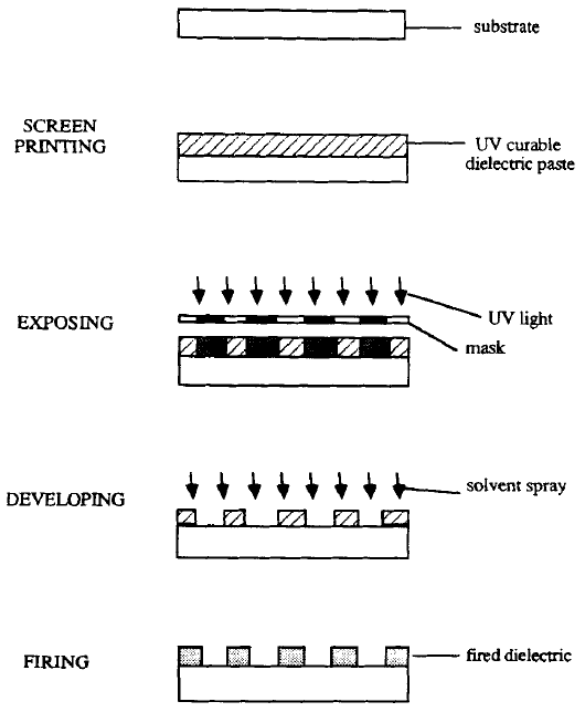

Figure 1.1.3.2.1. Schematic showing the steps used to pattern ceramic materials from UV curable polymeric composites [25].

After photo-exposure, a solvent spray is used to remove the uncured materials and a firing process is used to remove the organic components generating a green ceramic part.

While the report from Haertling et al. discussed only single-layer ceramic structures, Griffith et al. reported the fabrication of silica, alumina, and silicon nitride 3D green molds using stereolithography- another form of additive manufacturing [26]. Stereolithography is an additive manufacturing technique that fabricates 3D complex features by laser writing images of each cross-section of the feature unto a photomodifiable ceramic loaded composite system. The material system investigated is highly concentrated with 0.5-0.65 volume fraction of silica, alumina or silicon nitride particles. A schematic of the stereolithography (SLA) apparatus used in the report is shown in figure 1.1.3.2.2.

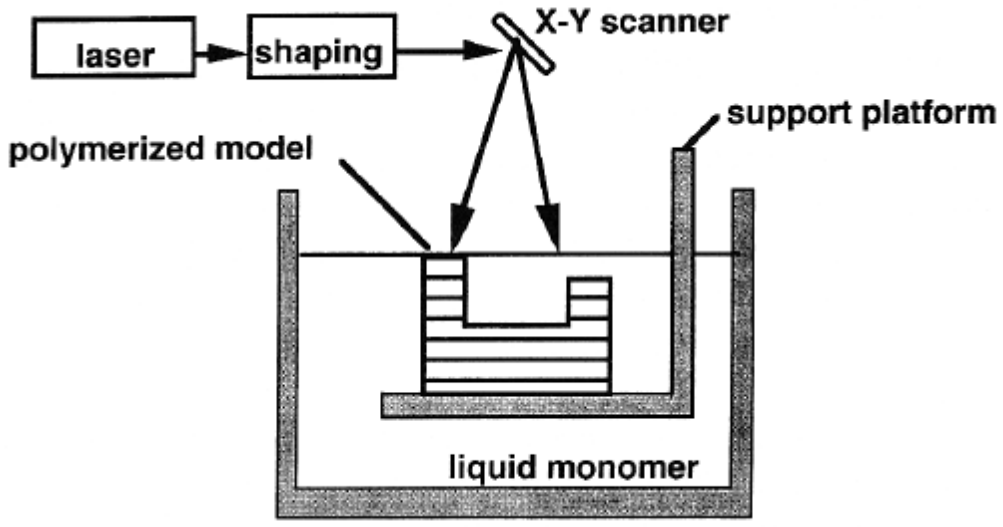

Figure 1.1.3.2.2. Schematic of the stereolithography apparatus for the fabrication of 3D objects [26].

The SLA apparatus consists of a laser and an X-Y scanner for registering patterns on the photopolymerizable material system. The support platform is the base that is lowered, after every exposure, by an amount equal to the cross-sectional thickness of the image projected. After the support platform is lowered, liquid resin flows unto the top surface of the cured part, and a recoating blade is used to create a uniform layer thickness. Various characteristics of the material systems were investigated including cure depth, viscosity, and refractive index. The report also discussed the sintering of the silica and alumina photocured parts to generate fully dense microstructures.

Micro-stereolithography, another recent advancement in additive manufacturing, fabricates 3D features with sub-micron resolution (1.2 μm). The technique was first reported by Zhang et al. and Ikuta et al., and it involves photoexposure from a focused (5μm) UV light source unto a photopolymerizable metal-loaded resin. The stage

containing the photo-polymerizable suspension has an x-y range of motion which can be used to determine the location to be polymerized during the act of photoexposure within a layer.

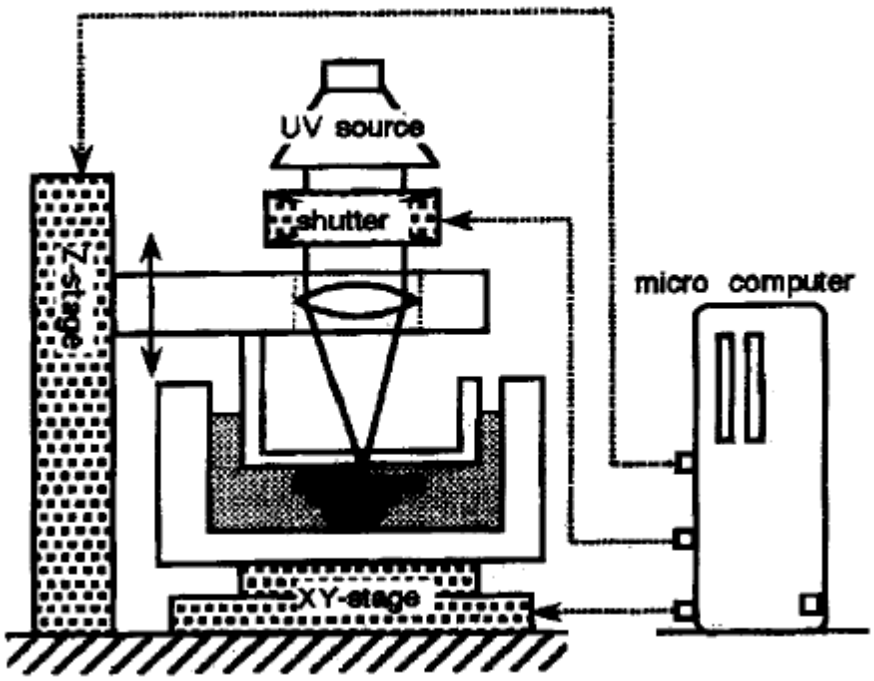

Figure 1.1.3.2.3. Schematic of the micro stereolithography apparatus [27].

After photo-exposure within a layer, the z-stage is moved up to allow a new layer of liquid to form. Although a "constrained surface" approach is shown here i.e the liquid surface is always in contact with a transparent glass through which photoexposure occurs, other methods involving a "free surface" approach has also been reported.

Attention in the literature has shifted from the design of new techniques for additive manufacturing, to the design and optimization of material systems for the already established additive manufacturing processes. The reason for this is the current

limitations to the industrial application of additive manufacturing techniques is based on the ability to design material systems with increased photosensitivity, low scattering, low shrinkage, low viscosity and low refractive index. The material systems should also, upon debinding and binder-burn-out, give green ceramic parts that can undergo high temperature sintering.

Hinczewski et al. investigated ceramic suspensions that are suitable for stereolithography [28]. A material system based on alumina was designed with an acrylate monomer serving as the binder and photoactive component. A dispersant was added to prevent the agglomeration of alumina micro particles, while a photoinitiator was used to initiate the photopolymerization reaction. The viscosity of the alumina-loaded acrylate material system developed was modified through the use of reactive diluents. The reactive diluent used is a monofunctional acrylate. Alumina green parts were obtained, after the debinding of the organic components at 580 ºC, by sintering at 1580 ºC.

A novel technique for monitoring in-situ degree of cure in photopolymerized ceramic composite system was also reported by Wu et al [29]. The technique, called realtime fourier infrared (RTFTIR) spectroscopy, was used to monitor degree of cure in alumina-filled acrylate material systems. Figure 1.1.3.2.4 shows the schematic of the RTFTIR.

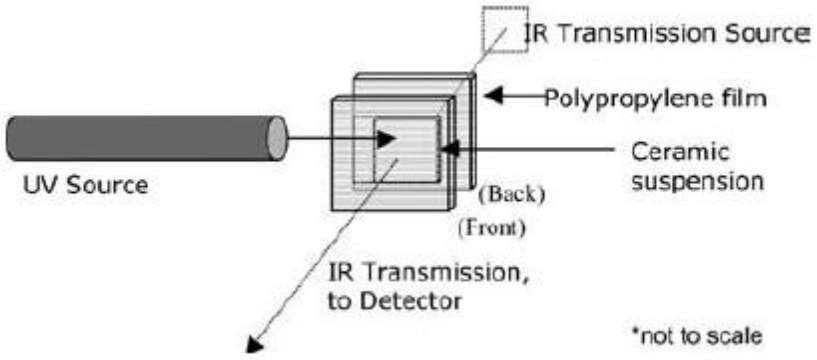

Figure 1.1.3.2.4. Schematic of the RTFTIR used to measure the degree of polymerization of an acrylate-allumina composite material system.

An alumina-acrylate suspension with phenylphosphineoxide (PPO) and hydroxyl-ketone (HK) photoinitiators was sandwiched between two propylene plates. Three stackings of transparent propylene glass sheets with 80μm spacing between the plates were investigated. The stacking allowed for the investigation of degree of cure as a function of cure depth, as well as print through curing effects. Degree of cure was obtained by directing UV light from a light pen at the alumina-acrylate suspension, with an IR beam incident perpendicular on the plate. The IR beam, from a Perkin Elmar FTIR was used to monitor the attenuation of the acrylate double bonds- an indication of photocuring.

Badev et al. reported a polyether acrylate ceramic filled material system for use in stereolithography [30]. The materials system reported consisted of amine modified polyether acrylate (PEAAM) as oligomer, hexane-dioldiacrylate as viscosity modifier, 2,2-dimethoxy-1,2-phenylacetophenone (DMPA) as photoinitiator, and yttria stabilized zirconia, silica or silicon carbide ceramic filler. RTFTIR was used to measure the degree of cure of the ether acrylate reactive oligomer as was done in the previous report. The rheology of the photocurable system was monitored by varying the concentration of the

reactive diluent, and fillers in the material system. Further work reported by Chartier et al. on polyetheracrylate silica-loaded material systems investigated the influence of ceramic loading on rheology, influence of increasing concentration of dispersant on the degree of conversion, influence of HDDA reactive diluent on the degree of conversion etc. In the report, PEAAM was found to have a Newtonian flow behavior; while PEAAM ceramic filled system exhibits a shear-thinning behavior at silica loading below 20%, and shear thickening behavior at higher loadings. Increasing dispersant concentrations form 1-5wt% was found to have no effect on the viscosity of the material system, but the degree of polymerization was found to reduce.

Tomechkova et al. have also developed theoretical models, validated against experimental results, that can be used to predict critical energy (E_c) and Depth of penetration (D_p) in an acrylate silica-loaded material system [31]. In the theoretical model, depth of penetration, a value that indicates the degree of sensitivity of the material system, is expressed in terms of scattering length, concentration and extinction coefficient of photoabsorbers, and the volume fraction of silica. The E_c on the other hand was modeled, with an inhibitor exhaustion model, and found to be a complex function of quinone and oxygen polymerization inhibitors, extinction coefficients and concentration of photoabsorbers, number of photons generating radicals etc.

Recent reports by Halloran et al. have reported the fabrication of 3D molds using the LAMP fabrication technique [32]. In the report an acrylate ceramic loaded composite system was used to fabricate integrally cored molds for investment casting of turbine blades. After photopolymerization and generation of the acrylate-ceramic 3D geometry, a binder burn-out sequence was used to remove the acrylate material. The resulting “green”

ceramic mold was subjected to a sintering process at elevated temperatures to induce the growth of crystals in the mainly amorphous green ceramic part.

1.1.3.3 Laser Interference Lithography

Laser interference lithography has been under the research spotlight lately. The reason for this is the ability to fabricate not only 2D features on substrates, but also the ability to fabricate 3 dimensional features using the concept of interfering beams. This literature review will summarize some of the key concepts of laser interference lithography, as well as organic materials that have been patterned using the interference procedure with relevance to this thesis.

Lasagni et al. reported laser interference induced ablation of a poly(3,4-ethylene dioxythiophene)-poly(4-styrene sulfonic acid) PEDOT:PSS layer on a gold-palladium coated substrate [33]. In this report, the ablation threshold for the PEDOT:PSS films was investigated and found to depend on the thickness of the films when the films are below 70nm thick. However, when the films were over 800nm thick, the ablation threshold became constant. The report further demonstrated the ability to fabricate line arrays of PEDOT:PSS films on a gold-palladium substrate without damaging the substrate, and also the ability to fabricate free-standing PEDOT:PSS films with patterned gold-palladium underlayers.

Fang et al. also reported the patterning and fabrication of polymer nanowires using laser interference ablation [34]. The materials patterned included polyethylene terepthalate (PET), polycarbonate, polyethylene, polypropylene, and polyvinyl acetate. The process involved laser interference ablation on thin films of organic polymers from a nanosecond Nd:YAG laser with a 266nm output wavelength. Nanowires were obtained

by placing the patterned substrates in inductive coupled plasma (ICP) chamber with Ar, O_2 and CF_4 reactive gases. The diameter of the as-fabricated nanowires varied from 100nm to 500nm depending on the periodicity from the laser interference ablation step. The report further demonstrated that the chemical nature of the polymeric nanowires was unchanged after the ICP etching process.

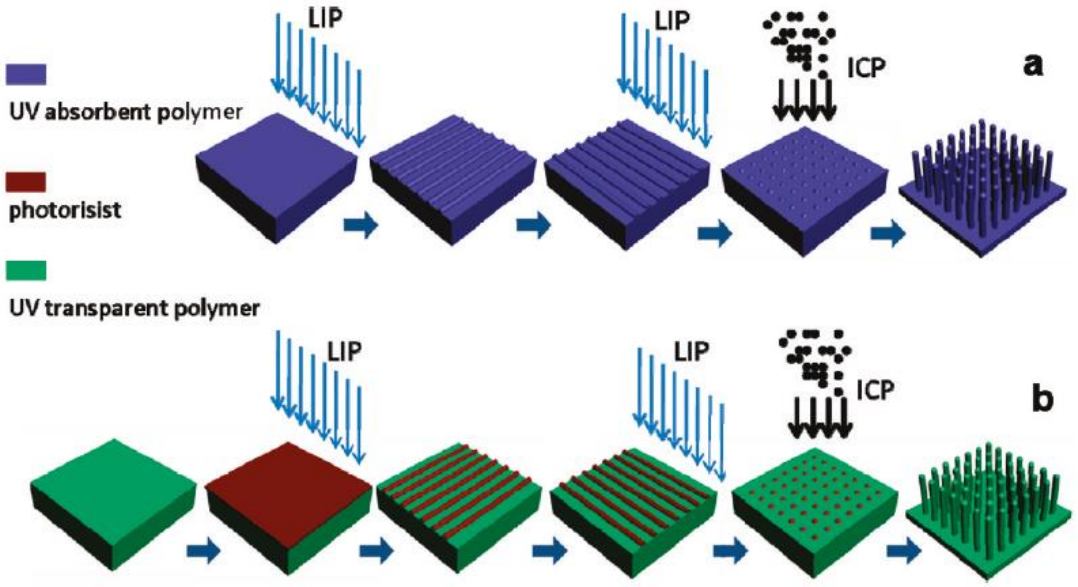

Figure 1.1.3.3.1. Schematic of the procedure used to fabricate polymer nanowires from laser interference ablation and inductive coupled plasma etching [34].

Lasagni et al. also reported the fabrication of periodic features on a pentarythritol triacrylate (PETIA) material system [35]. The material system used for the rapid fabrication of the periodic features contained a N-methyldiethanolamine (N-MDEA) photoinitiator, and a PETIA monomer. Patterning was done at a laser beam output wavelength of 355nm that represents the absorption maxima of the photoinitiator used. Line, square and honeycomb arrays were fabricated on a large scale using the as-

developed material system. The effect of increasing photoinitiator concentration was also investigated in the report.

Large area microlens array fabrication has also been demonstrated with the aid of laser interference lithography. Guo et al. reported the facile fabrication of microlens arrays on a flexible polycarbonate sheet [36]. The polycarbonate sheet, with good absorbance in the deep-UV wavelength band, was patterned with a nanosecond pulsed laser beam with a 266nm output wavelength. The uniformity (near spherical features in a square lattice) and surface smoothness of the as-fabricated microlens arrays was reported. The potential use of the as-fabricated micro lens arrays for parallel large-area patterning of underlying silicon substrates was also demonstrated.

Yuan et al. further demonstrated the ability to use laser interference ablation for the patterned growth of zinc oxide nanowire arrays [37, 38] The procedure involved the direct interference patterning of gallium nitride (GaN) films grown on sapphire substrates. Patterning of the substrate resulted in the generation of periodic square arrays of GaN on sapphire. This was subsequently followed by a low temperature hydrothermal growth of ZnO nanowires on the GaN square arrays. ZnO grows preferentially on GaN rather than sapphire because the lattice mismatch on sapphire is much greater than that on GaN.

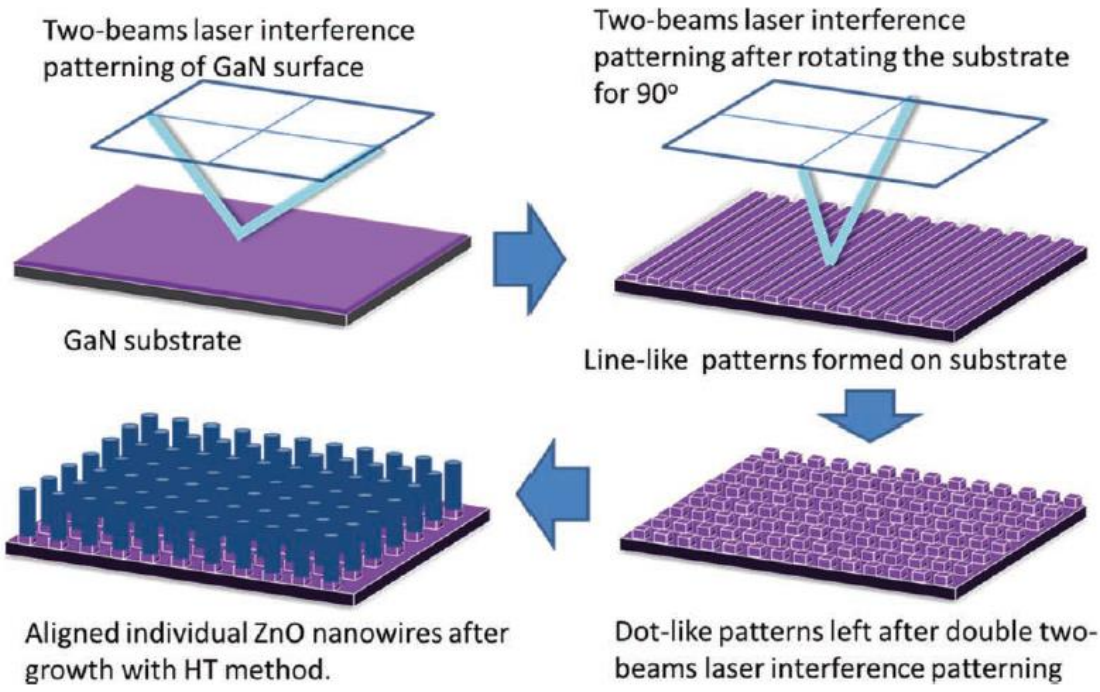

Figure 1.1.3.3.2. Schematic of the Process used to fabricate zinc oxide nanowire arrays from laser interference patterned gallium nitride substrate [37].

1.1 Dissertation Outline

The remainder of this dissertation is divided into 5 chapters.

Chapter 2 provides background information on the scientific fundamentals behind the techniques, and design methods used in this dissertation. This chapter discusses block copolymers: their synthesis and melt-phase behavior properties. This chapter also introduces laser physics, reactive ion etching, as well as the fundamentals of photochemistry and photophysics applicable to materials system design.

Chapter 3 presents a motivation for designing resists based on diblock copolymers. The limitations of conventional photoresists are discussed as well as the apparent advantages of switching to a blockcopolymer type resist. The concept of block copolymer laser interference ablation is introduced as a viable means for the generation

of features with ~30nm resolution. This technique is applied to two commercially available diblock copolymers: PS-b-P4VP and PS-b-PEO. The feature density improvement of patterned PS-b-P4VP block copolymers over commercially available resists is also discussed.

Chapter 4 presents a direct application of laser interference ablation of PS-b-P4VP block copolymer for the generation of functional metallic and ceramic features on various substrates including Si and SiO_2. Metal-loading of the laser-patterned block copolymers is used to generate hierarchical arrays of metallic gold and platinum as well as ceramic iron oxide and palladium oxide nanoarrays. The potential application of the hierarchical arrays in silicon, silicon oxide patterning as well as catalysed growth of nanowires is discussed.

In Chapter 5 patterning of silicon oxide and silicon substrates is demonstrated as one of the application of the patterned arrays of metallic and ceramic features. The fabrication of bluelight emitting silicon oxide nanowires is demonstrated with discussion on the apparent ferromagnetic effect of the resulting features. Super hydrophobic effect of the as-generated nanoscale features on silicon oxide is also demonstrated. Fabricated features on silicon are also presented with a discussion of the potential applications.

Chapter 6 discusses and presents data on vinylether, vinylether-epoxy and epoxy-acrylate material systems designed for LAMP fabrication based on dye sensitized, chemically-amplified, negative tone photoresist that uses radical, cationic and a combination of both for the photopolymerization of ceramic loaded resins. Cure depth measurements, viscosity measurements, TGA characterization, DMA analysis and degree

of cure analysis were done on these composite material systems to determine their potential applications in the LAMP fabrication technique.

Chapter 7 revisits the research objective of this dissertation and summarizes the contributions of this dissertation. Recommendations for future work are also provided.

CHAPTER 2

BACKGROUND

This chapter provides relevant background data on the various materials systems that have been investigated and reported in the literature. The various reaction pathways that have been utilized to synthesize and modify these organic material systems are also provided. Background information on the physics behind phase separation in block copolymers as well as physics governing laser interference ablation is provided. Also provided are background information on the photophysics and photochemistry of light assisted material modification, as well as the physics and chemistry of a plasma reactive ion etch.

2.1 Materials Chemistry Background

In this section, background information is provided on commercially available photoresists and block copolymers. The first section on photoresists discusses the photochemistry that occurs in resists during photoexposure to UV and other light sources. The second section discusses block copolymers and the techniques reported for the synthesis of block copolymers.

2.1.1. Photoresists

Polymeric resists can be divided into several classes based on their sensitivity to a given wavelength. Based on this criterion, resists can be divided into UV resists, e-beam resists, and X-ray resists. UV resists are further divided into near-UV (350-450nm), mid-UV (300-350nm), and deep UV (<300nm) resists. Resists can also be single component

resists or multicomponent resists depending on the composition and need for sensitization or chemical-amplification. Resists can also be classified as positive tone resists and negative tone resists based on the mode of development of the resists after photoexposure. After photoexposure, positive tone resists are developed in solvents that preferentially remove the photoexposed regions, while negative tone resists are developed in solvents that preferentially remove the non-photoexposed regions.

2.1.2. Non Amplified Photoresists

Non-amplified photoresists are resists that generate a single photochemical reaction/ or photo-event after the absorption of a photon. For non-amplified photoresists, quantum efficiency cannot exceed one; and this is a huge disadvantage for industrial scale macro/microfabrication. However, in nano-manufacturing these resists are still utilized for the precise fabrication of nanoresolved features on substrates. Described below are some commercially available non-amplified photoresists and the photochemical reactions they undergo during photoexposure.

2.1.2.1. Polymethyl isopropyl ketone (PMIPK)

This is a single component positive tone photoresist used for deep-UV and e-beam lithography. Upon photolysis, side chain scission from the ketone group results in the generation of metastable radicals. The metastable radiclals then undergo a β-chain scission to generate acyl-stabilized tertiary radicals. The products from the photolysis with a lower molecular weight compared to that of the starting polymer are thus preferentially attacked by a developer solvent than the starting resist.

Figure 2.1.2.1 shows the photolysis reaction mechanism for poly (methyl-t-butylketone). Photodissociation occurs through the formation of metastable t-butyl radicals and a radical ketone group.

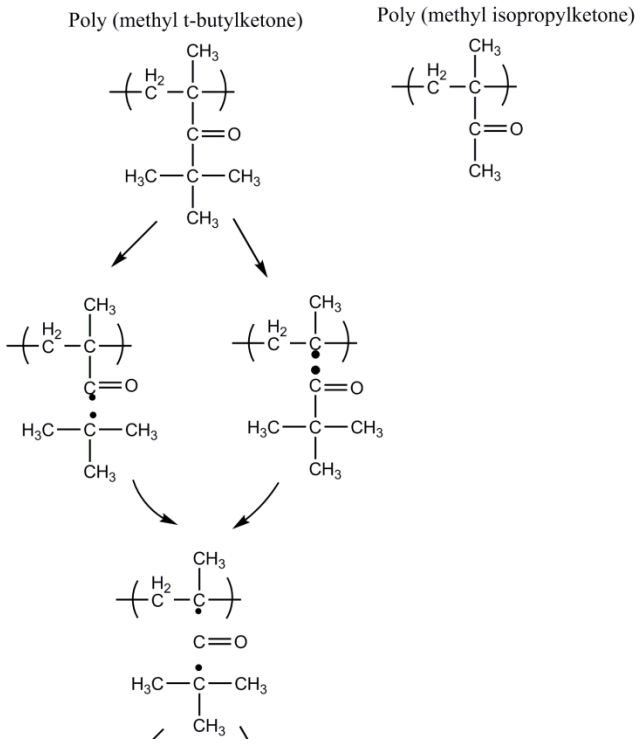

Figure 2.1.2.1 Poly(methyl isopropylketone) and the photochemical reaction equation for the photolysis of poly(methyl t-butylketone).

2.1.2.2. Copolymer of glycidyl methacrylate and ethylacrylate

This is a single component negative tone photoresist with crosslinkable side chains. It was developed for deep UV and e-beam lithography. Figure 2.1.2.2 shows the chemical formula and photochemical reaction equation for a glycidyl methacrylate and ethylacrylate copolymer. The photoresist upon exposure to radiation forms an anion via the oxirane ring opening. The anion formed can attack other oxirane groups causing subsequent polymerization and insolubilization. The material system however suffers from dark-curing/post-exposure reactions that limit its use for nano fabrication.

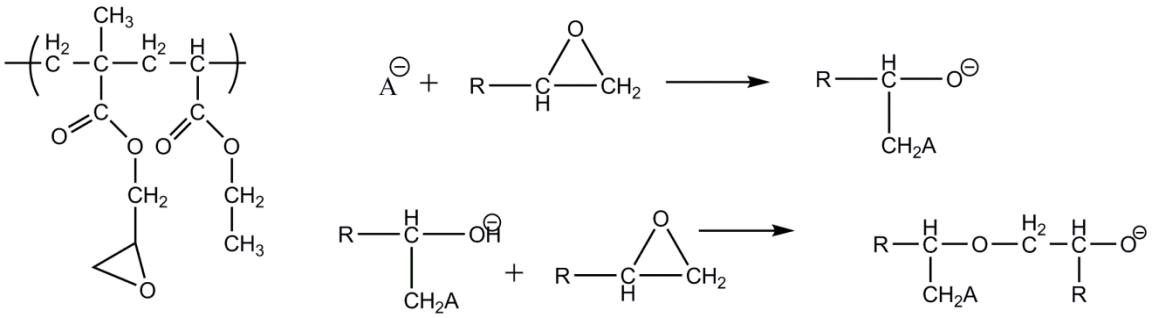

Figure 2.1.2.2 Photochemical reaction equations for the photolysis of a copolymer of glycidyl methacrylate and ethylacrylate.

2.1.2.3. Poly (4-formyloxystyrene)

This is a single component photoresist designed for deep-UV curing. It is a dual tone resist that undergoes a photo-fries rearrangement upon exposure to deep-UV light. A photofries rearrangement involves the cleavage of a carbonyl side group followed by hydrogen abstraction. This results in the release of CO gas and the generation of a phenolic pendant group. The change in polarity of the resist after photoexposure means that depending on the solvent used, the photoresist can either serve as a positive tone or a negative tone resist. Poly(4-formyloxystyrene) is soluble in organic solvents like chlorobenzene and anisole, while the poly(4-phenolstyrene) is soluble in polar solvents like alcohols and aqueous bases.

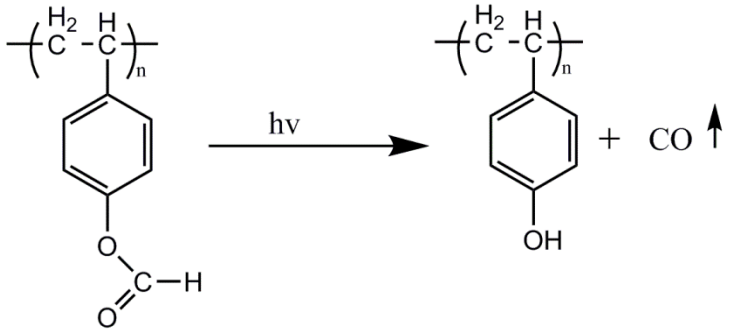

Figure 2.1.2.3.1 Photochemical reaction equation for the photofries rearrangement of poly(4-formyloxystyrene).

The photofries reaction can also be utilized in systems containing poly (phenylacrylate) resist. The photofries reaction in this case converts the starting material into ortho-poly (hydroxyphenone) and para-poly(hydroxyphenone) pendant groups. The photochemical product is thus polar and soluble in polar solvents unlike the non-polar starting material.

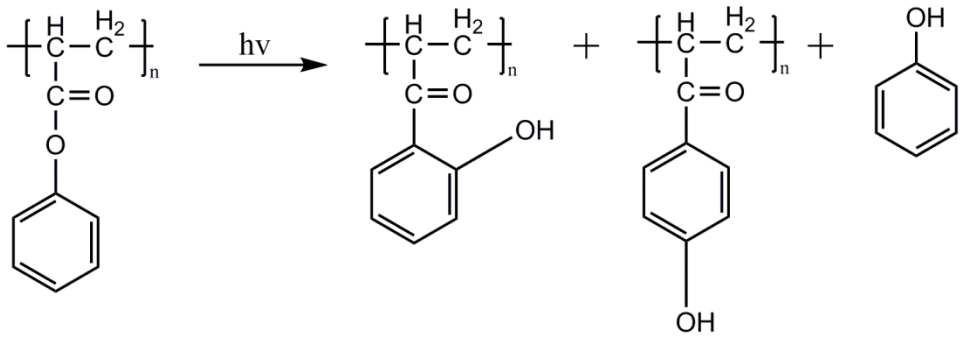

Figure 2.1.2.3.2 Photochemical reaction equation for the photofries rearrangement of ortho-poly(hydroxyphenone) to para-poly(hydroxyphenone).

2.1.2.4. Cis-1,4,-polyisoprene and bisazide(4,4'-diazidobenzophenone) photoresist

This is a dual component resist based on a diazide functional group, and an unsaturated polymer. Cyclized rubber, usually soluble in non-polar solvents like toluene and xylene, upon exposure to UV light, becomes insoluble due to the crosslinking of the unsaturated double bonds. Bisazide(4,4'-diazidobenzophenone), the photoactive component in the resist, upon UV exposure, generates a singlet excited state that cascades via intersystem crossing to form a triplet excited state. The excited triplet breaks down rapidly forming azonium radicals that initiate the photo crosslinking reactions.

The bisazide photochemical reaction mechanism is shown in figure 2.1.2.4.

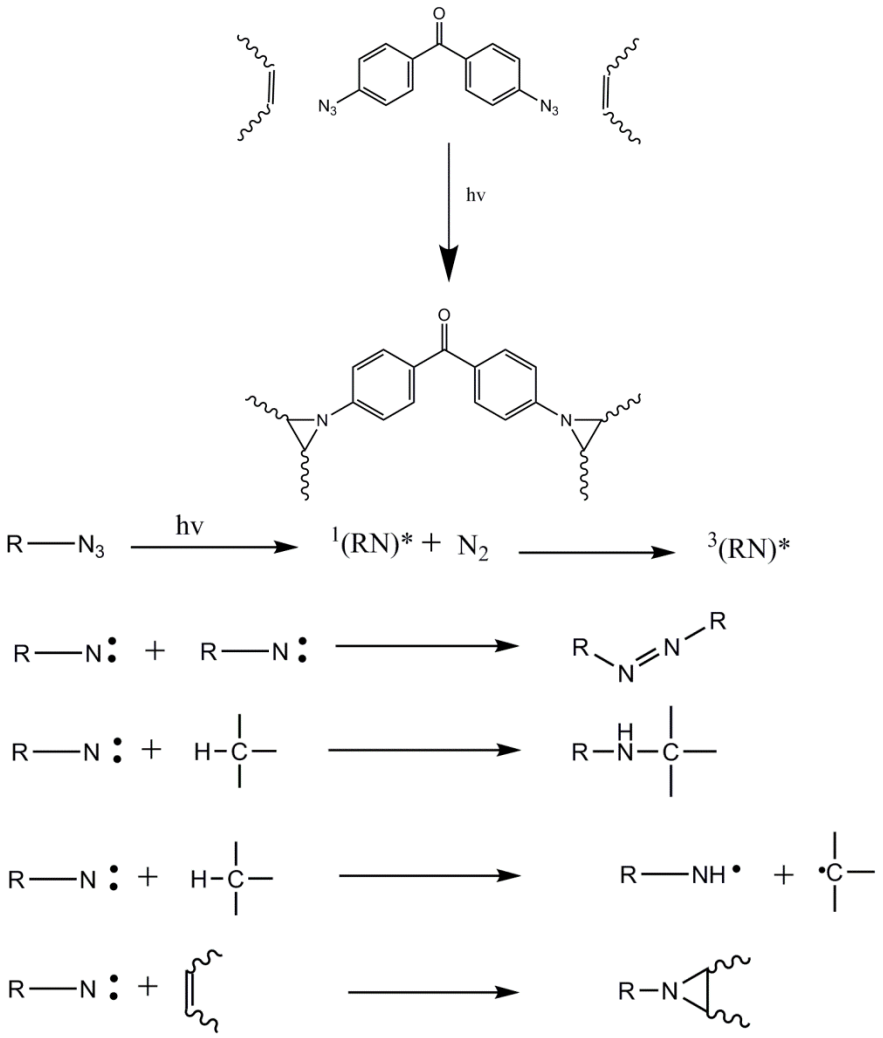

Figure 2.1.2.4 Photochemical reaction mechanism for the photolysis of a bisazide functional group and subsequent polymerization of cis-1,4-polyisoprene.

2.1.2.5. Diazonaphthoquinone:Novolac resist

This is also a dual component, positive tone resist designed to operate in the UV wavelength spectrum. Diazonaphthoquinone, the photoactive compound in this resist, serves as a dissolution inhibitor in aqueous base and other polar solvents. However, after exposure to UV light, a carbene intermediate of the sensitizer is formed. The carbene intermediate undergoes a Wolff rearrangement to generate a ketene group. Ketene reacts with water to form an indene-carboxylic acid. With these transformations- transformation

from a carbene to a carboxylic acid- the photoexposed region of the film becomes soluble in aqueous base.

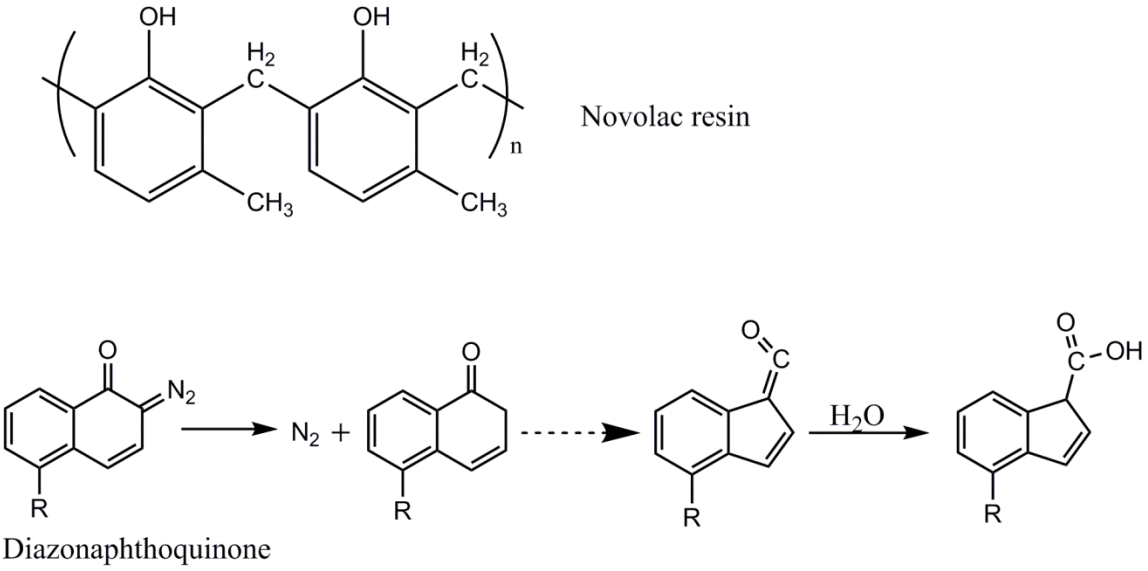

Figure 2.1.2.5.1 The novolac resin and a photochemical reaction mechanism showing Wolffe rearrangement after photolysis of diazonaphthoquinone.

Because diazonaphtoquinone is opaque to deep UV light, several analogs of the diazonaphthoquinone dissolution inhibitors have been designed and developed for deep UV lithography. An example is 2-diazo-1,3-diketocyclohexane-5-carboxylic ester shown in figure 2.1.2.5.2.

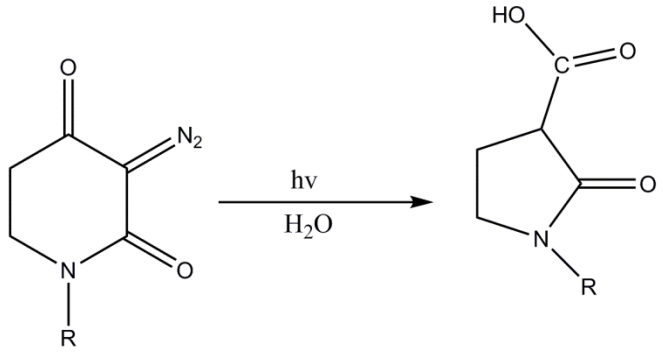

Figure 2.1.2.5.2 Photochemical reaction equation showing Wolffe rearrangement after photolysis of a diazodiketone derivative of cyclohexane.

2.1.3. Amplified Photoresists

Quantum yield plays a crucial role in the design and development of new materials sensitive to deep-UV, x-ray, and e-beam lithography manufacturing techniques. In non-amplified photoresists, where one absorbed photon results in a single photochemical reaction event, quantum yields cannot exceed one even for a perfect resist. However for industrial scale manufacturing, a quantum yield of over a hundred is required to make fabrication both economical and profitable. To achieve this, in 1982 the concept of chemically amplified photoresist was developed to improve the sensitivity of resists. In chemically amplified photoresists, one absorbed photon leads to a cascade of photochemical reactions that ultimately lead to the generation of a desired photochemical product. The photochemical product either leads to differential dissolution or inhibition when in contact with a solvent or can serve as a low molecular weight adducts or photopolymerized adduct of the initial resist. Chemically amplified photoresists are multicomponent resists containing a photoinitiator minor component and a matrix major component.

Described below are some of the commercially available chemically amplified photoresists with their photochemical reactions.

2.1.3.1. Styrene-allylglycidylether resist with an onium salt photoinitiator

This negative tone resist was developed for use in the mid UV wavelength spectrum. A generalized cationic photoinitiation mechanism is shown in figure 2.1.3.1. Upon exposure to UV light, a Bronsted acid or a Lewis acid is generated by the cationic photoinitiator. The acidic proton generated after photoexposure attacks the matrix material containing epoxy ring functional groups, opening the epoxy ring and setting up a cascade of reaction that results in the polymerization of the epoxy matrix.

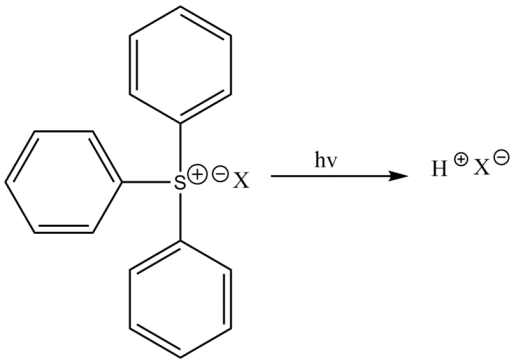

Figure 2.1.3.1.1. photochemical reaction euqation for the photolysis of triphenylonium salt and the generation of acidic proton.

A styrene-allylglycidyl ether copolymer, shown in figure 2.1.3.1.2, upon exposure to UV light with an onium salt photo-initiator will photopolymerize to form a network that is insoluble in alkaline solutions. The starting copolymer will dissolve faster in the alkaline solution.

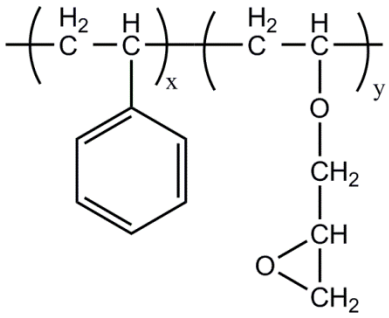

Styrene-allyl glycidyl ether

Figure 2.1.3.1.2. Chemical formula for styrene-allyl glycidylether.

Different copolymer adducts containing functional epoxy rings have also been designed and developed for cationic photo-polymerization following the same mechanism as styrene-allylglycidyl ether. An example is a polymeric episulphides.

2.1.3.2 Poly[4-(2-hydroxy-2-propyl)styrene] resist with a triphenylsulfoniumtriflate photoinitiator

This dual tone resist was developed for use in the mid UV wavelength spectrum. Although triphenylsulfonium triflate is the photoinitiator/photoacid generator used with this resist here, other types of photoacid generators (PAG) have also been developed for use in the photopolymerization of poly[4-(2-hydroxy-2-propyl)styrene]. The starting material is soluble in polar solvents due to presence of OH side group chains as shown in figure 2.1.3.2. However, photo-exposure of the material system to UV light generates photoacids that catalyse an intramolecular dehydration reaction shown in figure 2.1.3.2. The resulting product is an olefin that is non polar, and thus soluble in xylene and other non-polar solvents.

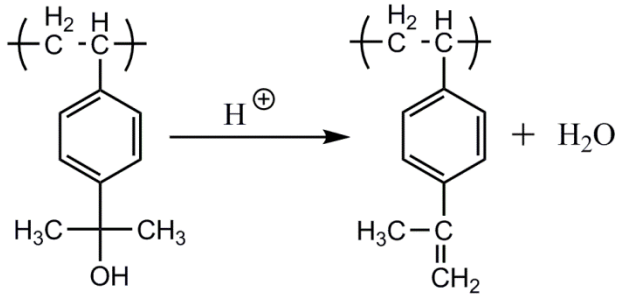

Figure 2.1.3.2. Photochemical reaction equation for acidic proton induced dehydration of poly[4-(2-hydroxy-2-propyl)styrene].

2.1.3.3 Poly (4-t-butoxycarbonyloxystyrene) resist and triphenylsulfoniumtriflate photoinitiator

This is a dual tone resist developed for deep-UV, e-beam and x-ray lithography. Triphenylsulfonium hexafluoroantimonate is the PAG used with this photoresist. Upon exposure of the resist to UV light the photoinitiator undergoes a reaction that generates acidic protons. The acidic protons promote scission of the tBOC side groups in an acidolysis type reaction shown in figure 2.1.3.3.1. Upon scission of the tBOC side group, the resist changes polarity. The tBOC side group, however continues to break down

forming carbon dioxide and 1,1-dimethylethylene final products. The acidic proton is regenerated at the end of the reaction which results in the amplification effect as desired in the resist system.

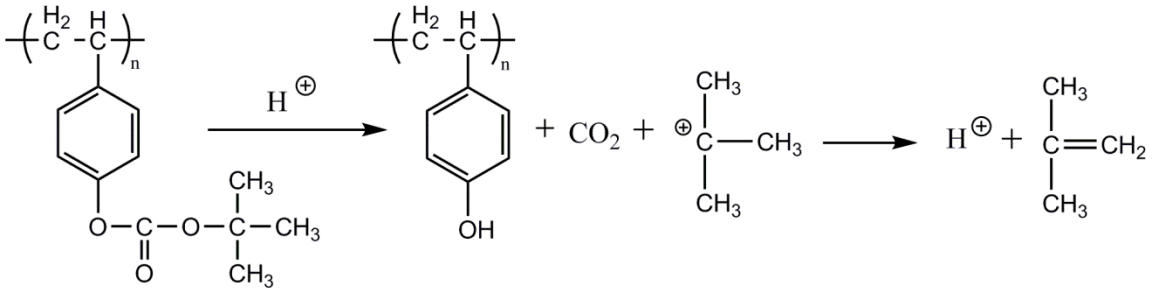

Figure 2.1.3.3.1. Photochemical reaction equation for acidic proton induced deprotection of poly(4-t-butoxycarbonyloxystyrene).

Resists have also been developed that undergo main chain scission upon photoexposure to X-rays in the presence or absence of PAG. Example of an X-ray sensitive resist is poly(4-t-butoxycarbonyloxystyrene sulfone) shown in figure 2.1.3.3.1. Upon exposure to X-ray beams the main chain scission of the resist generates sulphur oxide. The Sulphur oxide generated when exposed to water generates a strong acid that transforms the resist from a non-polar to a polar state. The photomodified resist is soluble in polar solvents while the starting material is soluble in non-polar solvents.

The reaction equation for X-ray induced main chain scission and deprotection of poly(4-t-butoxycarbonyloxystyrene sulfone) resist is shown in figure 2.1.3.3.2.

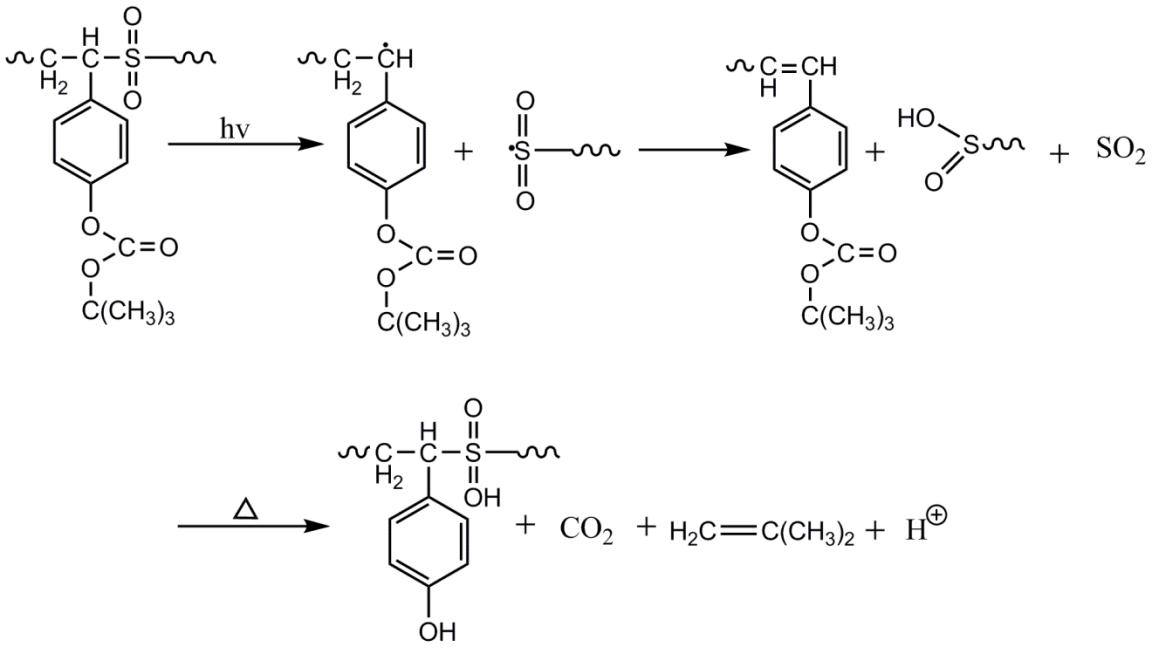

Figure 2.1.3.3.2. Photochemical reaction equation for X-ray induced chain scission of poly(4-t-butoxycarbonyloxystyrene sulfone) leading to the generation of a photo acid.

2.1.3.4. Poly(t-butyl 4-vinylbenzoate), Poly(t-butyl Methacrylate) photoresists and PAG photoinitiator

Resists with an ester or ether functional group, that form relatively stable carbo-cations upon A_{AL}-1 acidolysis, have also found use as dual tone photoresists. Exposure of such resist to UV or e-beam generates a photoacid that catalyses the heterolysis of the C-O ester or ether bond. Cleavage of the bond generates metastable chemical species that later undergo a β-proton elimination reaction forming an olefin and an acid as shown in the photoreaction mechanism in figure 2.1.3.4.

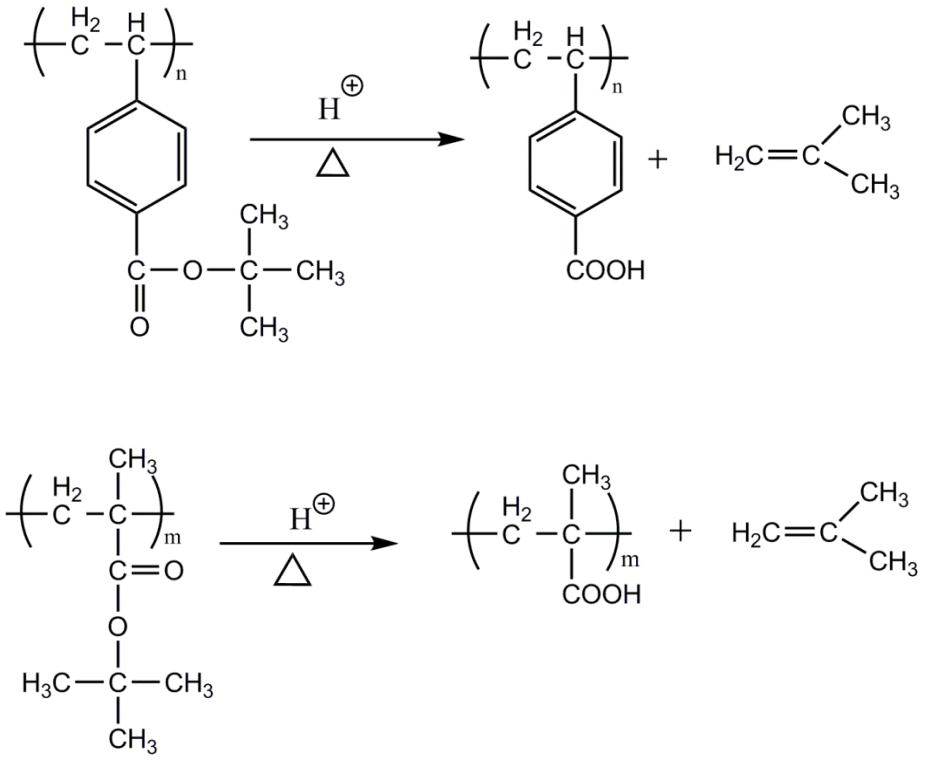

Figure 2.1.3.4. Photochemical reaction equation for acidic proton induced deprotection of (A) poly(t-butyl-4-vinylbenzoate) (B) poly(t-butylmethacrylate).

2.1.3.5 Poly[4-(trimethylsilyslester)styrene], poly[4-(tetrahydropyranylester)styrene] photoresists and PAG photoinitiator

Hydrolysis of protected poly(4-hydroxystyrene) polymers have also been utilized for the design of resists for deep-UV lithography. These positive tone resist are used for feature fabrication after photo-exposure and development with a tetramethylammonium hydroxide solvent. Photo-exposure of the resist containing a PAG generates acidic protons that catalyze the breakdown of the protective side groups on the 4-hydroxystyrene main chain. Once the protective groups are removed, the resist becomes polar and is susceptible to dissolution in polar solvents. The photochemical reaction equation for UV induced deprotection of poly[4-(trimethylsilylester)styrene] and poly[4-(tetrahydropyranylester)styrene] is shown in figure 2.1.3.5.

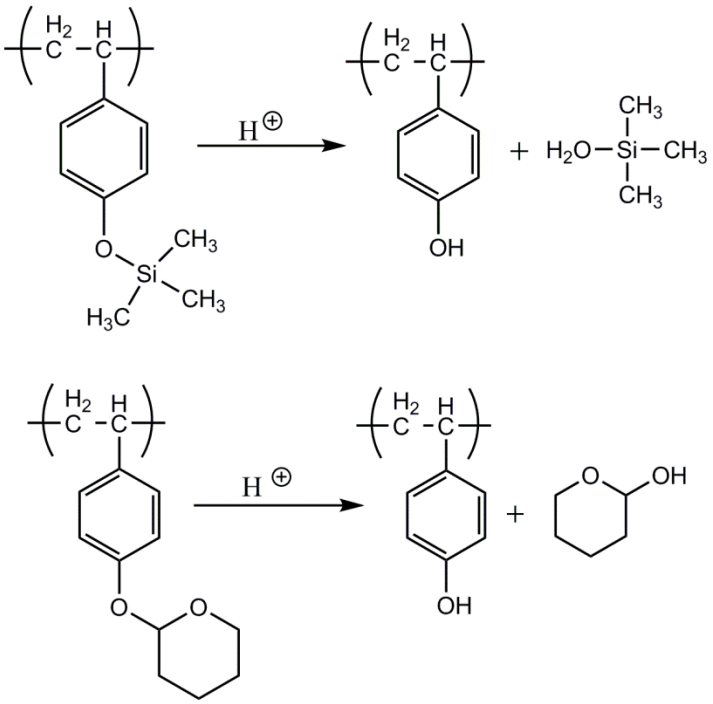

Figure 2.1.3.5. Photochemical reaction equation for cationic deprotection of (A) poly[4-(trimethylsilyslester)styrene and (B) poly[4-(tetrahydropyranylester)styrene].

2.1.3.6 Poly[3-methyl-2-(4-vinylphenyl)-2,3-butanediol) resist and triphenylsulfonium triflate photoinitiator

This is a dual tone resist designed to operate at deep-UV wavelength spectrum. Upon photoexposure of the resist, acidic protons are generated that catalyze pinacol rearrangement of the side chain resulting in the formation of an aldehyde. The aldehyde inhibits dissolution in aqueous bases and thus provides a negative replica of the exposure pattern. Figure 2.1.3.6 shows a photochemical reaction involving a pinacol rearrangement on poly(3-methyl-2-(4-vinylphenyl)-2,3-butanediol).

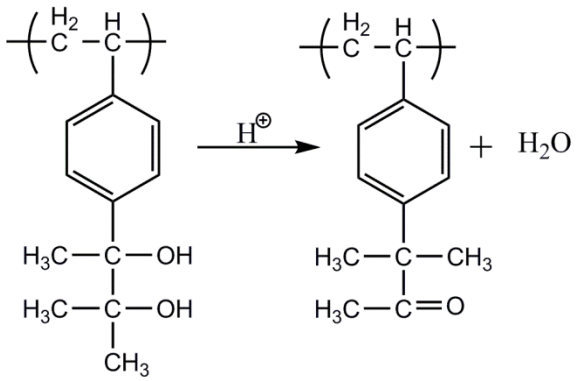

Figure 2.1.3.6. Photochemical reaction equation for cationic induced pinacol rearrangement in poly(3-methyl-2-(4-vinylphenyl)-2,3-butanediol).

2.1.4 Block copolymers [39]

Block copolymers are the product of the covalent bonding of two or more chemically distinct polymer blocks. The covalent bonding between two or more blocks in a block copolymer prevents macroscopic phase separation, but allows for microscopic/nanophase separation. The domain spacing between the phase-separated blocks varies from 10-100nm, and the feature type can vary from gyriodic, lamellar, hexagonal, to vertical cylindrical, and cubic arrangement.

Although block copolymers have not found any direct or specific use in industrial scale photolithography, one of the aims of this thesis is to demonstrate the potential for block copolymers to be used as a single component positive tone resist. Block copolymers, especially those containing a polystyrene block, can be photomodified at deep-UV wavelengths of 266nm [40, 41]. A major advantage of using block copolymers over conventional photoresists is that they can serve as resists that do not require any post-exposure development steps i.e. as dry resists.

In this sub-section, general approaches to the synthesis of commercially available block copolymers will be discussed, while the next sub-section will discuss the physics governing phase separation in block copolymers.

2.1.4.1 Synthesis of Block Copolymers

Major advances in the synthesis of small and large organic molecules have resulted in an increase in the variety of block copolymers commercially available. The types of block copolymers that have been reported in the literature include linear diblock copolymer type A-b-B, triblock copolymers type A-b-B-b-A, triblock terblock copolymers type A-b-B-b-C, star-block copolymers and graft block copolymers.

Block copolymers can be synthesized using different mechanisms. In this section we will be discussing some of the techniques that have been used to synthesize block copolymers. Examples of the block copolymer synthesized using the mechanism is provided along with the general procedure for synthesizing the block. The reaction mechanisms to be discussed for synthesizing block copolymers include:

a) Living Anionic polymerization,

b) Living cationic polymerization,

c) Living free radical polymerization,

d) Group transfer polymerization

e) and Ring opening metathesis polymerization (ROMP).

2.1.4.1.1 Living Anionic polymerization

Living anionic polymerization mechanism is used to synthesize block copolymers with well-defined molecular weight, composition, and architecture; provided that the termination of living anions by impurities and chain transfer reactions is well controlled.

Living anionic polymerization mechanism is initiated with organo-metallic compounds like tert-butyl lithium, n-butyl lithium, and some aluminum containing compounds. A requisite for choosing any living anionic initiator is that it must react with the starting material -monomers- at a faster rate, during the initial stages of the reaction, than it does react with the propagating chains of the polymer. This condition is required for the controlled length of the polymer chains in the reaction mixture at every point in time during the anionic polymerization.

2.1.4.1.1.1 Linear A-b-B diblock copolymers via anionic polymerization

In the literature, linear A-b-B diblock copolymers have been synthesized via the sequential addition of monomers to a reaction system. The polymerization reaction is terminated via the addition of a non-solvent that precipitates the desired block copolymer products from solution. Many styrene based diblock copolymers are synthesized using the anionic polymerization mechanism. Examples of diblock copolymers synthesized using anionic polymerization include: Polystyrene-b-polyisoprene [42], polystyrene-b-butadiene [43], polystyrene-b-polymethylmethacrylate [44], polystyrene-b-2-polyvinylpyridine [45], polystyrene-b-4-polyvinylpyridine [46], polystyrene-b-polyethyleneoxide [47], polystyrene-b-poly-ε-caprolactone, polystyrene-b-polyferrocenyldimethylsilane [48], polystyrene-b-polydimethylsiloxane [49].

The procedure to synthesize diblock copolymers containing a styrene block involves the sequential addition of styrene monomers with an organolithium initiator followed by the addition of other monomers. The chemical reaction steps for the synthesis of a polystyrene-b-polyisoprene block copolymer are shown in figure 2.1.4.1.1.1.1.

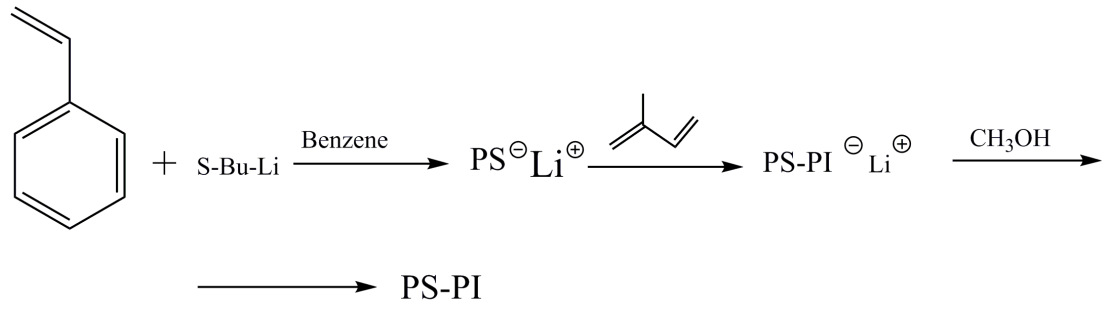

Figure 2.1.4.1.1.1.1. Scheme showing the reaction steps to synthesize polystyrene-b-polyisoprene.

Polystyrene-b-polysisoprene was synthesized by dissolving styrene monomer in benzene at -78ºC, followed by the addition of s-butyllithium. After homopolymerization of all the available starting monomers, isoprene is added to the reaction mixture. The living anionic reaction chain is quenched with methanol at the end of the reaction.

One main issue encountered during the synthesis of PS-b-PMMA diblock copolymer, with living anionic polymerization, is the attack of the carbonyl group present in the methacrylic monomer. To direct the attack of the anion to the double bond in the methacrylic acid, the living anion after homopolymerization of styrene can be rendered less reactive i.e sterically hindered via the addition of a non-homopolymerizing reagent-diphenylethylene (DPE). Figure 2.1.4.1.1.1.2 shows the chemical reaction steps for the synthesis of a polystyrene-b-polymethylmethacrylate block copolymer.

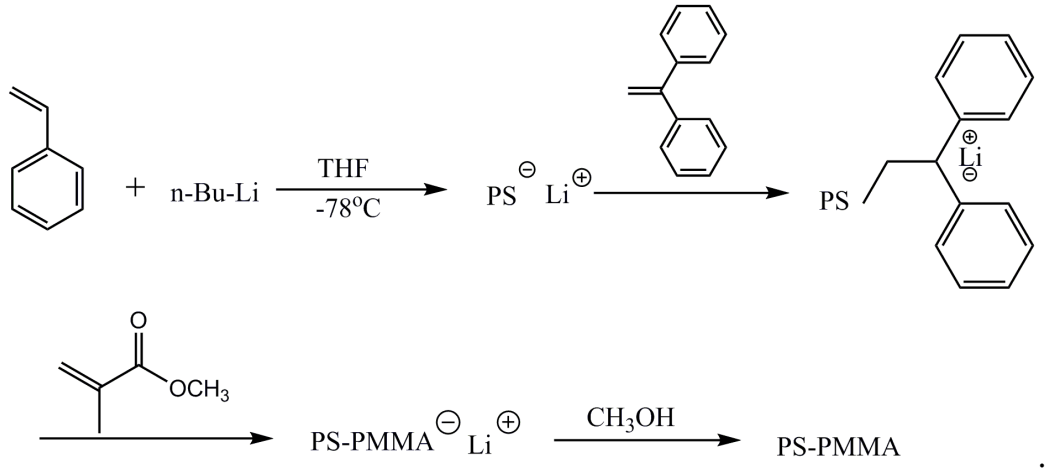

Figure 2.1.4.1.1.1.2 Scheme showing the reaction steps to synthesize polystyrene-b-polymethylmethacrylate.

The first step in the synthesis of PS-b-PMMA, is the homopolymerization of the styrene molecule with n-butyllithium anionic initiator. DPE is then added to the homopolymerization mixture to reduce the reactivity of the anion by forming a sterically hindered anion. Methylmethacrylate monomers are then introduced into the reaction mixture to form a diblock copolymer. The reaction is quenched with methanol.

Another important class of engineering block copolymers comprises of diblocks containing a 2-vinylpyridine or a 4-vinylpyridine block in the polymer chain. Diblock copolymers containing a vinylpyridine component are unique because the vinylpyridine component can complex with metallic salt solution. Complexation is possible via the donation of unshared electrons present on the nitrogen in the hetero-aromatic ring. Nitrogen in vinylpyridine has two free lone pair of electrons because it does not contribute these electrons to the aromatic ring. Diblock copolymers with 4-vinylpyridine component usually form complexes with metallic salt faster than diblock copolymers with 2-vinylpyridine component. The reason for this is because there are less steric

interactions from the polymer backbone chain in the 4-vinylpyridine component of a PS-b-P4VP block copolymer compared to the 2-vinylpyridine component of a PS-b-P2VP block copolymer.

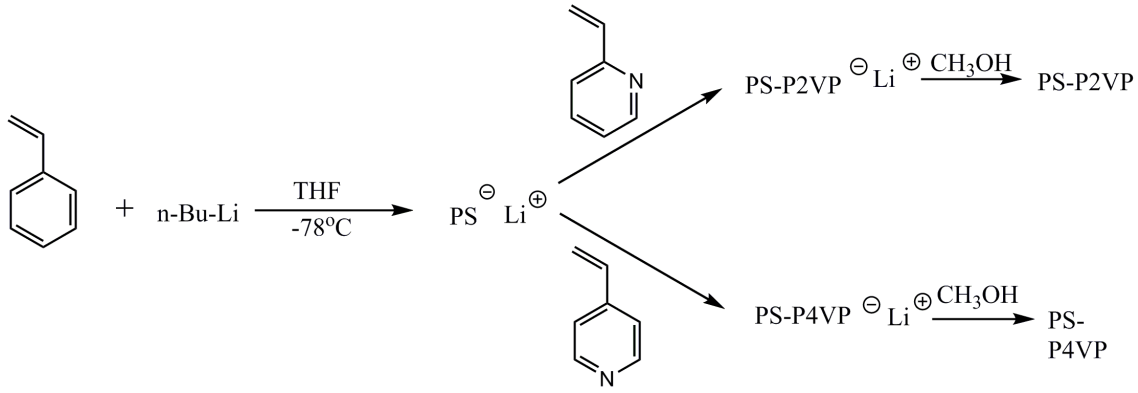

Figure 2.1.4.1.1.1.3. Scheme showing the reaction steps to synthesize polystyrene-b-poly-2-vinylpyridine and poly-4-vinylpyridine.

The first step, in the synthesis of PS-b-P4VP or PS-b-P2VP is the homopolymerization of the styrene molecule with a low molecular weight organometallic initiator. This is followed by the addition of either 2-vinylpyridine or 4-vinylpyridine monomers. The living anionic chain is terminated with methanol.

Another important class of diblock copolymers are amphiphilic block copolymers i.e block copolymers having a hydrophilic block and a hydrophobic block. The hydrophilic section in the block copolymer is synthesized from water compatible/soluble polymer blocks like polyethyleneoxide, polycaprolactone, polylactic acid etc. The hydrophobic section is made from blocks soluble in non-polar solvents like polystyrene, polyisoprene. Block copolymers having both hydrophobic and hydrophilic sections form micelles in solution preferential to one of the blocks. Because the core section within the micelle is protected from the external solvent, micelles are a means for targeted drug

delivery while protecting the delivery material during transportation within the host organism.

An engineering and commercially available block copolymer is the polystyrene-b-polyethyleneoxide. The organometallic initiators reported in the literature for the synthesis of PS-b-PEO are organo-potasium and organo-sodium initiators. They are used because the oxirane monomer, the precursor to generating polyethyleneoxide, is only soluble in polar solvents like THF. Figure 2.1.4.1.1.1.4 below shows the reaction steps for the synthesis of polystyrene-b-polyethyleneoxide block copolymer.

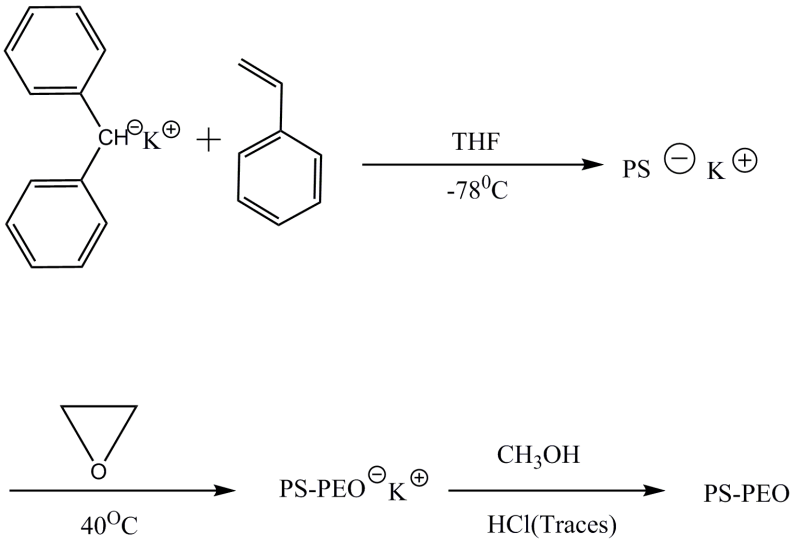

Figure 2.1.4.1.1.1.4. Scheme showing the reaction steps to synthesize polystyrene-b-polyethyleneoxide.

Another commercially available amphiphilic block copolymer is polystyrene-b-poly-ε-caprolactone. Amphiphilic block copolymer containing crystallizable ε-caprolactone can be synthesized following the reaction steps shown in figure 2.1.4.1.1.1.5. Polymerization of the styrene monomer is done using an s-butyl lithium initiator. After homopolymerization of the styrene monomer, the living anion is made less reactive and

more sterically hindered via the addition of DPE. After the addition of DPE, ε-caprolactone monomer is added to the reaction mixture. The reaction is usually terminated a few minutes after the addition of ε-caprolactone to prevent unwanted reactions that can lead to the degradation of the polymer chain.

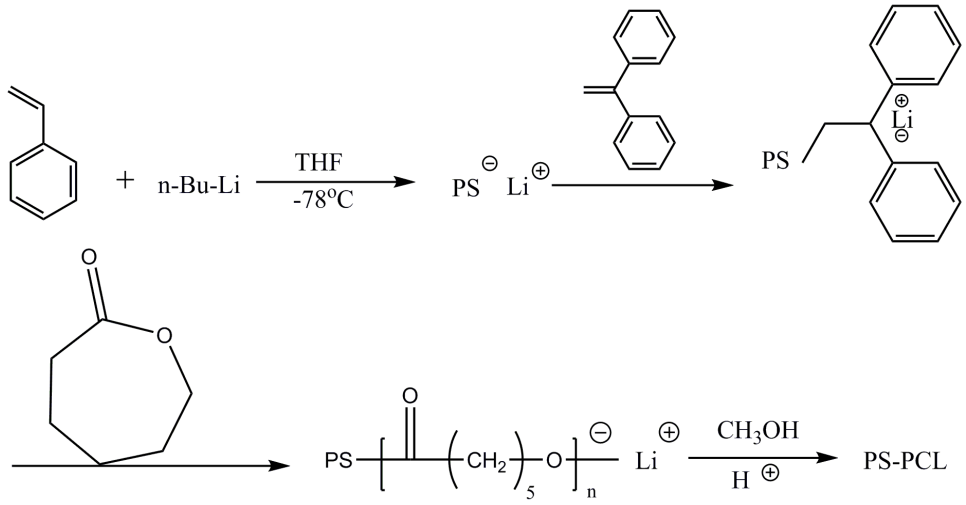

Figure 2.1.4.1.1.1.5. Scheme showing the reaction steps to synthesize polystyrene-b-poly-ε-caprolactone.

Diblock copolymers with very strong interaction between the two blocks are desirable for engineering applications. Block copolymers with such interactions easily phase separate into various morphologies without a need for extended temperature annealing. Strong interaction between different blocks in a block copolymer has a maximum value when one of the blocks is entirely made up of organic materials like PS,PMMA,PEO while the other block is made up of inorganic-organic materials. The highest reported interaction parameter between two blocks in a block copolymer was reported for polystyrene-b-polydimethylsiloxane (PS-b-PDMS) with a value of 0.26.

Other block copolymers like PS-b-PMMA has an interaction parameter value of 0.06, while PS-b-P2VP has an interaction parameter value of 0.18.

The first step in the synthesis of diblock copolymers containing a siloxane block is the homopolymerization of the organic block. As shown in figure 2.1.4.1.1.1.6, homopolymerization of isobutylene is first carried out using an s-butyl lithium initiator at a 40ºC temperature. After homopolymerization of the organic block, the reaction mixture is cooled to -20ºC followed by the addition of purified siloxane monomer. The reaction is terminated by the addition of trimethylsilyl chloride.

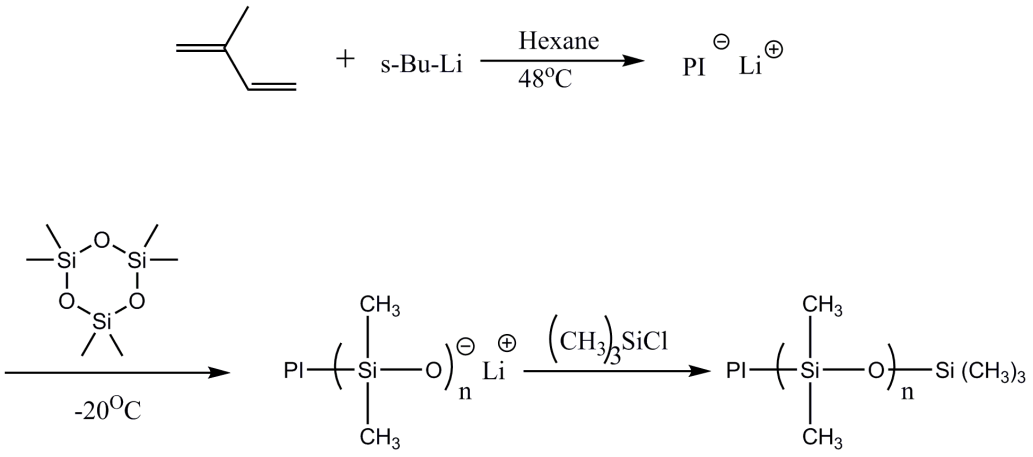

Figure 2.1.4.1.1.1.6. Scheme showing the reaction steps to synthesize polyisoprene-b-polydimethylsiloxane.

Block copolymers containing iron and silicon in a section of the block have been reported in the literature. These engineering materials demonstrate increased resistance to reactive ion etching because of the presence of iron and silicon inorganic materials. A polyferrocenyldimethylsilane-b-polymethylmethacrylate block copolymer is an example of such diblock copolymer. Figure 2.1.4.1.1.1.7 below shows the reaction steps for the synthesis of PFS-b-PMMA. The first step in the synthesis of PFS-b-PMMA diblock

copolymer is the homopolymerization of the ferrocene ring with a butyl lithium initiator. Addition of 1,1-dimethylsilacyclobutane (DMSB) to the reaction mixture allowed for the incorporation of the silane containing group into the propagating polymer block. DPE, a non-homopolymerizing monomer, is then added to the reaction mixture to create steric hindrance and thus prevent any nucleophilic attack of the carbonyl group present in the methacrylate monomer. Methacrylate monomers are added to the reaction mixture and the polymerization reaction is terminated with methanol.

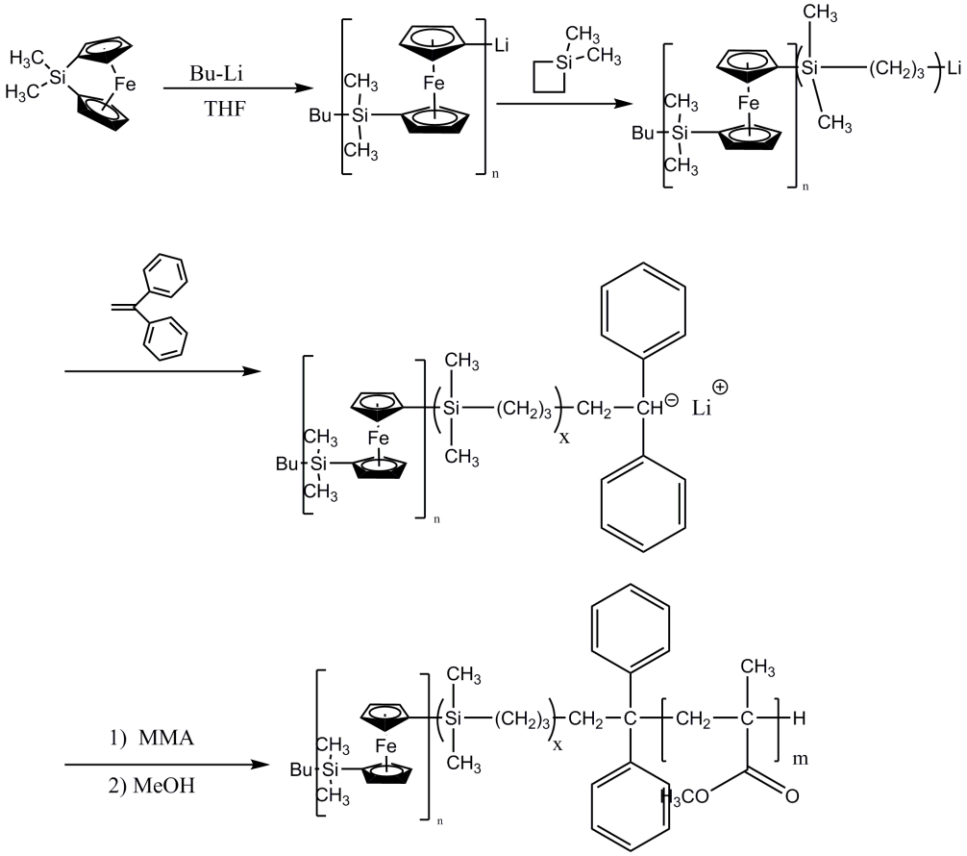

Figure 2.1.4.1.1.1.7. Scheme showing the reaction steps to synthesize polyferrocenyldimethylsilane-b-polymethylmethacrylate.

2.1.4.1.1.2 Linear triblock copolymer via living anionic polymerization [50, 51].

Although we have previously discussed diblock copolymer synthesized through living anionic polymerization, linear triblock copolymers can also be synthesized using living anionic polymerization. Linear triblock copolymers of type A-B-A have been synthesized via the sequential addition of monomers to a reaction mixture using living anionic polymerization.

A linear triblock copolymer, polystyrene-b-polybutylenediene-b-poystyrene, PS-b-PBd-b-PS, was synthesized using a difunctional organo-lithium anionic initiator 1,3-bis(1-phenylethenyl)benzene (PEB). When an organolithium compound is introduced to the difunctional initiator, in the presence of 1,3 dibutylene monomer, an homopolymer with two anionic ends is formed. Another monomer, styrene monomer, is then added to the reaction mixture to form the end group A-B-A triblock copolymer. Figure 2.1.4.1.1.2.1 below shows the reaction steps for the synthesis of polystyrene-b-polybutylenediene-b-polystyrene block copolymer.

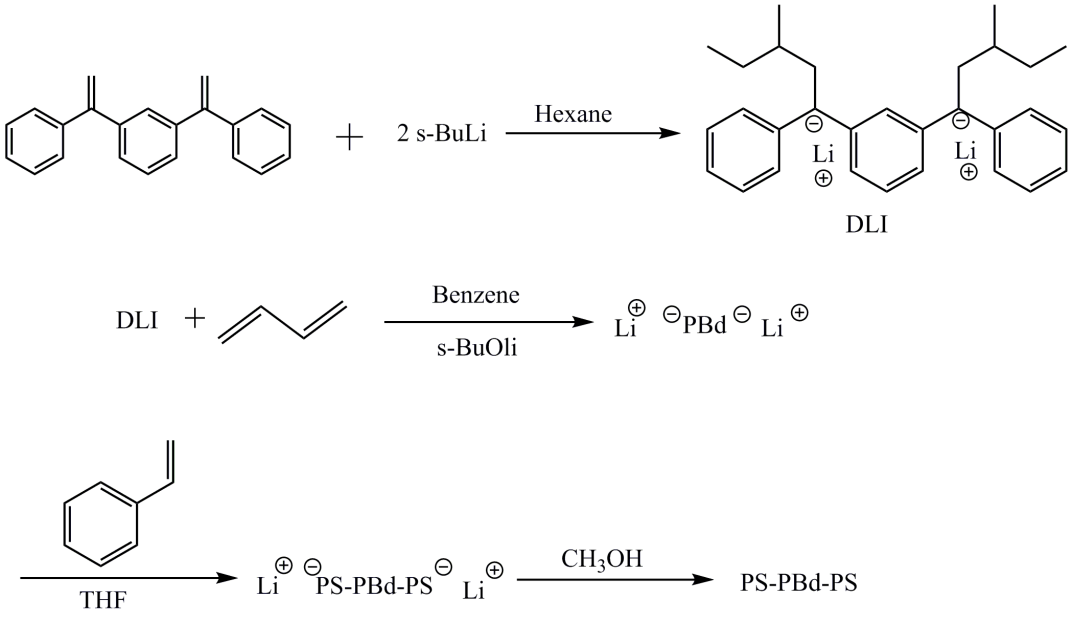

Figure 2.1.4.1.1.2.1. Scheme showing the reaction steps to synthesize polystyrene-b-polybutylenediene-b-polystyrene triblock copolymer.

Living anionic polymerization can also be utilized for the synthesis of linear triblock copolymer of type A-b-B-b-C. This can be done via the sequential addition of different monomeric units to the growing living chain as shown figure 2.1.4.1.1.2.2. To synthesize a polystyrene-b-polyisoprene-b-poly-2-vinylpyridine block copolymer (PS-PI-P2VP), sequential addition of PI to a homopolymerized PS reaction mixture followed by styrene monomers is sufficient. The need for a difunctional initiator is eliminated since the living anion can continue and sustain the growth of the block copolymer chain after each step.

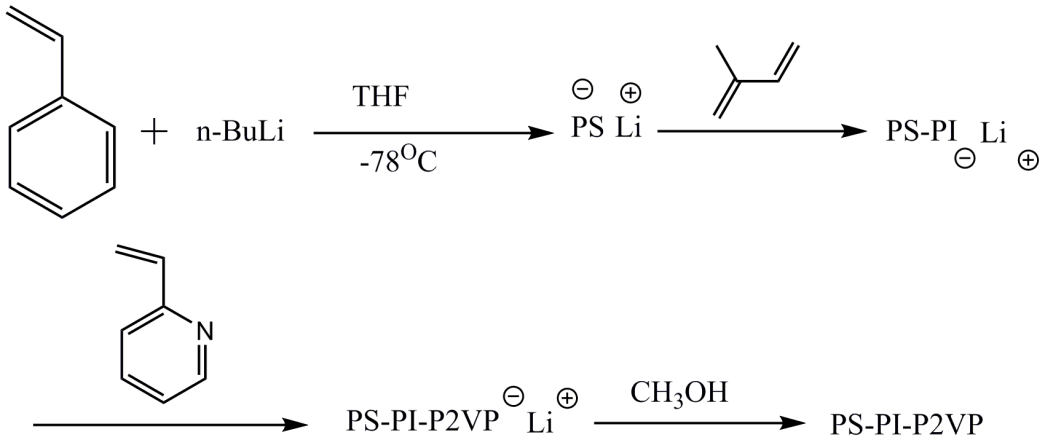

Figure 2.1.4.1.1.2.2. Scheme showing the reaction steps to synthesize polystyrene-b-polyisoprene-b-poly-2-vinylpyridine triblock terpolymer.

Living anionic polymerization has also been utilized in the literature for the synthesis of tetra-block, and penta-block copolymers. The synthesis of such complex block copolymers is made relatively easy by using the sequential addition of the monomeric starting units to grow the chains.

2.1.4.1.2 Living cationic polymerization

Living cations are another substitute mechanism that has been used in the literature for the synthesis of diblock, triblock and multiblock copolymers. Advances in the ability of chemists to stabilize cations in solution [52-54] have led to greater reliance on the synthesis of block copolymers using living cationic polymerization mechanisms. Cations for promoting living cationic polymerization are generated from a Lewis acid e.g. $TiCl_4$, BCl_3, etc.

2.1.4.1.2.1 Linear diblock copolymer via living cationic polymerization

The reaction steps shown in figure 2.1.4.1.2.1 were utilized for the synthesis of a linear polysiobutylene-b-polystyrene diblock copolymer using living cationic

polymerization. In the first reaction step, isobutylene monomer is introduced into a reaction mixture containing a lewis acid, titanium tetrachloride, at -80ºC. After cationic homopolymerization of isobutylene, styrene monomers are added to the reaction mixture to form a PIB-PS block copolymer.

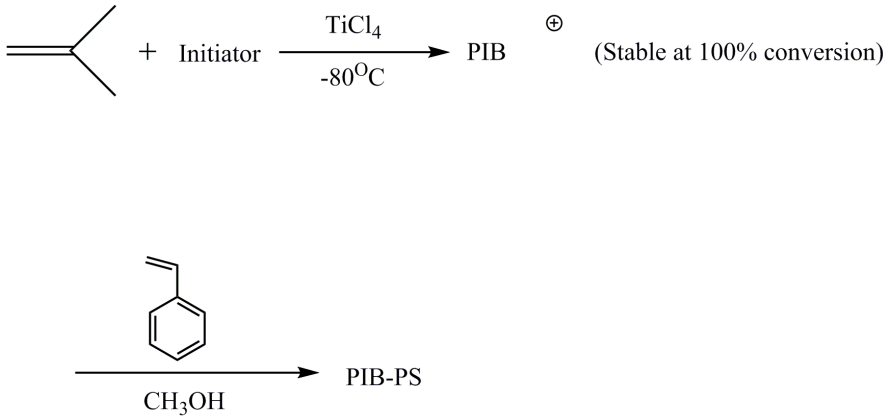

Figure 2.1.4.1.2.1. Scheme showing the reaction steps to synthesize polyisobutylene-b-polystyrene block copolymer.

In the reaction equations shown above, either monomer can be used as the starting material for homopolymerization due to the similar chemical reactivity of both monomers to the initiator. For monomers with varying reactivity to the cationic initiator, the more reactive monomer is first homopolymerised before the addition of the less reactive monomer. In the case of poly-α-methylstyrene-b-polyisobutylene (PαMeS-b-PIB), the αMeS monomer is more reactive to the cationic initiator than the isobutylene monomer. Therefore, homopolymerization of the methylstyrene monomer is carried out first using a less reactive Lewis acid, BCl_3. This is then followed by the block polymerization of the isobutylene monomer using a stronger Lewis acid like $TiCl_4$. Figure 2.1.4.1.2.1.2 below shows the reaction steps for the synthesis of PαMeS-b-PIB block copolymer.

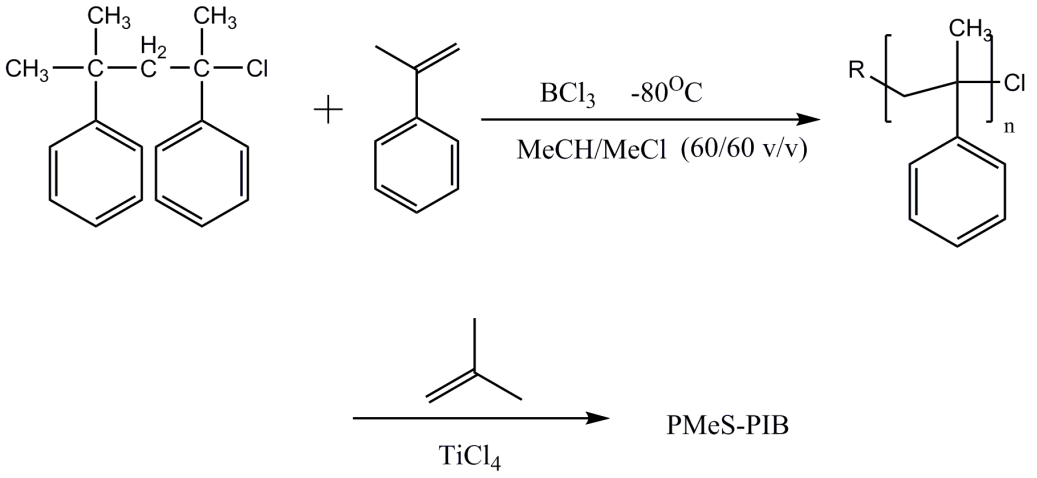

Figure 2.1.4.1.2.1.2. Scheme showing the reaction steps to synthesize poly-α-methylstyrene-b-polyisobutylene block copolymer.

2.1.4.1.2.2 Symmetric triblock copolymer via living cationic polymerization

Symmetric triblock copolymers with two similar blocks at the ends of the chain have been synthesized using living cationic polymerization. An example of a triblock copolymer synthesized with living cationic polymerization is poly-α-methylstyrene-b-polyisobutylene-b-poly-α-methylstyrene (PαMeS-b-PIB-b-PαMeS) triblock copolymer. Figure 2.1.4.1.2.2.1 shows the reaction steps for the synthesis of PαMeS-b-PIB-b-PαMeS block copolymer. Synthesis of PαMeS-b-PIB-b-PαMeS triblock copolymer starts with homopolymerization of the α-methylstyrene monomers using a weak lewis acid. The living cationic reaction is terminated with methanol, and subsequently end-capped with isobutylene. The homopolymerization of isobutylene is done in a different reaction beaker with $TiCl_4$- a strong lewis acid. The next step is the coupling of two homopolymer chains using coupling agents like 2,2-bis-[4-(1-phenylethenyl)phenyl]propane (BDPEP) or 2,2-bis[4-(1-tolylethenyl)phenyl]propane (BDTEP) etc.

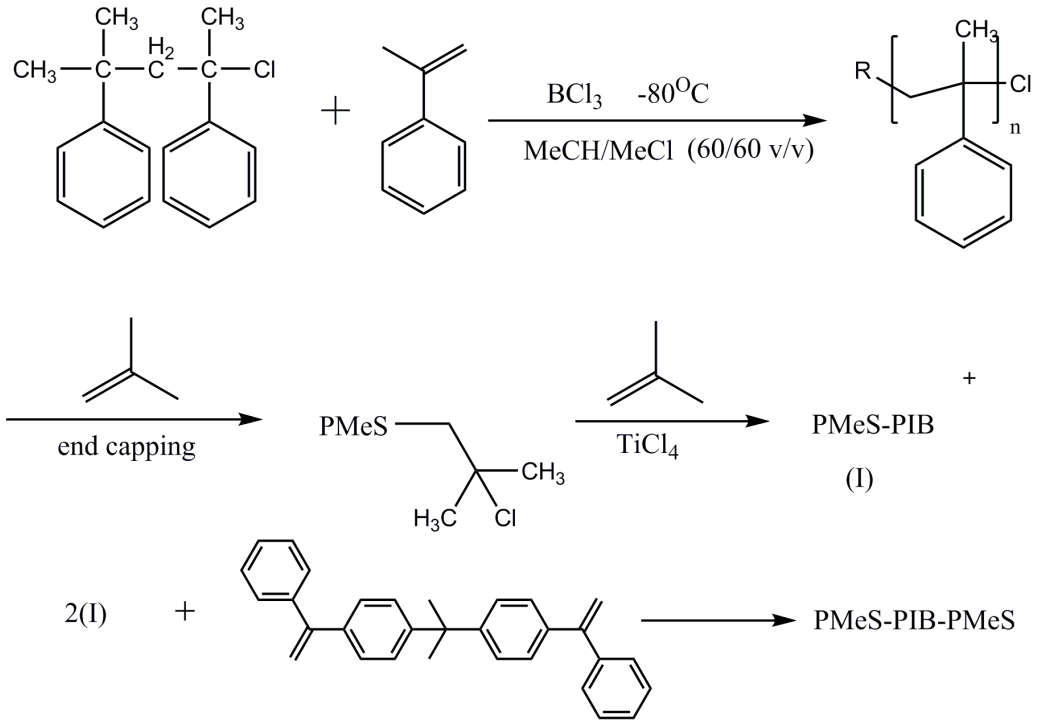

Figure 2.1.4.1.2.2.1 Scheme showing the reaction steps to synthesize poly-α-methylstyrene-b-polyisobutylene-b-poly-α-methylstyrene block copolymer.

2.1.4.1.3 Living Free Radical Polymerization

Because radicals can tolerate a broad range of solvents and monomer chemical functional groups, they appear to be ideal for synthesizing block copolymers. However, radicals are difficult to control and give a wider range of molecular weights due to unwanted chain termination and chain transfer reactions. Initiators that have been utilized for free radical polymerization include: Cubr/N,N,N',N",N"-pentamethyldiethylenetriamine and 2-methyl-2-bromopropionoate, 2,2'-azoisobutyronitrile (AIBN)/4-oxo-2,2,6,6-tetramethylpiperidinoxy(TEMPO) at 145ºC, AIBN/N-tert-butyl-N-(1-diethylphosphono-2,2-dimethyl)propyl nitroxide(DEPN) at

120ºC, TEMPO, camphosulphone and benzoylperoxide(BPO) [55],[56],[57],[58],[59, 60].

Living radical polymerization is thermally initiated by temperatures above 100ºC. At high temperatures, initiating radicals that promote the growth of polymer chains are generated. Usually a co-initiator like TEMPO provides the nitroxide ion required to stabilize the living radical. Transition metals are mainly utilized as radical initiators because of their unique property to easily change oxidation states. A variable oxidation state of the transition metals conjugated to other organic molecules guarantees the generation of radicals that promote the living radical polymerization.

2.1.4.1.3.1. Linear diblock copolymers via living radical polymerization

Nitroxide mediated free radical polymerization mechanism has been successfully utilized for the synthesis of diblock copolymers containing styrene or methacrylate blocks. Figure 2.1.4.1.3.1.1 below shows the reaction steps for the synthesis of poly-4-butoxystyrene-b-polystyrene (P4bS-b-PS) block copolymer. Initiation is carried out at 130ºC via the introduction of TEMPO:BPO into the reaction system containing the styrene monomer. After the homopolymerization of styrene, 4-butoxy-styrene is added to the living radical chain adding a PS chain to the P4bS chain.

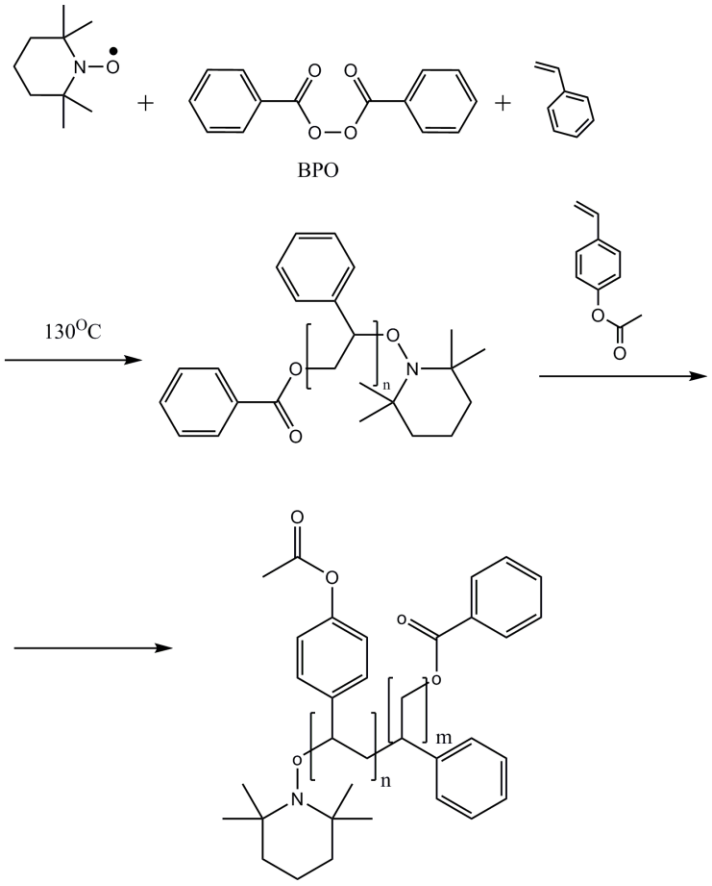

Figure 2.1.4.1.3.1.1 Scheme showing the reaction steps to synthesize poly-4-butoxystyrene-b-polystyrene block copolymer.

Diblock copolymers especially those containing fluorinated side chains have also been synthesized using atom transfer radical polymerization (ATRP)- a type of living free radical polymerization reaction. The initiators of the living radical reaction are a transition metal, and an halogenated organic molecule like 1-phenylethylbromide, (1-bromoethyl)benzene, 2-bromopropionoate. Complexing agents like pentamethyl-diethylenetriamine (PMDETA), hexamethyltriethylenetetramine (HMTETA) containing nucleophilic nitrogen are required in the living radical polymerization reaction to coordinate the transition metal.

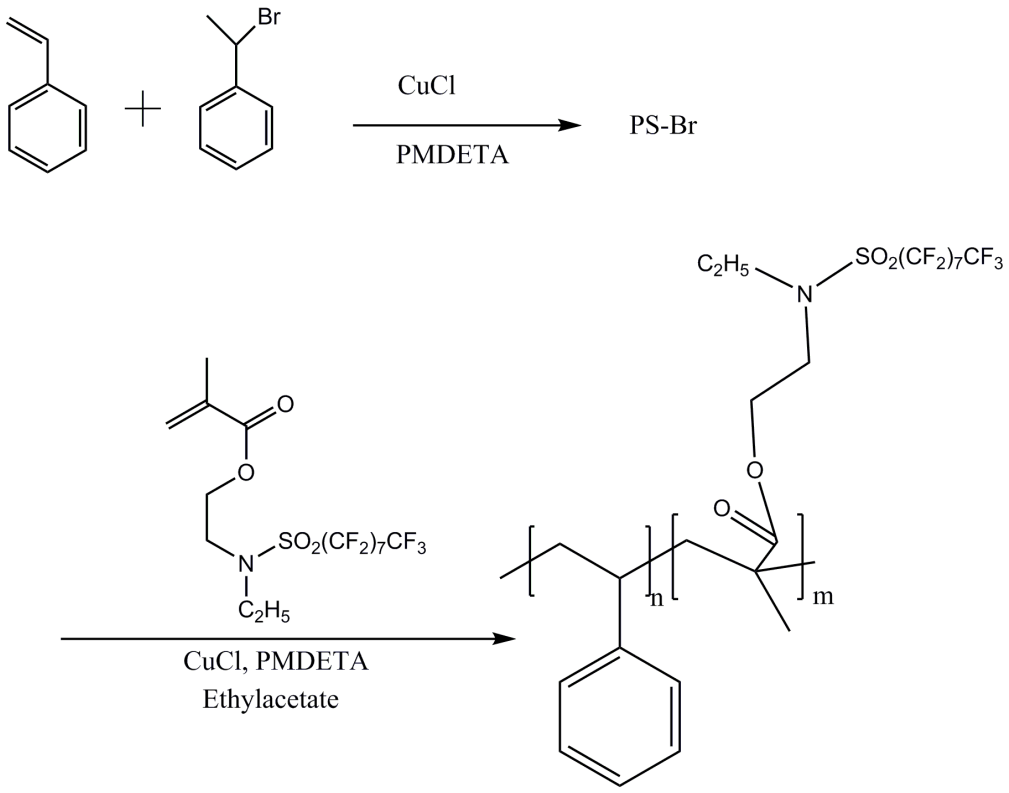

Figure 2.1.4.1.3.1.2 Scheme showing the reaction steps to synthesize polystyrene-b-PFx-14 block copolymer.

Figure 2.1.4.1.3.1.2 shows the reaction steps for the synthesis of polystyrene-b-poly,methylfloride (PS-b-PFx-14) block copolymer. The homopolymerization of the styrene block is first carried out with a copper(I)chloride, (1-bromoethyl)benzene as initiators and a pentamethyl-diethylenetetramine as a complexing agent. The addition of methyl floride Fx-14 to the living radical styrene chain results in the generation of a diblock copolymer having a PS-PFx-14 component.

A-B-A triblock copolymer can also be synthesized using living radical polymerization via the sequential addition of the monomers to the living radical. Figure 2.1.4.1.3.1.3 shows the reaction steps for the synthesis of poly(4-hydroxystyrene)-b-polystyrene-b-poly(4-hydroxystyrene) triblock copolymer.

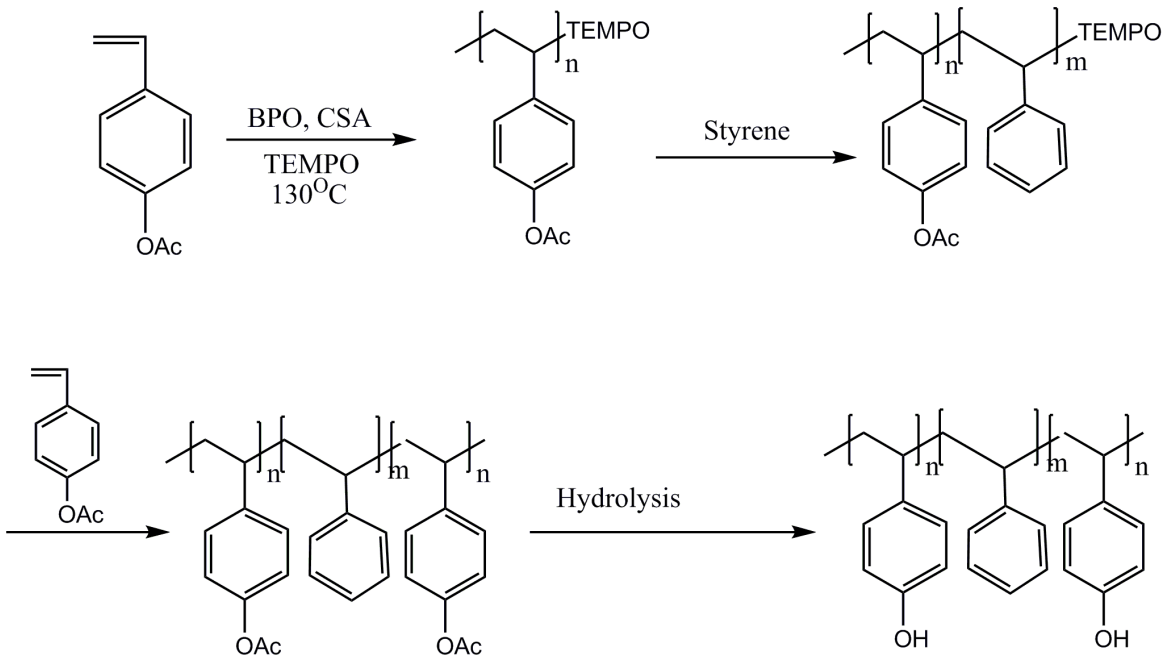

Figure 2.1.4.1.3.1.3 Scheme showing the reaction steps to synthesize poly(4-hydroxystyrene)-b-polystyrene-b-poly(4-hydroxystyrene) triblock copolymer.

Homopolymerization of acetylated parahydroxystyrene is done with a TEMPO:BPO living radical initiators. Styrene monomers are then added to the growing chain followed by the addition of more acetylated parahydroxystyrene. Once the triblock copolymer synthesis is complete, deprotection of the acetylated end chains can be done in the presence of a weak acid.

Living radical polymerization has also been utilized for the synthesis of A-B-C triblock terpolymer and tetrablock copolymer synthesis.

2.1.4.1.4 Group Transfer polymerization

Group transfer polymerization (GTP) is a Michael type addition mediated through silylalkane functional groups. The reaction involves transfer of the silylalkane group from one end group of the growing polymer chain to the new monomer attached to the chain.[61-65]. An advantage of group transfer reaction over anionic polymerization for the synthesis of diblock and triblock copolymers is that polymerization reactions can be carried out at room temperatures. In addition, group transfer polymerization reaction is tolerant to different side group functionalities on the monomer.

Group transfer polymerization reaction is used to synthesize diblock copolymers having an acrylate functional group. A-b-B diblock copolymers, A-b-B-b-A triblock copolymers and A-B-C triblock terpolymers have been successfully synthesized using group transfer polymerization reactions.

2.1.4.1.4.1 Linear diblock copolymer via GTP

Diblock copolymers can be synthesized using group transfer polymerization via the addition of a dimethylketenmethyl trimethylsilyl acetal as the initiator. A nucleophile, tris(dimethylamino) sulfonium bifluorate $TASHF_2$ or tetra n-butyl ammonium bibenzoate TBABD, serves as a co-initiator in GTP reactions. The co-initiator in the GTP reaction catalyses the attack of the silyl group, and this followed by the nucleophilic attack of the monomeric units.

Diblock copolymers containing methylmethacryalte and laurylmethacrylate have been successfully synthesized using the GTP reaction. Other block copolymers with a methylmethacrylate, glycidylmethacrylate blocks have also been synthesized using GTP

reactions. Figure 2.1.4.1.4.1.1 below shows the reaction steps for the synthesis of polymethylmethacrylate-b-polyglycidylmethacrylate PMMA-PGMA diblock copolymer.

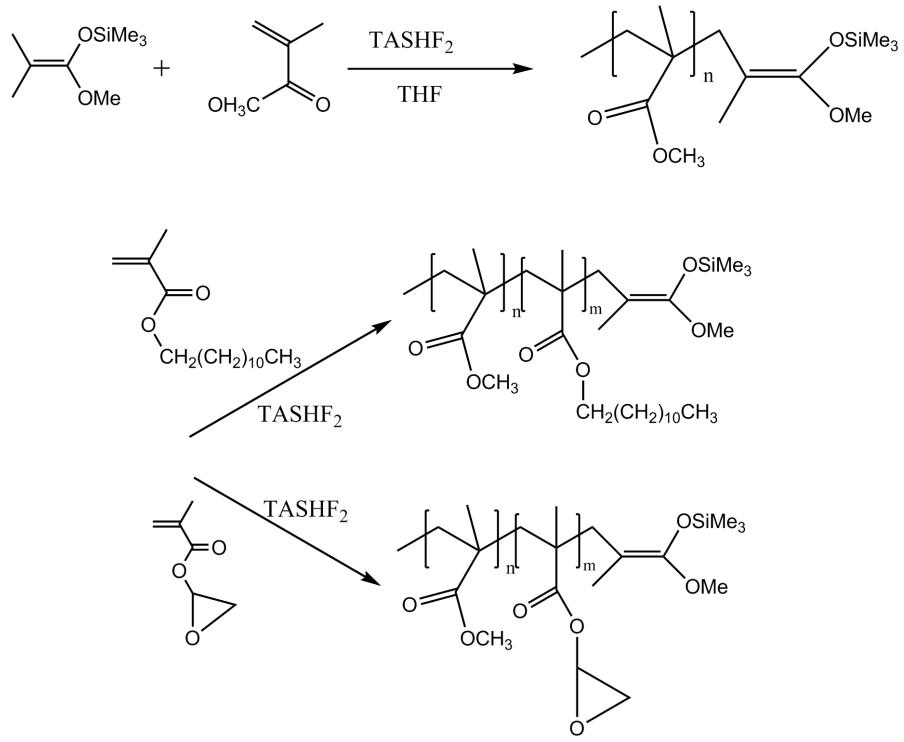

Figure 2.1.4.1.4.1.1 Scheme showing the reaction steps to synthesize poly(methylmethacrylate)-b-(polyglycidylmethacrylate) and poly(methylmetahcrylate)-b-poly(n-dodecylmethacrylate).

Group transfer polymerization has also been successfully used to synthesize A-B-A triblock copolymer using a difunctional disilyltrimethane initiator. Several initiators have been reported in the literature for use in the synthesis of triblock symmetric copolymers. Examples of the initiators are bis(methoxytrimethylsiloxy) cyclohexane (CHMTS), 1,5-bis(trimethylsiloxy)-1,5-dimethoxy-2,4-dimethyl-1,4-pentadiene (BDDP). Group transfer polymerization reaction is also used for the synthesis of A-B-C triblock terpolymer via sequential addition of the various monomeric units.

2.2 Material Physics Background: Melt Phase Behavior of Block Copolymers [66]

A remarkable property of block copolymers is their ability to phase separate and self-assemble on the nanoscale forming features with variable periodicities. Microphase separation in block copolymers is enthalpy driven; while the physical interactions, in the form of covalent bonds between the polymer blocks, prevent any form of macrophase separation. The engineering applications of block copolymers are based on the chemical interaction and distinction between the blocks of the polymer. The chemical interaction between the blocks of the block copolymer can be varied by varying temperature, chemical composition, molecular weight and molecular weight distribution or through other non-conventional techniques like electric field alignment, use of various solvent vapors etc. The important parameter that characterizes the chemical interactions between portions of a block copolymer is the Flory-Huggins interaction parameter.

2.2.1 Flory-Huggins Mean-Field Theory

Flory and Huggins were among the first to apply mean field lattice theory to polymer systems. The application of the mean field theory to polymer systems was used to derive the thermodynamic parameters of block copolymers including the entropy of mixing, enthalpy of mixing, and the free energy of mixing of block copolymers. The mean field theory can be derived for a polymer system in solution but the derived formulas can be applied to block copolymer melts.

2.2.1.1. Energies of mixing polymers and block copolymers

The thermodynamic probability distribution of block co polymers within a unit volume, using the mean field theory, can be given as:

$$\Omega = \frac{n!}{n_1!n_2!}$$ equation 2.2.1.1.1

Where n is the total number of lattice sites, n_1 total number of lattice sites occupied by block A ,and n_2 is the total number of lattice sites occupied by block B. The total Energy of interaction for a cell with volume V is thus given as:

$$Q = \sum_V e^{-E_v/k_BT} = \sum_l \Omega_l e^{-E_l/k_BT}$$ equation 2.2.1.1.2.

Where E_v, E_l are the energy of a volume (v) and a length (l) respectively occupied by polymer blocks, k_B is the Boltzman constant and T is the temperature.

Some parameters are introduced that will be used to provide an approximate solution to the free energy of mixing F_{mix} of a block copolymer in solution.

Φ_1= volume fraction of block 1= $n_1/(n_1+n_2)$

Φ_2= volume fraction of block 2=$n_2/(n_1+n_2)$

n_{11}= Number of pairs of type A-A

n_{22}= Number of pairs of type B-B

n_{12}= Number of pairs of type A-B

Given a unit cell z, then on average, a given block is surrounded by z Φ_1 of block A and z Φ_2 of block B. Therefore:

$$n_{11} = \frac{n_1 z\Phi_1}{2}, n_{22} = \frac{n_2 z\Phi_2}{2}, n_{12} = \frac{1}{2}\left(n_1 z\Phi_1 + n_2 z\Phi_2\right)$$ equation 2.2.1.1.3.

The total energy of interaction of the block copolymer can be mathematically expressed as equation 2.2.1.1.4. Where ε_{11}, ε_{22}, are the energies of interaction between similar

blocks or components represented as 1-1 and 2-2 interactions, while ε_{12} represents interactions between two dissimilar components represented as 2-1 or 1-2 interactions.

$$\overline{E} = n_{11}\varepsilon_{11} + n_{22}\varepsilon_{22} + n_{12}\varepsilon_{12}$$

$$\overline{E} = -nz\left(\frac{1}{2}\varepsilon_{11}\phi_1^2 + \frac{1}{2}\varepsilon_{22}\phi_2^2 + \varepsilon_{12}\phi_1\phi_2\right) \qquad \text{equation 2.2.1.1.4}$$

$$Q \approx \Omega e^{-\overline{E}/k_B T}$$

The free energy of a system is related to the temperature (T), Boltzmann's constant k_B and the energy of the system Q in equation 2.2.1.1.5

$$F = -k_B T \ln Q = -k_B T\left(\ln\Omega - \overline{E}/k_B T\right) = -k_B T \ln\Omega + \overline{E} \qquad \text{equation 2.2.1.1.5}$$

Using Sterling's approximation: ln(n!) = n ln(n) - n,

$$\ln\Omega = n\left(\phi_1 \ln\phi_1 + \phi_2 \ln\phi_2\right) \qquad \text{equation 2.2.1.1.6}$$

The final formula for the change in free energy of a diblock is given in equation 2.2.1.1.7.

$$\Delta F_{mix} = F - \left(F_1 + F_2\right)$$

$$\Delta F_{mix} = nK_B T\left(\phi_1 \ln\phi_1 + \phi_2 \ln\phi_2\right) + nz\left(\varepsilon_{12} - \frac{\varepsilon_{11} + \varepsilon_{22}}{2}\right)\phi_1\phi_2 \qquad \text{equation 2.2.1.1.7}$$

From the free energy the Flory Huggins interaction parameter (enthalpy parameter) of polymer blends that induces phase separation is given in equation 2.2.1.1.8.

$$\chi = \frac{z}{k_B T}\left[\varepsilon_{12} - \frac{\varepsilon_{11} + \varepsilon_{22}}{2}\right] \qquad \text{equation 2.2.1.1.8}$$

While the entropy value contributing to the free energy is given in equation 2.2.1.1.9.

$$\frac{-\Delta S_{mix}}{K_B n} = \phi_1 \ln\phi_1 + \phi_2 \ln\phi_2 \qquad \text{equation 2.2.1.1.9}$$

The Flory-Huggins interaction parameter is a very important parameter for determining the kinetics of phase separation in block copolymers. A positive value for the

Florry-Huggins interaction parameter indicates repulsion between the blocks in a di, tri, penta block copolymer. A positive Flory-Huggins interaction parameter also favors demixing and phase separation between the blocks in the block copolymer.

However, a negative value for the Flory-Huggins interaction parameter indicates chemical similarity and potential mixing of the blocks in the block copolymer. Although the Flory-Huggins interaction parameter is important in determining the phase separation kinetics, the contributions from the entropy of the polymer system also plays a vital role in determining the time duration for phase separation to occur. To incorporate entropy contributing factors into the Flory-Huggins parameter, the degree of conversion of the block copolymer N is introduced. The value χN includes both the enthalpy and entropy contributions to phase demixing and separation in a block copolymer. Based on the values of χN, phase separating block copolymers have been divided into block copolymers at the strong segregation limit (SSL) with $\chi N>100$; and block copolymers at the weak segregation limit (WSL) with $\chi N\sim10$. There is also an intermediate group for block copolymers at the intermediate regime $\chi N\sim100$.

The next 2 sub-sections will briefly discuss block copolymers at the two extreme of the segregation limits. The formulas for interdomain spacing within these limits will also be derived and discussed.

2.2.1.3 Strong segregation limit (SSL) $\chi N>>10$

At the strong segregation limit, narrow interfaces are formed in a block copolymer. Within the SSL, the domain width is highly dependent on the χ interaction parameter, while the characteristic domain feature and ordering is dependent on the

composition of the block copolymers i.e the volume fraction F of one block in relation to another.

The self-consistent filed theory has been used to predict the interdomain spacing between blocks phase separating in the SSL regime. This theory assumes that the main contributing factors to the free energy in the SSL limit are:

1) Contact enthalpy between the A and B microdomains at the interface
2) Entropy loss of the block due to chain stretching at the interface
3) Confinement entropy via localization of covalently linked sections of the two blocks at the interface.

Based on the assumptions, the domain free energy of a chain within the SSL scales as a Gaussian chain, and is given by the formula:

$$\frac{F_{Domain}}{KT} \sim \frac{d^2}{a^2 N} \qquad \text{equation 2.2.1.3.1.}$$

Where d is the interdomain spacing, N is the degree of conversion, and α is the statistical segment length.

This indicates that within the interdomain spacing chains behave like a Gaussian coil. The energy within the interdomain spacing must be interfacial free energy per chain as given in equation 1.3.2.3.2.

$$\frac{F_{Interface}}{KT} \sim \sigma\gamma \sim \frac{Na\chi^{\frac{1}{2}}}{d} \qquad \text{equation 2.2.1.3.2}$$

Where σ is the area per chain given by $\sigma \sim \frac{N\alpha^3}{d}$, and γ is the interfacial tension given by $\gamma \sim \chi^{\frac{1}{2}} a^{-2}$. The value for the interdomain spacing then becomes:

$$d \sim aN^{\frac{2}{3}}\chi^{\frac{1}{6}}$$ equation 2.2.1.3.3

Helfand and Wasserman with the assumption that block copolymers are not strongly stretched after phase separation have proposed that the microdomain period should scale as:

$$d \sim \alpha N^{\frac{9}{14}}\chi^{\frac{1}{7}}$$ equation 2.2.1.3.4

A final note here is that block copolymers used in most engineering applications phase separate or have interaction parameters under the strong segregation limit. The reason for this is that phase separation kinetics is faster under the strong segregation limit when compared to phase separation of block copolymers under the weak segregation limit. Furthermore, the dissimilarity between blocks phase separating under the SSL regome more often than not translates to differential affinity of the blocks to chemicals and this can be exploited for the transfer of the phase-separated features to underlying silicon, silicon oxide substrates.

2.2.1.4 Weak segregation limit (WSL) χN~10

Block copolymers in the weak segregation limit are modeled using the mean field theory with the incorporation of a Landau-Ginzburg theory. The ordering parameter for an A-b-B block copolymer under the weak segregation limit is given by:

$$\psi(r) = \langle \rho_A(r) - f \rangle$$ equation 2.2.1.4.1

Where $\rho_A(r)$ is the local number density of block A, and f is the average composition of block A. Using the Landau-Ginzberg theory, the free energy function $F[\psi(q)]$ can be expanded as an order parameter $\psi(q)$ which is a fourier transform of $\psi(r)$ as shown in equation 2.2.1.4.2.

$$F\left[\psi\left(q\right)\right]=\frac{1}{2!}\int_{q}S^{-1}(q)\psi(q)\psi(-q)+\frac{1}{3!}\int_{q}\int_{q^1}\mu\left(qq^1-q-q^1\right)\psi(q)\psi(q^1)\psi(-q-q^1)$$

$$+\frac{1}{4!}\int_{q}\int_{q^1}\int_{q^{11}}\lambda\left(qq^1q^{11}-q-q^1-q^{11}\right)\psi(q)\psi(q^1)\psi(q^{11})\psi(-q-q^1-q^{11})$$

equation 2.2.1.4.2.

The cubic term,μ, in the free energy function is zero while the quartic term, λ, is positive to ensure stability. The structure factor in the equation above is given by:

$$S(q)=\frac{W(q)}{\left[\sum(q-2\chi W(q))\right]}$$ equation 2.2.1.4.3.

Where W is a determinant matrix for correlation functions.[67] The calculations of S_{ij} within the random phase approximation limit gives:

$$S_{11}(q)=Ng(f,x)$$
$$S_{22}(q)=Ng(1-f,x)$$ equation 2.2.1.4.4.
$$S_{12}(q)=S_{21}(q)=\frac{1}{2}N\left(g(1-x)-g(f,x)-g(1-f,x)\right)$$

The debye function under the random phase approximation is given by:

$$g(f,x)=2\left[fx+\exp(-fx)-1\right]/X^2$$ equation 2.2.1.4.5.

$$X=\frac{q^2Na^2}{6}=F^2Rg^2$$

Under the weak segregation limit the domain spacing for block copolymers is found to scale as:

$$d\sim N^{\frac{1}{2}}$$ equation 2.2.1.4.6.

It should be noted here that block copolymers in the weak segregation limit are less frequently used for engineering applications because of the huge dependence of the

interdomain spacing on the weight of the blocks. The kinetics of phase separation are slow under this regime, and there is chemical similarity between the two blocks making it difficult to transfer the microdomain phase separation to other substrates for use in engineering applications. Most commercially available block copolymers have phase separation in the strong segregation limit.

2.3. Optical Physics

This sub-section provides relevant background information on the physical concept behind the interference of coherent light beams. The photophysics and photochemistry behind photoinduced modification of organic material systems are also treated in detail in this section.

2.3.1. Laser interference ablation [68]

2.3.1.1. LASERs

Laser is an acronym for light amplification via stimulated emission of radiation (LASER). The first lasing machines created about 100 years ago were called modulated amplification of light via stimulated emission of radiation (MASER). Although all lasing machines operate with the same principles, lasing machines can be classified into classes using different criteria. One of the criterion used to classify lasers is the type of gain media. Another criterion is the output wavelength of the laser and the ability to vary the output wavelengths from the laser.

Figure 2.3.1.1.1 shows the schematic for a lasing machine. A lasing machine has four basic components: a high reflector, a gain medium, an output coupler, and a power supply.

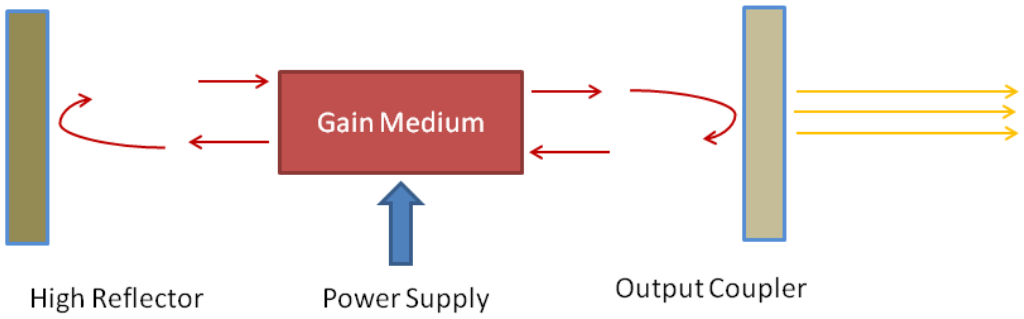

Figure 2.3.1.1.1 Schematic of a lasing set-up showing the gain medium, output coupler, and high reflector

The power supply for a laser is in the form of a light source. The light source can either be a UV lamp source, or an infrared (IR) lamp source. The function is to generate enough energy that will result in stimulated emission and population inversion in the gain medium. The gain medium used for lasers varies, and determines to a larger extent the output wavelength from the lasing machine. It also determines the temporal and spatial coherence of the output light beam. Lasers can be classified into solid state, gas state and liquid based lasers based on the type of gain medium used. The choice of gain media is dependent on application as well as robustness of the laser machine, but most state of the art lasers for research applications are solid state lasers. Solid state gain media are made from ceramics and crystals doped with rare earth elements. The output wavelength for solid state lasers is sometimes modified with non-linear optical materials like potassium floride, potassium titanyl phosphate etc. An example of a solid state gain media is a neodymium doped yttrium aluminum Nd:YAG garnet laser. Another example of a solid state laser is a Ti:Al_2O_3 laser made from titanium doped sapphire crystals. Examples of gaseous state excimer based lasers ares argon fluoride (ArF) with an output wavelength

of 193, xenon chloride (XeCl) laser with an output wavelength of 308 nm. Gas state lasers with output wavelength in the IR region have a CO_2 gain media.

Lasers with liquid gain media used less frequently for research and industrial applications due to ease of transportation. Examples of commercially available liquid state dye lasers are Rhodamine 6G laser emitting at 580nm. The gain media for this laser is rhodamine.

The high reflector and the output coupler in figure 2.3.1.1.1 maintain the path of the light beam travelling back and forth within the laser set-up. After oscillating back and forth within the laser set-up, the initial light beam is amplified by several orders of magnitude. The light is later transmitted out through of the set-up, via the output coupler, as an amplified coherent and monochromatic laser beam.

2.3.1.2. LASER PHYSICS- GAIN MEDIA

The major component of any lasing machine is the gain medium. The precondition for a laser beam to occur is that the lasing medium must be able to undergo a stimulated emission under the influence of the light source. Stimulated emission in a gain media can occur if there is a net-increase in intensity of a light beam after every passage through the gain media. The gain coefficient of a media is a value that tells us by how many times the intensity of a light source is increased on passing through the gain media.

$$I(x+dx) = I(x) + \gamma I(x)dx$$

$$= I(x) + dI$$

$$dI = \gamma I dx$$

$$I(x) = I(o)\exp(\gamma x) \qquad \text{equation 2.3.1.2.1}$$

Where γ is the gain coefficient of the media, I(x) is the intensity at a region of distance x, and I(o) is the initial intensity of the light beam.

Equation 2.3.1.2.1 shows that the intensity of a laser beam grows exponentially with every passage through the gain media. A net-increase in intensity of light occurs in a gain media if a phenomenon called population inversion occurs in the gain media.What is population inversion? When gases, solids atoms are in thermal equilibrium at room temperature the number of atoms in the ground state is more than the number of atoms in the excited state. Population inversion is a phenomenon whereby the population of atoms within the excited states of a gain media, upon stimulation by an external light source, is higher than the number of atoms in the ground state. Figure 2.3.1.2.1 shows a pictorial representation of population inversion leading to laser emission from a three energy level gain media.

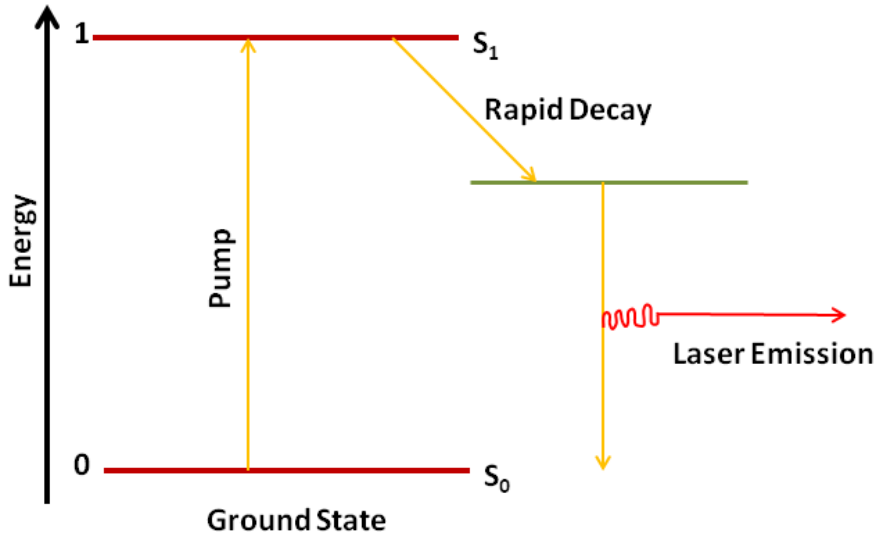

Figure 2.3.1.2.1 Energy diagram showing population inversion in a 3 level laser

Three energy level lasers usually operate in the pulsed mode, and an example of a 3 level laser is the Ti:Al_2O_3 Ruby laser. A ruby laser operates with a UV power source

that pumps and activates atoms from the ground state (S_0) to the excited state (S_1). The excited atoms, in the S_1 state are short lived and preferentially cascade to adjacent triplet state (T_1). The triplet state in a ruby crystal is long lived and thus more stable that the S_1 state. Continuous pumping of the ruby crystal with a UV source would lead to an increase in the amount of excited electrons in the T_1 state. Then population inversion occurs when the number of atoms populating the T_1 state exceeds the number of atoms at the ground state S_0. Lasing from the ruby crystal occurs when atoms in the T_1 state decay radiatively to the ground state releasing photons in form of monochromatic light waves.

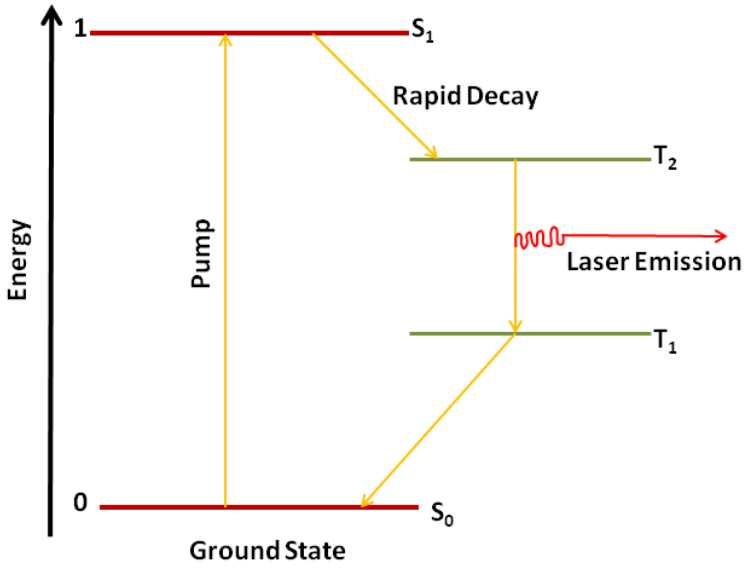

Figure 2.3.1.2.2. Energy diagram showing population inversion in a 4 level laser

Lasers with 4 level systems, however, can operate in continuous mode because of the presence of an added energy level that can maintain population inversion for a longer period. Population inversion is maintained by creating more obstacles, stable triplet states, for excited electrons to tunnel through during their cascade to the ground state S_0. Figure 2.3.1.2.2 shows a pictorial representation of population inversion leading to laser emission from a four energy level gain media. Examples of lasers that operate with the 4

level scheme include Nd:YAG, ArF lasers. An Nd:YAG laser operates with a UV power source that pumps and activates atoms from the ground state (S_0) to the excited state (S_1). The excited atoms, in the S_1 states are short lived and preferentially cascade to the adjacent triplet state (T_2). The triplet state (T_2) in a YAG crystal is long lived and thus more stable that the S_1 state. Atoms form the T_2 state then radiatively decay to another long lived triplet state (T_1). Continuous pumping of the YAG crystal with a UV source would lead to an increase in the amount of excited electrons in the T_1 and T_2 states. Population inversion in this case can be sustained longer since the excited atoms do not return to the ground state after radiative emission. Lasing from the YAG crystal occurs when atoms in the T_1 state decay radiatively to the T_2 state releasing photons in form of monochromatic light waves.

2.3.1.3 Properties of Laser Beams

Laser beams are preferred to other conventional discharge lamps light sources for industrial fabrication and research purposes for several reasons some of which are:

1) Monochromatic light- Emission of light from a laser always corresponds to one of many atomic transitions and thus results in monochromatic light waves unlike broad wavelength light waves from discharge lamps.
2) Coherence of light- Laser beams have both long spatial and temporal coherence. Spatial coherence of a light beam refers to irregularities in a section of the beam while temporal coherence refers to the distance over which the beam plane is well defined.
3) Pulsed Generation- Lasers can also be made to operate in a pulsed mode or as continuous sources of light with controlled time duration between pulses. Controlled

duration between pulses can be used for probing and analyzing optical events with lifetimes from nanosecond, femtosecond and picosecond lasers.

4) Intensity- Unlike discharge lamps with very low power per unit area, laser beams by virtue of amplification give very high power per unit area. Furthermore, the spectral brightness of laser beams is much higher than those of conventional light sources.
5) Directionality- Laser beams have very consistent directionality over large distances.

Because of these inherent properties of laser beams, they are routinely utilized in the electronics industry for photolithography. Furthermore, due to the large power per unit area of laser beams, lasing machines are aroutinely employed in metallurgy for processing metals and other alloys. The ultrashort pulses obtainable from lasers enables there use in for lifetime measurements of novel photoactive materials as well as other transient intra and intermolecular transitions.

The rational design and fabrication of sub 50nm functional materials in the electronics industry involves the complex manipulation of light from commercially available lasers. An example of a relatively inexpensive laser is the Spectra Physics Nd:YAG Pro 6500 series pulsed laser having a base wavelength of 1064nm. Nd:YAG pro 6500 series laser also comes with an harmonic generator for giving output wavelengths of 550nm, 350nm and 266nm.

An effective method in the literature for reducing the periodic distribution and increasing the resolution of light from laser beams is laser interference. Interference of electromagnetic waves involves the combination of two, three or more laser beams at a given point. The result of two or three beam interference is the periodic variation of light intensity in 2 dimensional space. The periodic variation of light intensity in 3 dimensional

space occurs with the interference of four or more laser beams. The variation in light intensity in 2D or 3D space when applied to a photosensitive material system can be used for generation of periodic materials having sub-wavelength periodicity. The 2D projection of the light intensity distribution gives a square, oblique, rectangular, triangular or rhombus lattice points.

2.3.1.4 Mathematical representation of a laser interference pattern

Periodic features in 2D and 3D space can be represented mathematically using a Fourier function, while the intensity distribution from interfering light beams can be represented using Maxwell's equations. The mathematical representation of periodic functions in 2D or 3D space can be generated and then compared with the intensity distribution function of interfering light beams.

In 3D space, periodic features can be represented using a Fourier function given by:

$$f(x,y,z) = a_{ooo} + \sum_{n}\sum_{m}\left\{ a_{nmp}\cos\left(2\pi\left(\frac{nx}{a}+\frac{my}{b}+\frac{pz}{c}\right)\right) + b_{nmp}\sin\left(2\pi\left(\frac{nx}{a}+\frac{my}{b}+\frac{pz}{c}\right)\right)\right\}$$

equation 2.3.1.4.1.

In 2D space, the Fourier function in equation 1.4.3.1.1 transforms to equation 1.4.3.1.2.

$$f(x,y) = a_{oo} + \sum_{n}\sum_{m}\left\{ a_{nm}\cos\left(2\pi\left(\frac{nx}{a}+\frac{my}{b}\right)\right) + b_{nm}\sin\left(2\pi\left(\frac{nx}{a}+\frac{my}{b}\right)\right)\right\}$$ equation 2.3.1.4.2.

Where n,m,p are integer numbers and a_{ooo}, $a_{oo,}$ a_{nmp}, a_{nm}, b_{nm} and b_{nmp} are real constants. a, b and c are lengths of a rectangular unit cell. The constants a_{ooo}, $a_{oo,}$ a_{nmp}, a_{nm}, b_{nm} and b_{nmp} are called Fourier coefficients.

A laser beam, like all electromagnetic transverse waves, has an electric field vector (E) oscillating at right angles to a magnetic field vector (H). The electromagnetic laser beam also propagates along a wave-vector (k). A propagating electromagnetic wave can be written in terms of Maxwell's divergence and curl equations as:

$$\nabla \cdot D = 0 \qquad \nabla \times E = -\frac{\partial B}{\partial t}$$
$$\nabla \cdot B = 0 \qquad \nabla \times H = \frac{\partial D}{\partial t}$$

equation 2.3.1.4.3.

Maxwell's divergence equations Maxwell's curl equations

Where D,B are electric field displacement and magnetic induction field vectors respectively. The constitutive parameters that help incorporate material dependent characteristics into the propagating waves are the electric permittivity (ε), and the magnetic permeability (μ). And there relationships to the electric field displacement and magnetic induction field are shown below.

$$D = \varepsilon E$$
$$B = \mu H$$

equations 2.3.1.4.4.

In order to use the Maxwell relations, the following assumptions have to be made about the material, block copolymer in this case, through which the laser beam propagates:

(a) Isotropic: ε, μ have values independent of the direction of propagation of the laser

(b) Homogenous: ε, μ have the same values at every point in space i.e $\varepsilon \neq \varepsilon(r)$, $\mu \neq \mu(r)$

(c) Non-conducting: Electromagnetic energy is conserved

(d) Linear: ε and μ is independent of the electric and magnetic field vectors

(e) Non-dispersive: ε and μ is independent of the frequency of the laser beam propagating through the material medium.

Under these assumptions, the constitutive equations transforms into equations 2.3.1.4.5.

$$\nabla \cdot E = 0 \qquad \nabla \times E = -\mu \frac{\partial H}{\partial t}$$
$$\nabla \cdot H = 0 \qquad \nabla \times H = \varepsilon \frac{\partial E}{\partial t}$$

equations 2.3.1.4.5

Invoking the vector identity notations shown in equations 2.3.1.4.6, a set of partial differential equations can be obtained, and the solution to the set of equations is given in equation 2.3.1.4.7.

$$\nabla \times (\nabla \times E) = -\nabla^2 E + \nabla(\nabla \cdot E) \qquad \nabla \cdot E = 0$$

$$\nabla^2 = \frac{\partial^2}{\partial x^2} + \frac{\partial^2}{\partial y^2} + \frac{\partial^2}{\partial z^2}$$

equations 2.3.1.4.6

$$\nabla \times (\nabla \times E) = -\mu \frac{\partial(\nabla \times H)}{\partial t} = -\mu \frac{\partial}{\partial t}\left(\varepsilon \frac{\partial E}{\partial t}\right) = -\mu\varepsilon \frac{\partial^2 E}{\partial t^2}$$

equation 2.3.1.4.7

Introducing a new parameter that characterizes the speed of light (υ), in terms of electric permittivity (ε), and magnetic permeability (μ) is shown in equation 2.3.1.4.8.

$$\nu = \frac{1}{\sqrt{\varepsilon\mu}}$$

equation 2.3.1.4.8

A partial differential equation of the second order is obtained when equation 2.3.1.4.8 is introduced into equation 2.3.1.4.7.

$$\nabla^2 E = \frac{1}{\nu^2} \frac{\partial^2 E}{\partial t^2}$$

equation 2.3.1.4.9

The same sequence of steps can be done for the magnetic field constitutive equation as shown below to obtain a partial differential equation.

$$\nabla\times\left(\nabla\times H\right)=-\nabla^{2}H+\nabla\left(\nabla\cdot H\right)$$

$$\nabla\cdot H=0$$

$$\nabla^{2}H=\frac{1}{\varepsilon^{2}}\frac{\partial^{2}H}{\partial t^{2}} \qquad \text{equation 2.3.1.4.10}$$

The solutions to the partial differential equations 2.3.1.4.9 and 2.3.1.4.10 are given below for the electric and magnetic components in an electromagnetic wave.

$$E\left(r,t\right)=\mathrm{Re}\left(E_{0}\exp\left(i\left(kr-wt\right)\right)\right)$$
$$H\left(r,t\right)=\mathrm{Re}\left(H_{0}\exp\left(i\left(kr-wt\right)\right)\right) \qquad \text{equations 2.3.1.4.11}$$

The solutions to the partial differential equation can be introduced into the constitutive equations given in equation 2.3.1.4.9 and 2.3.1.4.10. The wave vector is dependent on the wavelength, wave frequency and the speed of the light.

$$\nabla^{2}\left[\mathrm{Re}\left(E_{o}\exp\left(i\left[k.r-wt\right]\right)\right)\right]=\frac{1}{v^{2}}\frac{\partial^{2}}{\partial t^{2}}\left[\mathrm{Re}\left(E_{o}\exp\left(i\left[k.r-wt\right]\right)\right)\right]$$

$$\mathrm{Re}\left[\nabla^{2}Eo\exp\left(i\left[k.r-wt\right]\right)\right]=\frac{\mathrm{Re}}{v^{2}}\left[\frac{\partial^{2}}{\partial t^{2}}\exp\left(i\left[k.r-wt\right]\right)\right]$$

$$-\left(k.k\right)\mathrm{Re}\,Eo\exp\left(i\left[k.r-wt\right]\right)=-\frac{w^{2}}{v^{2}}\mathrm{Re}\left(E_{o}\exp\left(i\left[k.r-wt\right]\right)\right)$$

$$k^2 = \frac{w^2}{v^2}$$

$$k = \frac{2\pi f}{v} = \frac{2\pi}{\lambda}$$

The solution to the constitutive equation can now be applied to the interference of laser beams. Assuming that there are three interfering laser beams each with energy $E_1(r,t)$, $E_2(r,t)$ and $E_3(r,t)$, the solution to the electric component of the electromagnetic spectrum will be:

$$E_1(r,t) = \mathrm{Re}\left(E_{01}\exp\left(i\left(k_1 r - wt\right)\right)\right)$$

$$E_2(r,t) = \mathrm{Re}\left(E_{02}\exp\left(i\left(k_2 r - wt\right)\right)\right)$$

$$E_3(r,t) = \mathrm{Re}\left(E_{03}\exp\left(i\left(k_3 r - wt\right)\right)\right)$$

The overall electric energy and the overall intensity of the interfering laser beams is therefore given as:

$$E_T(r,t) = E_1(r,t) + E_2(r,t) + E_3(r,t)$$

$$I_1 = \left|E_{01}\right|^2, I_2 = \left|E_{02}\right|^2, I_3 = \left|E_{03}\right|^2$$

$$I_T(r) = \left|E_{01}\exp\left(ik_1 r\right) + E_{02}\exp\left(ik_2 r\right) + E_{03}\exp\left(ik_3 r\right)\right|^2$$

The interfering beams contain real and imaginary values resulting in nine terms in the interference equation shown below. The nine terms include: three constant energy terms and six variable terms.

$$I_T(r) = |E_{01}|^2 + |E_{02}|^2 + |E_{03}|^2 + 2\,\mathrm{Re}\left(E_{01}\cdot E^*_{02}\right)\cos\left[(k_1 - k_2)\cdot r\right]$$
$$-2\,\mathrm{Im}\left(E_{01}\cdot E^*_{02}\right)\sin\left[(k_1 - k_2)\cdot r\right] + 2\,\mathrm{Re}\left(E_{01}\cdot E^*_{03}\right)\cos\left[(k_1 - k_3)\cdot r\right]$$
$$-2\,\mathrm{Im}\left(E_{01}\cdot E^*_{03}\right)\sin\left[(k_1 - k_3)\cdot r\right] + 2\,\mathrm{Re}\left(E_{02}\cdot E^*_{03}\right)\cos\left[(k_2 - k_3)\cdot r\right]$$
$$-2\,\mathrm{Im}\left(E_{02}\cdot E^*_{03}\right)\cos\left[(k_2 - k_3)\cdot r\right]$$

2.3.2. **Macromolecular Photophysics and Photochemistry**

Grottham–Draw's law stipulates that photochemical reactions can only be initiated upon light absorption by macromolecules. Macromolecules absorb light of wavelengths from 200-700nm because the bonding electrons of these molecules oscillate at a frequency of 10^{11} to 10^{16} s^{-1} which correspond to the UV wavelength region. Photochemical reactions, via light absorption, occur mainly through an intermediate electronic excited state which possess a higher energy and a different spin state from the ground state. The ground state, residing at a minimum energy level, is symbolized by S_o, and it has two electrons with anti-parallel spins. Two electrons with antiparallel spins reside at the ground state according to Pauli's exclusion principle. The first excited state transition involves the promotion of an electron from the ground state S_o to a state S_1^*. Electrons residing in the first excited state, S_1, are singlets with antiparallel spin. T_1 is the first triplet excited state with a slightly lower energy than the S_1^*. Apart from the energy differences between T_1 and S_1^* states, electrons in the T_1 energy level have parallel spin states. Physical properties of materials in the electronic excited state differ considerably from the properties of those materials in the ground state. In addition to differences in physical properties, the chemical reactivities of the materials also differ. A diagram that describes the physical and chemical processes that occur during the interaction of light with macromolecules is the Jablonski diagram shown below.

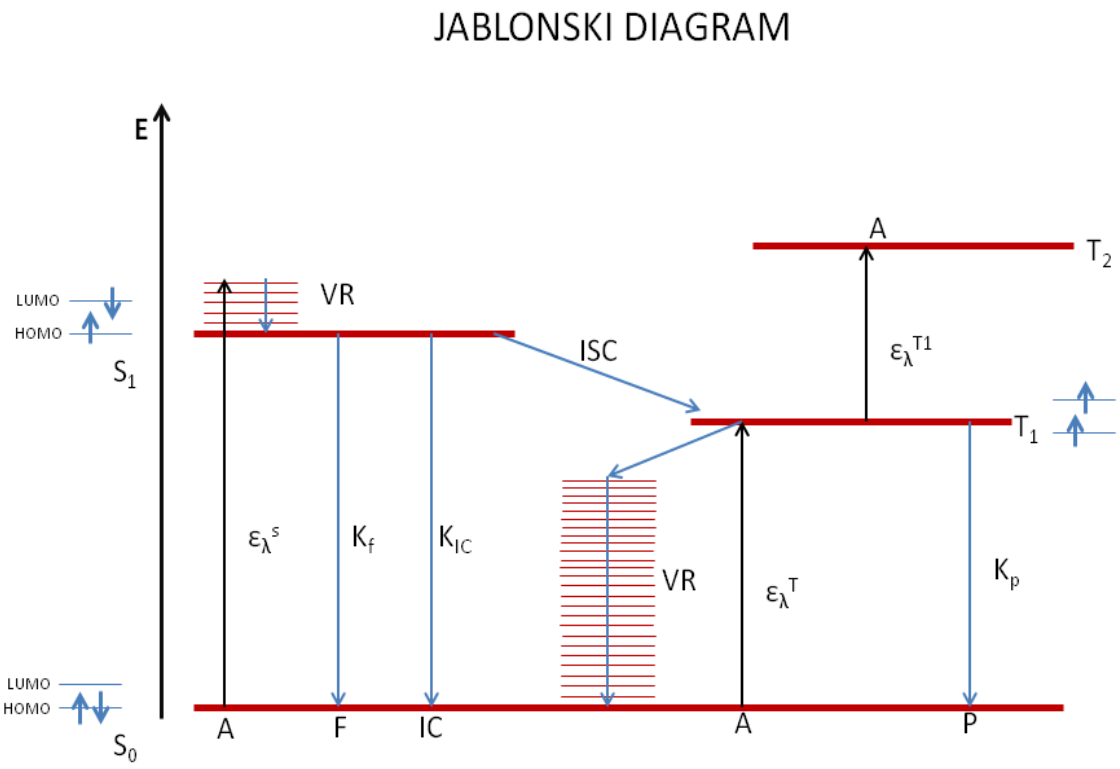

Figure 2.3.2.1. Jablonski diagram showing the various energy transfer processes during the absorption of light.

In the Jablonski diagram in figure 2.3.2.1,

Absorption (A) - is the promotion of an atom from an HOMO- higher occupied molecular orbital ground state (So), to an excited split spin state(S_1).

Fluorescence (F) - is the radiative transitions from excited singlet states such as (S_1) to a lower energy singlet state e.g. the ground state (S_O). The rate constant for such transitions varies from $K_f = 10^5\text{-}10^9\ s^{-1}$

Phosphorescence (P) – is also called delayed flourescence and is characterized by radiative transition between a triplet state and a singlet state. The rate constant for such transitions varies from $K_p = 10^{-1}\text{-}10^6\ s^{-1}$. The low value for the rate constant indicates that the life time of the excited state that results in phosphorescence is long. During the period of existence of the excited state leading to phosphorescence, several

photochemical processes and reactions can occur between the excited molecule and other interacting molecules.

Internal conversion (IC) - This represents all the internal non-radiative processes that result in the transition from an excited state to a ground state within the same spin multiplicity. Non-radiative photophysical processes usually evolve energy in the form of heat. The rate constant for intersystem crossing varies from $K_{IC} = 10^{8}$-$10^{12}s^{-1}$

Intersystem Crossing (ISC) - This represents all the non-radiative transitions between states of different spin multiplicity. The rate constant for intersystem crossing varies from $K^{s}_{ISC} = 10^{7}$-$10^{10}s^{-1}$

Vibrational relaxation (VR) - This represents all transitions between different vibrational excited states. The rate constant for vibrational relaxation varies from $K_r = 10^{10}$-$10^{12}s^{-1}$

From the Jablonski diagram it is evident that with the absorption of a photon by an organic molecule, several potential pathways are open that can lead to the deactivation of the excited molecule. However, the only useful deactivation pathway is the pathway that leads to a photochemical reaction. Deactivation processes leading to photochemical reactions are termed photochemical processes, while other processes that result in the release of heat are photo-physical processes. An organic molecule can be used for a photo-initiated reaction only when the photochemical pathways leading to the deactivation of its excited state occur much faster than the photo-physical pathways to deactivation.

The photochemical and photophysical deactivation processes in an organic molecule are called either singlet to singlet, singlet to triplet, triplet to triplet, triplet to singlet electronic transitions. Furthermore, singlet to singlet, singlet to triplet electronic transitions in organic molecules are classified into σ,σ^*; n, σ^*; n,π^*; π,π^* depending on the chemical nature of the absorbing group present in the molecule. The chemical specie

absorbing light within a molecule is called the chromophore group. Chromophore groups based on unsaturated double bonds and triple bonds fall into the π,π* groups of electronic transitions, while chromophore groups based on ketones fall into the n,π* group of electronic transitions. Other chromophore groups based on the azide functional group fall into the n, σ*; n, π* group of electronic transitions.

For photochemical monomolecular reactions involving either intramolecular rearrangement or homolytic bond cleavage to proceed, the rate constant for the photochemical reactions K_r^s must be greater than or equal to the rate constant for all other photo-physical processes K_f, K_{IC} and $K^s_{ISC.}$

$$K_r^s \sim \Sigma(K_f + K_{IC} + K_{ISC}^S) \qquad \text{equation 2.3.2.1.}$$

Where K_r^s is the rate constant for the photochemical reaction proceeding from an excited singlet state. Examples of photochemical reactions proceeding via a monomolecular pathway are radical photopolymerization reactions. In radical photopolymerization reactions, radicals are generated via the hemolytic cleavage of the photoinitiator species.

Meanwhile, for bimolecular photochemical reactions involving the formation of excited state complex to proceed, the rate constant for the photochemical reactions K_r^T must be greater than or equal to the sum of rate constants for the phosphorescence and intersystem crossing reactions (K_p and K_{ISC}^T).

$$K_r^T \sim \Sigma(K_p + K_{ISC}^T) \qquad \text{equation 2.3.2.2.}$$

Where K_r^T is the rate constant for a photochemical reaction proceeding from a triplet excited state. An example of photochemical reactions proceeding via the bimolecular pathway is sensitized cationic photopolymerization reactions.

Monomolecular photochemical reactions usually proceed faster than bimolecular photochemical reactions. One of the reasons for this is the inevitable loss of energy during transfer of excited stage energies between different molecules. Other reasons

include quenching of fluorescence lifetime by impurities present between interacting molecules as well as the requirement for short distances between interacting molecules. However, most commercially available photoinitiated material systems undergo photomodification via the bimolecular photochemical reaction route. Bimolecular reactions can be divided into a Forster and a Dexter type bimolecular photochemical reaction mechanism.

2.3.2.1. Forster Mechanism for Bimolecular Photochemical Reaction

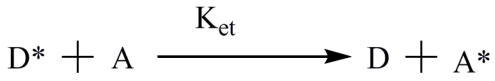

Figure 2.3.2.1.1. Reaction equation for a Forster bimolecular photochemical reaction.

A generalized Forster reaction equation is shown in shown in figure 2.3.2.1.1. In a Foster bimolecular reaction, light absorption by an organic/organo-metallic molecule D produces an excited state D*. D* then undergoes radiative decay via fluorescence and transfers the emitted photon to an absorber molecule A forming an excited state molecule A*. The rate constant for a Foster bimolecular photochemical reaction equation is affected by the energy overlap between the emitted photon by D^* and the absorption spectrum of the absorber species A. The fluorescence intensity of the donor atom as well as its fluorescence lifetime also affect the rate constant of a Forster bimolecular photochemical reaction.

The rate constant for a Forster bimolecular photochemical reaction, is given by:

$$K_{et} = 1/\tau_S^D (R_o/R)^6 \qquad \text{equation 2.3.2.1.1.1}$$

2.3.2.2. Dexter Mechanism for Bimolecular Photochemical Reaction

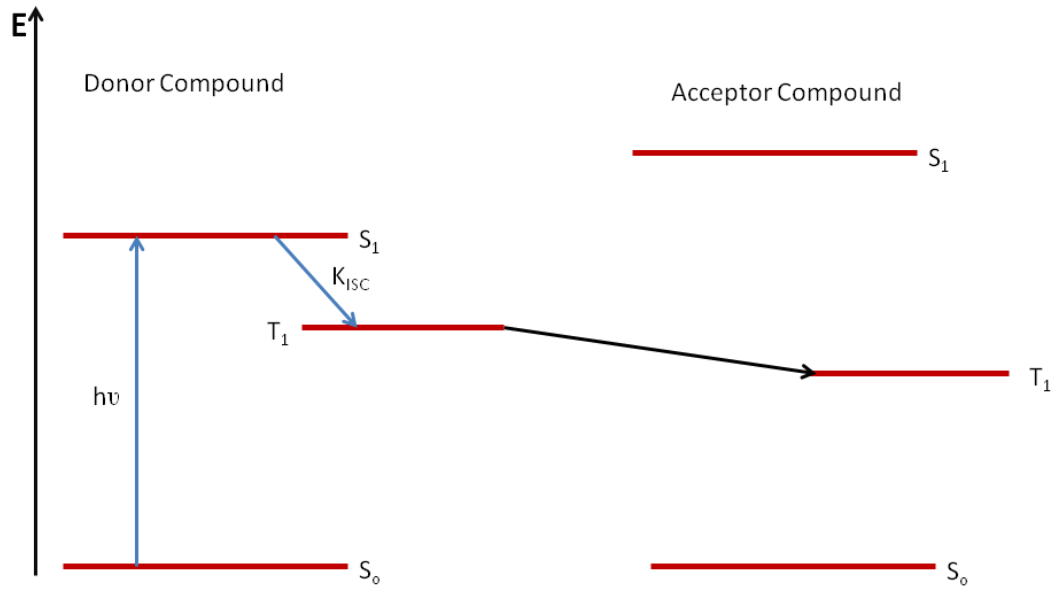

Figure 2.3.2.2.1 Schematic showing a Dexter bimolecular photochemical reaction.

The Dexter bimolecular reaction mechanism is associated with dye-sensitized photochemical reactions. These reactions proceed with the formation of a complex between an excited state donor and an acceptor. Several conditions must be fulfilled for a Dexter bimolecular reaction to proceed. One of the conditions is that the donor compound must absorb at a longer wavelength than the acceptor compound. In addition, the acceptor compound must possess a triplet state energy level that is less than the triplet state energy of the donor compound. If all these conditions are fulfilled, then the energy transfer rate constant in Dexter photochemical reactions increases as the rate constant of inter system crossing K_{ISC} increases. As discussed earlier, all other radiative and non-radiative deactivation pathways not leading to photochemical reactions have to be minimal under photochemical reaction conditions.

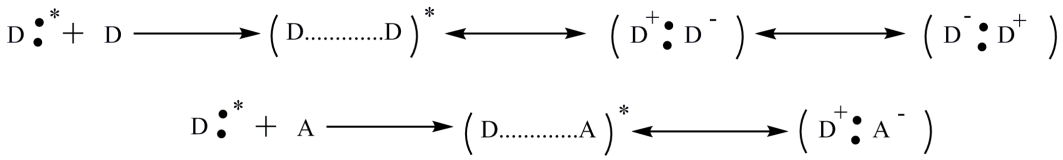

Figure 2.3.2.2.2 A generalized photochemical reaction equation for a Dexter bimolecular energy transfer reaction.

Dexter bimolecular photochemical reactions proceed through the formation of an excimer or an exciplex. An excimer is formed when similar molecules serve as both donor and acceptor agents during a photochemical reaction, while an exciplex is formed when different molecules act as donor and acceptor agents during a photochemical reaction.

When an exciplex is formed, the different electronic properties of the D: and A results in electronic separation within the exciplex. As a result D: is oxidized and the acceptor A is reduced. Ionic radicals formed during the oxidation-reduction photochemical reactions react via dark chemical reactions to give final products- cross-linked polymeric materials.

2.4 Plasma Reactive Ion Etching (RIE)

A glow discharge plasma can be described as a partially ionized gas consisting of electrons, ions, and a variety of neutral species. Industrial manufacturing techniques in the electronics industry that incorporate reactive ion etching make use of low pressure discharge tubes excited at radio frequencies. The electron densities in such tubes can range from 10^{8}-10^{13} cm^{-3} with energies from 1-10 eV. It should be noted that low pressure glow discharge plasmas form weakly ionized gases that contain a significant molecules, atoms and radicals. Therefore the chemical reactions occurring in a plasma chamber is governed by the concentration of the afore mentioned materials as well as their density at the surface of the substrate in the chamber.

Plasma reactive ion etching is preferred for the generation of micron, sub-micron and nano-resolved features because a high degree of anisotropy can be achieved compared to more established wet chemical etching processes. Furthermore, plasma reactive ion etch takes place at relatively low temperatures, dry conditions which limits user exposure to toxic chemicals and solvents. In addition, plasma reactive ion etching allows the user greater flexibility in determining the etching conditions by simply varying parameters like gas pressure, gas flow rate, and electrode potentials.

The two fundamental processes that occur in a plasma chamber are:

1) Electrons produced by the discharge tube collide with gas molecules in the chamber producing reactive species at low temperatures.
2) The discharge tube then drives the reactive gases consisting of molecules, radicals and ions to the surface of a substrate present in the chamber to cause its chemical modification.

2.4.1. Physical/Electrical driving force in plasma RIE

The physical driving force in a plasma chamber is the accelerating electrons. The electrons created in a discharge tube upon collision with the process gases in the chamber dissociate and ionize the gases forming highly reactive molecular fragments like ions and radicals. The electrons are accelerated by the application of an electric field gradient across the plasma chamber. During the initial stages of electron acceleration, electrons bombard the walls of the chamber forming a depletion layer near the walls and electrodes. The depletion layer formed during the initial stage then accelerates positive ions as well as other electrons towards the substrate placed in the plasma chamber. The

high mobility of electrons within a plasma chamber means that all surfaces within a plasma chamber assume a more negative potential than that of the bulk plasma.

2.4.2 Chemical driving force in plasma RIE

The chemical processes taking place in a plasma RIE can be categorized into six basic steps. In the first step, the reactive species are generated by electron bombardment of process gases within the plasma chamber. This is a crucial step because the processing gases do not react with the substrates directly without plasma inhibited dissociation. For example SF_6 gas cannot etch silicon by itself. It is the F^+ ions produced during electron bombardment that etch the silicon substrate.

The second step is the diffusion of the reactive species to the surface of the substrate. This step is usually facilitated by potential difference existing between the electrodes: The rate of diffusion is therefore dependent on the electrode potential. Higher potential may likely increases the rate of etch and induce some degree of isotropy, while a lower potential may reduce the rate of etch but maintain a high anisotropy.

After arrival at the surface of the substrate, adsorption of the radical species onto the substrate is a crucial step for chemical reactions to occur. Adsorption is usually facilitated by substrate affinity for the reactive gases and substrate cleanliness.

Step four is the chemical reaction between the adsorbed species and the substrate. After the chemical reaction, desorption of the reacted species from the substrate is the next step. For desorption to occur, the vapor pressure of the products formed after the reaction must be high.

Step six then involves the diffusion of the product species back into the bulk gas and away from the substrate.

Chapter 5 goes into more details on the specific chemical reactions occurring during the plasma induced RIE of silicon and silicon oxide substrates in various processing gas conditions.

CHAPTER 3

BLOCK COPOLYMER LASER INTERFERENCE ABLATION

This chapter presents a motivation for designing resists based on diblock copolymers. The limitations of conventional photoresists as well as the apparent advantages of switching to a block copolymer type resist are discussed. The concept of block copolymer laser interference ablation is introduced as a means to the generation of features with ~30nm resolution. The technique is applied to two commercially available diblock copolymers: PS-b-P4VP and PS-b-PEO. The feature density improvement from patterned PS-b-P4VP block copolymers over commercially available resists is also discussed.

3.1 Introduction to Block copolymer Laser Interference Ablation

Surface engineering and surface modification has been at the forefront of science for decades. Recent advances in the area of surface science and surface engineering has led not only to the continuous miniaturization of devices according to Moore's law [69-71], but also to the fabrication of novel devices with exciting and new properties. -These properties have been harnessed for optical, electrical [72], magnetic [73], chemical [74], mechanical [75-76] and biological [77-79], applications. Devices based on nano-scaled features that have been fabricated include sensors for bio-detection [80,81], free standing magnetic and semiconducting nano-pillars[73,82-83] for data storage media, transistors and other electronic devices, and nano catalysts for growth of nanowires [51]. The performance of these devices is not only dependent on the material properties of the nano-scaled features, but also on the their density on the given support or substrate [84].

The science of surface modification or engineering resulting in the generation of nano-scale and micro-scale features on substrates has evolved over the years, with the

introduction of new techniques including: soft lithography [79,85], e-beam lithography [86-87], laser interference lithography [74,88], dip-pen lithography [89-90], block copolymer lithography [15,83]etc. Although these techniques have found active use in research laboratories, they are plagued with several disadvantages and the ultimate fabrication technique would most probably employ a combination of two or more of these fabrication techniques [91-92].

The two most important issues plaguing the industrial application of the above listed techniques are: 1) cost, and 2) high through put. Based on cost, with the current trend in the manufacturing world where profit maximization and cost minimization are a key aim of an organization, the lowest cost technique would be block copolymer nanolithography.

Block copolymers are the product of the covalent bonding of two or more chemically dissimilar polymers. The resultant copolymer, when dissolved in a suitable solvent and later spin-coated on a substrate or when left to vaporize in a container, spontaneously reorganizes, forming nanodomains with dimensions/periodicity of order 10-100nm [93]. The periodicity and feature type [94] in block copolymers can be tuned by changing the degree of polymerization of each block, the segment length of each block, the solvent used to dissolve the blocks, the annealing temperature [95] and annealing environment [6,96], and the interphase /boundary interactions between the block and substrate [97]. All of these factors create an unfavorable (negative or approaching zero) entropy energy of mixing and a favorable enthalphic energy that causes the spontaneous formation of micro domains in thin films of block copolymers [98]. The domain spacing for phase-separated block copolymers has been obtained using

the Self Consistent Field Theory (SCFT) [99] and depending on the regime of phase separation, leads to either a strong segregation limit (SSL) or a weak segregation limit (WSL) [98]. Under the SSL designated according to the χN parameter, where the value of χN is greater than 10 (χN $\gg$ 10), the general formula for estimating the inter domain spacing is given in equations 2.2.1.3.3 and 2.2.1.3.4, with different values for the scaling coefficients published by various authors.

When a high throughput process is required for the large-area fabrication of periodic structures on substrates, one of the fastest methods of producing such structures is laser interference patterning (LIP) [100-101]. Laser interference ablation involves the combination of light beams at an angle on a substrate leading to the periodic variation of intensity on the surface [102]. This periodic variation of intensity when applied to a surface having a photo-modifiable polymer thin film results in the generation of features having the same periodicity as the interference pattern [103-104] . **Scheme 3.2** shows a typical set-up for two-beam laser interference used in the laser interference ablation of block copolymers.

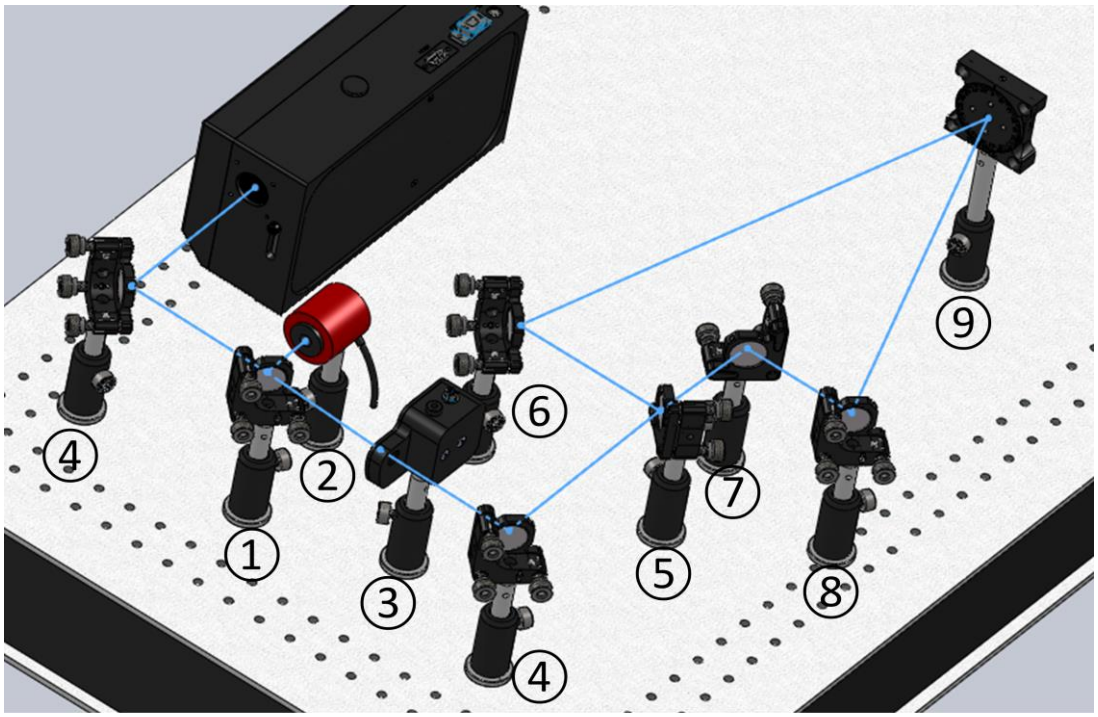

Scheme 3.1 Experimental setup for Laser Interference ablation comprising of a 10% reflection beam splitter for monitoring the laser power (1), a high threshold power meter (2), an electromechanical shutter (3), reflection mirrors (4,6,7,8), a 50/50 beam splitter (5), and a rotary stage sample holder (9).

The beam from a frequency doubled 266nm Nd:YAG nanosecond laser source goes through a reflection beam splitter, an electromechanical shutter and a reflection mirror before passing through a 50/50 beam splitter. The first reflection beam splitter sends 10% of the beam into a high threshold power meter for monitoring the laser power while the 50/50 beam splitter splits the beam into two beams allowing 50% of the beam intensity to pass through while the rest is reflected. The two beams are later converged together on the substrate thus forming an interference fringe. Through the adjustment of parameters for the periodicity of the interfering light beams, namely the wavelength λ, the intensity of the laser beams, and the angle of interference θ, one can easily obtain a range

of values for the periodicity of features ranging from 200nm to hundreds of microns. The formula for the periodicity of features (P) from laser interference ablation is given by:

$$P = \frac{\lambda}{2\, n\, Sin\, \theta} \qquad \text{equation} \qquad 3.2$$

where n is the dielectric constant of the medium of propagation of the laser beams.

3.2. Laser Interference Ablation of Block Copolymers.

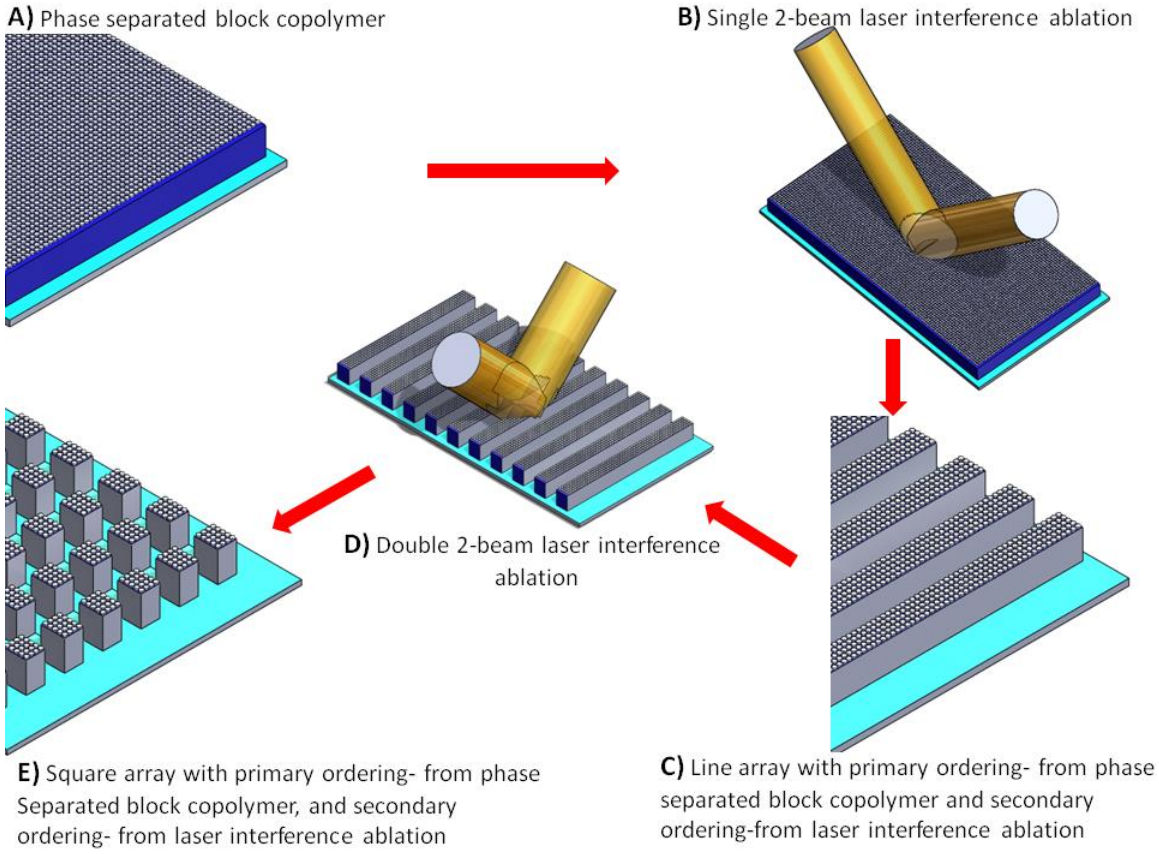

Scheme 3.2.1A. A scheme showing the increased feature density obtained from using a block copolymer laser interference lithography technique with the block copolymer acting as the photoactive media.

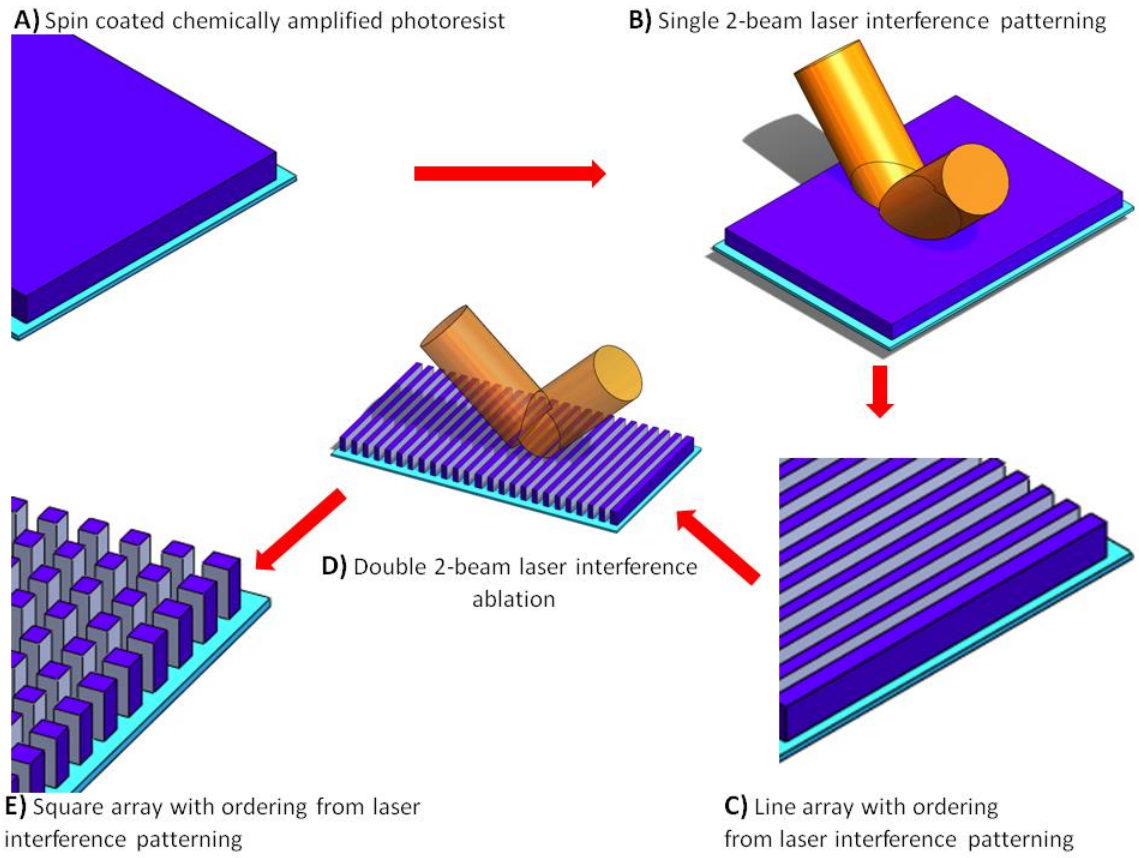

Scheme 3.2.1B. A scheme showing the feature density obtained from using a conventional laser interference lithography technique with a photoresist acting as the photoactive media.

Scheme 3.2.1A illustrates the steps used to obtain multi-scaled and multifunctional features using block copolymer laser interference ablation. One of the advantages of this technique is that it is substrate independent, and does not require a primer layer coating. The first step, shown as step A in scheme 3.2.1A, is the spin coating of a thin layer of block copolymer on the substrate. The spin-coated block copolymer is introduced into an enclosed chamber with optimized conditions necessary for phase separation and generation of hexagonal cylindrical arrays. The function of the block

copolymer, at this step, is to serve as a resist to replicate, in 2D, the variation of light beam intensity on the substrate.

Another important, but latent function of the block copolymer is the inherent ability of the blocks to differentially complex with chemicals. This latent function can be harnessed by introducing a metallic salt solution into one of the blocks: a functional resist is created that can etch different length scale dimensions onto a substrate depending on the type of gas present in the plasma chamber. Further discussion on harnessing the multifunctional property of laser-ablated block copolymers will be done in the chapter 4 of this dissertation.

As comparison, scheme 3.2.1B shows the steps used for fabricating features with conventional photoresists using LIP. Proceeding from steps B to C usually involves a prebake, postbake and solvent development steps that can affect the feature resolution. Furthermore, chemically amplified photoresists lack any form of functionality after photoexposure, and thus can only give features with resolution determined by the wavelength of light as well as the capability of the focusing optics. Block copolymers acting as functional photoresists on the other hand can give features with resolution based on the wavelength of light, as well as on the phase separation kinetics of the block copolymer.

3.3.1. PS-b-P4VP Block copolymer: Phase separation and Properties

3.3.1.1. Chemical and Physical Properties

One of the block copolymers that was investigated in this dissertation is Poly (styrene-b-vinylpyiridine) block copolymer.

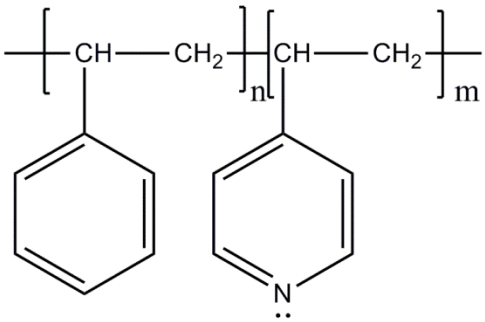

Figure 3.3.1.1.1. Chemical formula for a PS-b-P4VP block copolymer

The styrene component of the block copolymer acts as a plasma RIE resist for feature transfer to silicon and silicon oxide substrates, and it is used routinely in the electronics industry. The high plasma etch resistance of styrene, to fluorine and chlorine containing gaseous plasma systems, is due to the presence of strong aromatic bonds in the benzene side group. The pyridine block is the active functional component of the block copolymer: it is chemically different from styrene, being hydrophilic due to the presence of the heterocyclic nitrogen containing aromatic group-pyridine. Furthermore, the pyridine component can be protonated to form complexes with metallic salt solutions.

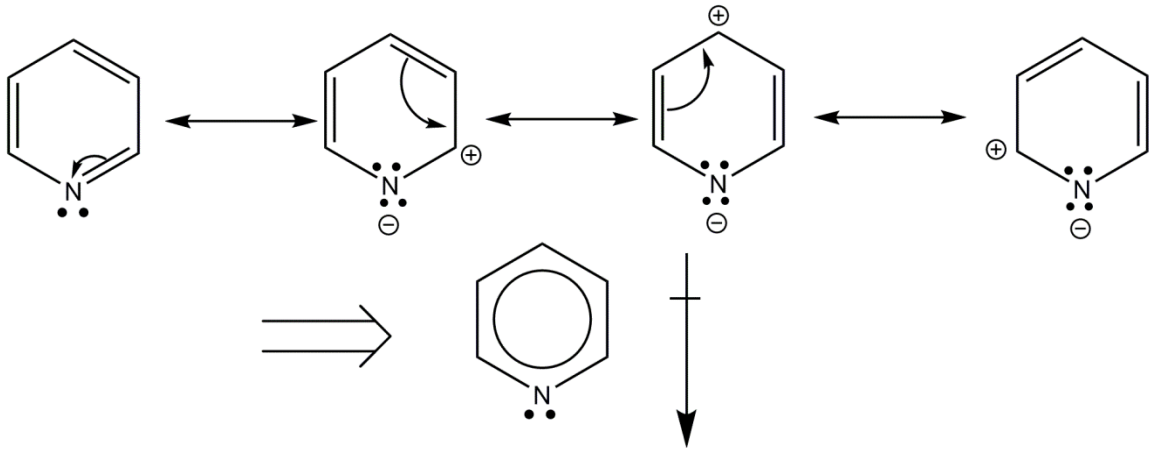

Figure 3.3.1.1.2. Electron cloud movement in a Heterocyclic six member aromatic ring of poly(vinyl-4-pyridine)

Nitrogen in the hetero-aromatic ring is in sp^2 hybridization as shown in figure 3.3.1.1.2, and the lone pair of electrons on nitrogen does not take part in the aromatic ring structure. The greater electro-negativity of nitrogen compared to carbon generates a dipole moment in the vinylpyridine molecule. The dipole moment allows for easy protonation of pyridine. Protonation of pyridine generates a pyridinium group that retains the aromaticity of the heterocyclic compound, thus making the pyridinium ion a very stable compound. Because of the stability of the pyridinium group shown in figure 3.3.1.1.3, pyridine is a base with a pKa≈5.2. Thus when pyridine is placed in a solution with a pH of 5.1, 50% of the pyridine is protonated; while if placed in a solution with a pH of 6.1, 10% of the pyridine is protonated. When pyridine is placed in a solution with a pH of 4.1, 90% of the pyridine is protonated. This property of pyridine can be utilized to complex pyridinium cations with other complex metallic salts.

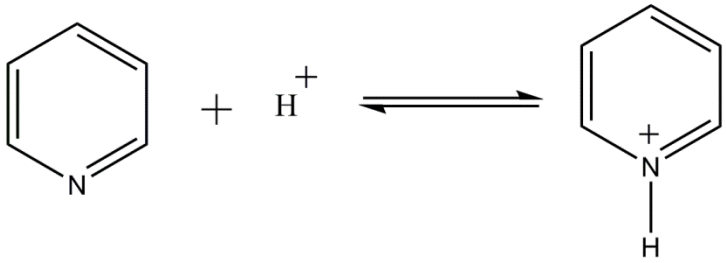

Figure 3.3.1.1.3. Protonation of poly(vinyl-4-pyridine) to form a pyridinium cation

3.3.1.2. Phase Separation

An asymmetric PS-P4VP block copolymer was purchased from Polymer Source Incorporated., Canada. The molecular weights of the Styrenic component and the vinylpyridine component of the PS-P4VP block copolymer are 24000 kDa and 9500 kDa, respectively. The PDI (poly-dispersity index), i.e the ratio of the weight average M_W to

the number average molecular weight M_n, for the PS-P4VP block copolymer, is 1.10. Anhydrous toluene and tetrahydrofuran (THF) used for phase separation were purchased from Sigma Aldrich and used without further purification. The silicon wafers Si (100) with a 10µm thermal oxide layer and the Si(100) wafers, used in this experiment, were purchased from University Wafers and had a thickness of 564µm. The substrates were cleaned and made hydrophilic by overnight immersion in a H_2O_2:H_2SO_4 solution followed by rigorous rinsing in deionised water.

Phase-separated vertical cylindrical domains of the PS-P4VP block copolymer were obtained by dissolving the block copolymer in a Toluene:THF (80:20 v/v) mixture before spin coating a thin layer (150nm) onto a clean silicon substrate. The thin film was solvent annealed in a Toluene:THF environment for 5 hours to induce the reorganization of micelles into vertical cylinders. The chamber used for annealing the block copolymer is shown in figure 3.3.1.2.1.

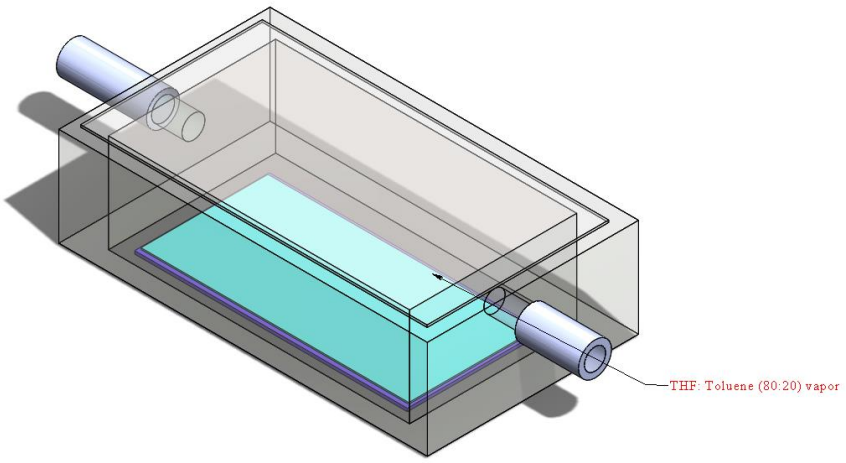

Figure 3.3.1.2.1 Pictorial representation of an Annealing Chamber for solvent annealing PS-b-P4VP block copolymer in a THF:Toluene solvent vapor.

Atomic Force Microscopy (AFM) was used to obtain high resolution phase and surface topographical images from a Dimension 3000 (Digital Instruments) AFM in the light tapping mode using a commercial silicon nitride micro cantilever probe tip having a resonant frequency of 360 KHz with an aluminum backside coating.

To obtain hexagonal vertical cylindrical arrays of P4VP in a PS matrix, PS-P4VP block-co-polymer was dissolved in a THF:Toluene mixture with varying volume concentration of THF. Solutions of PS-b-P4VP containing THF:Toluene (50:50), THF:Toluene (30:70), and THF:Toluene (20:80) volume % were investigated. The AFM phase contrast images shown below in figures 2.3.1.2.2A, B, and C, indicate that phase separation from micelles of PS-P4VP occur faster, and give more regular and ordered structures when spun from a solution containing (20:80) volume % of THF:Toluene.

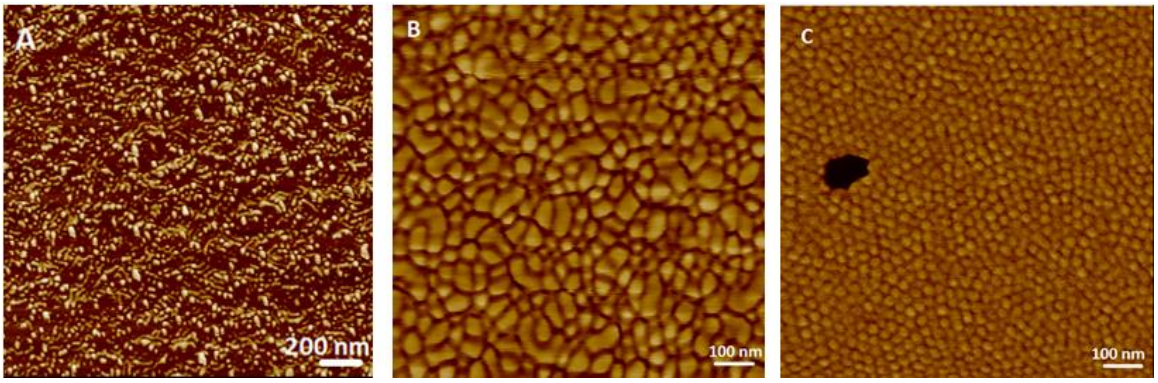

Figure 3.3.1.2.2. AFM phase contrast images of phase-separated PS-b-P4VP block copolymers solvent spun from a 0.5 wt% solution containing (A) 50:50 THF:Toluene (B) 30:70 THF:Toluene (C) 20:80 THF:Toluene.

The vapor pressure within the annealing chamber was also varied to optimize parameters required for obtaining large scale hexagonal ordering. It was observed that as the annealing chamber vapor pressures of THF:Toluene reduces, the degree of long range ordering also reduces. Figure 3.3.1.2.3A and B are AFM topographical and phase

contrast images obtained after annealing a PS-b-P4VP block copolymer in a large chamber made with a 100ml beaker, with a few drops of THF:Toluene (80:20) vol% for a period of 5 hours. The relative vapor pressure within the confined vessel was obtained by taking the ratio of volume of the container containing the annealing solvent and the annealing chamber. The relative vapor pressure was 0.33. The annealing conditions used to obtain phase-separated PS-b-P4VP block copolymer in figure 3.3.1.2.3 had the least relative vapor pressure and lamellar like features were obtained as shown in the phase and topographical AFM images.

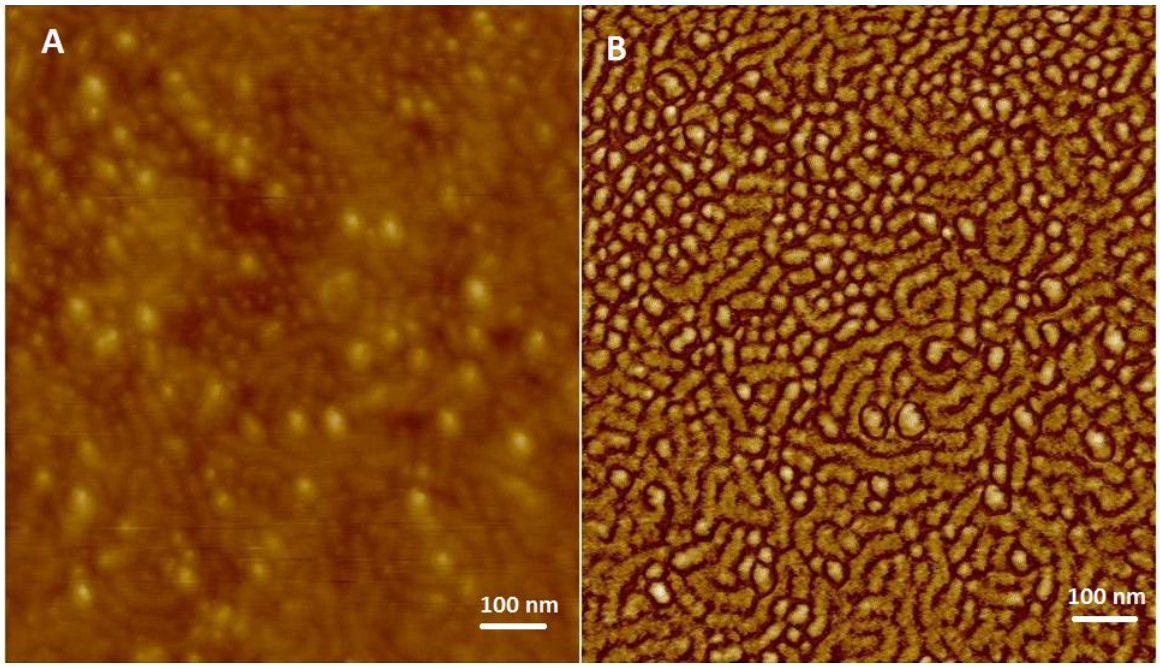

Figure 3.3.1.2.3. AFM (A) Topographical (B) Phase contrast images of phase-separated PS-b-P4VP block copolymer showing lamella like features.

The relative vapor pressure of THF:Toluene in the annealing chamber can be increased by increasing the diameter of the container with the annealing solvent at constant annealing chamber dimensions. Another way to increase the vapor pressure can

be by reducing the overall dimensions of the annealing chamber while keeping the dimensions of the container with the annealing solvent constant. By increasing the relative vapor pressure of THF:Toluene, it is possible to move away from the lamellar to the spherical orientation/ domain of phase separation. The AFM topographical and phase contrast images shown in figures 3.3.1.2.4A and B are from a PS-b-P4VP block copolymer after annealing in a THF:Toluene environment with a relative vapor pressure of 0.454 for a day. No long range hexagonal packing is visible in this regime, and the domains appear to have irregular sizes.

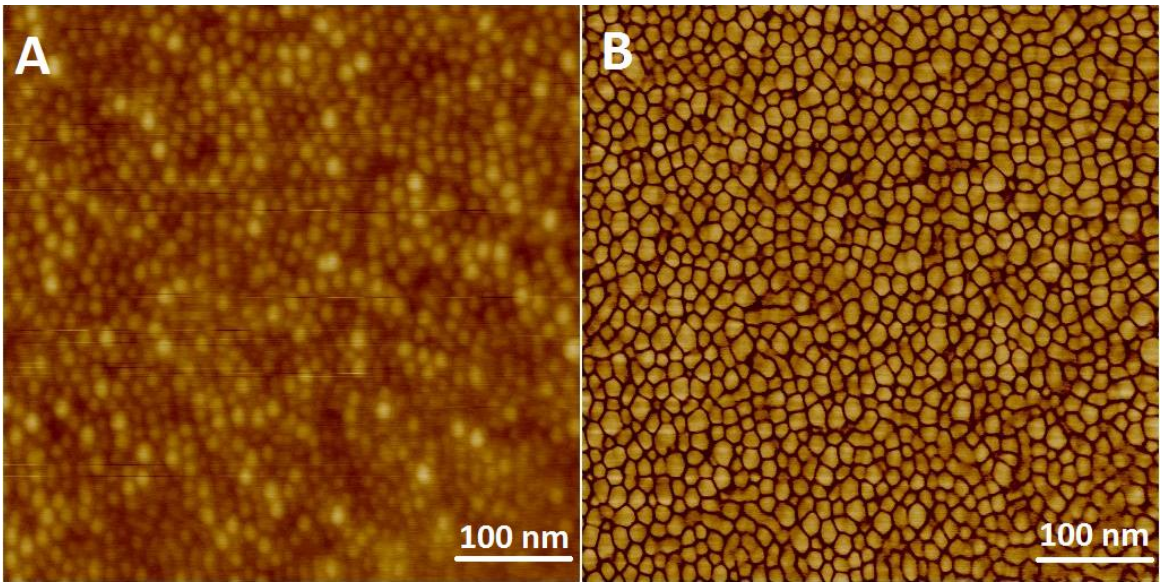

Figure 3.3.1.2.4. AFM (A) Topographical (B) Phase contrast images of phase-separated PS-b-P4VP block copolymer showing random vertically oriented cylinders of P4VP in a PS matrix.

The vapor pressure of the annealing environment was increased to 0.61 by reducing the volume of the annealing chamber. The result was a longer range hexagonal ordering on the phase-separated PS-b-P4VP block copolymers. The domain sizes at this regime are more uniform and measure ~25nm and the interdomain spacing measure

~30nm measured from the AFM topographical and phase contrast images in figures 3.3.1.2.5A and B respectively.

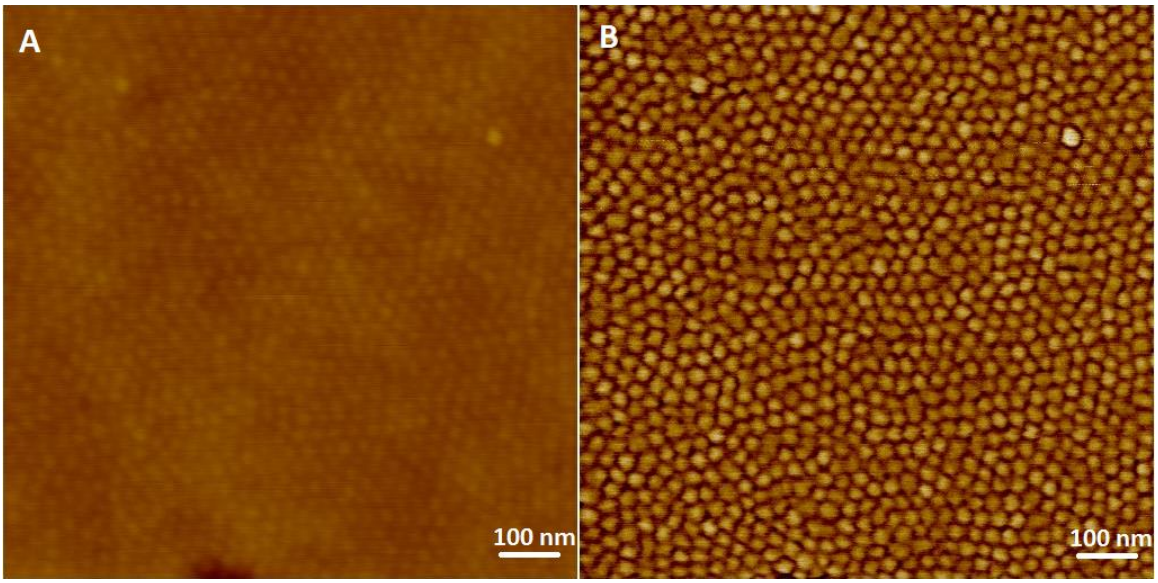

Figure 3.3.1.2.5. AFM (A) Topographical (B) Phase contrast images of phase-separated PS-b-P4VP block copolymer showing hexagonal packing of vertically oriented cylinders of P4VP in a PS matrix.

The extent of the long range ordering is seen in the large area 3μm×3μm topographical image of a phase-separated PS-b-P4VP block copolymer in figure 3.3.1.2.6.

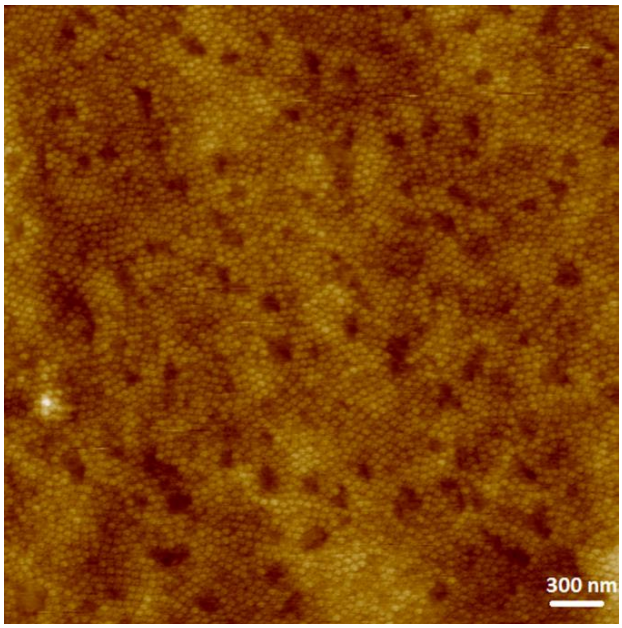

Figure 3.3.1.2.6. AFM Topographical contrast image of phase-separated PS-b-P4VP block copolymer showing long range ordering with defects of vertically oriented cylinders of P4VP in a PS matrix.

3.3.2. PS-b-PEO Block copolymer: Phase Separation and Properties

3.3.2.1. Physical and Chemical Properties

Another commercially available block copolymer with potential use as photoresist- poly (styrene-b-ethyleneoxide)- was also investigated for laser interference ablation.

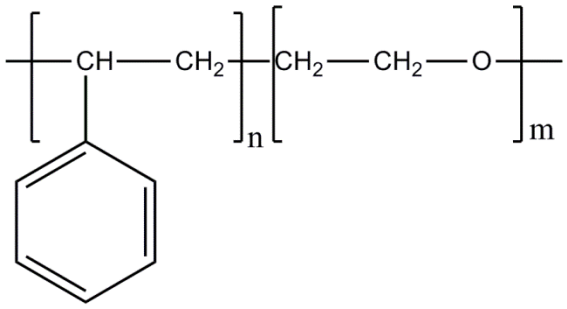

Figure 3.3.2.1.1. Chemical formula for a PS-b-PEO block copolymer

The styrene component of the block copolymer serves as a plasma resist due to the strong aromatic benzene ring side chains present in the poly styrene block, while the ethylene oxide component of the block is the functional component that can be used for the formation of complexes with metallic salt solutions.

PS-b-PEO block copolymer falls into a special class of block copolymers called amphiphilic block copolymers. The amphiphilic nature is due to the lipophilic character of the polystyrene block and the lipophobic character of the ethylene oxide block. The hydrophilic nature of ethylene oxide means that it readily dissolves in aqueous solutions, and the presence of two lone pairs of electrons on oxygen means that it can readily form complexes with metallic salt solution.

3.3.2.2. Phase separation

An asymmetric PS-PEO block copolymer was purchased from Polymer Source Incorporated., Canada. The molecular weights of the styrene component and the vinylpyridine component of the PS-P4VP block copolymer are 18000 kDa and 7500 kDa respectively. The PDI (poly-dispersity index), i.e the ratio of the weight average M_W to the number average molecular weight M_n, for the PS-PEO block copolymer, is 1.05. Anhydrous benzene used for phase separation was purchased from Sigma Aldrich and used without further purification. The silicon wafers Si (100) with a 10µm thermal oxide layer and the Si(100) wafers, used in this experiment were purchased from University Wafers and had a thickness of 564µm. The substrates were cleaned and made hydrophilic, by overnight immersion in a H_2O_2:H_2SO_4 solution followed by rigorous rinse in deionised water.

Phase-separated PS-b-PEO block copolymer was obtained by dissolving the blocks in a benzene solution up to 2 wt% concentration. This was followed by spin coating the 2wt% solution onto a silicon or silicon oxide substrate, and annealing the substrate in a benzene vapor environment. This resulted in the generation of vertical cylindrical arrays of PEO blocks in a PS matrix.

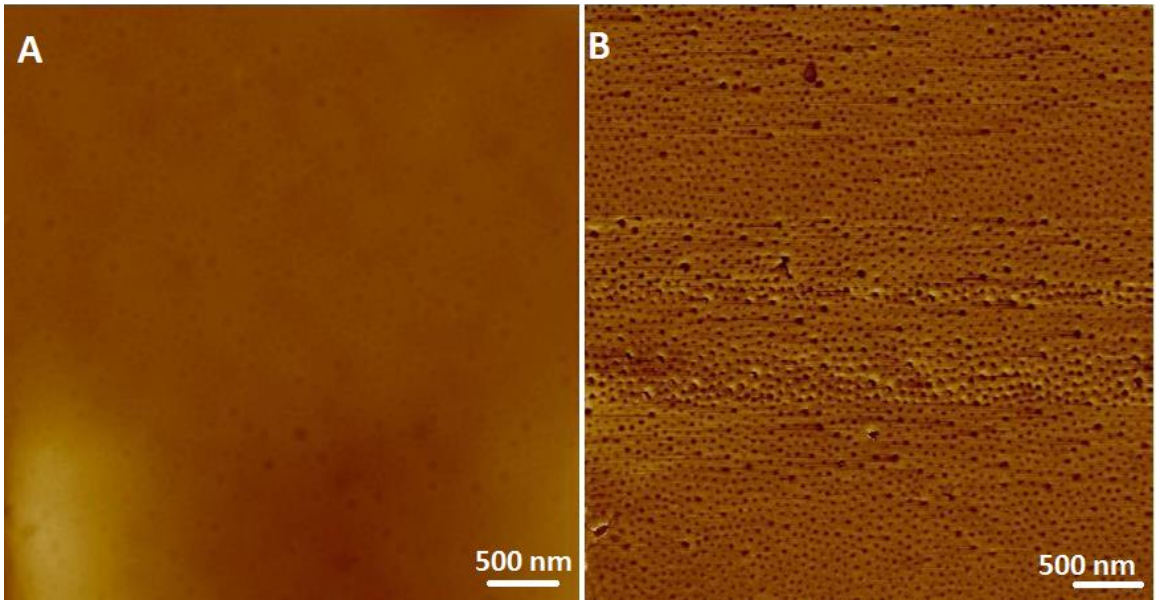

Figure 3.3.2.2.1. AFM (A) Topographical and (B) Phase contrast images of phase-separated PS-b-PEO block copolymer.

3.3.3. Laser Interference Ablation of PS-b-P4VP and PS-b-PEO

Laser interference ablation was conducted using the 266nm wavelength (fourth harmonic) of a 10ns pulsed Neodymium doped Yttrium Alluminum garnet (Nd:YAG) laser. The wavelength of the laser light source was tuned to 266 nm. Two-beam laser interference was obtained by using a beam splitter to split the initial beam from the laser source shown in scheme 3.2. This is followed by the convergence of the beams on the substrate using a mirror. The combined beams give an interference fringe. The

interference fringe can be represented in space as a 3-dimensional variation in light intensity shown in figure 3.3.3.1. The interference fringe is a result of the vector addition of two electromagnetic waves as was discussed previously in the background section of chapter 2.

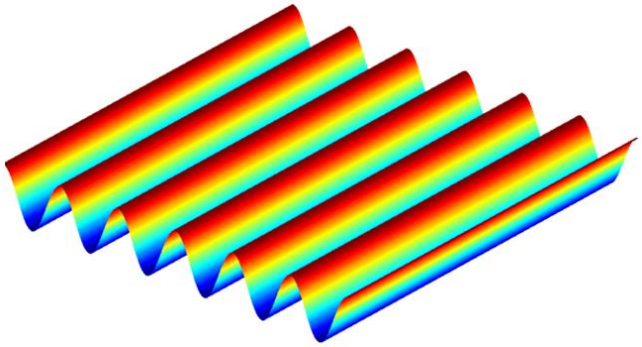

Figure 3.3.3.1. Simulated intensity distribution on a substrate from a two beam laser interference ablation.

Two successive exposures to a laser beam are required for the generation of a square pattern. The two exposures are at a 90º orientation to one another. The resultant interference fringe in 3D space is shown below.

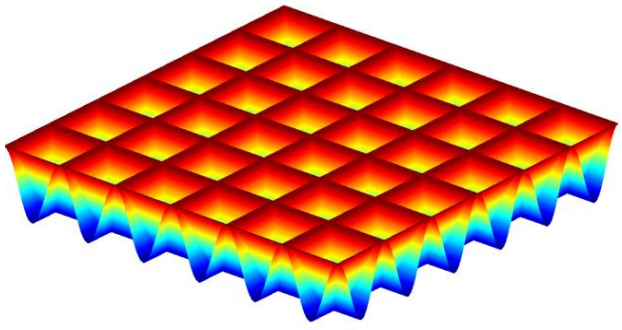

Figure 3.3.3.2. Simulated intensity distribution on a substrate from two simultaneous laser interference ablation. The first laser interference pattern is 90^0 rotated with respect to the second laser interference pattern.

Laser ablated PS-b-P4VP bock copolymers as well as PS-b-PEO block copolymers were analyzed using an AFM to determine the periodicity of the features generated. Line arrays of laser ablated block copolymer show a periodicity of 2µm and a feature depth of 120 nm. The width of the generated features is dependent on the intensity of the laser beam, and the ablation threshold of the block copolymer. The ablation thresholds for the block copolymers were obtained by exposing a phase-separated PS-b-P4VP or PS-b-PEO block copolymer thin film to an interfering beam, and the resulting line widths were measured at varying intensity of the laser beam. Figure 3.3.3.3 is a graph of block copolymer line width (um) versus laser fluence. From the graph, the ablation threshold values for PS-b-P4VP and PS-b-PEO were found to be 17.5 mJ/cm^2 and 145.27 mJ/cm^2 respectively.

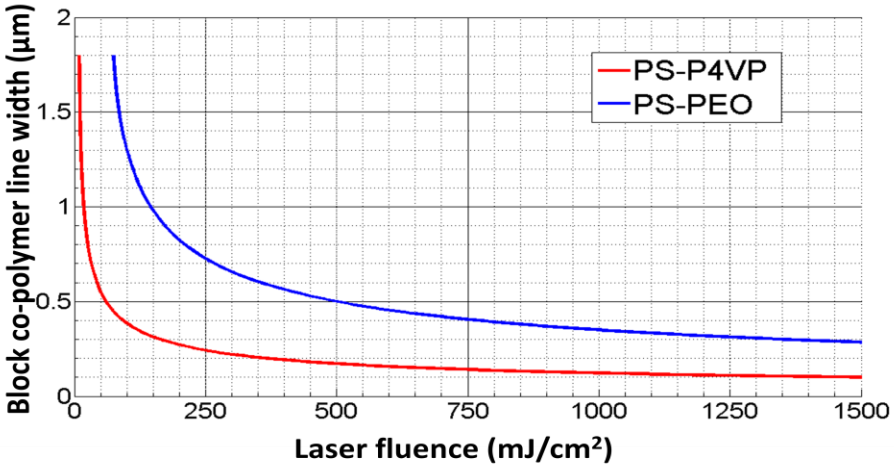

Figure 3.3.3.3. A simulated graph obtained from AFM and SEM analysis of a laser patterned block copolymer thin film showing the variation in ablation line width with increasing laser fluence.

The high ablation threshold of the PS-b-PEO block copolymer can be attributed to the transparency of the ethyleneoxide block to deep UV light. Therefore, PS-b-P4VP block

copolymer due to its low ablation threshold value, as a result of a large UV absorption coefficient of polystyrene and poly(4-vinylpyridine), is a more desirable material as a multifunctional photoresist.

Figures 3.3.3.4A, B, C are AFM analysis of line arrays form a PS-b-P4VP block copolymer. Figure 3.3.3.4A is the topographical AFM image showing line arrays with a 2µm periodicity; while a cross sectional analysis of the sample in figure 3.3.3.4B indicates that the line arrays have a depth of 120 nm. A 3 dimensional representation of the patterned line arrays is shown in figure 3.3.3.4.C.

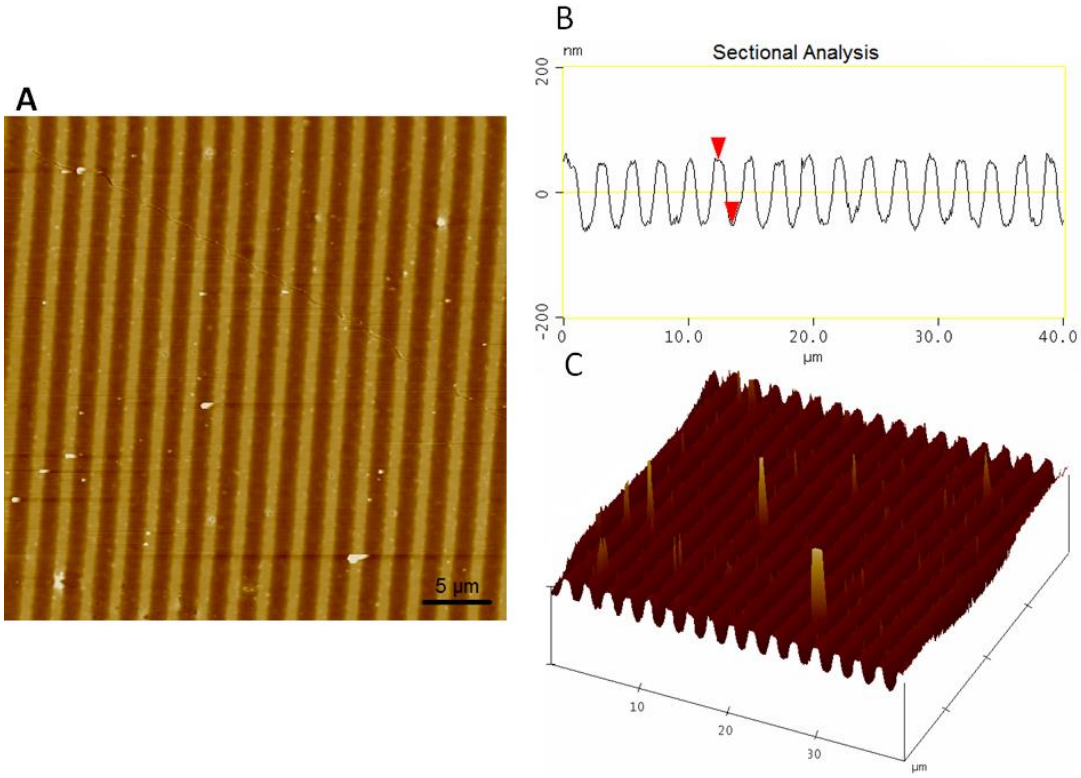

Figure 3.3.3.4.(A) AFM topographical image of a laser-ablated PS-b-P4VP block copolymer thin film (B) AFM cross-sectional analysis of a laser-ablated block copolymer thin film showing the topographical information on the surface (C) A 3D AFM simulated image of a laser-ablated block copolymer thin film.

Figures 3.3.3.5A, B, C are AFM analysis of square arrays form a PS-b-P4VP block copolymer. Figure 3.3.3.5A is the topographical AFM image showing square arrays with a 2 μm periodicity; while a cross sectional analysis of the arrays indicates that the square arrays taper at their apex and have a height of about 120 nm. A three dimensional representation of the line patterned arrays is shown in figure 3.3.3.5C. As inset in figure 3.3.3.5A, is the AFM phase contrast image of a domain within one of the squares in the square array. Hexagonal ordering of the block copolymer domains with defects is clearly visible in the phase contrast image.

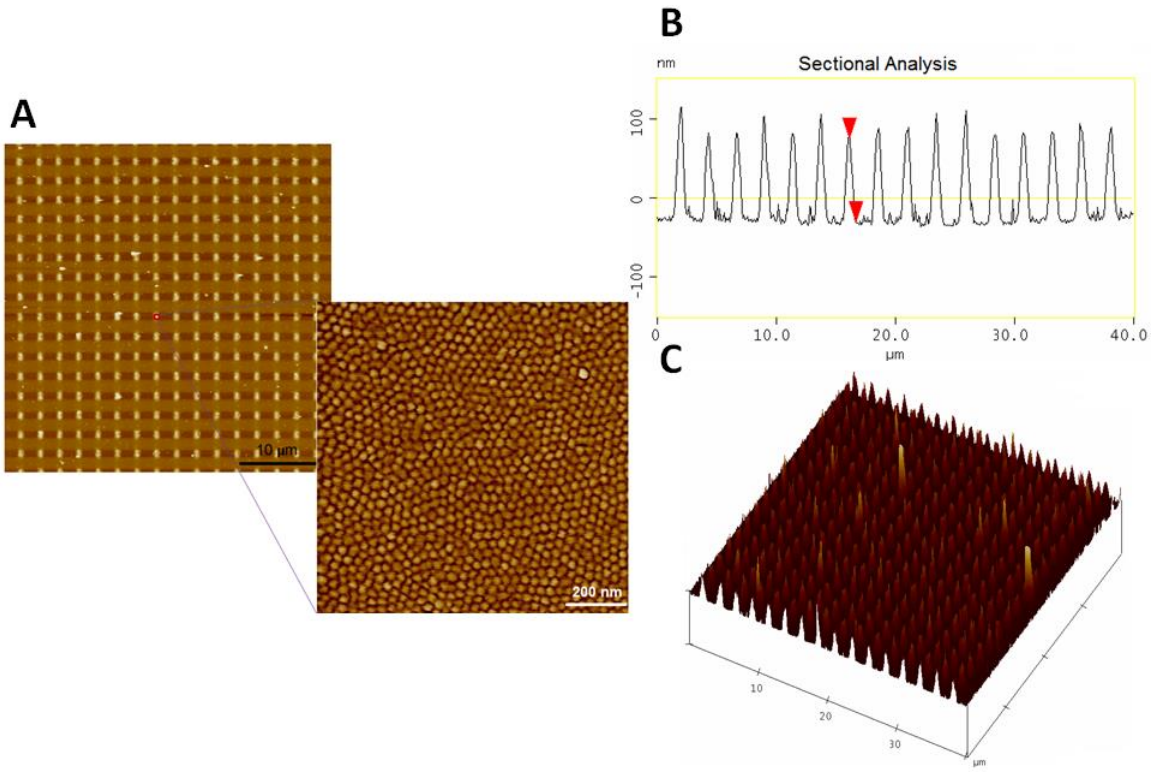

Figure 3.3.3.5. (A) AFM topographical and phase contrast images showing the hierarchical assemblies in a laser-ablated PS-P4VP block co polymer. The image on the left is the AFM topographical image showing the large area periodic structures obtainable using laser interference ablation (physical secondary ordering). The image on the right is the AFM phase contrast image showing the features present in each domain of the periodic array (chemical primary ordering) (B) AFM cross-sectional analysis of a laser-ablated block copolymer thin film showing

Figure 3.3.3.5. (continued) the topographical information on the surface. (C) 3D AFM simulated image of a laser-ablated block copolymer thin film.

Laser interference ablation of phase-separated PS-b-P4VP block copolymers always results in the physical modification of the film. However, physical modification of the film surface does not penetrate through the thickness of the film. What this implies is that although, some regions of the block copolymer that are exposed to the laser are not completely ablated. Furthermore, regions that are supposed to have received a low dose of laser beam below the ablation threshold, still have some form of chemical modification. The modification appears in form of agglomeration of domains and sometime loss of ordering within the domains. Figure 3.3.3.6 below shows the AFM phase contrast image of a PS-b-P4VP block copolymer after exposure to a laser beam.

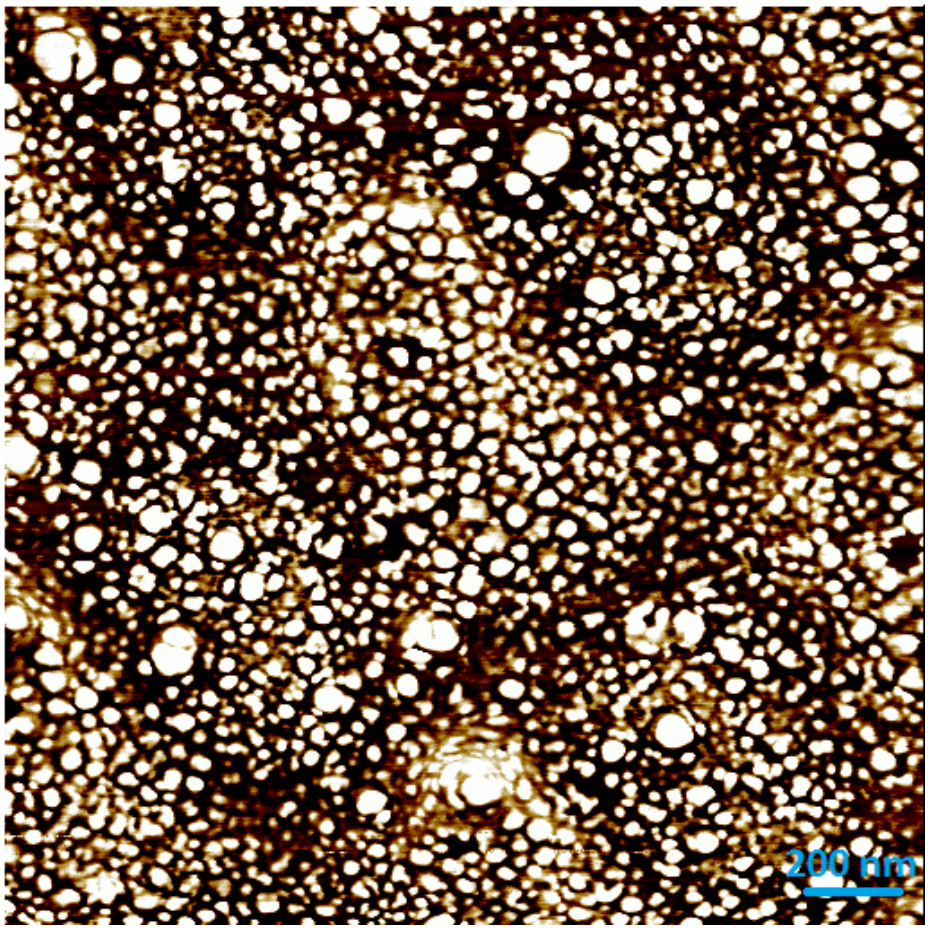

Figure 3.3.3.6. AFM Phase contrast image of a laser patterned, phase-separated PS-b-P4VP block copolymer showing domain coalescence of the P4VP.

Figures 3.3.3.7A and B are SEM images of periodic line and square arrays obtained from LIA of PS-b-P4VP block copolymer. The SEM images show similar periodicity of 2μm as those obtained from the AFM images in figures 3.3.3.4 and 3.3.3.5. The peripheral region of each domain appears to be swollen compared to the inner region. The effect of this defective outer boundary region on the value of the experimental feature density will be discussed further in chapter 4.

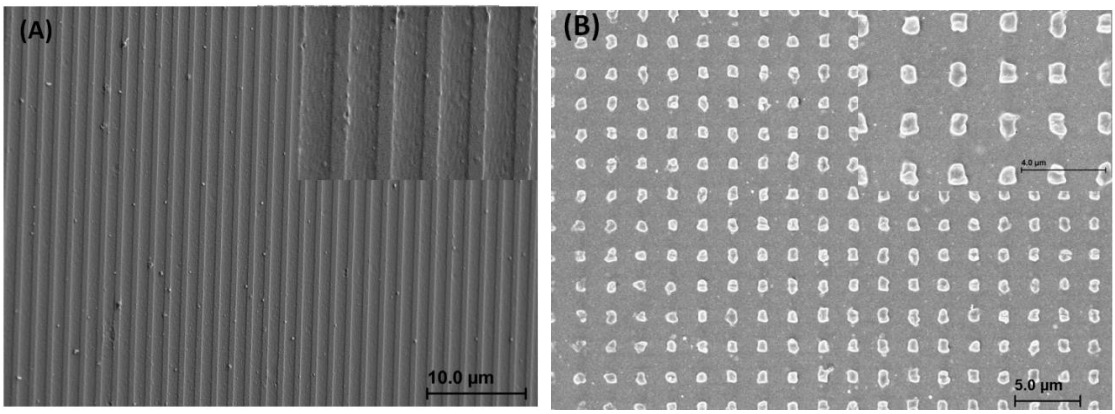

Figure 3.3.3.7. Scanning electron micrograph of a laser ablated PS-P4VP block copolymer showing (A) periodic line arrays (B) periodic square arrays.

Laser interference ablation is a robust technique, and although we have been mainly discussing about line and square arrays on phase-separated PS-b-P4VP block copolymers, LIA can also be used to generate regular triangular arrays –figure 3.3.3.8C, hexagonal packed hole arrays –figure 3.3.3.8D, and island arrays – figure 3.3.3.3.8E.

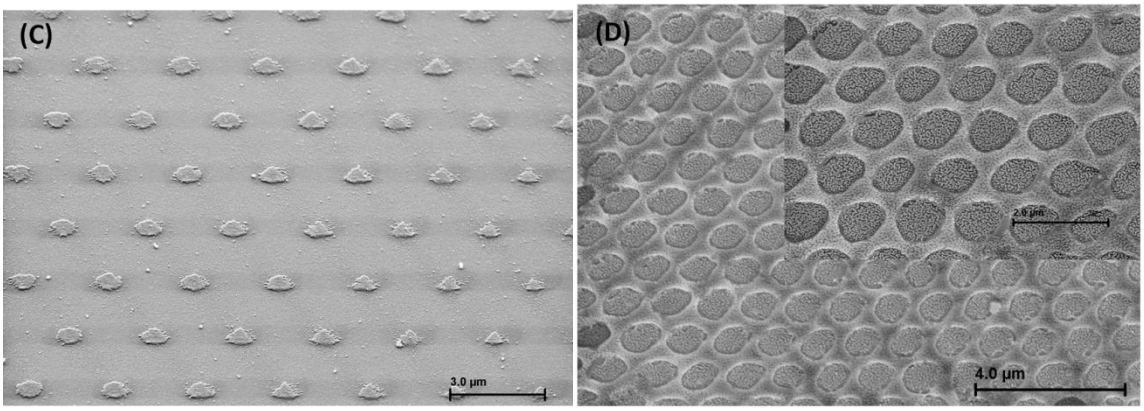

Figure 3.3.3.8. Scanning electron micrograph of a laser ablated PS-P4VP block copolymer showing (C) periodic triangular arrays: the triangular pattern was obtained by the interference of two laser beams on the thin film followed by 2 successive ablations at 60º between each shot (D) hexagonally packed array of holes.

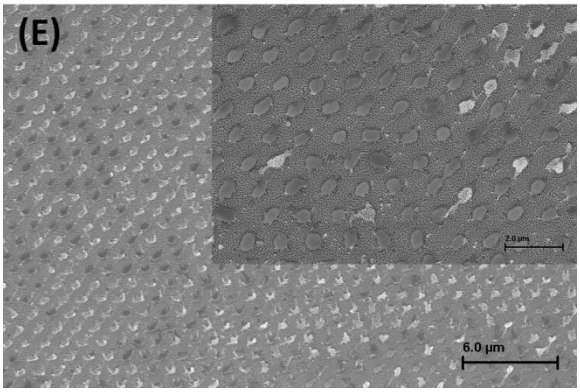

Figure 3.3.3.8. (continued) Scanning electron micrograph of a laser ablated PS-P4VP block copolymer showing (E) hexagonally packed array of islands: the hexagonal packed pattern was obtained by a single exposure to the interference pattern from three laser beams.

X-ray photoelectron spectroscopy (XPS) was carried out to investigate the presence or absence of chemical modification of the block copolymers before and after laser ablation. The functional components of the blocks PEO and P4VP were analyzed. XPS spectra were obtained using a Fisher Thermo Kα XPS with an Aluminum X-ray light source. The incident photon energy was 1486 eV and the size of the xray beam used to probe the sample was kept below 200 µm, while the samples before xray analysis were kept below 5.8×10^{-08} torr.

The survey spectra of unpatterned PS-b-P4VP and PS-b-PEO block copolymers are shown in figures 3.3.3.9.A and B respectively. From the spectra, the presence of nitrogen and carbon at their binding energies correlating to PS-P4VP and PS-b-PEO block copolymers is observed. After patterning a new peak, at 104 eV, is observed at the binding energy for silicon indicating the exposure of the underlying substrate during the ablation process.

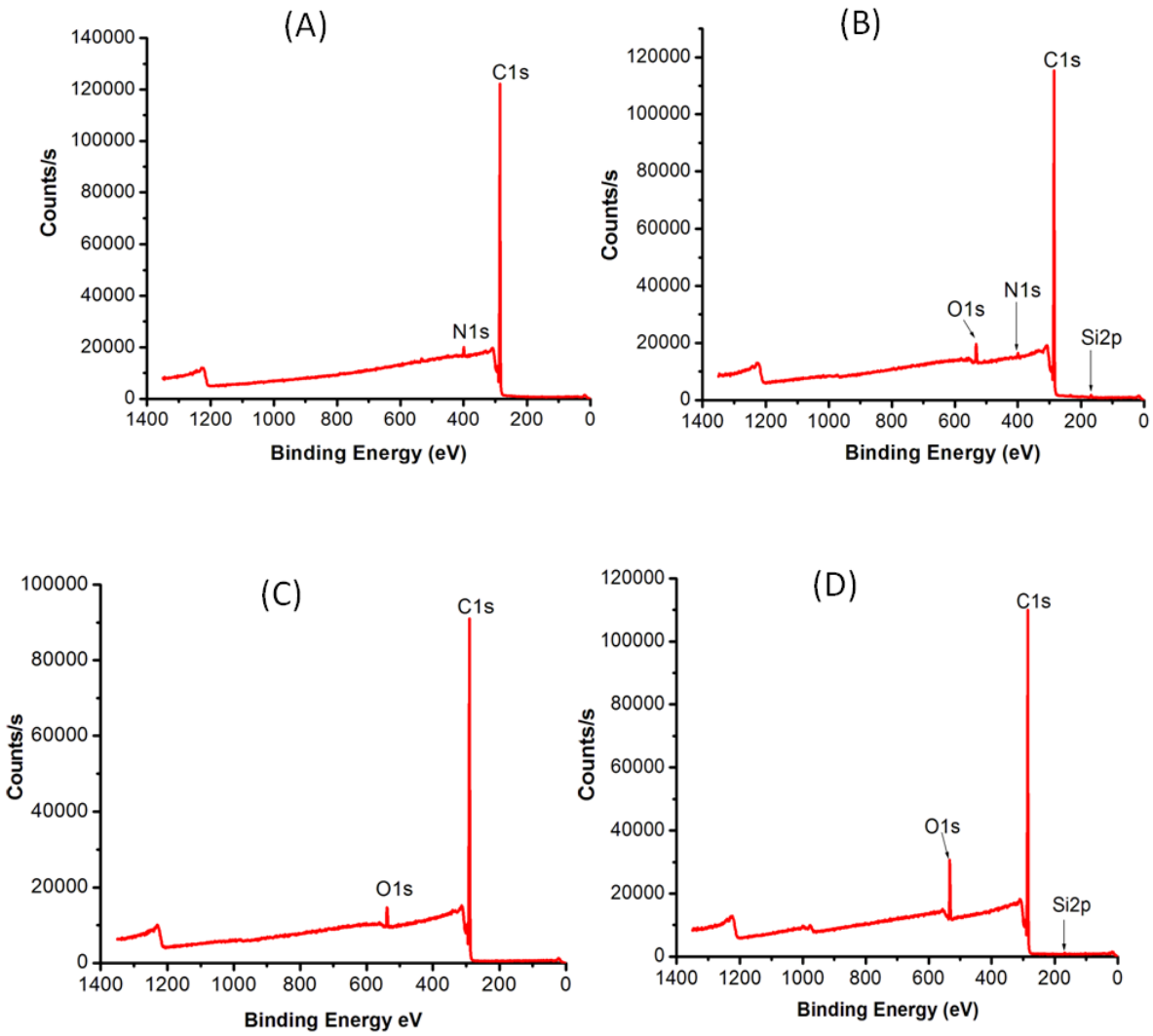

Figure 3.3.3.9. An XPS spectra of (A) an unpatterned PS-P4VP block copolymer showing the peaks corresponding to the binding energies of nitrogen and carbon.(B) patterned PS-P4VP block copolymer showing a new peak corresponding to the binding energy of silicon (C) an unpatterned PS-PEO block copolymer showing the peaks corresponding to the binding energies of carbon and oxygen. (D) a patterned PS-PEO block copolymer showing a new peak corresponding to the binding energy of silicon.

Figures 3.3.3.10A and B show the carbon and the nitrogen spectra of patterned and unpatterned PS-P4VP block copolymer. From the spectra, there appears to be no shift in the binding energies of the carbon and nitrogen indicating that there are no chemical

modifications to the remaining polymer blocks after laser exposure. The drop in intensity of the nitrogen peak (figure 3.3.3.10B right) for the patterned sample can be linked to the expected removal of some of the PS-P4VP during the laser patterning of the substrate.

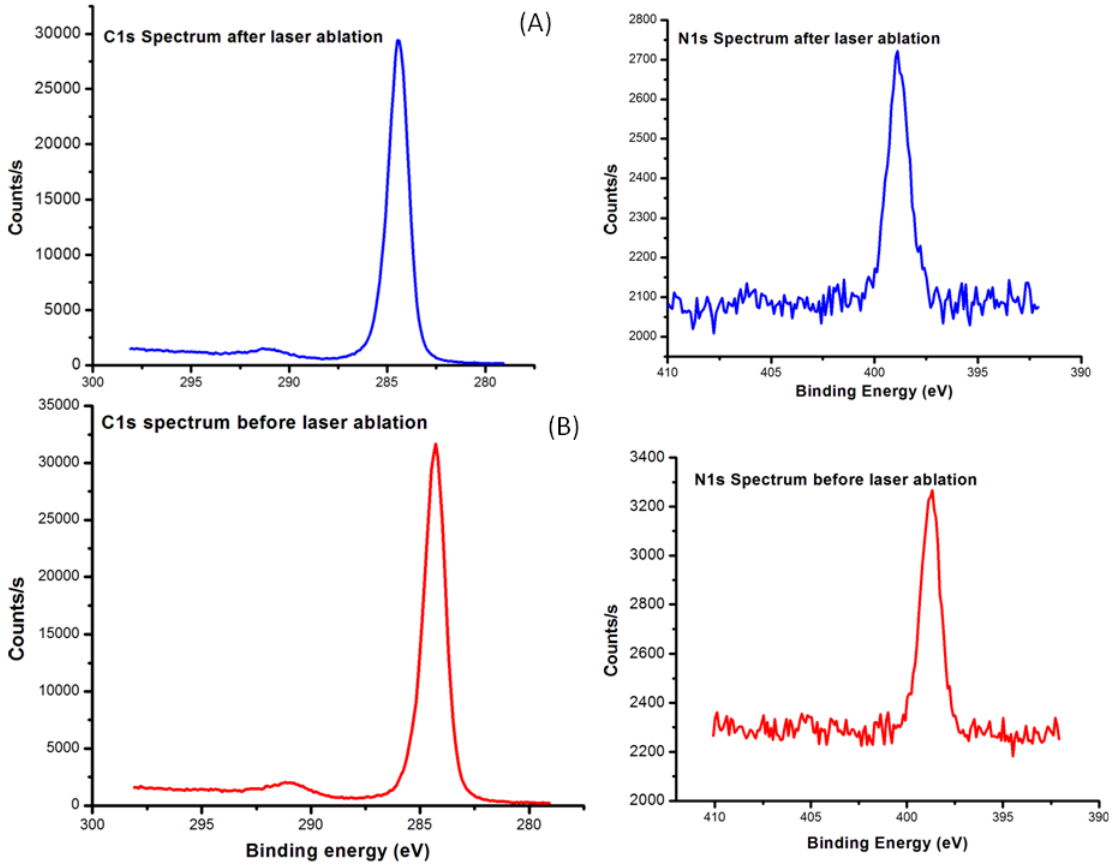

Figure 3.3.3.10. An elemental XPS spectra of (A) C 1s and N1s of a PS-b-P4VP block copolymer after laser interference ablation (B) C 1s and N 1s of a PS-b-P4VP block copolymer before laser interference ablation.

Figures 3.3.3.11A and B show the carbon and the oxygen spectra of patterned and unpatterned PS-PEO block copolymer. From the XPS spectra, there appears to be no shift in binding energies for the carbon and oxygen peaks in both the patterned and unpatterened samples. The elemental carbon XPS spectra has a small shoulder that

remains the same in intensity, before and after laser interference ablation as shown in figure 3.3.3.11A and B. On the other hand, the intensity count (counts/s) for elemental oxygen after the laser ablation patterning is found to increase. The reason is that the intensity contribution to the Oxygen 1s peak is coming not only from the ethylene oxide component, but also from the underlying silicon oxide substrate on which the block copolymer was spun.

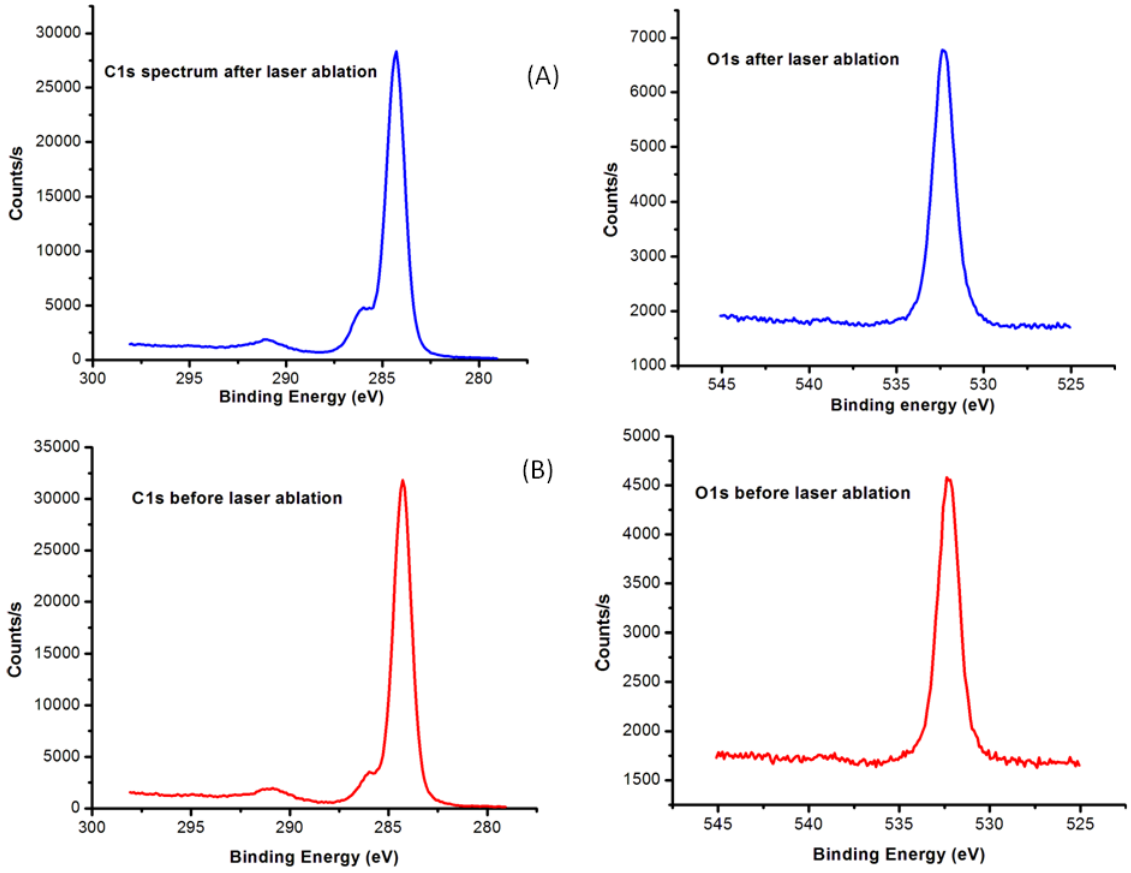

Figure 3.3.3.11. An elemental x-ray photoelectron spectra (XPS) of (A) C 1s and N1s of a PS-b-P4VP block copolymer after laser interference ablation (B) C 1s and N 1s of a PS-b-P4VP block copolymer before laser interference ablation.

3.3.4. Mathematical Estimation of Feature Density

The use of a laser interference ablation technique combined with block copolymer phase separation can potentially result in the generation of hierarchical features on a substrate. The primary chemical ordering: ordering as a result of phase separation, combined with the secondary physical ordering: ordering as a result of laser interference ablation, results in a dual scale hierarchical ordering on the substrate. The feature density as a result of the primary chemical ordering is several orders of magnitude greater than through conventional chemically amplified photoresist patterning techniques. The primary ordering generated correlates with the ordering of the block copolymer domains, as proposed in the theoretical calculations using SCFT and mean field theory calculations, while the secondary ordering correlates with the periodicity of the laser interference pattern as expected from theoretical calculations using Maxwell's equations and Fourier transform.

An estimate of the feature density can be determined, *a priori*, by equating the periodicity of the laser interference beams multiplied by a coefficient dependent on the intensity of the laser beam, with the equation containing parameters that include the material composition of the block copolymer, the inter-domain spacing from a phase separating block copolymer, and other dimensionless variables. A dimensionless variable can be generated by dividing the resultant feature density by the feature density achievable by using a conventional photoresist.

Thus combining equation (3.2) and equations 2.2.1.3.3 and 2.2.1.3.4; and introducing a dimensionless variable F_L, which represents a feature density normalized

against the feature density from a conventional lithography process using chemically amplified photoresist on a periodic line.

$$F_L\ \alpha N^{\delta}\chi^{\nu} = \frac{\varphi\lambda}{2n\ sin\ \theta} \qquad \text{equation 3.2.2.1}$$

From equation 3.2.2.1, the feature density on a periodic line is thus given by the formula:

$$F_L \sim \frac{\varphi\lambda N^{-\delta}\chi^{-\nu}}{2n\alpha\ sin\ \theta} \qquad \text{equation 3.2.2.2}$$

Using the same analogy, the feature density in a periodic area F_a obtained from two successive two-beam laser interference pattern exposures with a 90^0 rotation between exposures can also be calculated under the assumption that the periodic area has a length and width equal to the period *P*. Under this assumption, the area of a given period is given by the area of a square. The equation for feature density in a periodic square area is therefore given by:

$$F_a \sim \frac{\varphi^2\lambda^2 N^{-2\delta}\chi^{-2\nu}}{4\ n^2\alpha^2\ sin^2\theta} \qquad \text{equation 3.2.2.3}$$

For two-beam laser interference patterns with 60^0 rotations between successive exposures, elliptical, hexagonal and oval like periodic arrays can be generated on a substrate [105,103]. In such cases, the generated elliptical and oval features can to a large extent be approximated as a circle and the area of the periodic structure A_p within the period having a diameter equal to the period of the laser interference beam is given by:

$$A_p = \pi\ \frac{\varphi^2\lambda^2}{16\ n^2\ sin^2\ \theta} \qquad \text{equation 3.2.2.4}$$

The feature density in a given elliptical or oval periodic area A_{ac} is thus given by:

$$F_{ac} \sim \frac{\pi\varphi^2\lambda^2 N^{-2\delta}\chi^{-2\nu}}{16n^2\ \alpha^2\ sin^2\ \theta} \qquad \text{equation 3.2.2.5}$$

Table 3.3.4.1 shows the different values for the feature density in periodic line, periodic square, oval, elliptical shaped area for a laser interference ablation technique that employs a phase separating block copolymer as photoresist under the SSL regime using different approximations for the scaling parameters ν and δ from literature.

Table 3.3.4.1. A table with equations for estimating the values for normalized feature density per unit periodic line, per unit periodic square area, and per unit periodic circular area for block copolymers under the Strong Segregation Limit using different scaling parameters.

	Strong Segregation Limit (SSL)		
	$\delta = {}^{9}/_{14}\,, \nu = {}^{1}/_{7}$	$\delta = {}^{2}/_{3}\,, \nu = {}^{1}/_{6}$	Phenomenological approximation. $(d \sim N^{\frac{2}{3}})$
F_L	$\varphi\lambda N^{-\frac{9}{14}}\chi^{-\frac{1}{7}} / 2\alpha n\, Sin\,\theta$	$\varphi\lambda N^{-\frac{2}{3}}\chi^{-\frac{1}{6}} / 2\alpha n\, Sin\,\theta$	$\varphi\lambda N^{-\frac{2}{3}} / 2n\, Sin\,\theta$
F_a	$\varphi^2\lambda^2 N^{-\frac{9}{7}}\chi^{-\frac{2}{7}} / 4n^2\alpha^2\, Sin^2\,\theta$	$\varphi^2\lambda^2 N^{-\frac{4}{3}}\chi^{-\frac{1}{3}} / 4n^2\alpha^2\, Sin^2\,\theta$	$\varphi^2\lambda^2 N^{-\frac{4}{3}} / 4n^2\, Sin^2\,\theta$
F_{ac}	$\pi\varphi^2\lambda^2 N^{-\frac{9}{7}}\chi^{-\frac{2}{7}} / 16n^2\alpha^2\, Sin^2\,\theta$	$\pi\varphi^2\lambda^2 N^{-\frac{4}{3}}\chi^{-\frac{1}{3}} / 16n^2\alpha^2\, Sin^2\,\theta$	$\pi\varphi^2\lambda^2 N^{-\frac{4}{3}} / 16n^2\, Sin^2\,\theta$

Verification of the theoretically derived values for feature density will be done in chapter 4. In chapter 4, patterned line and square arrays of PS-b-P4VP block copolymers are converted to metallic and ceramic features that can then be easily analyzed with an AFM, and the metallic and ceramic features can be counted using the Image J analysis program to determine and compare experimental feature density values with theoretical feature density values.

3.3.5. Conclusion

In this chapter we have demonstrated that block copolymers can effectively serve as low-ablation threshold, dry, positive tone photoresists when combined with a laser interference ablation technique. We have proved this using a Nd:YAG nanosecond pulsed laser light source having a wavelength of 266nm and have been able to generate features having both primary and secondary ordering with periodicities replicating those of the block copolymer and the laser interference light pattern respectively. Topographical information of laser-patterned thin films was obtained using both AFM and SEM. To investigate the chemical state of laser-ablated thin films, a surface sensitive XPS experiment was also performed. Formulas were also proposed for the calculation of feature density on substrates *a priori* to fabrication. Finally, we showed that the theoretical density of features obtained from the combination of the two lithographic processes is much higher than is obtainable from the use of a laser interference technique with conventional photoresists.

CHAPTER 4

HIERARCHICAL METALLIC AND CERAMIC NANOARCHITECTURES

This chapter presents an application of laser interference ablation of PS-b-P4VP block copolymer to the generation of functional metallic and ceramic features on substrates including Si and SiO_2. Metal-loading of the laser patterned block copolymers is used to generate hierarchical arrays of metallic gold and platinum as well as ceramic Iron oxide and palladium oxide nanoarrays. The potential application of the hierarchical arrays in silicon, silicon oxide patterning as well as for the catalysed VLS growth of nanowires is discussed.

4.1 Hierarchical Metallic and Ceramic Nanoarchitectures from Laser Interference Ablation of Block copolymers

The optical [106-108], electrical [109], thermal [110-111], magnetic [112-113], and chemical [114-115] properties of nano-scaled metallic and ceramic materials differ remarkably from their bulk counterparts. Harnessing such properties for device-oriented fabrication has led to numerous researches into directed assembly of nano-materials on surfaces. The placement and ordering of nano-features and nano-architectures on surfaces has been achieved using several techniques including soft lithography [116], dip-pen nanolithography [89-90,117] laser interference lithography (LIL) [50,104,118-121] laser interference ablation (LIA) [37,122], block copolymer nanolithography [2,8,15,123-124], e-beam lithography [125-126] etc. Of all the above listed techniques for controlled placement of nano-features on surfaces, the two robust, inexpensive and high throughput

techniques inarguably are the LIA technique and block co-polymer phase separation (BCPS).

Features having a secondary ordering given by the periodicity of the laser interference pattern and a primary ordering given by the inter-domain spacing of the phase-separated block copolymers can be generated by combining the two techniques. Block co-polymers during the laser interference ablation process, as discussed in chapter 3, serve as a positive tone photoresist. By loading the block co-polymer with a metallic salt prior to or after the LIA, and selectively removing the polymer via an oxygen plasma reactive ion etching, it is possible to generate metallic or ceramic nano-domains on the substrate with a superposition of the periodicity of both the block co-polymer phase and the LIA technique.

This chapter provides results obtained through the fabrication of hierarchical metallic and ceramic nanostructures using a novel hybrid technique combining microscale periodic patterning using LIA, and nanoscale patterning using BCPS. The hierarchical structures have a primary ordering domain periodicity of about 30-100nm corresponding with the primary ordering present in the sacrificial PS-b-P4VP phase separating block copolymer, and a tunable secondary periodicity depending on the number of interfering laser beams, the angle between the beams, and the intensity of the laser beam. The secondary periodicity ranges from 250 nm to 2 μm. The robustness of this technique is demonstrated through the fabrication of patterned hierarchical arrays of Au, PtO_x, Fe_xO_y, and PdO_x hierarchical nano-domains. The technique can also be applied to generate several other types of metallic and ceramic features including Ni, Co etc. In comparison to other techniques discussed above for generating patterned nanoscale

features, the technique introduced in this chapter has reduced processing and fabrication time. Furthermore, other techniques work well for generating hierarchical nanofeatures for a specific material type, but the technique described here can be used to generate a broad range of hierarchical patterns with different metallic and ceramic materials. The as-generated metallic features have potential applications in areas such as electronics where they can be used as masks for the inexpensive fabrication of patterned arrays of free standing features on silicon and other semiconducting substrates. In addition, the as-generated gold features could potentially be used for the catalysis and growth of patterned arrays of silicon and germanium nanowires for solar applications and potential use as biosensors, photonics and optoelectronic applications.

4.1.1 Metal-loading of PS-b-P4VP Block copolymers

4.1.1.1. Gold Salt Solution

Anhydrous salt of gold, $HAuCl_4$, was purchased from Sigma Aldrich and used without further purification. Hydrochloric acid was made to 1M concentration and used to dissolve $HAuCl_4$ to 0.1 wt% concentration. 0.01M hydrochloric acid was mixed with 1wt% gold solution in a ratio (90:10) vol% to give the standardized solution that was used for loading metallic gold salt into the phase-separated PS-b-P4VP block copolymers.

4.1.1.2. Palladium Salt Solution

Anhydrous salt of palladium, Na_2PdCl_6, was purchased from Sigma Aldrich and used without further purification. Hydrochloric acid was made to 1M concentration and used to dissolve Na_2PdCl_6 to 0.1 wt% concentration. 0.01M hydrochloric acid was mixed with 1wt% concentrated palladium solution in a ratio (90:10) vol% to give the

standardized solution that was used for loading metallic salts into the phase-separated PS-b-P4VP block copolymers.

4.1.1.3 Iron Salt Solution

Anhydrous salt of iron, K_3FeCN_6, was purchased from Sigma Aldrich and used without further purification. Hydrochloric acid was made to 1M concentration and used to dissolve K_3FeCN_6 to 0.1 wt% concentration. 0.01M hydrochloric acid was mixed with 1wt% concentrated Iron solution in a ratio (90:10) vol% to give the standardized solution that was used for loading metallic salts into the phase-separated PS-b-P4VP block copolymers.

4.1.1.4 Platinum Salt Solution

Anhydrous salt of platinum, K_2PtCl_4, was purchased from Sigma Aldrich and used without further purification. Hydrochloric acid was made to 1M concentration and used to dissolve K_2PtCl_4 to 0.1 wt% concentration. 0.01M hydrochloric acid was mixed with 1wt% concentrated Platinum solution in a ratio (90:10) vol% to give the standardized solution that was used for loading metallic salts into the phase-separated PS-b-P4VP block copolymers.

4.1.2 Plasma reactive ion etching of patterned metal-loaded PS-b-P4VP Block

Etching of the patterned, metal-loaded PS-b-P4VP block copolymer thin films was done using a plasma thermal reactive ion etching (RIE) tool. The RIE tool operates with a radio frequency of 13.56 MHz supplied to the triodes. At that radio frequency, gases present in the chamber are dissociated and ionized forming reactive species. The reactive ion gases are accelerated to the substrate with a 100 kHz frequency applied to the cathode. The reactive gaseous species etch a substrate via chemical reactions as well as

ion assisted etching processes leading to the formation of gaseous products that are evacuated from the chamber.

Depending on the nature of the substrate to be etched, and the degree of anisotropy required during the etching process, different combination of gases can be optimized for use in the plasma etch chamber. Table 4.1.2.1 shows the different gases that can be used to etch silicon, silicon oxide and block copolymers. Also shown in the table are the materials susceptible to the etching gases as well as products and inhibitors that are formed during the plasma etch. Etching of the organic components was done under a pressure of 350 mTorr and a temperature of 27^{o}C. Oxygen flow into the RIE chamber was maintained at 50 cm^3min^{-1} and the power was 120W while the etch time was set for 60 minutes.

Table 4.1.2.1. Shows the various gas combinations, susceptible materials, inhibitors, and products from a plasma thermal reactive ion etch.

RIE Gas(es)	Susceptible Material	Inhibitor	Products
SF_6/O_2	Si	$Si_xO_yF_z$	SiF_4, SOF_4
CHF_3/O_2	SiO_2	$Si_xO_yF_z$	SiF_4
Cl_2	Si	Cl	$SiCl_4$
Br_2	Si	Br	$SiBr_4$
O_2	Polymers		CO_2, CO

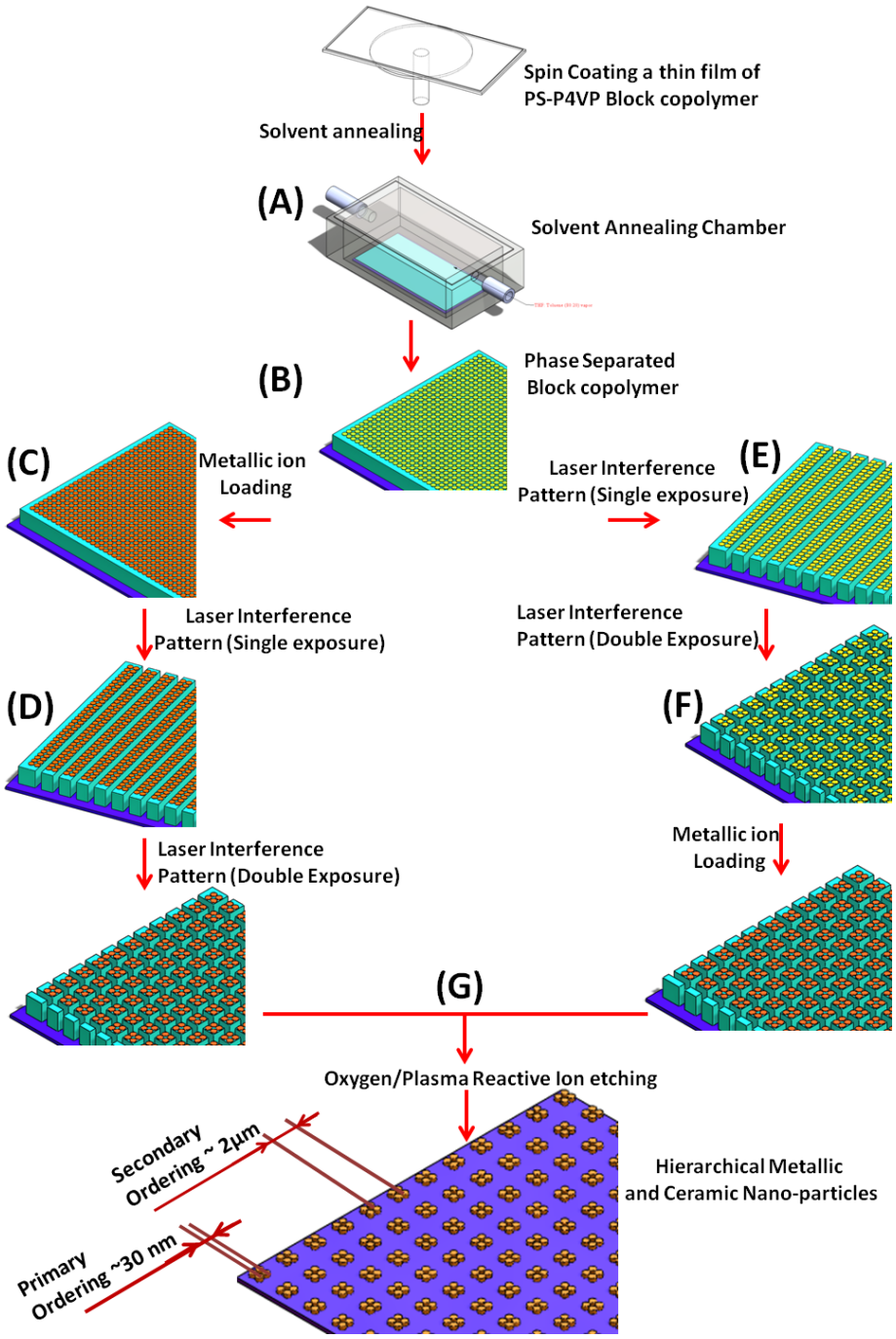

Scheme 4.1.2.1. Scheme showing the steps followed for the generation of hierarchical functional ceramic and metallic nanoparticles using block copolymer phase separation and laser interference ablation.

Scheme 4.1.2.1 shows the steps that were followed for loading phase-separated PS-b-P4VP block copolymers with metallic salt solutions. The substrate is first coated with a thin film of a PS-b-P4VP block copolymer. After solvent annealing thin films of the PS-b-P4VP block copolymer in a THF:Toluene (80:20) environment, two different approaches can be utilized for the metal-loading of the block copolymer.

In the first approach, scheme 4.1.2.1A-B-C-D, metal-loading of phase-separated PS-b-P4VP block copolymer is carried out by dipping the substrate with block copolymer in any of the metallic salt solutions discussed previously. After immersing the substrate in a metallic salt solution for 1-2 minutes, the substrate is vigorously rinsed in deionized water followed by laser interference ablation. As shown in the scheme 4.1.2.1D, a single exposure to 2-beam laser interference pattern results in linear arrays on the substrate. Subsequent exposure of the same substrate to another 2-beam laser interference pattern at 90º to the previous exposure results in periodic square arrays on the substrate. Hierarchical metallic and ceramic nanofeatures can be obtained as shown in scheme 4.1.2.1G after the RIE of the patterned substrates with oxygen gas. Another approach investigated, shown in scheme 4.1.2.1A-B-E-F, involves laser patterning of the phase-separated PS-b-P4VP block copolymer to generate line or square arrays followed by the metal-loading of the block copolymer.

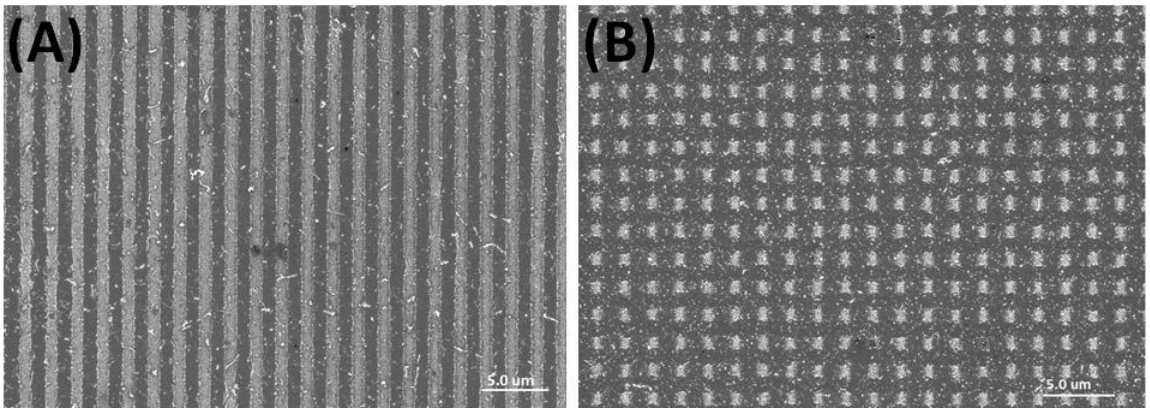

Figure 4.1.2.2. SEM images of (A) hierarchical periodic linear array of metallic and ceramic nanoparticles and (B) hierarchical periodic square array of metallic and ceramic nanoparticles obtained through Scheme 4.1.2.1A-B-C-D-G (First Approach).

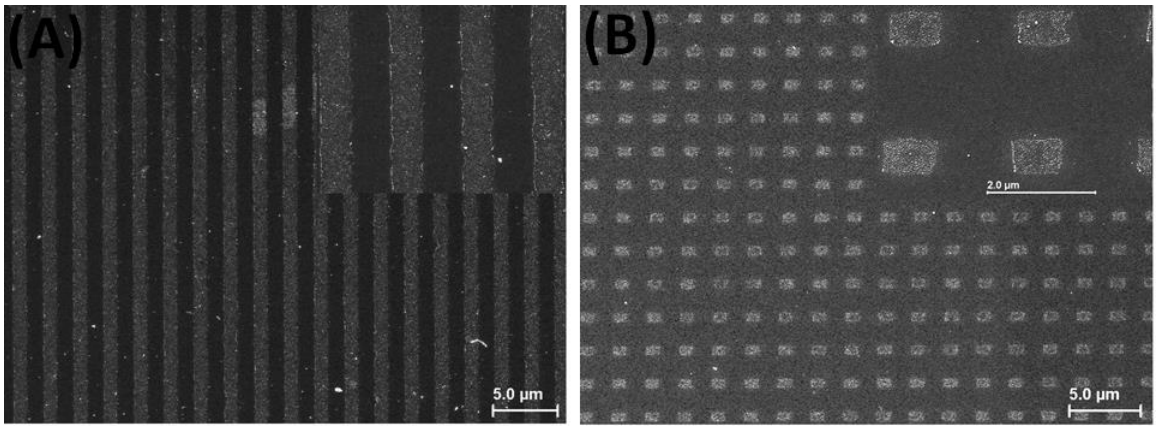

Figure 4.1.2.3. SEM images of (A) hierarchical periodic linear array of metallic and ceramic nanoparticles and (B) hierarchical periodic square array of metallic and ceramic nanoparticles obtained through Scheme 4.1.2.1A-B-E-F-G (Second Approach).

As shown in figures 4.1.2.2 and 4.1.2.3 above, laser interference ablation of metal-loaded PS-b-P4VP block copolymer results in the generation of hierarchical metallic and ceramic components on the silicon and silicon oxide substrates. A

disadvantage apparent from the SEM images in figures 4.1.2.2A and B, is that the first approach generates a lot of nanoparticle droplet at regions between periodic line and square arrays. The second approach gave better results with negligible nanoparticle contamination at the domains between the linear and square periodic arrays. All further experiments for generating hierarchical metallic and ceramic nanofeatures were conducted using the second approach.

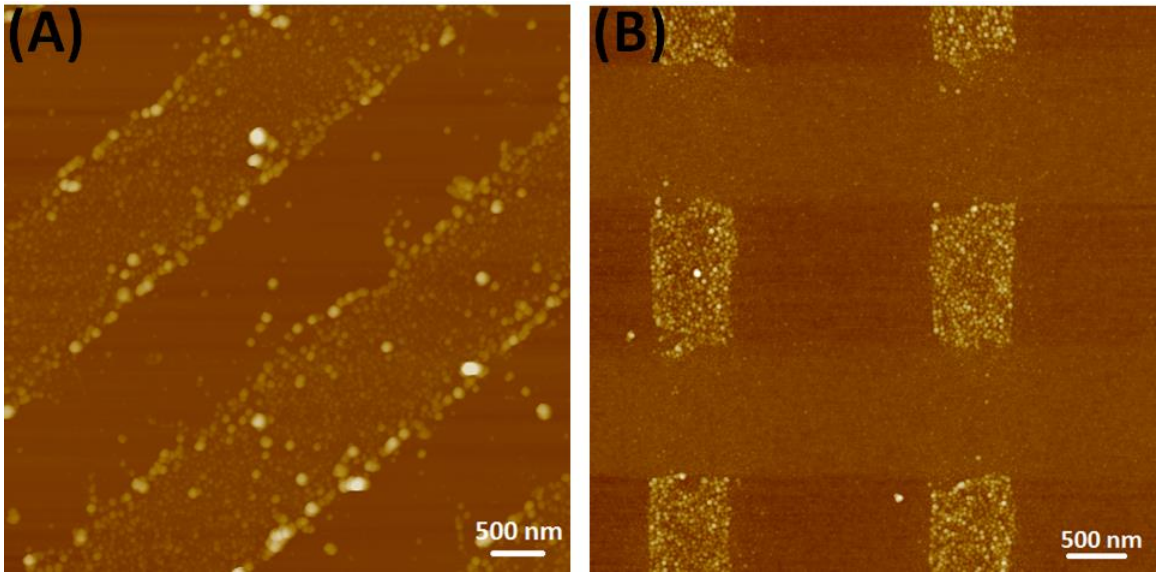

Figure 4.1.2.4. AFM topographical contrast image of (A) hierarchical line array of gold nanoparticles (B) hierarchical rectangular array of gold nanoparticles.

Figures 4.1.2.4A and B are AFM topographical images, of metal-loaded, and laser-patterned PS-b-P4VP block copolymers, taken after reactive ion etching. The secondary ordering of the metallic nanoparticles formed from the LIA is clearly visible. The periodicity of the line and square arrays is ~2μm. Also visible in the AFM topographical images is the apparent non-aggregation of the nanoparticles, forming the

primary ordering that replicate the phase separation pattern of the PS-b-P4VP block copolymer.

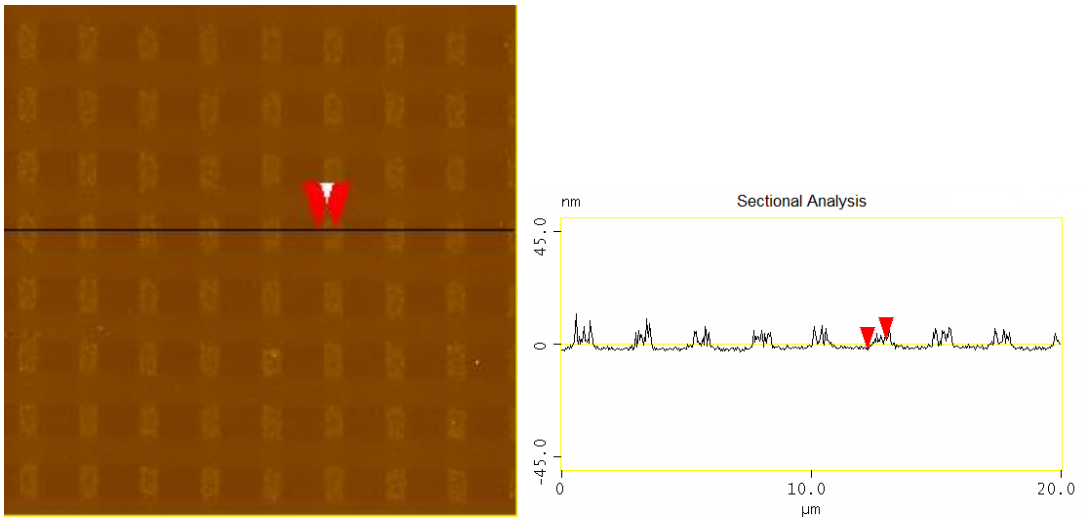

Figure 4.1.2.5. AFM cross sectional analysis of hierarchical rectangular array of gold nanoparticles.

Figure 4.1.2.5 shows the cross sectional analysis of hierarchical gold nanoparticles on a silicon oxide substrate. The sectional analysis of the patterned nanoparticles indicates single domain, free standing nanoparticles and little or no metallic nanoparticle contaminations at the ablated regions. The vertical height of the metallic nanoparticles is ~7-10nm.

4.1.3 Feature Density Prediction

Feature density, a term that characterizes the number of components including transistors, logic and memory devices, interconnects etc; that can be fabricated per unit area, has been used in several reports. Increasing the feature density of electronic components can be linked directly to the increased speed and efficiency of computers as well as continuous miniaturization of electronic devices. The feature density described

here is a value that has been normalized with respect to a unitary feature density value obtained from a lithography technique that incorporates chemically amplified photoresist for the fabrication of features.

There is an apparent coalescence of domains at the edges of the as-fabricated line and square arrays, because of the relatively harsh conditions of LIA. The transition region after LIA, is characterized by coalesced domains, and loss of ordering. The coalesced domains can grow to form large droplets with ~100nm diameter, and can cover a length space of ~400nm. The AFM phase contrast image in figure 4.1.3.1 shows transition regions highlighted with periodic white lines and 200nm width on either side of the periodic line arrays. The transition region increases in size with increasing laser power. Thus for square arrays, having twice the power dose than line arrays, the transition region is larger.

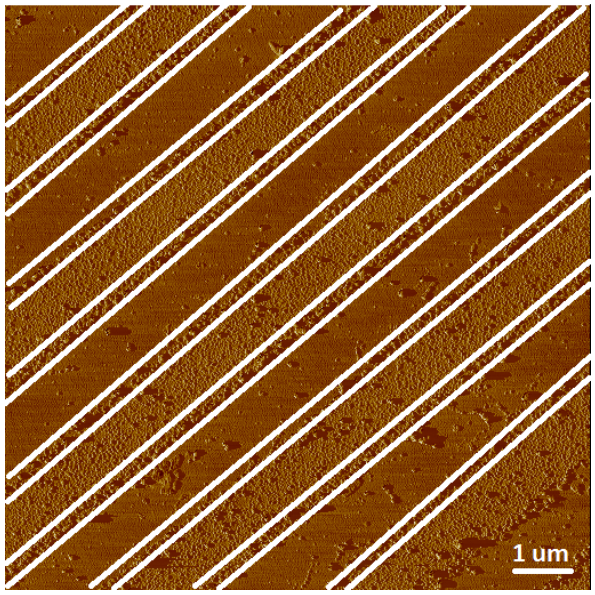

Figure 4.1.3.1. AFM phase contrast image of hierarchical linear array of gold nanoparticles

The coalescence of nanoparticles at the edges of periodic arrays is a major factor that results in loss of feature density, and a mismatch between theoretically estimated feature density and experimental values of feature density. In table 4.1.3.2, the experimental and theoretical values of the feature density are given using a Florry Huggins interaction parameter χ = 0.18 obtained from the literature. Other parameters like the degree of conversion N, the wavelength of the laser beam λ, the statistical segment length α, angle between interfering laser beams θ were either calculated or had been previously known. The value for φ (fractal dimension to switch from periodicity to actual line width) can be obtained from the graph of line width versus laser energy dose for PS-b-P4VP and PS-b-PEO shown in figure 3.3.3.3. From the experimental values obtained, there is a loss of approximately half of the theoretical normalized feature density. The reason can be attributed to agglomeration at the transition regions of the laser patterned films, and inter-domain coalescence. However, the feature density obtained using PS-b-P4VP block copolymer with a LIA technique is about an order to two orders of magnitude higher than through conventional chemically amplified photoresist patterning techniques.

4.1.3.2. Table with values provided for feature density per unit periodic line, per unit periodic square area, and per unit periodic circular, oval and hexagonal periodic segment for block copolymers under the strong segregation limit using different scaling parameters.

	Strong Segregation Limit (SSL)		
	λ = 266nm ; χ = 0.18 ; N = 33500 kDa ; α = 0.0432 nm ; θ = 3.296°		
	$\delta = {}^{9}/_{14}$; $\nu = {}^{1}/_{7}$	$\delta = {}^{2}/_{3}$; $\nu = {}^{1}/_{6}$	
	Theoretical Feature Density	Theoretical Feature Density	Experimental Feature Density
F_L	44	36	25
F_a	1936	1298	565
F_{ac}	1520	1020	415

4.1.3. XPS analysis of hierarchical metallic and ceramic nanofeatures.

To confirm metal-loading directly into the pyridine component of the diblock copolymer, XPS spectra of as-annealed and metal-loaded thin films were obtained. Figure 4.1.3.1 shows the XPS spectra for the nitrogen component in the heterocylcic aromatic vinylpyridine component of PS-P4VP block copolymer. From the XPS spectra, there is an upward shifted in the binding energy of nitrogen from 398.75 eV to 400 and 402.5 eV. The shift in the binding energy can directly be linked to the complexation of the vinyl pyridine component. Since nitrogen in pyridine has two free electrons that do not contribute to the aromatic ring structure, upon complexation the lone pair of electrons is donated to the metallic anion complex, thus increasing the valency of nitrogen from 0 to +1. This ultimately results in the shift to a higher binding energy as seen in the XPS spectra in figure 4.1.3.1.

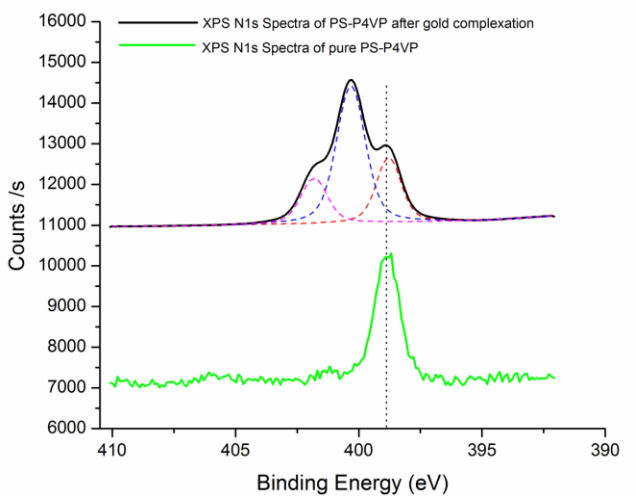

Figure 4.1.3.1. XPS N1s spectra of nitrogen in PS-b-P4VP and metal-loaded PS-b-P4VP diblock copolymer.

The XPS spectrum in figure 4.1.3.2A shows the binding energies for the Fe $2P_{3/2}$ and the Fe $2P_{1/2}$ for the complexed iron salt and the oxide of iron obtained after the reactive ion etching step. After reactive ion etching there is a shift to a higher binding energy for the doublet peak indicating the formation of a state of higher valency i.e the oxides in this case. Furthermore, the peak appears to broaden indicating that iron may exist in several valence states after etching. On the other hand, from the XPS spectra shown in figure 4.1.3.2B, gold has two doublets for the Au $4F_{7/2}$ and Au $4F_{5/2}$ indicating that gold may be present in two different oxidation states or chemical bonding states in the complexed metallic salt solution. Upon etching there is a shift in the binding energy of gold to a lower binding energy indicating that elemental gold is being deposited on the sample upon etching. The XPS spectra for palladium, in figure 4.1.3.2.C, indicate a single doublet for Pd $3d_{5/2}$ and Pd $3d_{3/2}$ before and after reactive ion etching of the complexed salt. After reactive ion etching there is a shift in the binding energy of palladium to higher binding energies indicating the potential formation of oxides of palladium. Platinum also

follows the same general trend, as shown in figure 4.1.3.2.D, like palladium, although the shift in the binding energy for platinum's Pt $4F_{7/2}$ and Pt $4F_{5/2}$ is ~ 5eV compared to the 1eV change in binding energy for palladium. Elemental palladium, iron and platinum hierarchical nanoparticles can be obtained from their oxides via argon reactive ion etching for a period of about 30 mins but the elemental features are themselves unstable in air and rapidly oxidize back to the oxide state upon exposure to ambient environments.

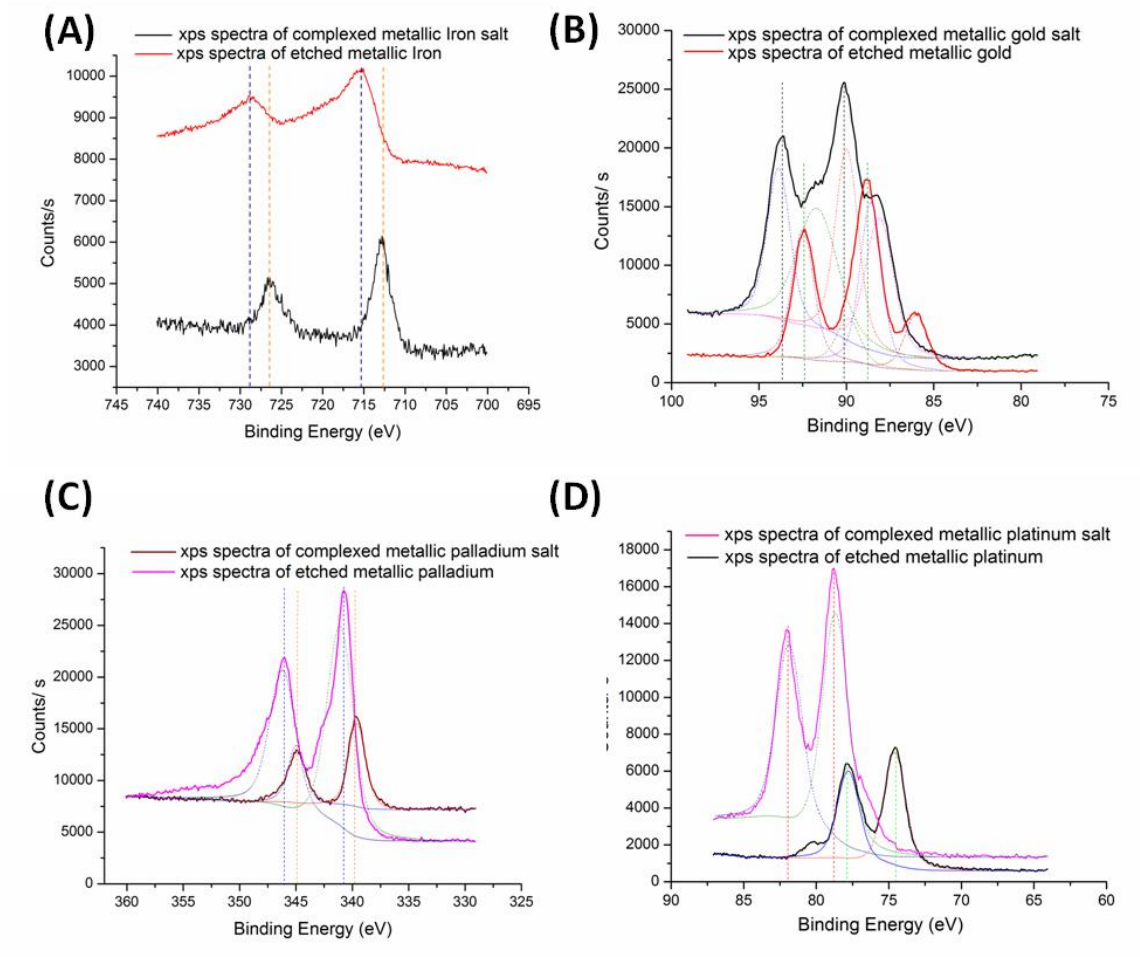

Figure 4.1.3.2. . XPS spectra of (A) metallic Iron salt complexed with P4VP before and after reactive ion etching (B) metallic Gold salt complexed with P4VP before and after reactive ion etching (C) metallic Palladium salt complexed with P4VP before and after reactive ion etching (D) metallic Platinum salt complexed with P4VP before and after reactive ion etching.

4.1.4. Conclusion

In this chapter we have demonstrated the ability to fabricate hierarchical arrays of gold, platinum, palladium and iron nanofeatures on silicon and silicon oxide substrates using a novel approach that combines the primary ordering inherent in phase separating block copolymers and the secondary ordering obtainable from a laser interference ablation technique. We have further demonstrated the ability of the as-generated hierarchical features to function as catalysts through XPS elemental analysis showing the conversion of the metallic salt solutions during RIE into nobel metals and metallic oxides. The potential use of such hierarchical metallic and ceramic features are numerous and include: potential use for growth of patterned carbon nanotubes, germanium and silicon nanowires as well as zinc oxide nanowires, they can also find use as metallic masks for the generation of sub 40nm features on various semiconducting substrates for use in next generation inexpensive microchip fabrication as well as the fabrication of optoelectronic gadgets.

CHAPTER 5

SILICON AND SILICON OXIDE HIERARCHICAL NANOARCHITECTURES

This chapter demonstrates applications of hierarchical nanometallic and ceramic features as nanomasks and nanocatalysts for pattern transfer to silicon and silicon oxide substrates. The fabrication of blue light emitting silicon oxide nanowires is demonstrated. The apparent ferromagnetic effect of iron-capped silicon oxide nanowires is discussed and the electromechanical behavior of the iron-capped silicon oxide nanowires is demonstrated. The transfer of features to silicon is also demonstrated using hierarchical gold metal as nanocatalysts.

5.1 Introduction to Fabrication of Silicon Oxide Nanowires

The unique physical properties of one dimensional nanomaterials has continued to generate interest amongst scientific researchers for years. 1D nanomaterials are features having at least one dimension in the 1-100nm length scale, and they include nanowires, nanorods, nanobelts and nanotubes. The properties of 1D nanomaterials as a result of quantum confinement can generate size dependent excitation from specific wavelengths as well as emission of specific wavelengths of light [127], they can also result in increased or ballistic transport in the 1D nanomaterials [128]. Other properties affected by reduced dimensions of 1D nanomaterials include changes in the band gap that can lead to insulator-metal transitions and vice versa [129]. These unique properties have been utilized in optoelectronic [130], electromechanical, optical [131] , photovoltaic [132-133] and sensor type [134] nanodevice fabrication.

There have been numerous reports on the fabrication of 1D nanofeatures from ZnO [135] , TiO_2 [136-138], Pd [139], Si [140-142] , Ge [143-145], SiO_2 [69,146-147], carbon [128,148], indium phosphide [149-150]etc. Of all the nanofeatures, nanofeatures made from silicon and silicon oxide, by virtue of their abundance, should primarily be the most accessible, integrable and easy-to-fabricate into nanowires.

Silicon oxide nanowires have been gaining continued interest in the literature due to some unique band gap properties that lead to blue light photoluminescence [76], localization of light, near-field optical effects as well as low-dimensional waveguide. One of the problems plaguing the direct application of 1D nanofeatures including silicon oxide nanowires for device fabrication is the harsh processing conditions used for the fabrication of the nanowires [70,80,146,151]. The VLS fabrication technique for silicon oxide nanowire fabrication uses temperatures greater than 800ºC which makes the process not only expensive, but also limits the type of supporting substrates that can be used to fabricate such features. Moreover, other low temperature fabrication techniques [75,152-153] have not been successful in fabricating high aspect ratio, aligned silicon oxide nanowires. The high temperature processing conditions thus limit the integration of silicon oxide nanowires into industrial fabrication processes in the electronic industry.

The ideal fabrication technique for silicon oxide nanowires should be easily integrable into current fabrication technologies used in the semiconducting and electronic industry, and should also be robust enough to accommodate specifications for various pattern and aspect ratios of nanowires for different applications.

We report here a top-down fabrication technique that enables control over the type of secondary scale pattern as well as the aspect ratio of the silicon oxide nanowires.

The fabrication of amorphous silicon oxide nanowires using a reactive ion plasma chamber under room temperature can be easily integrated into the manufacturing process in the semi-conductor and electronics industry. A potential optoelectronic property of the nanowire was also investigated and the blue light photoluminescence of the as–fabricated nanowires was established. The as-fabricated nanowires were investigated using TEM, XPS, SEM and AFM characterization techniques.

5.1.1. Fabrication of Silicon Oxide Nanoforest

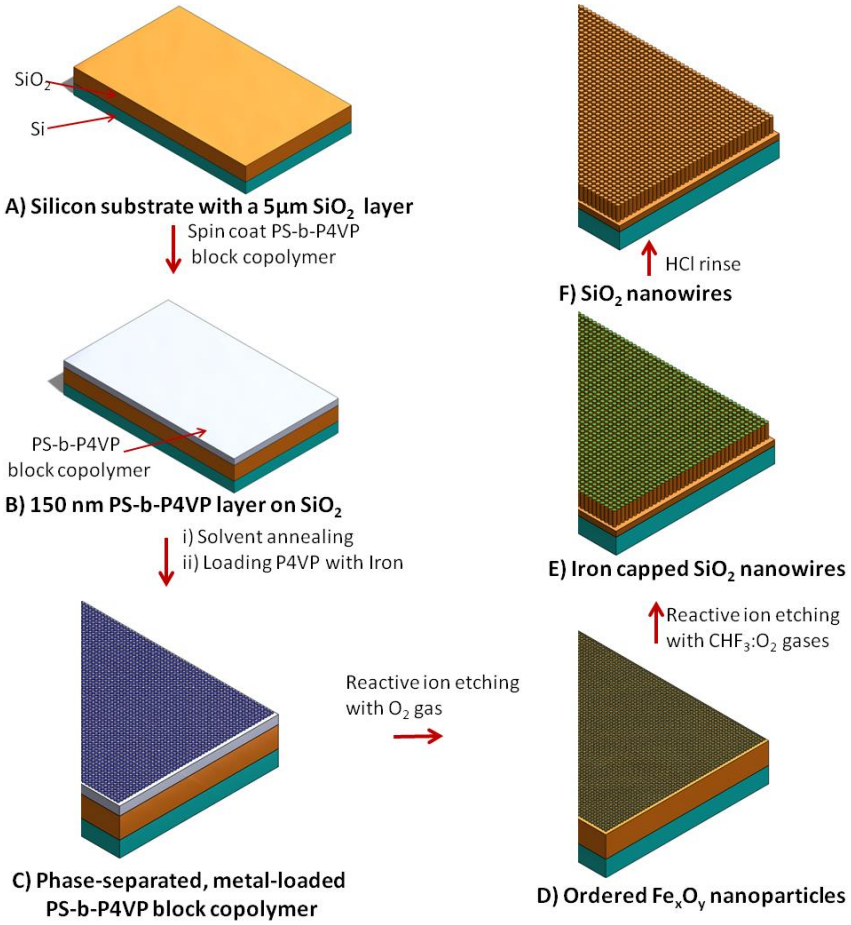

Scheme 5.1.1.1. Scheme showing the steps followed for the generation of silicon oxide nanowire arrays on a silicon substrate.

Scheme 5.1.1.1 shows the steps for obtaining Silicon oxide nanowire arrays. A silicon substrate with a 5 µm thermal oxide layer is coated with a 150nm thin film of PS-b-P4VP block copolymer as shown in scheme 5.1.1.1B. Silicon oxide substrate with the block copolymer thin film is solvent annealed in an enclosed chamber to produce phase-separated domains having P4VP vertical cylinders in a PS matrix. The width of the P4VP domain is ~30nm, and the inter-domain spacing is ~40nm measured from AFM anlaysis of the phase-separated PS-b-P4VP block copolymer shown in figures 5.1.1.1A and B.

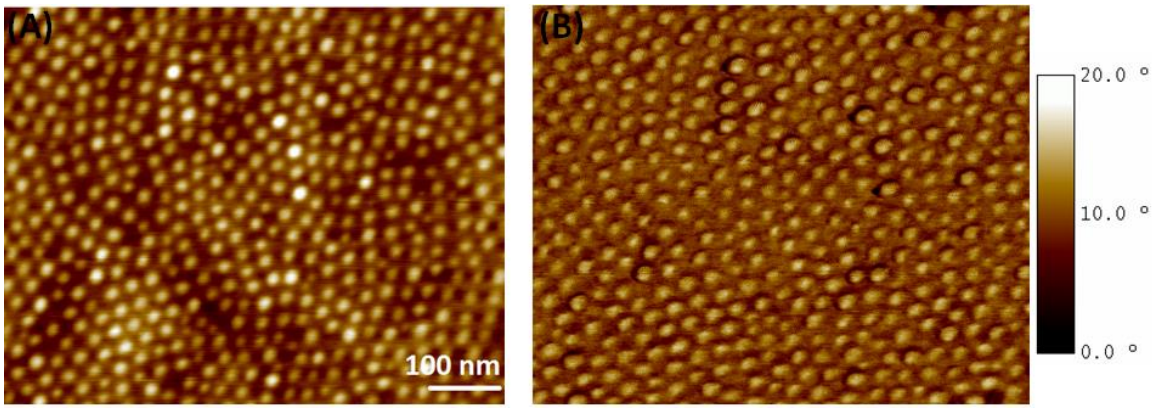

Figure 5.1.1.1.AFM (A) topographical and (B) phase contrast images of phase-separated PS-b-P4VP block copolymer.

Solvent annealing was done in a Toluene:THF (20:80) environment to induce the formation of vertically oriented cylinders as discussed in chapter 3. The block copolymer is loaded with metallic iron via immersion in an iron salt solution for 2 mins leading to the complexation of iron to the P4VP domain as shown in scheme 5.1.1.1C. This is followed by an RIE in an O_2 gas environment to remove all the organic compounds i.e styrene and vinylpyridine, from the substrate. This resulted in the formation of iron-oxide ceramic hierarchical nano-particles on the silicon oxide substrate as shown in scheme 5.1.1.1D. Without removing the substrate from the chamber, pattern transfer to

underlying silicon oxide substrate via RIE in a CHF_3:O_2 gas mixture is performed resulting in the generation of iron-capped, silicon oxide nanowire arrays as shown in scheme 5.1.1.1E.

Various chemical reactions take place in the plasma chamber during the reactive ion etch.

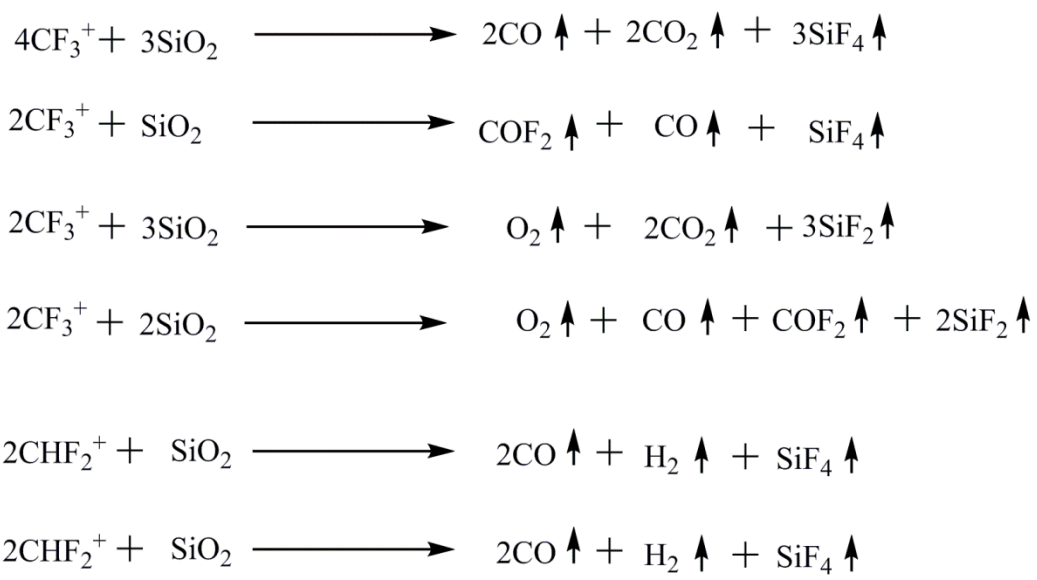

Figure 5.1.1.2. Figure showing potential chemical reactions that take place during the etching of SiO_2 in a plasma chamber containing CHF_3:O_2 gases.

The first reaction that takes place in a plasma chamber is usually the ionization and dissociation of the gases within the chamber. CHF_3 and O_2 gases are broken down to CF_3^+, CHF_2^+ and O^+. The gases are then accelerated towards the substrate and react with the substrate to form various gaseous products. The gaseous products formed include SiF_4, CO_2, COF_2, H_2, O_2, CO and SiF_2. These gaseous products are evacuated from the reaction chamber as they are formed thus exposing a new layer of the substrate for further etching. To create an anisotropic etch profile, the main gas that generates the radicals that

etch silicon oxide- CHF_3 and CF_4- has to be diluted with O_2 gas. The O_2 gas thus serves to improve the degree of anisotropy of the SiO_2 etch in the plasma chamber. RIE of silicon oxide was done using flow rates of $5cm^3min^{-1}$ and $45cm^3min^{-1}$ for O_2 and CHF_3 respectively. The power in the plasma chamber was set to 200W and pressure was 40mTorr. Free standing silicon oxide nanowires can be obtained from the iron oxide-capped silicon oxide nanowires by immersion of the resultant features in a hydrochloric acid solution as shown in scheme 5.1.1.1F.

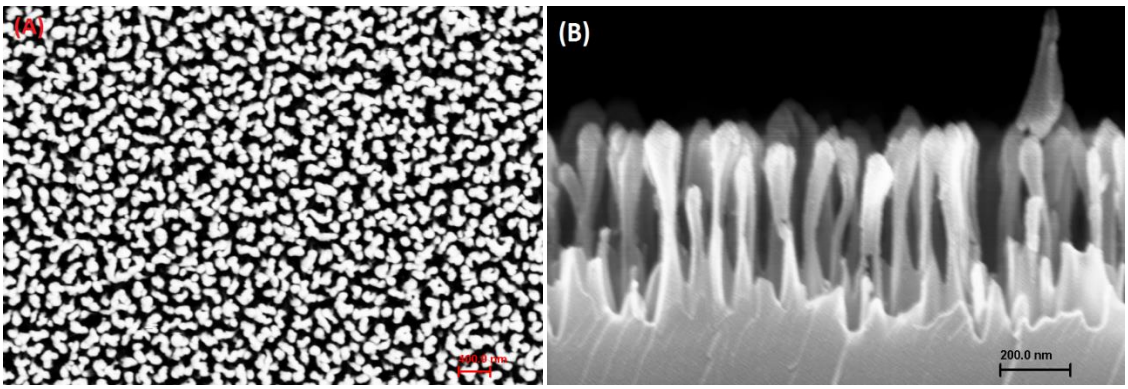

Figure 5.1.1.3. (A) Planar view and (B) sectional view of silicon oxide nanowires.

Figure 5.1.1.3A shows the top down view of the silicon-oxide dense nanoforest arrays. The mean diameter of the silicon oxide nanoforest arrays is about the same as the domain size of the block copolymers ~30-40nm. The sectional view of the nanowire arrays is shown in figure 5.1.1.3B. From figure B, the vertical orientation of the nanowires is clearly visible. Furthermore, it is possible to calculate the aspect of the nanowires.

As discussed earlier, the robustness of this technique is that by simply changing the duration of etch, using CHF_3:O_2 reactive plasma chemistry, the aspect ratio and

height of the nanowires can be varied. Figure 5.1.1.4 is a graph showing the variation in height of the silicon oxide nanowires with the duration of etch in a plasma RIE chamber.

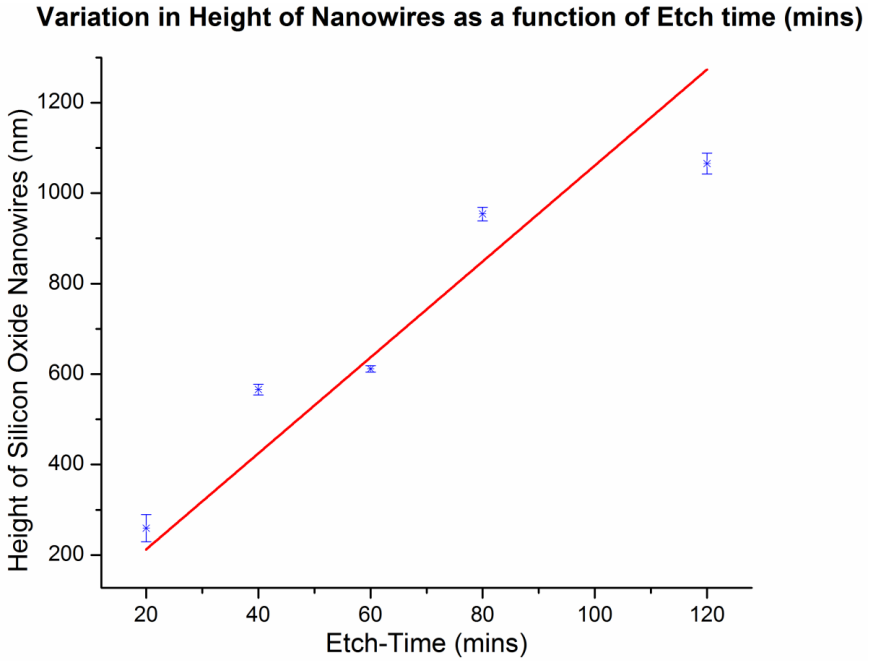

Figure 5.1.1.4. Graph showing a plot of height of silicon oxide nanowires (nm) versus etch-time (mins).

The graph shows a linear relationship between the height of the silicon oxide nanowires and the duration of etch. The aspect ratio of the as-fabricated silicon nanowire arrays can vary from 1:16 to about 1:20 and beyond. With increasing etch time however, the nanowires taper along their length as shown in the SEM cross-sectional images in figures 5.1.1.5A, B, C and D.

Figure 5.1.1.5A shows the cross-sectional image of silicon nanowires obtained after 20mins etch in an RIE chamber. From the SEM image, the nanowires appear to be vertically oriented and tapered at the tip end. The average diameter of the nanowires was

found to be 65nm while the height of the nanowires was 280nm. This is an isotropic etch regime for the silicon oxide nanowires, and the aspect ratio of the nanowires is ~1:4.

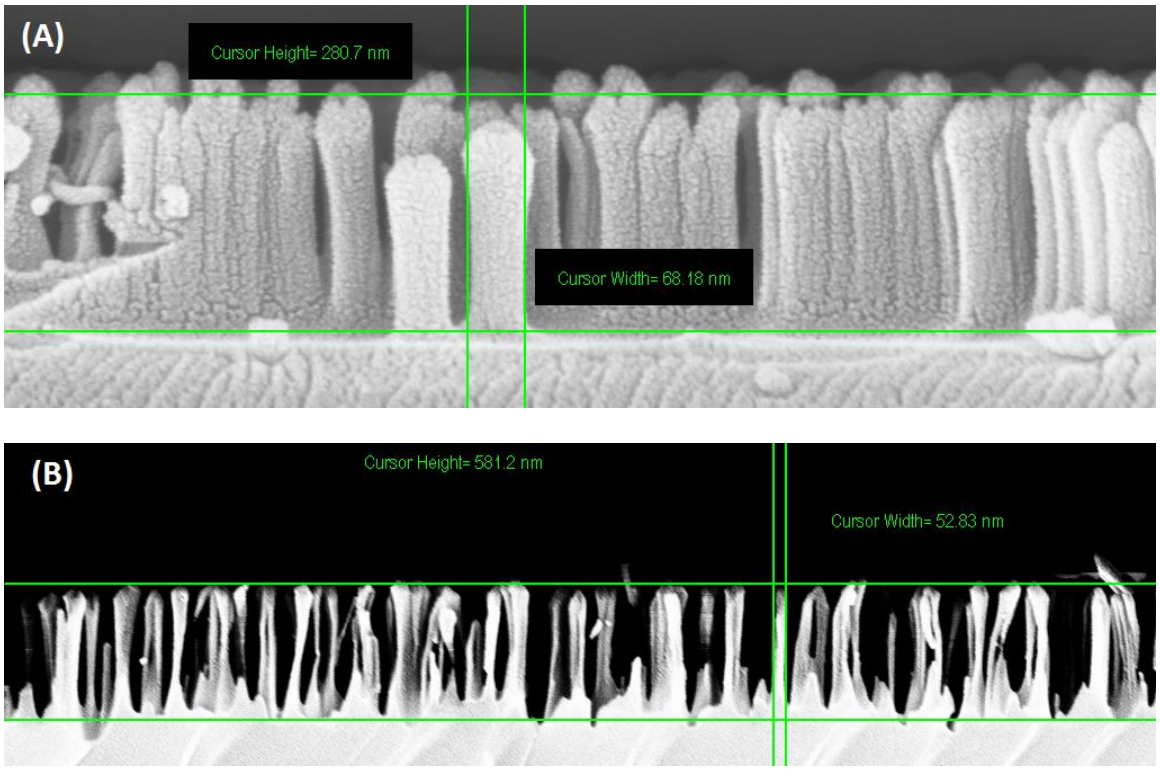

Figure 5.1.1.5. Cross sectional SEM images of silicon oxide nanowire obtained after etching in CHF_3:O_2 gas mixture for (A) 20 mins (B) 40 mins.

Figure 5.1.1.5B shows the cross-sectional image of silicon nanowires obtained after 40mins etch in an RIE chamber. From the SEM image, the nanowires appear to be vertically oriented and tapered at both the tip end and along the sides. The average diameter of the nanowires was found to be 52 nm while the height of the nanowires was 580 nm. At this regime, we are already deviating from the anisotropic region and moving towards the isotropic region. The aspect ratio of the nanowires after 40mins of etch is ~1:10.

Figure 5.1.1.6C shows the cross-sectional image of silicon nanowires obtained after 60mins etch in an RIE chamber. From the SEM image, the nanowires appear to be vertically oriented and even more tapered at both the tip end and along the sides. The average diameter of the nanowires was found to be 51 nm while the height of the nanowires was found to be 600 nm. At this regime, we are already deviating from the anisotropic region and moving towards the isotropic region. The aspect ratio of the nanowires after 60mins of etch is ~1:12.

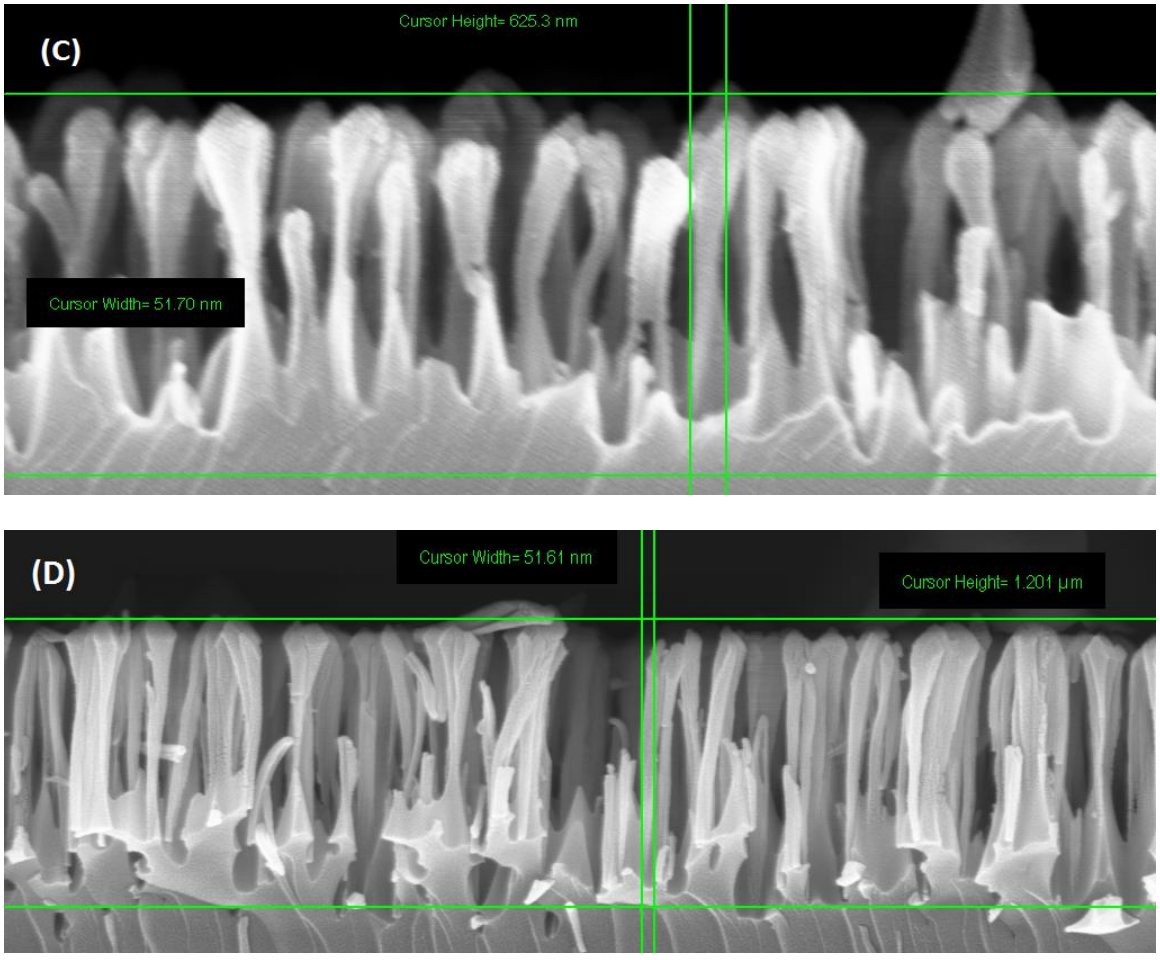

Figure 5.1.16. Cross sectional SEM images of silicon oxide nanowire obtained after etching in CHF_3:O_2 gas mixture for (A) 60 mins (B) 120 mins.

Figure 5.1.1.6D shows the cross-sectional image of silicon oxide nanowires obtained after 120 mins etch in an RIE chamber. From the SEM image, the nanowires are still vertically oriented, but they are also more tapered along the sides and tip. Some nanowires also appear to be broken. The average diameter of the nanowires was found to be 50 nm while the height of the nanowires was found to be ~1.2 μm. The aspect ratio of the silicon oxide nanowires is ~1:20.

High resolution transmission electron microscope (TEM) images of iron-capped silicon oxide nanowire arrays were obtained using a JEOL 100CX TEM operating at an accelerating voltage of 100kV. Sample preparation for TEM involved dicing of wafers containing silicon oxide nanowires, followed by sonication of the wafers in isopropyl alcohol to disperse the nanowires. The TEM image was taken of silicon oxide nanowires that have been etched for a period of 120 mins.

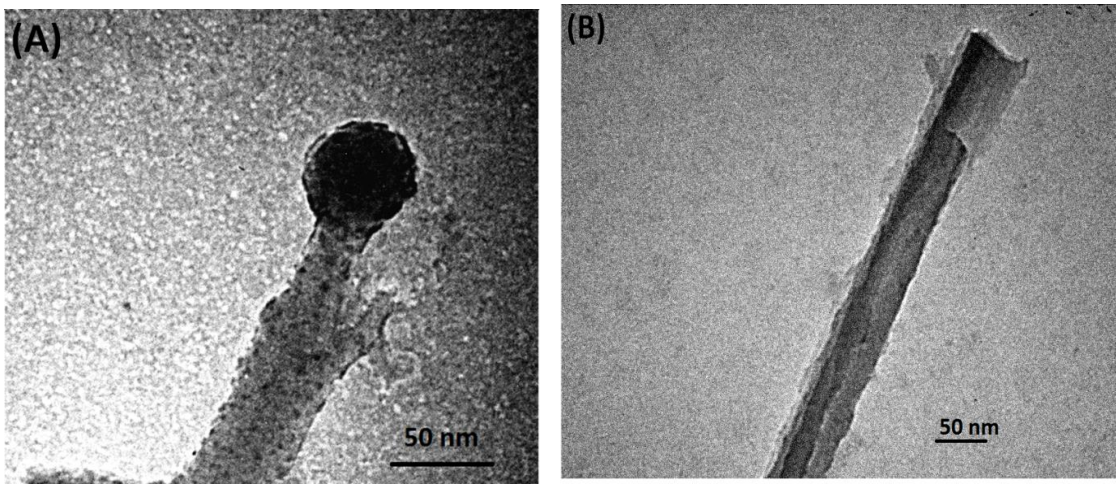

Figure 5.1.1.7 High resolution TEM image of a silicon oxide nanowire showing the (A) iron-capped end of the wire and (B) bare silicon oxide nanowire.

From the TEM image, the iron-capped section of the nanowire is clearly seen as the dark spot on the nanowire. The silicon oxide nanowires are amorphous. The iron tipped section of the nanowire has a diameter of ~50 nm while the nanowire has varying diameter along its length.

5.1.2. Chemical composition analysis of silicon oxide nanowires.

The chemical composition of the nanowires was determined from XPS analysis. From the XPS survey spectra, the nanowires are composed of silicon, oxygen, iron and doped with fluorine. Figure 5.1.2.A shows the XPS spectrum of Si 2P. The binding energy for silicon is upward shifted compared to the binding energy of silicon oxide. The reason for this behavior may be because fluorine is replacing some of the oxygen present in SiO_2. Figure 5.1.2.B shows the XPS spectrum of a doublet Fe $2P_{3/2}$ and Fe $2P_{1/2}$. The presence of iron oxide is confirmed by the binding energies at 715eV and 740eV for Fe $2P_{3/2}$ and Fe $2P_{1/2}$ respectively. Figure 5.1.2.C shows the XPS spectrum of F 1s. The presence of fluorine is confirmed by the binding energy of 688eV for the compound form of fluorine. Figure 5.1.2.D shows the XPS spectrum of O 1s. The presence of oxygen is confirmed by the binging energy of oxygen at 535 eV. The atomic composition of oxygen and fluorine from the XPS survey spectra analysis are 29% and 31% respectively, indicating that the silicon oxide has been doped with fluorine atoms. The atomic composition of silicon was found to be 17%.

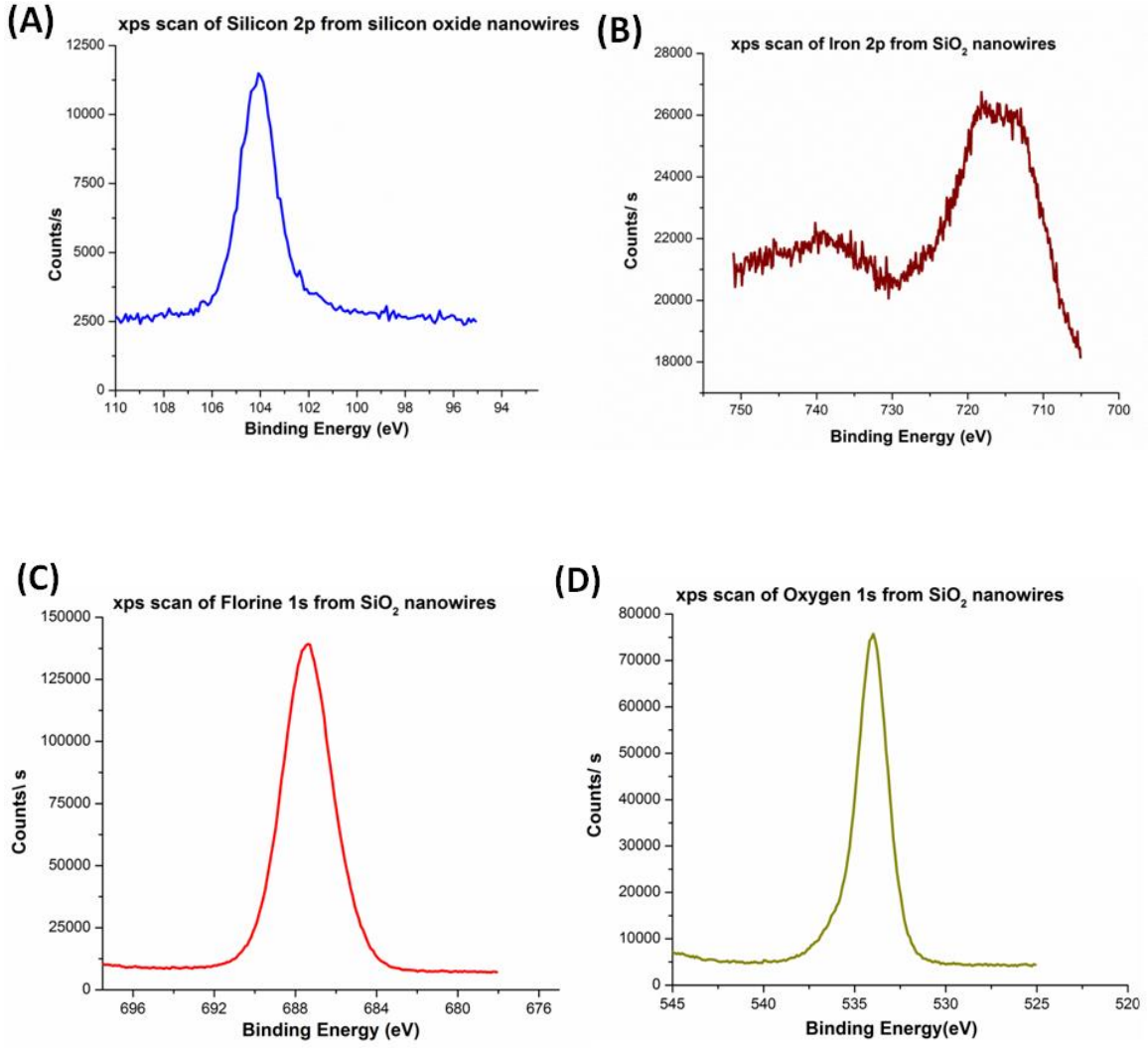

Figure 5.1.2. XPS spectra of (A) silicon in silicon oxide nanowires. (B) iron on silicon oxide nanowires. (C) fluorine in silicon oxide nanowires. (D) oxygen in silicon oxide nanowires.

Based on the atomic composition from XPS analysis, silicon oxide nanowires fabricated using RIE probably have an external layer with a SiO_xF_y chemical composition and an internal layer composed of SiO_2. The chemical composition of the external layer can be of the form $Si(OF)_x$.

5.1.3. Fabrication of Patterned Arrays of Silicon Oxide Nanowires

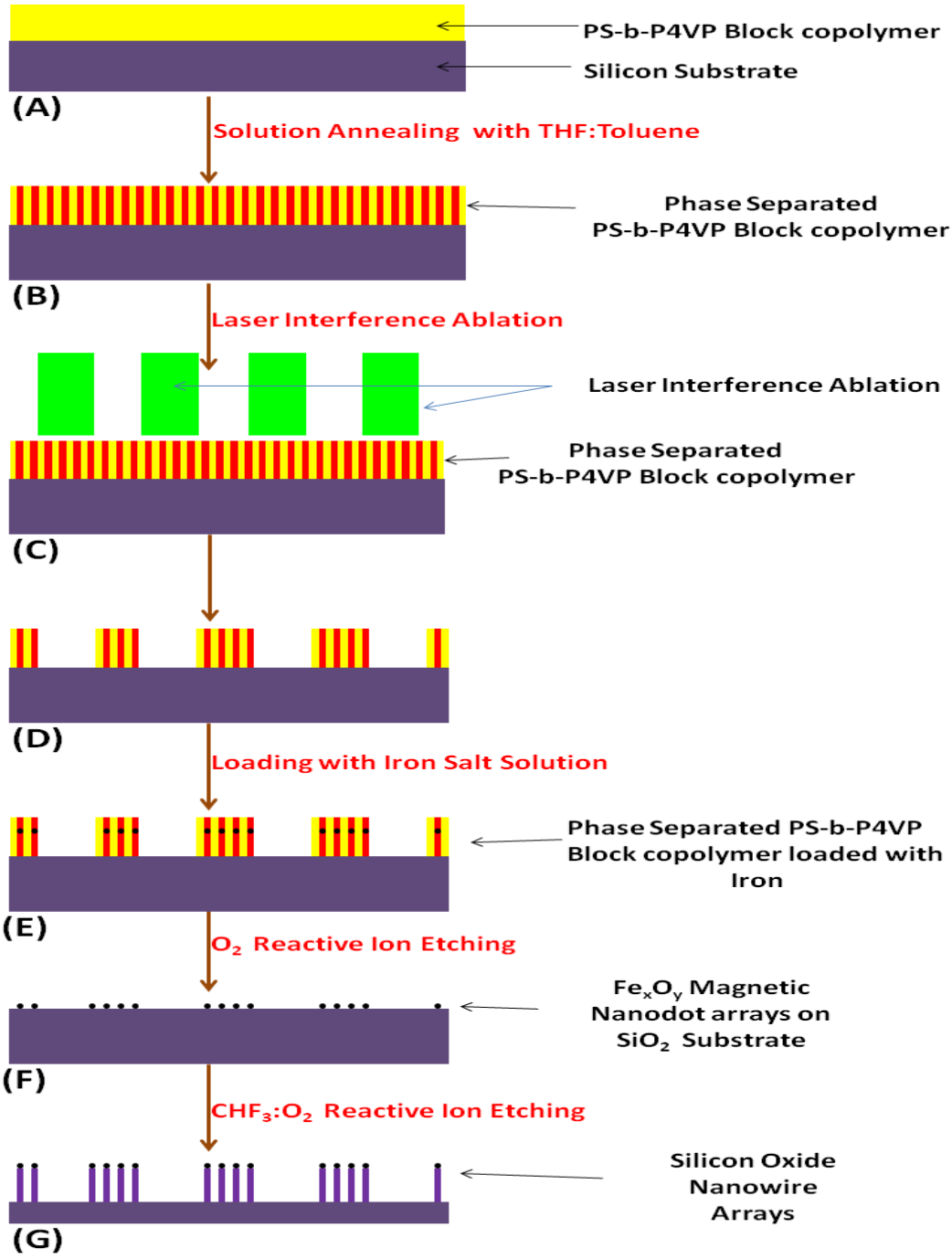

Scheme 5.1.3.1 Scheme showing steps followed for the generation of patterned array of silicon oxide nanowires.

Scheme 5.1.3.1 shows the steps that were followed for the fabrication of line and square patterns of iron-capped, silicon oxide nanowires. The steps look fairly similar to those used for the fabrication of silicon oxide nanowires. A silicon substrate with a 5 μm thermal oxide layer is coated with 150 nm thin film of PS-b-P4VP block copolymer. Silicon oxide substrate with the block copolymer thin film is solvent annealed in an enclosed chamber to produce phase-separated domains having P4VP vertical cylinders in a PS matrix, shown in scheme 5.1.3.1B. The laser interference ablation step in scheme 5.1.3.1C, allows for the generation of hierarchical arrays of block copolymers with both primary and secondary ordering corresponding to the inter-domain spacing of the phase-separated block copolymer, and the periodicity of the interfering light beams respectively. The block copolymer is loaded with metallic iron via immersion in an iron salt solution for 2 mins leading to the complexation of iron to the P4VP domain as shown in scheme 5.1.3.1D. RIE in an O_2 gas environment is used to remove all the organic compounds- styrene and vinylpyridine- from the substrate. This resulted in the formation of patterned iron-oxide nanoarrays on the silicon oxide substrate as shown in scheme 5.1.3.1F. Without removing the substrate from the chamber, pattern transfer to underlying silicon oxide substrate via RIE in a CHF_3:O_2 gas mixture is performed resulting in the generation of patterned, iron-capped, silicon oxide nanowire arrays as shown in scheme 5.1.3.1G.

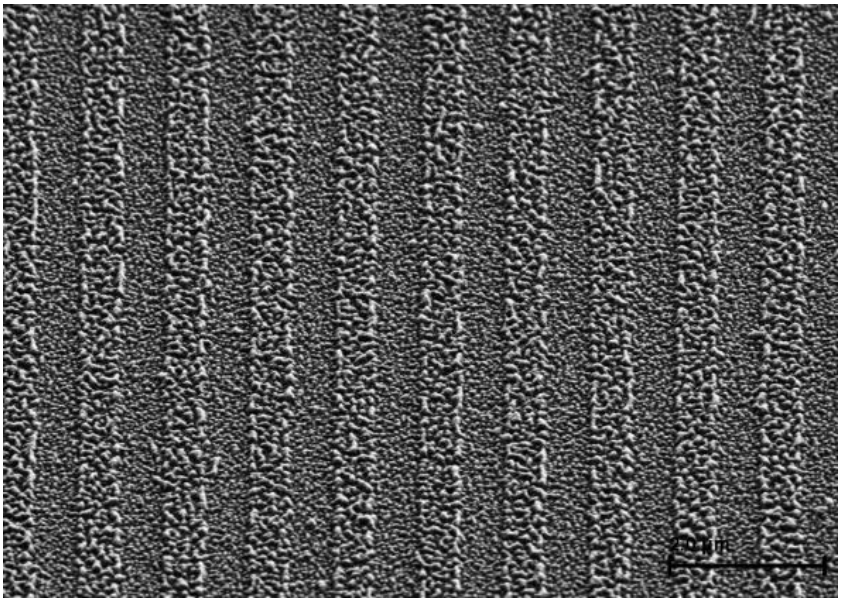

Figure 5.1.3.1. SEM image of hierarchical line arrays of silicon oxide nanowires.

Figure 5.1.3.1 shows an SEM image of hierarchical line arrays of silicon oxide nanowires. The ordering of the line arrays is ~1μm, while the primary ordering of the silicon oxide nanowires was difficult to ascertain from the SEM image.

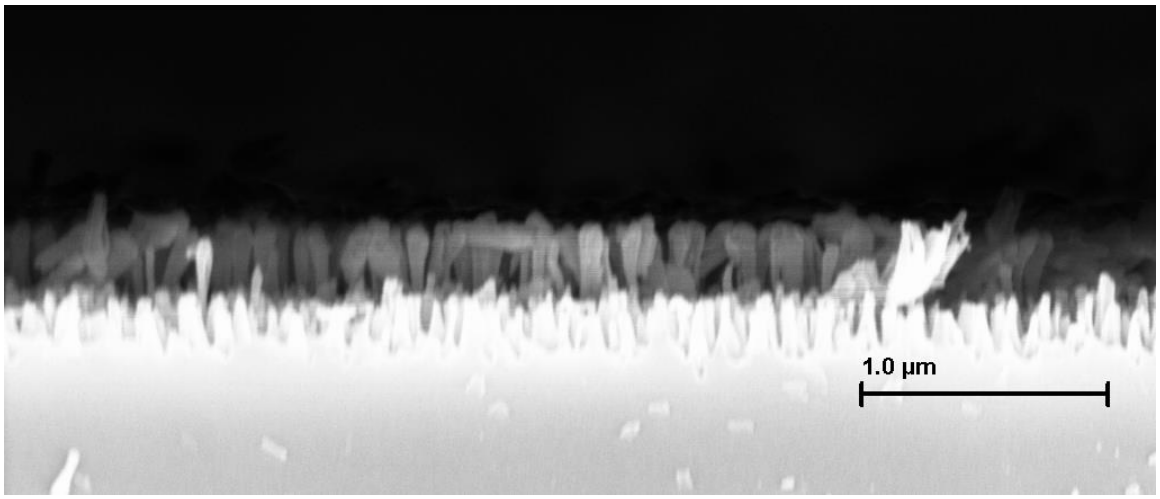

Figure 5.1.3.2. SEM cross sectional image of hierarchical line arrays of silicon oxide nanowires.

Figure 5.1.3.2 shows a sectional SEM image of hierarchical line arrays of silicon oxide nanowires. The sample was diced through the inter-domain of the primary periodicity. The hierarchical ordering of the silicon oxide nanowires is clearly evident through this section. Shorter nanowires, of ~100nm height, appear between domains, while taller nanowires having ~600nm height, occur at regions that have not been exposed to the laser beam.

5.1.4. Potential application of silicon oxide nanowires

5.1.4.1. Blue light emitting silicon oxide lasers.

The photoluminescence property of silicon oxide nanowires can be utilized for making blue light lasers as shown in figure 5.1.4.1.1. Photoluminescence from silicon nanomaterials comes from the S band in silicon. The decay time of the S band photoluminescence, at room temperature, is several microseconds.

The silicon oxide nanowires are excited with a wavelength of 350 nm, and this result in the emission of a wavelength of 450 nm. The blue light emission from silicon oxide nanofeatures can be utilized for the fabrication of solid state lasers

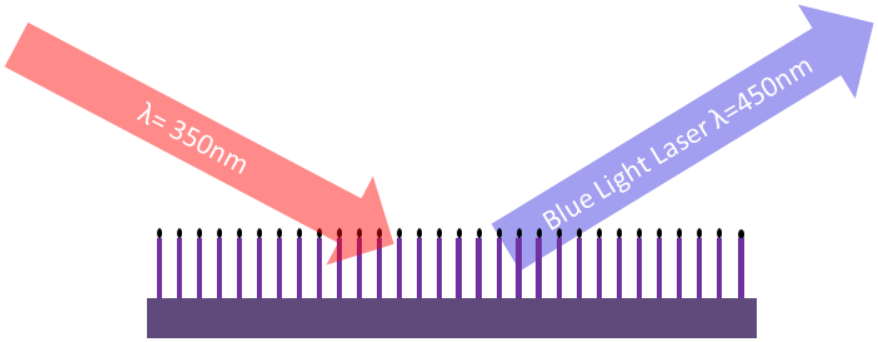

Figure 5.1.4.1.1. The blue light, photoluminescence property of silicon oxide nanowire is demonstrated using an excitation wavelength of 350nm.

The intensity of the blue light photoluminescence from the as-fabricated silicon oxide nanowires was measured using a Shimadzu fluorescent spectrometer having a Xenon lamp excitation light source. 350nm was chosen as the excitation wavelength, while the emission spectrum of the silicon oxide nanowires shows peaks from 420-480nm. This emission correlates to the blue wavelength region of the electromagnetic spectrum. Figure 5.1.4.1.2 below shows the photoluminescence spectra of silicon oxide nanowires.

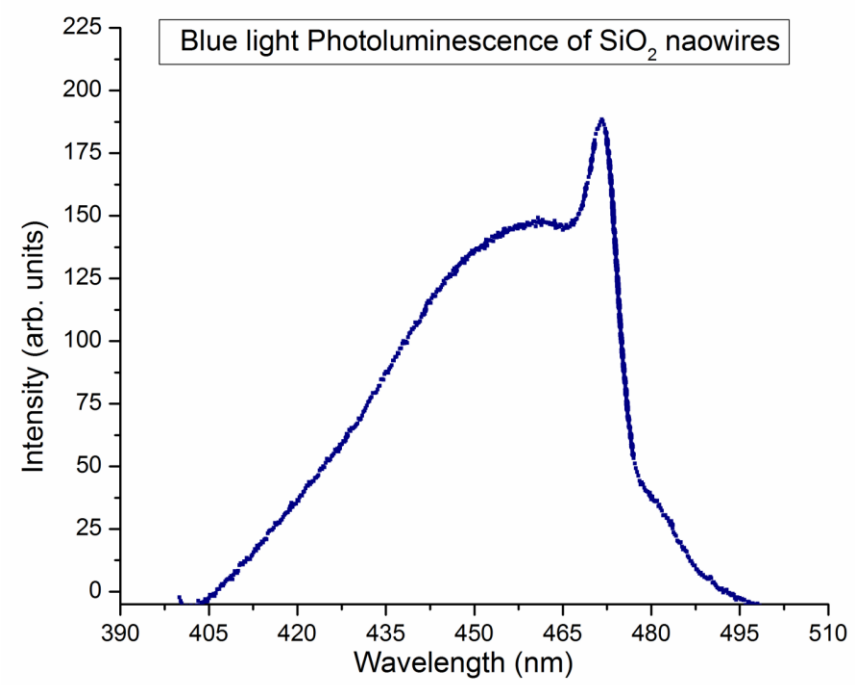

Figure 5.1.4.1.2. Photoluminescence spectra of SiO_2 nanowires.

5.1.4.2. Electromechanical sensors based on SiO_2 nanowires.

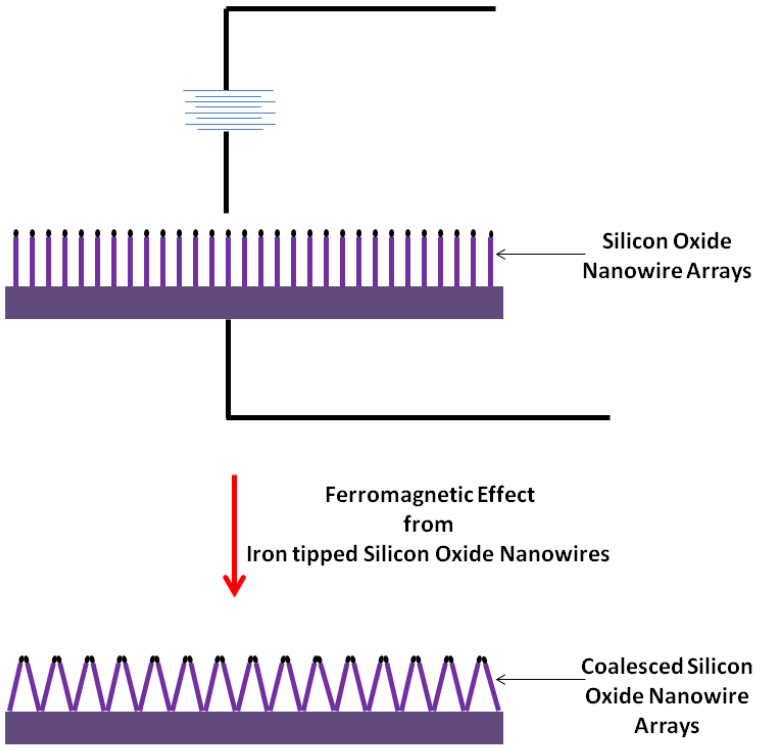

Figure 5.1.4.2.1. Scheme demonstrating the ferromagnetic effect from iron-capped silicon oxide nanowires.

Figure 5.1.4.2.1. is a scheme showing the potential application of silicon nanowires as electromechanical based sensors due to the presence of the iron-tipped section of the nanowires. The presence of iron oxide on the tip of the silicon oxide nanowires makes it possible, under the influence of an applied electric current/magnetic field to induce magnetism in the tipped region of the nanowires. The ferromagnetic/parasitic-ferromagnetic property of α-Fe_2O_3, a component of the tip-section of the as-fabricated silicon oxide nanowires, should generate forces that will induce the coalescence of neighbouring silicon oxide nanowires.

This effect was indeed observed in the as-fabricated silicon oxide nanowires under the SEM. During imaging with an SEM under high magnification, the current supplied to the

electromagnetic lens is high. The high current increases the strength of the magnetic field in the SEM causing the electron beams to raster over a smaller area. It is the increased magnetic field strength during high resolution scan under the SEM that induces magnetism in the ironoxide nanowires and thus results in coalescence of neighbouring nanowires. A media file showing the coalescence of the nanowires is attached to the digital copy of this dissertation.

5.2. Fabrication of Nanofeatures on Silicon

In the previous sections of this chapter, we have demonstrated that PS-b-P4VP block copolymer in combination with LIA can be used for the fabrication of sub-70nm hierarchical silicon oxide nanowire arrays. In this section however, we demonstrate the application of PS-b-P4VP block copolymer with LIA for the fabrication of submicron, and nano scale features on silicon substrates. By demonstrating the ability to fabricate features on different substrates -silicon and silicon oxide substrates, we are further emphasizing the robustness of the block copolymer phase separation and LIA techniques. The first sub-section describes the fabrication of sub-micron line and square arrays on silicon substrates, while the next sub-section describes the fabrication of inverted features on silicon substrates.

5.2.1. Fabrication of sub-micron line and square arrays on silicon.

Scheme 5.2.1.1 shows the steps followed for the fabrication of sub-micron line and square arrays on a silicon substrate. A single crystal silicon substrate, orientation <100>, is coated with 150 nm thin film of PS-b-P4VP block copolymer. Silicon substrate with the block copolymer thin film is solvent annealed in an enclosed chamber to produce phase-separated domains having P4VP vertical cylinders in a PS matrix, shown in scheme 5.2.1.1B. Because here we are interested in demonstrating the ability to fabricate

sub-micron resolution features, the phase-separated nano-domains present in the PS-b-P4VP block copolymer are not functionalized as shown in scheme 5.2.1.1.

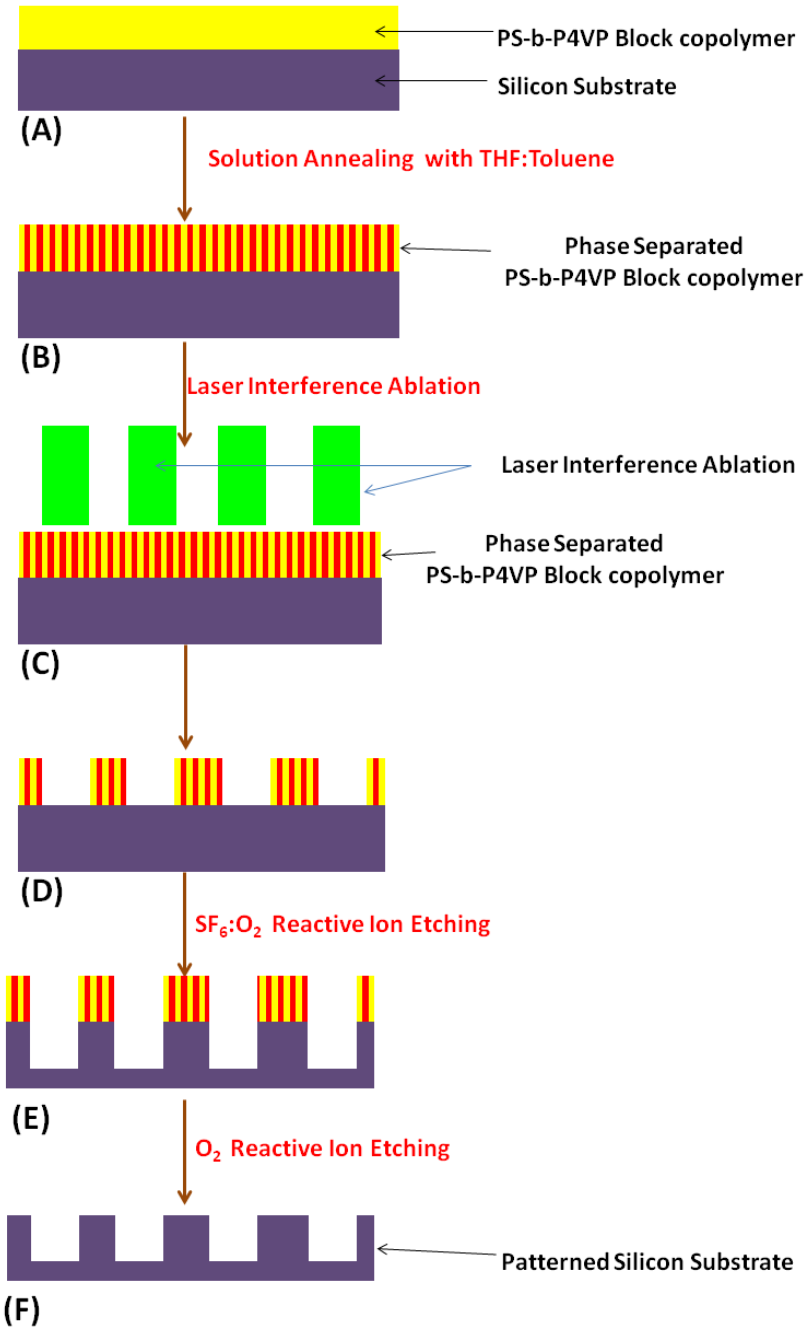

Scheme 5.2.1.1. Scheme showing the steps followed for the fabrication of sub-micron line and square arrays on silicon.

The laser interference ablation step, in scheme 5.2.1.1C, allows for the generation of line, square arrays of block copolymers with periodicity corresponding to the periodicity of the interference light beams. With the block copolymer acting as a plasma resist, pattern transfer to underlying silicon substrate is done via RIE in a SF_6:O_2 gas mixture as shown in scheme 5.2.1.1.E. Etching of silicon using SF_6 and O_2 reactive gases under plasma generates volatile products including SiF_4 and SOF_4 as shown in the chemical reaction in figure 5.2.1.1.

$$Si + 2SF_5^+ + 2F^+ + 2O^+ \longrightarrow 2SOF_4\uparrow + SiF_4\uparrow$$

Figure 5.2.1.1. A chemical reaction showing the volatile products from the plasma induced etch of silicon.

The duration of etch of the silicon substrate, with patterned block copolymer, was maintained at 30 secs. After serving as a resist layer for pattern transfer to underlying silicon substrate, the block copolymer was removed using an O_2 RIE for 60 mins.

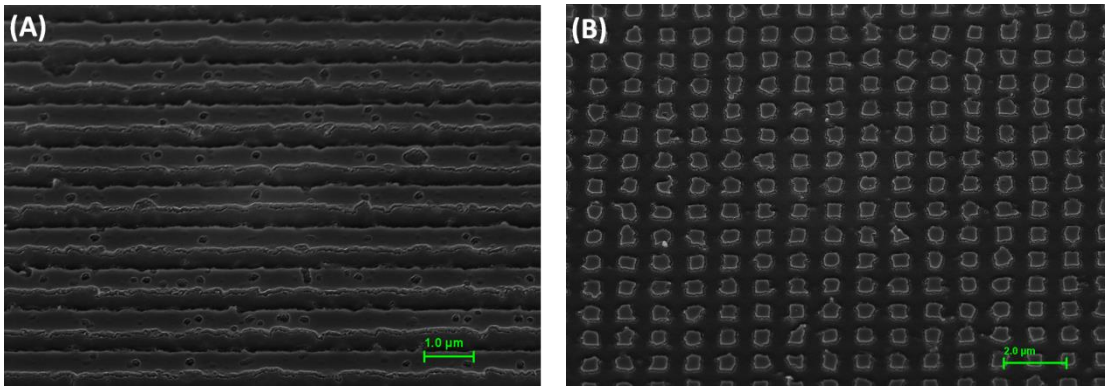

Figure 5.2.1.2. SEM image of silicon <100> (A) periodic line arrays and (B) periodic square arrays.

Figures 5.2.1.2A and B show the SEM images of periodic line and square arrays from silicon <100> substrates. The images were taken at a 45º tilt of the substrate under the SEM. The periodicity of the line and square arrays figures 5.2.1.2A and B is 1 µm. The width of the line arrays is ~600 nm, and the width of the square arrays is ~500nm. The etch rate of silicon <100> in the plasma chamber was calculated by measuring the depth of feature fabricated and dividing that against the etch duration.

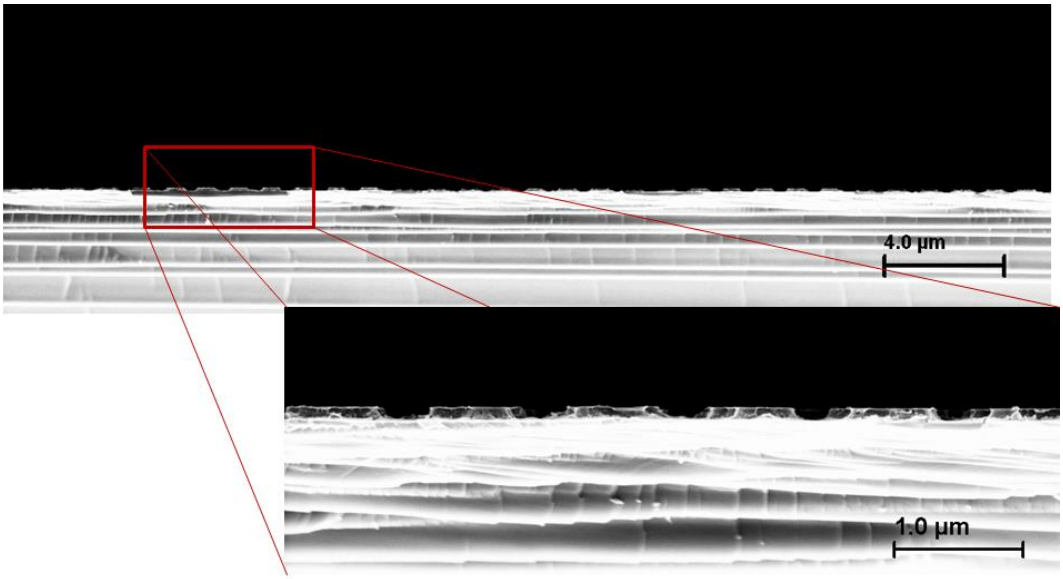

Figure 5.2.1.3. SEM cross sectional image of square arrays of silicon <100>

Figure 5.2.1.3 is the cross section of a silicon substrate that has been etched in a plasma chamber containing SF_6:O_2 gases for 30 sec followed by an O_2 etch for 60mins. The height of the features measured from the SEM cross-sectional image above is ~70nm. The etch rate of silicon in SF_6:O_2 reactive ion plasma is 2.33nm/sec. From the cross sectional image in the figure above, sub-micron line and square features fabricated on silicon <100> have a constant height with slightly tapering edges.

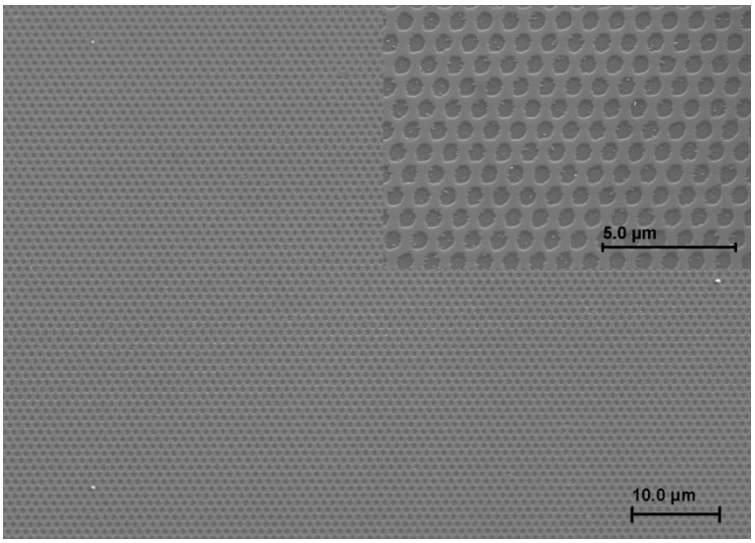

Figure 5.2.1.4. SEM image of hexagonal packed array of holes fabricated on silicon <100>.

As shown in chapter 3, figure 3.3.3.8.2D, hexagonally packed array of holes of PS-b-P4VP block copolymer can be made from the interference of three laser beams on a substrate. It is also possible to transfer such features to underlying silicon <100> substrates following scheme 5.2.1.1. Figure 5.2.1.4 is an SEM image obtained for hexagonally packed array of holes on a silicon <100> substrate. The inset shows a higher magnification image of the hexagonal packed array. The hexagonally packed arrays of holes have a diameter of 500nm, and a 1µm periodicity.

5.2.2. Fabrication of inverted line and square arrays on silicon

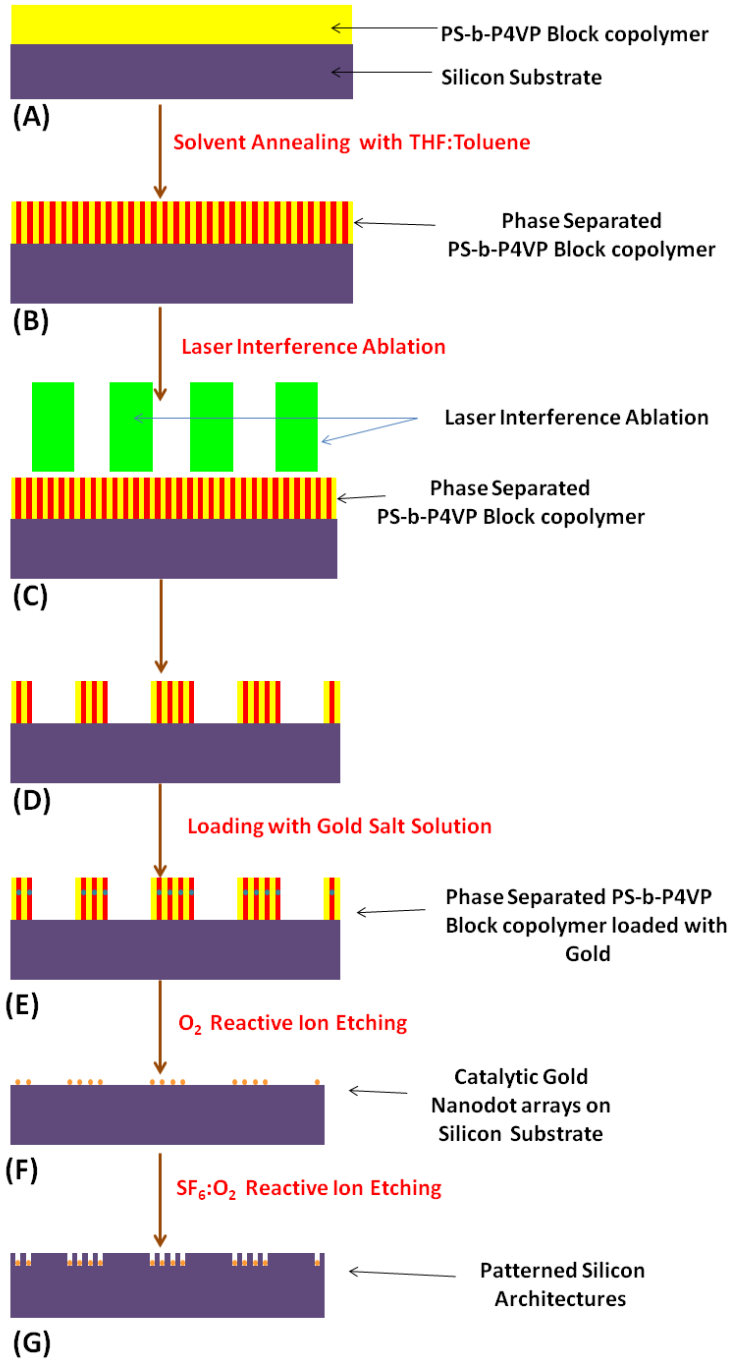

Scheme 5.2.2.1. Scheme showing the steps followed for the fabrication of inverted arrays of line and square nanofeatures on silicon.

In the late 80's, Fedynyshyn et al reported the mask dependent etch rates of silicon and silicon oxide substrates under RIE environments [119,154-156] They attributed the reason for the increased etch of silicon under RIE etch environments to the surface area catalyzed decomposition and generation of fluorine radicals induced by the presence of metals. The metals investigated included Ag, Al, Cu, Cr, Fe etc. We decided to investigate the potential use of the phenomenon for the fabrication of inverted multi scaled features on silicon.

Scheme 5.2.2.1 shows the steps followed for the fabrication of inverted multi-scale line and square arrays on a silicon substrate. A single crystal silicon substrate, with a <100> orientation, is coated with 150 nm thin film of PS-b-P4VP block copolymer. Silicon substrate with the block copolymer thin film is solvent annealed in an enclosed chamber to produce phase-separated domains having P4VP vertical cylinders in a PS matrix, shown in scheme 4.2.2.1B. After phase separation of the PS-b-P4VP block copolymer, laser interference ablation of the block copolymer generates line and square arrays of phase-separated PS-b-P4VP block copolymer. These line and square patterned arrays are then loaded with gold from a gold salt solution. The laser interference ablation step in scheme 5.2.2.1C, allows for the generation of hierarchical arrays of block copolymers with both primary and secondary ordering corresponding to the inter-domain spacing of the phase-separated block copolymer, and the periodicity of the interfering light beams respectively. The block copolymer is loaded with gold via immersion in a gold salt solution for 1 minute leading to the complexation of gold to the P4VP domain as shown in scheme 5.2.2.1D. RIE in an O_2 gas environment is later used to remove all the organic compounds- styrene and vinylpyridine- from the substrate. This resulted in the

formation of patterned gold nanoarrays on the silicon substrate as shown in scheme 5.2.2.1F. Without removing the substrate from the chamber, pattern transfer to underlying silicon substrate, via gold catalyzed RIE in an SF_6:O_2 gas mixture, is performed resulting in the generation of inverted line and square multi-scaled features on silicon <100> as shown in scheme 5.1.3.1G.

The behavior of gold in this technique is unlike the behavior of iron nanoparticles as described in sections 5.1.1 and 5.1.3. The gold nanoparticles serve as catalyst centers to increase the etch rate on a silicon substrate, while iron in sections 5.1.1 and 5.1.3, served as masks to reduce the etch rate on silicon oxide substrates.

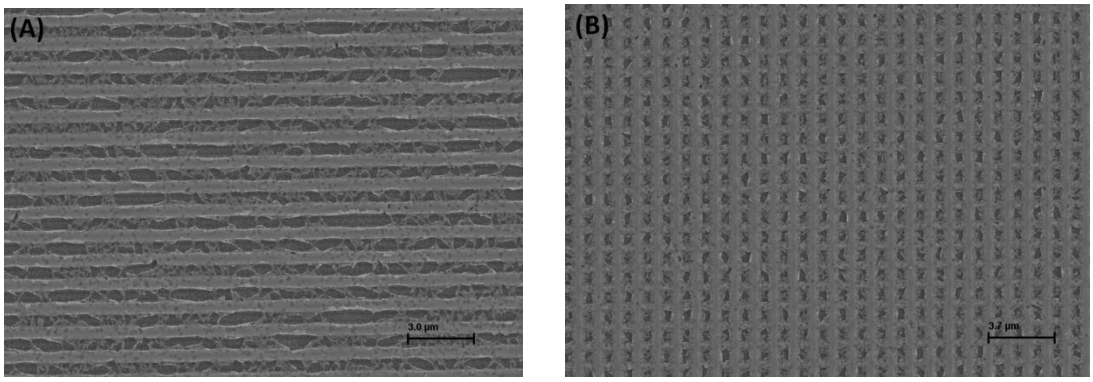

Figure 5.2.2.1 SEM image of inverted nanofeatures of (A) line arrays (B) square arrays on a silicon <100> substrate.

Figures 5.2.2.1A and B show periodic line and square arrays of inverted nano architectures fabricated on a silicon <100> substrate. The inverted line arrays shown in the SEM image in figure 5.2.2.1A have a 1µm periodicity. The inverted architectures formed by the gold nanoparticles are the darker features shown in the line and square arrays. The zoomed in images of the line and square arrays are shown in figures 5.2.2.2A and B respectively. The presence of these features confirms the hypothesis proposed by

Fedynyshyn et al. on the catalysis of RIE etches in the presence of high surface area metals.

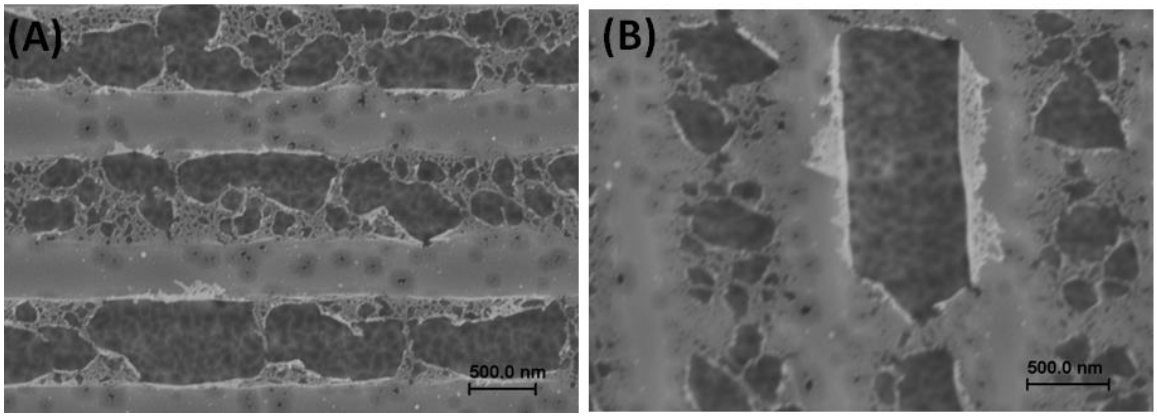

Figure 5.2.2.2. Zoomed-in SEM images of inverted nanofeatures of (A) line arrays (B) square arrays on a silicon <100> substrate.

The line and square inverted arrays were fabricated by RIE etching of silicon with gold nano-architectures for duration of 30 sec. Although etching silicon, with an SF_6:O_2 gas mixture, in an RIE tool can be optimized to give anisotropic etching; the result to be expected for a catalyzed RIE should be the combination of an isotropic and an anisotropic etching profile. An anisotropic etch profile will be expected during the initial stages of etch when the combined catalysis from the gold mediated formation of reactive fluorine molecules nanoparticles, and reactive ion etching are equal. After prolonged etching, the effect from gold mediated formation of reactive fluorine will prevail resulting in the formation of sub-micron square holes as shown in figure 5.2.2.3.

The periodicity of the hole arrays appears to be about 900nm, while the length of each side of the holes is ~400nm.

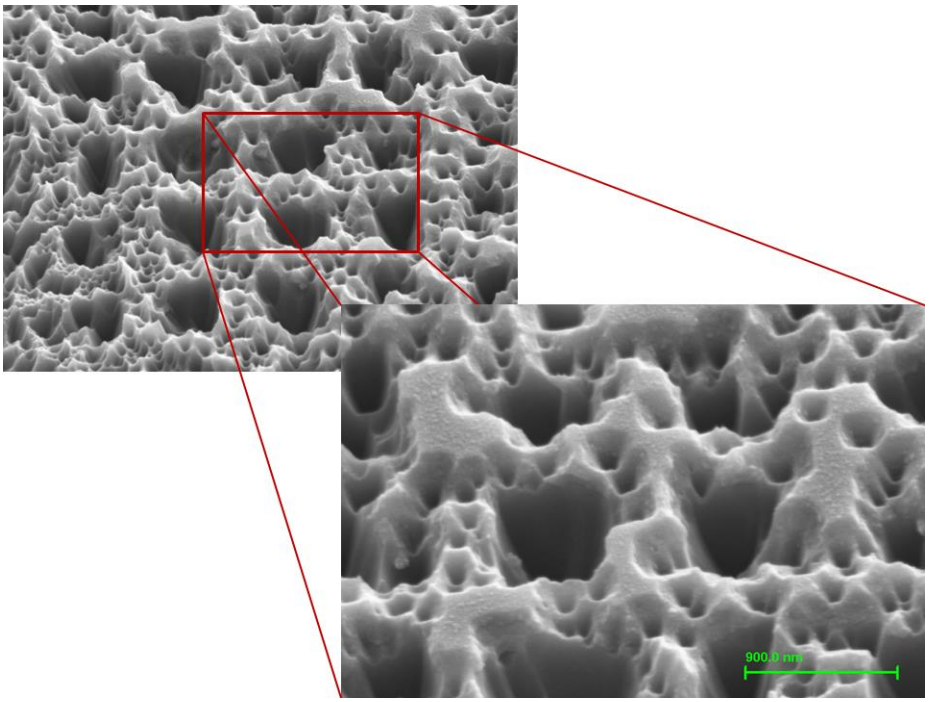

Figure 5.2.2.3. SEM image of silicon <100> periodic square arrays transformed into periodic square hole arrays.

5.3. Conclusion.

In this chapter we have shown that block copolymer in combination with LIA can be utilized for the fabrication of features on SiO_2 and Si <100> substrates. We demonstrated this by using block copolymer LIA for low-cost fabrication of dense patterned array of SiO_2 nanowires for use in the electronics and optoelectronics industry. We further demonstrated the use of block copolymer combined with LIA for the fabrication of line, square, hexagonally packed arrays as well as novel inverted architectures on silicon <100> substrates. The potential use of such multi-scaled features is enormous, for example, the inverted features fabricated on silicon <100> substrate can be used for sequestering materials on the sub-micron scale. Furthermore, because the porosity of silicon increases considerably after the fabrication of inverted features, there

is potential application of the modified silicon as a porous media. The silicon oxide features on the other hand can be utilized for the fabrication of blue-light emitting lasers, and can also be used as electromechanical sensors.

CHAPTER 6

MATERIAL SYSTEMS DEVELOPMENT FOR LAMP FABRICATION

This chapter presents and discusses data on the material systems designed for LAMP fabrication based on amplified photoresist that use cationic and radical photopolymerization mechanisms.

6.1. Introduction to epoxy-acrylate, vinylether, vinylether-acrylate, and vinylether-epoxy material systems for LAMP fabrication

Since the advent of additive manufacturing in the early 80's, followed by the development of the first stereolithography apparatus by 3D systems in 1986 [23,157], there have been numerous reports in the literature on the potential of the technique. There have been reports on the potential use of additive manufacturing/solid free form fabrication in biomedical applications [158], industrial applications which includes free form fabrication of polymer-ceramic composite geometries [26], electronics applications, as well as for investment casting of metals [159]. Although several modifications of stereolithography have been reported [160-161], the fundamental concept of stereolithography still remains the same- photopolymerisation of a pure organic resin or a composite resin for the layer-by-layer fabrication of complex geometries. This emphasizes that the limitations of the stereolithography fabrication technique, and other modifications to the technique, are a function partly on the materials system formulation, and partly on the resolution capability of the UV photoexposing optics. The advent of the digital micromirror device (DMD) by Texas instruments has helped facilitate massively

parallel UV photoexposure with resolutions approaching 15 microns, thus eliminating the optics limitation issue of stereolithography. However, the materials limitation issue does not have a single solution, because depending on the type of material to be fabricated, filler loading of the material system, emission spectrum of the UV light source etc; different material systems have to be designed. It is therefore not surprising the immense research that has been put into the design and study of material systems for use in stereolithography and other additive manufacturing processes [31,162-164].

Although several reports have focused on the development of low-shrink photomodifiable monomeric material systems based on epoxy [165-168], ether acrylate [30], epoxy-acrylate [169]; most studies carried out on monomeric ceramic-loaded material systems for stereolithography applications are still being done with an acrylate monomeric material systems. The disadvantages inherent with using an acrylate based material system includes high shrinkage, and oxygen inhibition effects [31]. The high shrinkage value coupled with the oxygen inhibition effect of the radical photopolymerization mechanism, in the acrylate material system can result in loss of resolution of as-fabricated geometries and potentially limit the advancement of the stereolithography technology for meeting the 21st century's industrial and global manufacturing needs.

We demonstrate here the design and study of photomodifiable ceramic-loaded material systems based on vinylether, vinylether-acrylate, and acrylate-epoxy low shrink material systems for visible light mediated curing with potential application in the field of additive manufacturing. The cationic photopolymerization mechanism coupled with the low shrinkage value of the as-designed material systems will extend the applicability of

the photopolymerization fabrication techniques as well as create additional database of materials that can be used in such techniques. The properties of the photomodifiable monomeric material systems before photoexposure was studied using UV-Vis spectrometer and viscometer; while the properties after photoexposure was measured using thermo gravimetric analyser (TGA), dynamic mechanical analyser (DMA), Fourier transformed infrared spectrometer in attenuated total internal reflectance mode (FTIR-ATR) and through cure depth measurements.

6.2. The LAMP Fabrication Technology

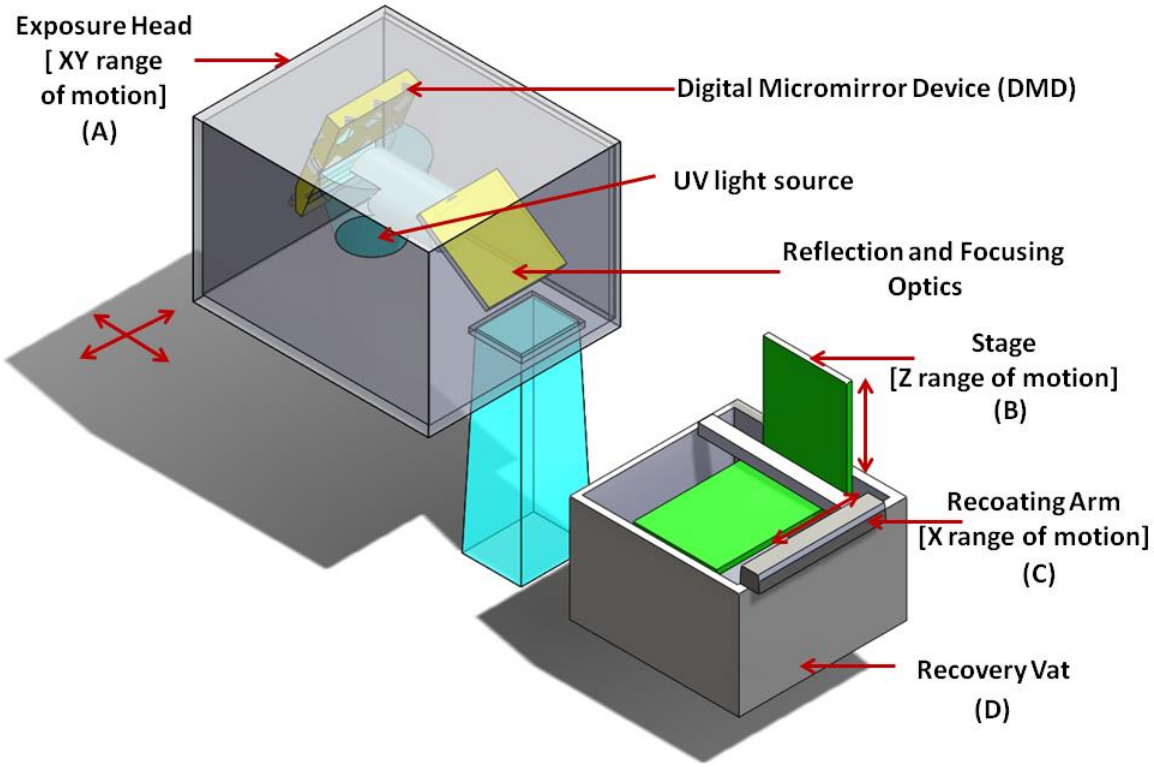

Scheme 6.2. A figure showing the (A) exposure head, (B) stage, (C) recoating arm, and (D) recovery vat: The major components of the LAMP fabrication process.

Large area maskless polymerization (LAMP) is an advanced form of additive manufacturing technique for layer-by-layer fabrication of complex shapes and

geometries. Layer-by-layer fabrication, with ~100 µm resolution, is aided by a UV light source incident on a photocurable ceramic resin. The main components of a LAMP fabrication process includes: exposure head, stage, recovery vat and a recoating arm. The exposure head, shown in figure 6.2A, consists of the high pressure UV mercury light source, a digital micromirror device (DMD), reflecting, and focusing optics. The exposure head has range of motion in the x and y directions. The high pressure mercury lamp is the light source used for LAMP fabrication, and it has emission maxima at ~405 and 437 nm. Figure 6.2.1 shows the emission spectrum for the UV light source.

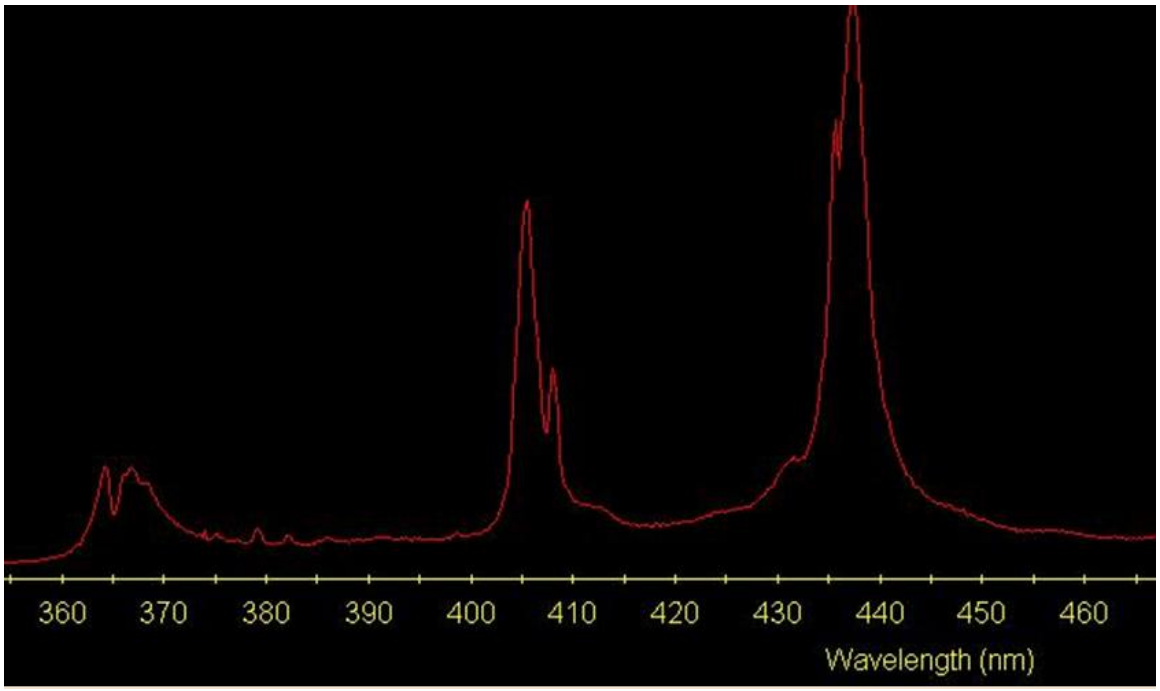

Figure 6.2.1. Emission spectrum of the high pressure mercury light source used for LAMP.

Light from the UV light source is reflected by mirrors and then focused on a DMD chip. The DMD chip consists of over 1 million micromirrors. Each micromirror is of size 17µm × 17µm, and determines the pixel resolution of the LAMP technique. Each

mirror on the DMD chip can be individually manipulated to an ‘ON’ or ‘OFF’ position by adjusting the angle orientation of the mirror. When data from a bitmap image, corresponding to a slice from a 3D object, is sent from a computer to the DMD chip, the chip interprets the black and white data set as a logic data set. The regions of the slice having white are interpreted on the DMD as areas where the mirrors are in the “ON” position, while regions of the slice with black are interpreted on the DMD as areas where the mirrors are in the “OFF” position.

The light reflected from the DMD chip, is then sent through other reflective and focusing optics until it emerges from the exposure head as a patterned light beam with information about the layer of reference from the computer.

The stage, in scheme 6.2B, is another key component of the LAMP fabrication process. The stage has a range of motion in the z-direction with 1μm accuracy. After the exposure of a layer of photopolymerizable composite resin, the stage goes down by exactly 1 layer thickness. The recoating arm, with x-range of motion, delivers a predefined layer thickness of ceramic composite resin unto the stage.

A material system must possess certain characteristics for it to serve as a good ceramic composite for LAMP fabrication. The most important property is photosensitivity. The material system must be sensitive/photomodifiable at the emission maxima of the high pressure mercury light source. Unlike conventional light sources with emission maxima in the 350nm wavelength region, as shown in figure 5.2.1, the emission maxima of the light source used in LAMP is blue-shifted. Thus most conventional photoinitiators would either not work or work inefficiently with the LAMP fabrication process. This further emphasizes the need for rational design of materials for use in the

LAMP fabrication process. Another important property a material system must possess for use in the LAMP fabrication process is low to medium range viscosity. Because the recoating arm, shown in figure 6.2C, dispenses a uniform layer of liquid suspension (~100-200µm) onto the z-stage; there is a need for precise control over the viscosity, and other flow properties of the material system. Any material system designed for LAMP fabrication should have a viscosity less than 350 mPas. The viscosity restraint rules out the use of aromatic epoxy resins in LAMP. However, low-viscosity resins including: acrylates, urethane acrylates, ether acrylates, vinylethers, can be designed for use with the LAMP. The design of resins for use with LAMP involves the rational selection of photoinitiators and photosensitizers with absorption properties matching the emission characteristics of the high pressure mercury light source.

6.3. Cure Depth Measurements.

Cure depth measurements of material systems designed for LAMP fabrication was done using scheme 6.3, shown below.

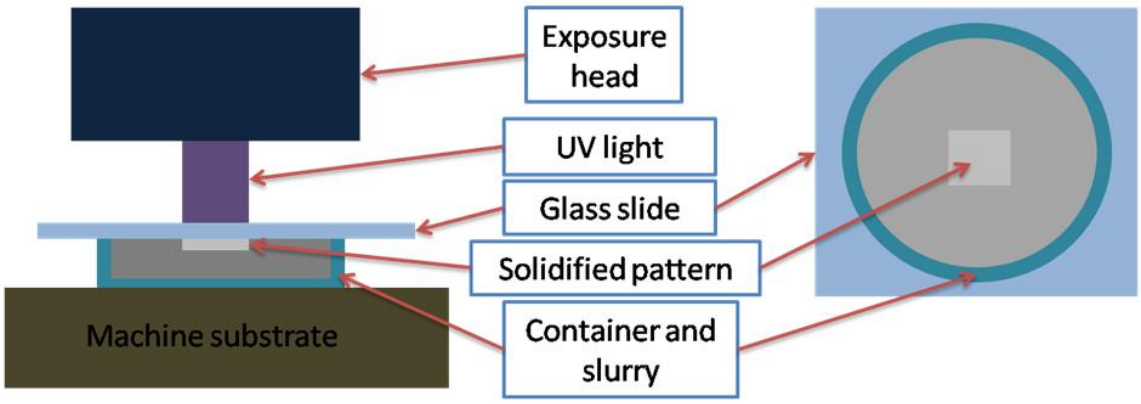

Scheme 6.3. Figure showing how cure depth of the as-designed material system was obtained from the LAMP set-up.

The material system under investigation is placed in a transparent plastic container. The container is placed on the z-stage, and the z-stage is put at a height such that the output UV light is incident on the surface of the material system. After UV exposure, the cured material is rinsed with isopropyl alcohol for ~1min, and then allowed to sit for a minute. Cure depth was measured using a caliper with ~10μm resolution.

Based on classical Lambert-Beer's law, transmittance of light through a substance is a logarithmic function of the absorption coefficient of the substance, α. and the distance travelled by light through the material, ℓ.

$$T = \frac{I}{I_0} = 10^{-\alpha \ell} = 10^{-\varepsilon \ell c} \qquad \text{equation 6.3.1.}$$

Where I is the intensity of light after passage through the material, I_o, is the intensity of the incident light beam, ε, is the extinction coefficient of the material, and c, is the molar concentration of the material. Because light can be described as packets of photons that carry energy, lambert-Beer's law can be rewritten in terms of energy.

$$T = \frac{E(c)}{E_0} = \exp(-\alpha_{Total} C) \qquad \text{equation 6.3.2.}$$

Where E(c) and E_o are the energy of transmitted light at depth C, and energy of incident light respectively. $\boldsymbol{\alpha}_{\text{Total}}$ is the absorption coefficient of all materials in the media absorbing the UV light. The modified Lambert-Beer's law can be rewritten, to show intrinsic properties of the material systems, as:

$$C_d = \frac{1}{\alpha_{Total}} \ln\left[\frac{E_o}{E_C}\right] \qquad \text{equation 6.3.3.}$$

$$\alpha_{Total} = \frac{1}{D_p} = \alpha_{PI} + \alpha_{Absorber} + \alpha_{Scattering} \qquad \text{equation 5.3.4.}$$

Where E_c is the critical energy dose below whish gelation does not occur, and C_d is the cure depth at the critical energy does. The absorption coefficient, $\boldsymbol{\alpha}_{Total}$, is a sum total of the absorption coefficient of the photoinitiator, $\boldsymbol{\alpha}_{PI}$, the absorption coefficient of absorber, $\boldsymbol{\alpha}_{absorber}$, and attenuation from composite fillers acting as scatterers, $\boldsymbol{\alpha}_{sacttering}$. The inverse of the absorption coefficient, $\boldsymbol{\alpha}_{Total}$, is depth of penetration, D_p. The depth of penetration is a value that tells us the degree of sensitivity of the material system.[31] This means that by simply taking cure depth measurements of photo-exposed layers using the figure shown in scheme 6.3, it is possible to obtain several intrinsic properties of the designed material system.

6.4. Epoxy-acrylate ceramic loaded material system.

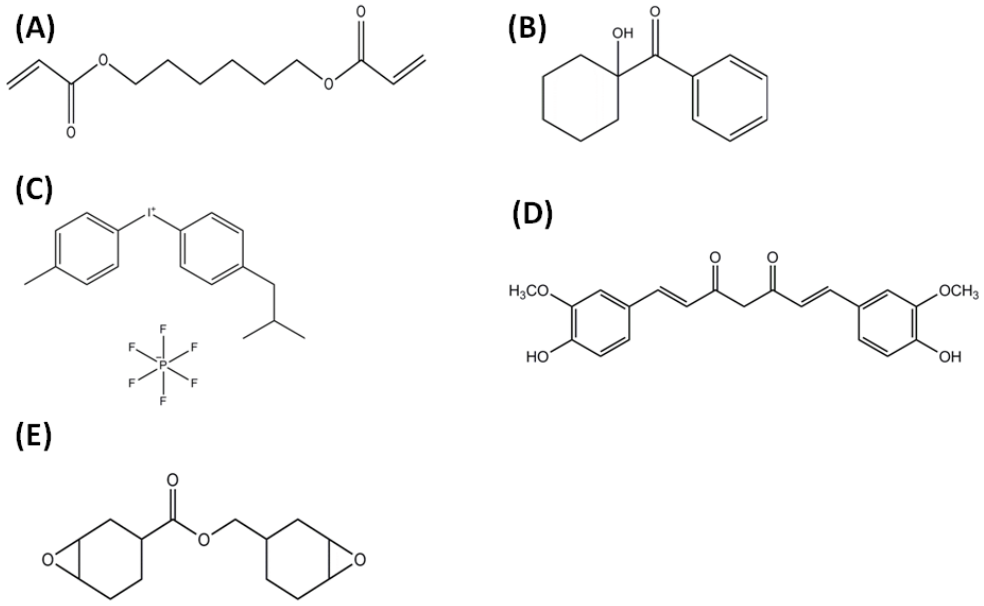

Figure 6.4. An epoxy-acrylate material system consisting of (A) Hexane dioldiacrylate (HDDA) (B) Irgacure 184 (C) Irgacure 250 (D) Curcumin (E) 3,4-epoxycyclohexylmethyl 3',4'-epoxycyclohexane carboxylate.

3,4-epoxycyclohexylmethyl 3',4'-epoxycyclohexane carboxylate was purchased from Sigma Aldrich and used without further purification. The epoxy monomer is a colorless liquid with a viscosity of 245 mPas, density of 1.17g/cm^3, and molecular weight of 252.31 g/mol. The extremely high viscosity of epoxy excludes the use of the monomer as the main resin for LAMP fabrication. The viscosity of epoxy material systems after adding silica becomes 500-600 mPas.

A difunctional monomer, 1,6-hexanediol diacrylate (HDDA) purchased from Sartomer, USA, was used to dilute the high viscous epoxy monomer system. HDDA has a viscosity of 9 mPas, density of 1.02 g/cm^3 and a molecular weight of 226 g/mol. The HDDA monomer is miscible with the epoxy monomer at all concentrations.

Fused silica TECO-SPHERE Microdust used for all the experiments in this section was purchased from C-E minerals. The silica contains 95% non-crystalline and 5% crystalline components with a density of 2.2g/cm^3.

Diethyl polypropoxy-2-hydroxyethyl ammonium acetate (Variquat CC-55) was purchased from Evonik industries and used without further purification. Variquat CC-55 was used as the dispersant for the ceramic micro particles.

The material system was made photoactive to the UV light source via the addition of two photo initiators: A cationic photoinitiator, and a radical photoinitiator.

The cationic photoinitiator, iodonium (4-methylphenyl)[4-(2-methylpropyl)phenyl]-hexafluorophosphate(1-) (Irgacure 250), was purchased from BASF with a density of 1.46 g/cm^3 and used without further modification. The absorption spectrum of Irgacure 250 measured with a UV/Vis spectrometer is shown in figure 6.4.1. The absorption spectrum shows an absorption maximum for the cationic photoinitiator at 300 nm.

Considering that the emission spectrum of the UV light source has maxima at 405 and 440 nm, Irgacure 250 cannot be used as a direct cationic initiator for the photopolymerization of the epoxy monomer. A photosensitizer with absorbance in the 400-450nm range will be needed for a Dextar-type bimolecular photochemical reaction to occur. The Dextar bimolecular photochemical reaction was discussed in the background section of chapter 2.

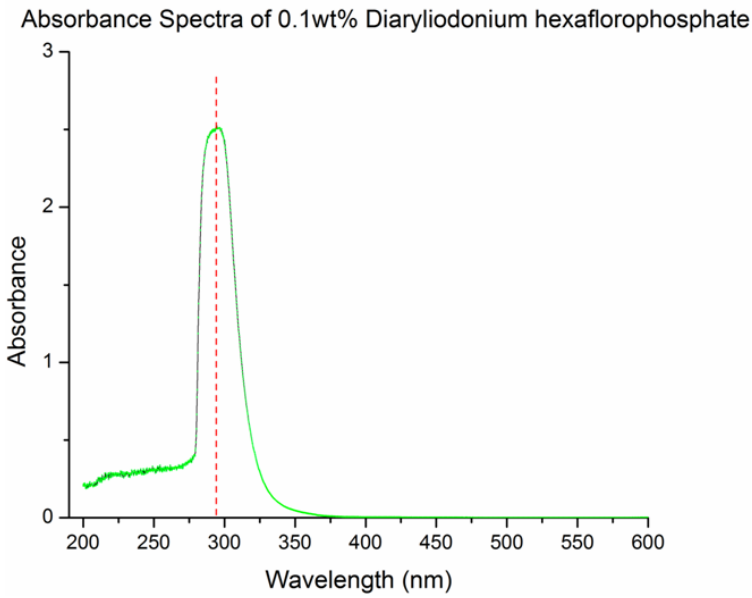

Figure 6.4.1. The absorption spectrum of 0.1wt% diaryliodonium hexafluorophosphate.

(E,E)-1,7-bis(4-hydroxy-3-methoxyphenyl)-1,6-heptadiene-3,5-dione (curcumin) is a photosensitizer that was purchased from Sigma Aldrich and used as-purchased. Curcumin is a yellow solid with a molecular weight of 368.38 g/mol. The absorption spectrum of the curcumin photosensitizer is shown in figure 5.4.2. From the spectrum, curcumin photosensitizer has a broad band absorption from 375-450 nm. The absorption spectrum of curcumin photosensitizer makes it an ideal material for the

photosensitization of Irgacure 250 photoinitiator in cationic photopolymerization of epoxy.

The cationic photopolymerization mechanism of the epoxy monomer is shown in scheme 6.4.3. After UV light exposure, an exciplex is formed between curcumin and irgacure 250.

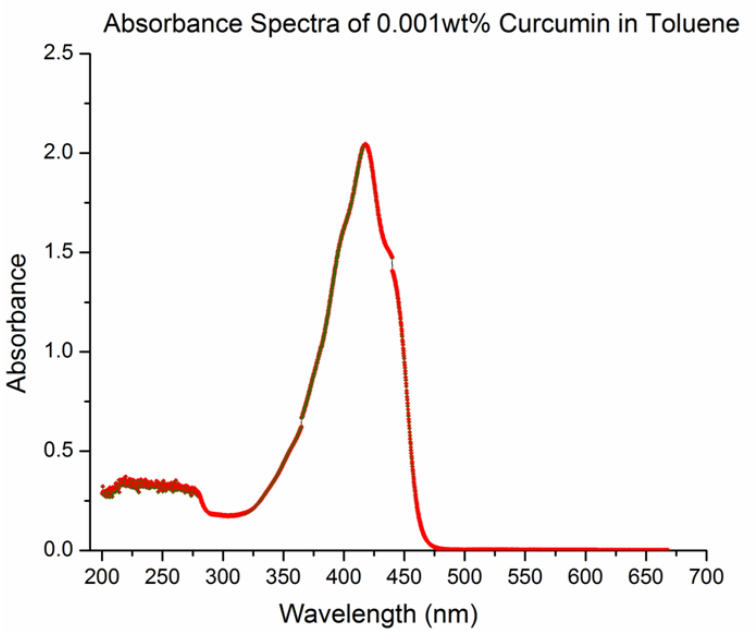

Figure 6.4.2. The absorption spectrum of 0.001wt% curcumin photosensitizer

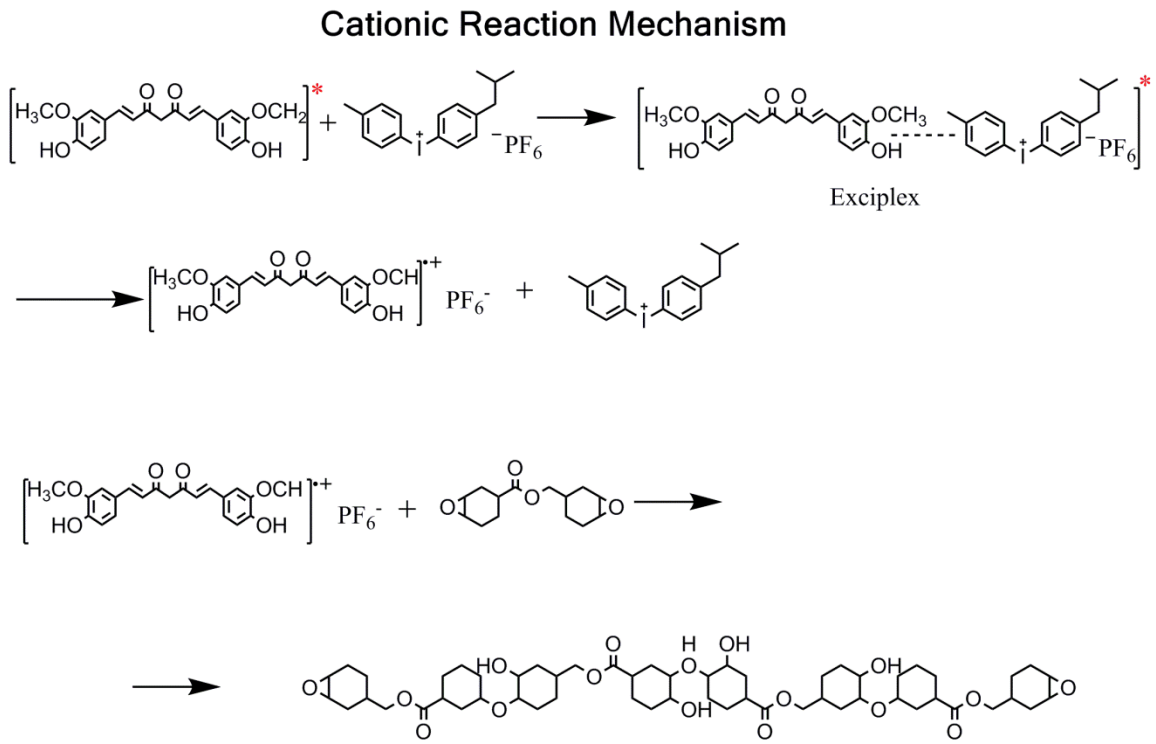

Scheme 6.4.3. Cationic photopolymerization mechanism of an Epoxy monomer

Upon break down of the exciplex, a reactive carbocation is formed that catalyses the polymerization of the epoxy monomer.

The radical photoinitiator, 1-hydroxy-cyclohexyl-phenylketone (Irgacure 184), was purchased from BASF as a white powder, density 1.2 g/cm^3, and used without further purification. The absorption spectrum of Irgacure 184 measured with a UV/Vis spectrometer is shown in figure 6.4.4. The absorption spectrum shows an absorption maximum for the radical photoinitiator at ~300 nm and a shoulder from 310-350 nm.

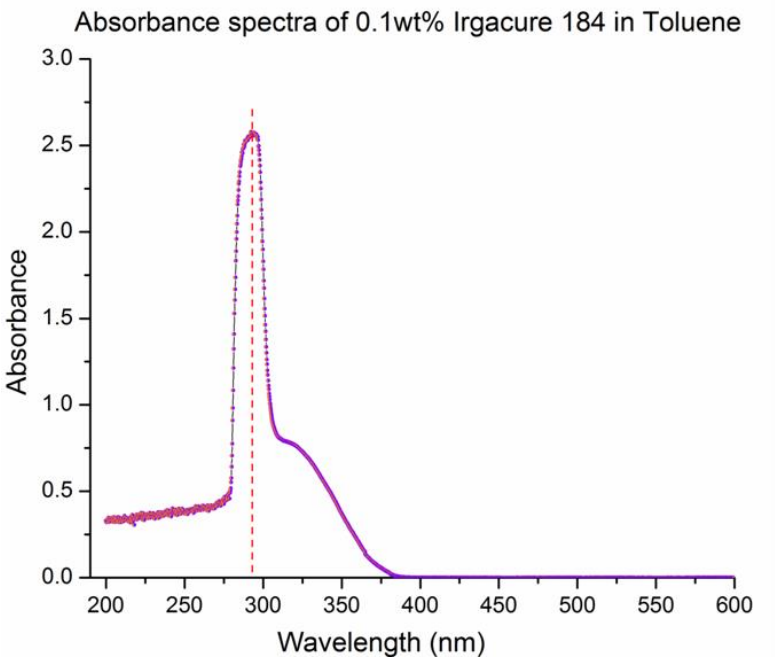

Figure 6.4.4. The absorption spectrum of 0.1 wt.% Irgacure 184

Although using Irgacure 184 as a photoinitiator, without the aid of a photosensitizer, does result in a low quantum yield, the rate of propagation of the acrylate radical is so fast ($K_{p(acrylate)} = 3.1 \times 10^7$) that gellation occurs momentarily. This allows the use of HDDA monomer together with Irgacure 184 as a photoinitiator.

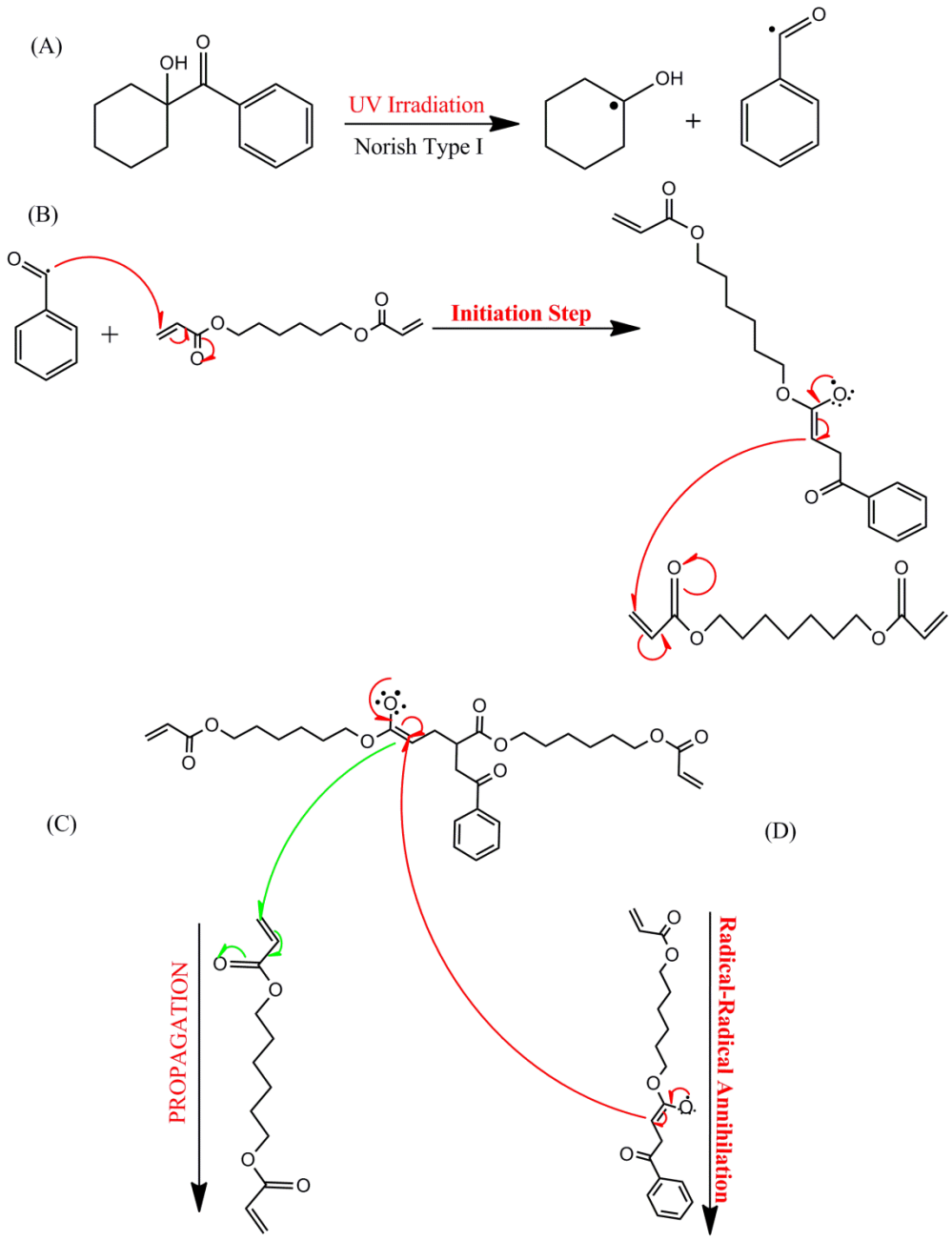

Scheme 6.4.5. Radical photopolymerization mechanism of HDDA

The radical photopolymerization mechanism of HDDA is shown in scheme 6.4.5. Photoexposure of Irgacure 184 to a UV light source generates a stable benzylketone radical. The photo-generated radical attacks the double bond present in HDDA, and

initiates the radical polymerization mechanism. Steps C and D show the propagation and annihilation reactions during the radical-initiated photopolymerization of HDDA with an Irgacure 184 photoinitiator.

6.4.1. Cure depth measurements

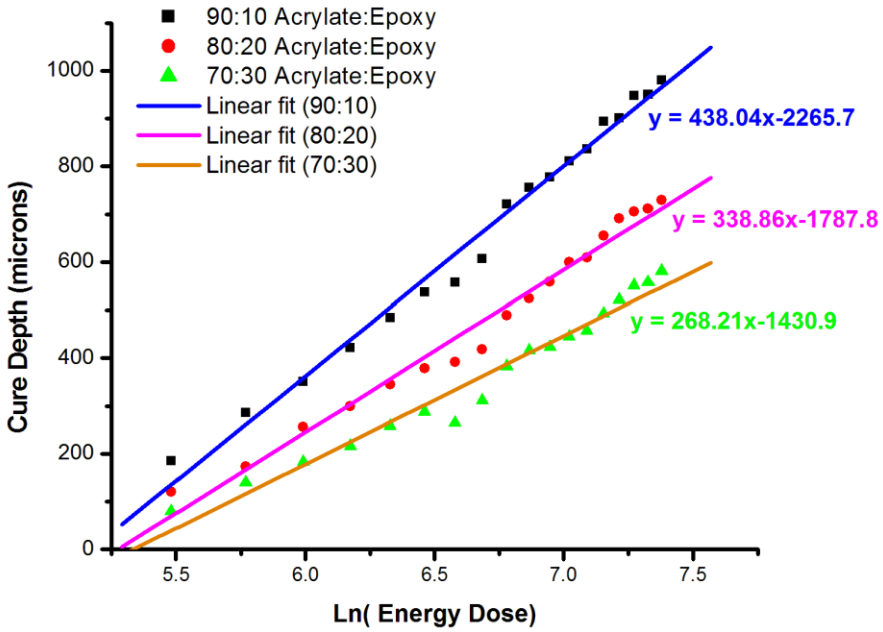

Figure 6.4.1.1. A plot of cure depth in microns versus natural logarithm of energy dose.

Equation 5.3.3 can rewritten as a linear equation of the form Y= MX+C, as shown below:

$$\boldsymbol{C_d = D_p \ell n\,(E_O) - D_p \ell n(E_C)} \qquad \text{equation 6.4.1.}$$

Plotting a graph of cure depth versus natural logarithm of energy dose will give a straight line having a slope equal to D_p, and an intercept equal to $-D_p \ell n(E_c)$. From the graph two intrinsic material system properties, D_p and E_c, can be obtained. Figure 6.4.1.1 shows a graph of cure depth (in micrometers) against natural logarithm of energy dose for acrylate: epoxy material system having 10wt%, 20wt% and 30wt% epoxy. The composition of the epoxy-acrylate material system developed is given in figure 6.4.1.2.

The D_p of the epoxy-acrylate material system increases with reducing wt% concentration of epoxy as shown in figures 6.4.1.1 and 6.4.1.3.

Figure 6.4.1.2. Table showing the composition of epoxy-acrylate material system designed for LAMP.

Material	Composition
Fused Silica	55g to 100g of epoxy-HDDA monomers
Irgacure 184	6g to 100g of HDDA
Dispersant	8.24g to 100g of fused silica
Irgacure 250	6g to 100g epoxy monomer
Curcumin	3g to 100g Irgacure 250
Tinuvin 171	0.25g to 100g HDDA monomer

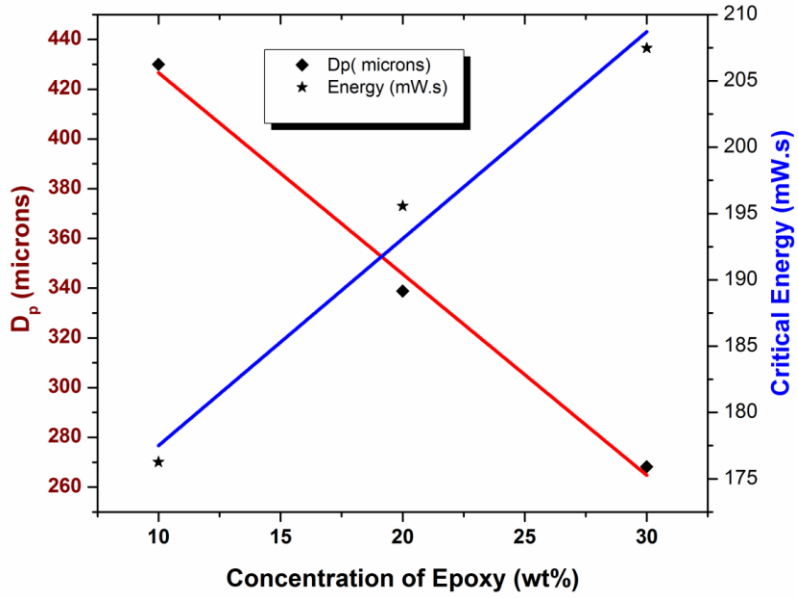

Figure 6.4.1.3. Graph showing the plot of Dp and E_c versus wt.% Conc of Epoxy.

The linear decrease in the Dp value with increasing wt% concentration of epoxy is clearly seen in figure 5.4.1.3. The decrease in Dp or increase in total absorption coefficient, $\boldsymbol{\alpha}_{Total}$, is as a result of the combined effect of the slow photopolymerization kinetics of epoxy, and the light absorption by the curcumin photosenstizer. A linear increase in Ec can also be seen from figure 6.4.1.3.

An epoxy-acrylate material system ideal for LAMP will have a maximum value for D_p and a minimum value for E_c. Trade-offs on the D_p and E_c values have to be made to incorporate an epoxy monomer into an acrylate material system for LAMP fabrication purposes.

6.4.2. Degree of Conversion Measurements

Degree of conversion measurements on the epoxy-acrylate material was done using a Brucker Fourier Transformed Infrared spectrometer (FTIR) in attenuated total internal reflectance (ATR) mode.

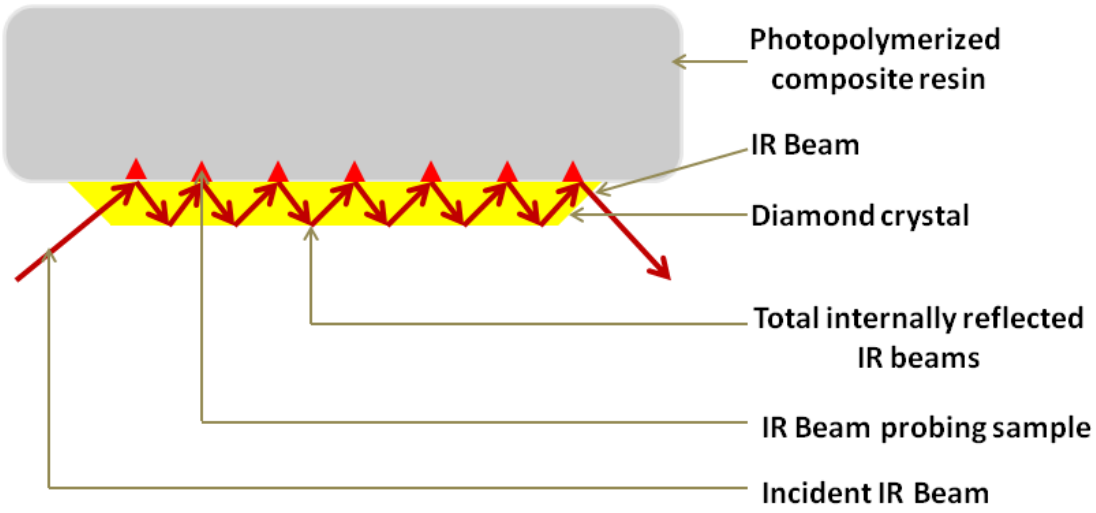

Figure 6.4.2.1. Scheme showing the working principle of an FTIR in ATR mode.

The working principle of an FTIR in ATR mode is shown in figure 6.4.2.1. An incident IR beam undergoes total internal reflection at the face in contact with a sample, and also at the opposing face. Total internal reflection of the beam, at the inner surface in-contact with the sample, allows the IR beam to probe ~0.5-2µm into the sample. Upon exiting the diamond crystal, the IR beam is collected by a detector.

Figure 6.4.2.2. shows the FTIR spectra of epoxy-acrylate ceramic composite before and after photopolymerization. The peak observed at 1700 cm^{-1} is from the carbonyl group present in both the epoxy and HDDA monomers, while the peaks at 1650 cm^{-1} and 1450 cm^{-1} is from the carbon-carbon double bond group. Other peaks at 1100 cm^{-1} and 1000

cm^{-1} come from the ester group also present in the epoxy and HDDA monomers, while peaks at 750 cm^{-1} and 800 cm^{-1} come solely from the ozirane group present in the epoxy monomer. After UV exposure, the peaks from the ozirane functional group diminishes in intensity while there is an increase in the intensity of the peaks from the ester functional group. The carbonyl peak remains constant during the whole photopolymerization experiment and can be used as a reference peak for measuring the degree of conversion.

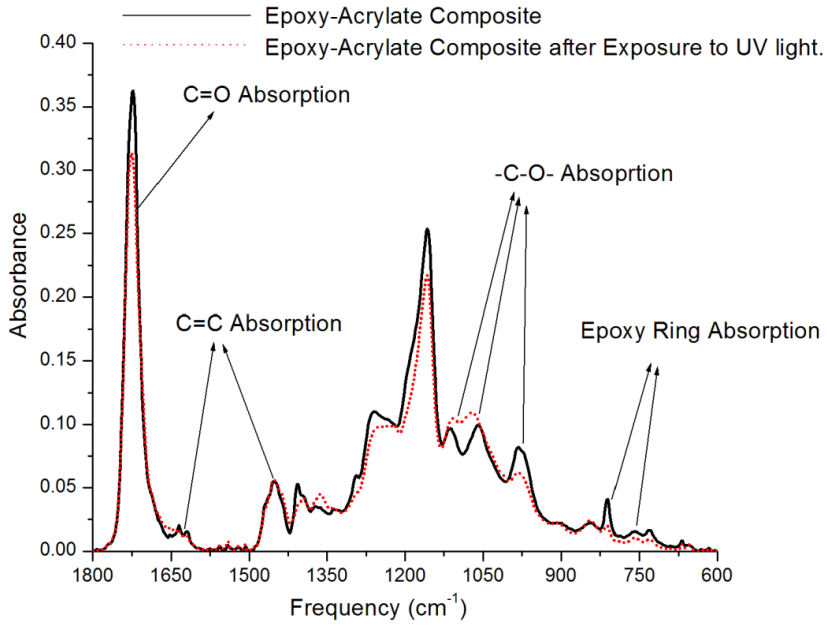

Figure 6.4.2.2. FTIR spectra of an epoxy-acrylate ceramic composite.

The degree of conversion for the acrylate material system in the epoxy-acrylate ceramic composite was determined using the formulas indicated below.

$$\alpha(t)_{acrylate} = \frac{\left[\frac{Area\ 1620 + Area\ 1420}{Area\ 1750}\right]_0 - \left[\frac{Area\ 1620 + Area\ 1420}{Area\ 1750}\right]_t}{\left[\frac{Area\ 1620 + Area\ 1420}{Area\ 1750}\right]_0} \times 100$$

Here, $\boldsymbol{\alpha(t)_{acrylate}}$ is the degree of conversion of the acrylate material system. Area 1620, area 1420, and area 1750 represent the integration of the areas under the respective peaks in the FTIR spectra. Based on the areas calculated, and the relationship between the areas prior to and after photoexposure, the degree of conversion of the acrylate material in the two-material system composition can be calculated. Figure 6.4.2.3 shows the degree of conversion measurements for a 20 wt.% of epoxy in an acrylate ceramic composites.

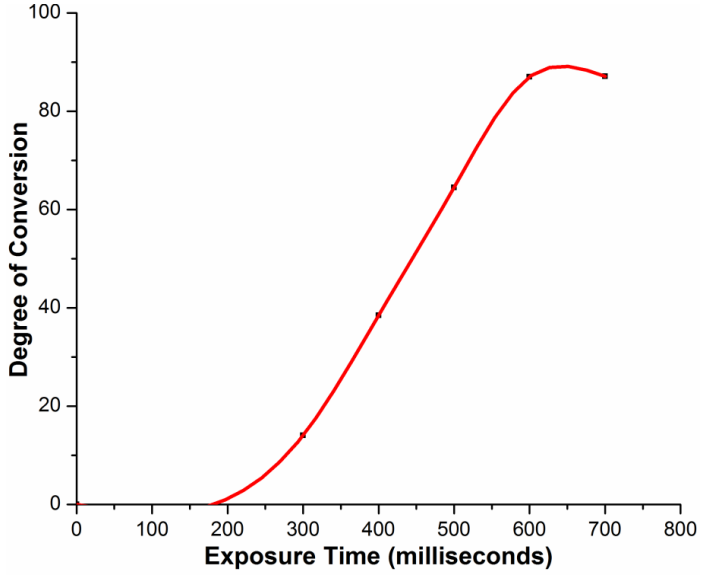

Figure 6.4.2.3. Graph showing the degree of conversion versus exposure time for 20 wt.% concentration of epoxy monomer in acrylate ceramic composite.

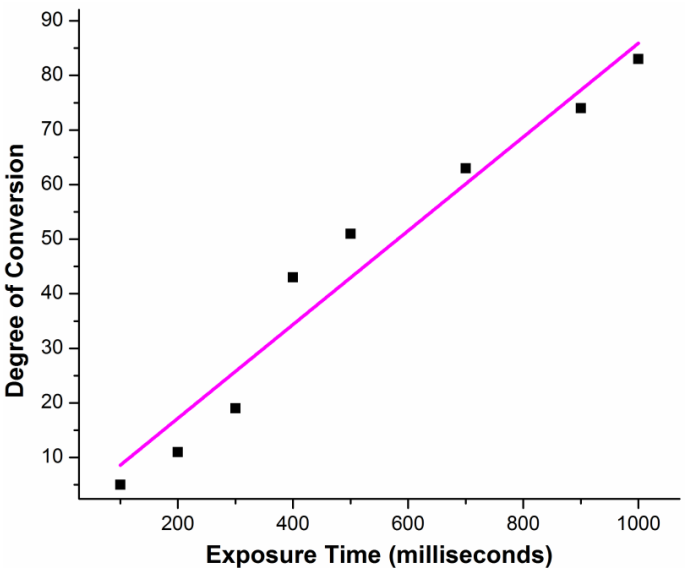

Figure 6.4.2.4. Graph showing the degree of conversion versus exposure time for an acrylate ceramic composite.

As a comparison, graph of the degree of conversion of an acrylate ceramic composite is shown in figure 6.4.2.4. From the graphs, at lower exposure times, below 300 millisec, the degree of conversion from acrylate ceramic composite systems is greater than the degree of conversion from an epoxy-acrylate ceramic composite material system. Because cationic photopolymerization of epoxy material systems occur via a Dextar bimolecular pathway, the rate of polymerization after photoexposure is slow compared to the faster rate of polymerization from the radical photopolymerization process in a acrylate based material system. The reduced rate of polymerization during low exposure doses is as a result of the need for excited state energy transfer from the dye material (curcumin) to the cationic photoinitiator (Irgaccure 250). Because the dye and photoinitiator (Irgacure 250) are present in small amounts, and the lifetime of the excited state of the dye is relatively short; at short exposure doses, most of the dye excited upon

UV exposure returns back to the ground state through other photophysical processes other than a photochemical process.

However, at higher exposure doses, the degrees of conversion of the epoxy-acrylate and acrylate ceramic composite systems appear to be relatively similar. A plateau is observed in the degree of conversion for the epoxy-acrylate ceramic loaded material system at ~80% while the acrylate ceramic composite system plateaus at exposure times greater than 1mins.

6.4.3. Thermo gravimetric analysis

Information on the thermal decomposition of photopolymerized acrylate, epoxy and vinylether material systems is required for successful binder burn-out. During the binder burn-out sequence, photocured acrylate ceramic composite molds are introduced into a chamber where the temperature is gradually ramped up to the decomposition temperature of the acrylate material. The temperature within the chamber is held at that temperature for a few hours to ensure removal of most of the polymeric material. The temperature is then gradually ramped up to 600ºC to ensure the complete removal of the organic components.

Thermal decomposition information of acrylate, vinylether and epoxy material systems was obtained using a TA instruments Q500 thermal gravimetric analyzer (TGA) apparatus equipped with nitrogen and air flow gases. The temperature ramp rate was chosen as 5ºC min^{-1} while thermal decomposition was carried out under nitrogen gas.

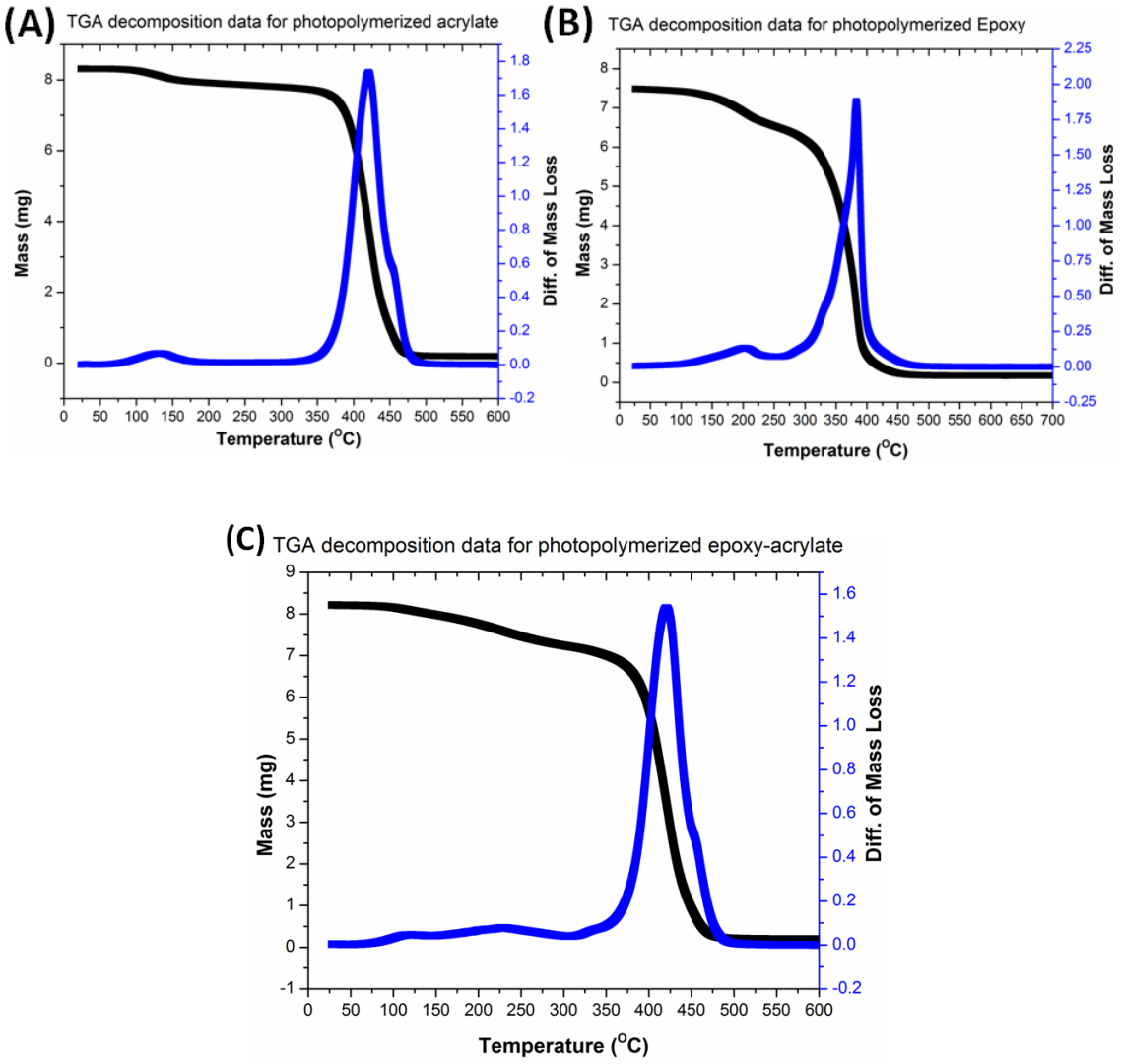

Figure 6.4.3.1. Graphs showing the mass-loss versus temperature rise for (A) photopolymerized acrylate material system. (B) photopolymerized epoxy material system and (C) photopolymerized epoxy-acrylate material system.

From the TGA data in figure 6.4.3.1A and B, the photopolymerized acrylate material system has a maximum decomposition temperature around 425ºC while a photopolymerized epoxy material system has a maximum decomposition temperature around 375ºC. This means that during binder burnout, an epoxy material system will be removed at a lower temperature than an acrylate material system. Thus potential

substitution of acrylate with some epoxy material can reduce the time required during the binder burn-out step. Figure 6.4.3.1C is the TGA data for a 80:20 wt.% acrylate-epoxy photopolymerized material system.

Another potential advantage of substituting acrylate with an epoxy material is the narrow temperature range of decomposition of an epoxy material system. In figure 6.4.3.1B the graph showing the differential of mass loss against temperature shows a narrower peak than that present in figures 6.4.3.1A.

6.4.4. Viscosity Measurements

Viscosity measurements were done using a DV-II+Pro viscometer from Brookfield engineering laboratories incorporated. The viscosities of 10, 20 and 30 wt.% epoxy in acrylate ceramic loaded systems as a function of temperature is shown in figure 6.4.4. Temperature was chosen as an independent/variable parameter because temperature can be easily controlled, and has direct impact on the viscosity of the material system. By varying the temperature, the viscosity can be changed without changing composition and other vital photomodifiable parameters of the ceramic loaded epoxy-acrylate material system.

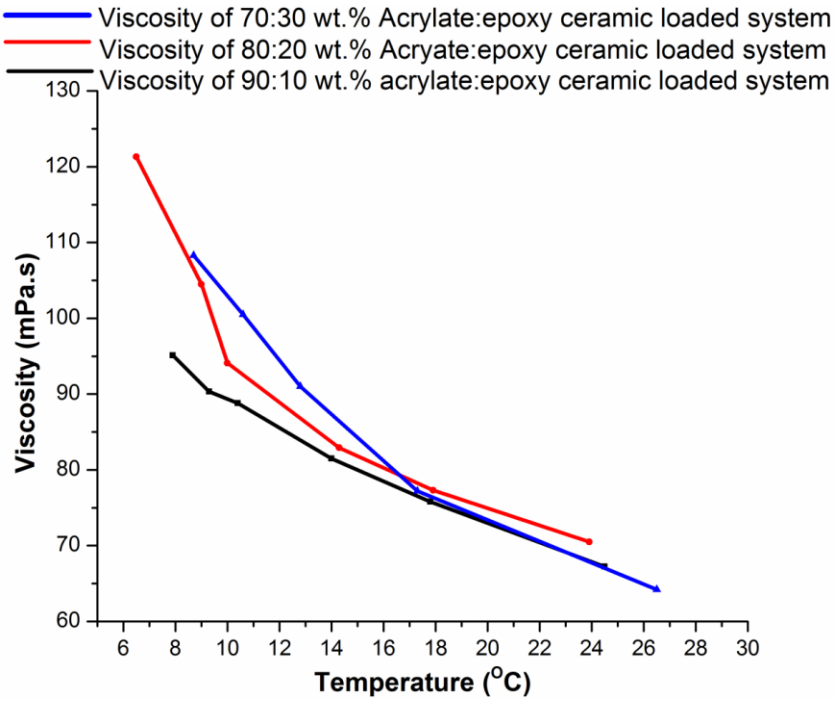

Figure 6.4.4. Graph showing the variation of viscosity (mPa.s) versus temperature (ºC) for acrylate-epoxy ceramic loaded material system.

With decreasing temperature, the viscosity of the material system increases for all three material systems compositions under investigation. Furthermore, increasing concentration of epoxy from 10 to 30 wt.%, leads to an increase in the viscosity of the epoxy-acrylate ceramic loaded material systems.

6.4.5. Dynamic Mechanical Thermal Analysis

Dynamic mechanical thermal analysis (DMA) was obtained using a TA instruments Q200 dynamic mechanical thermal analyser. Tensile measurements were done using a multiple frequency sweep at a frequency of 1Hz and a strain of 0.1%. Temperature for all measurements was varied from -60 ºC to 100 ºC.

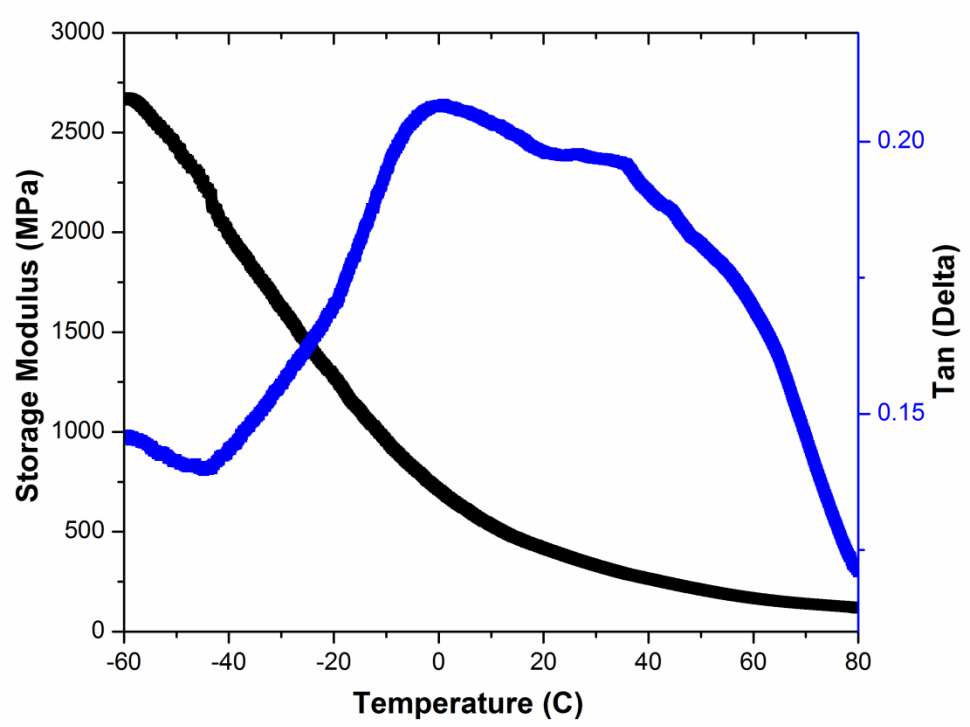

Figure 6.4.5.1. Dynamic mechanical analysis on a photopolymerized 20:80 wt.% epoxy-acrylate ceramic composite system.

Figure 6.4.5.1 shows a plot of storage modulus and tan (δ) as a function of temperature. The storage modulus for the epoxy-acrylate ceramic loaded sample can be seen to decrease from 2.75 $\times 10^9$ Pa at the glassy state to ~0.5 $\times$ 10^9 Pa at the rubbery state. The width of the tan δ curve indicates that the glass transition temperature spreads over a large range of temperatures. This indicates that the photopolymerized resin is structurally heterogeneous with a wide distribution of relaxation times. As comparison, figure 6.4.5.2 below shows the plots of storage modulus and tan (δ) as a function of temperature for a photopolymerized acrylate ceramic composite system.

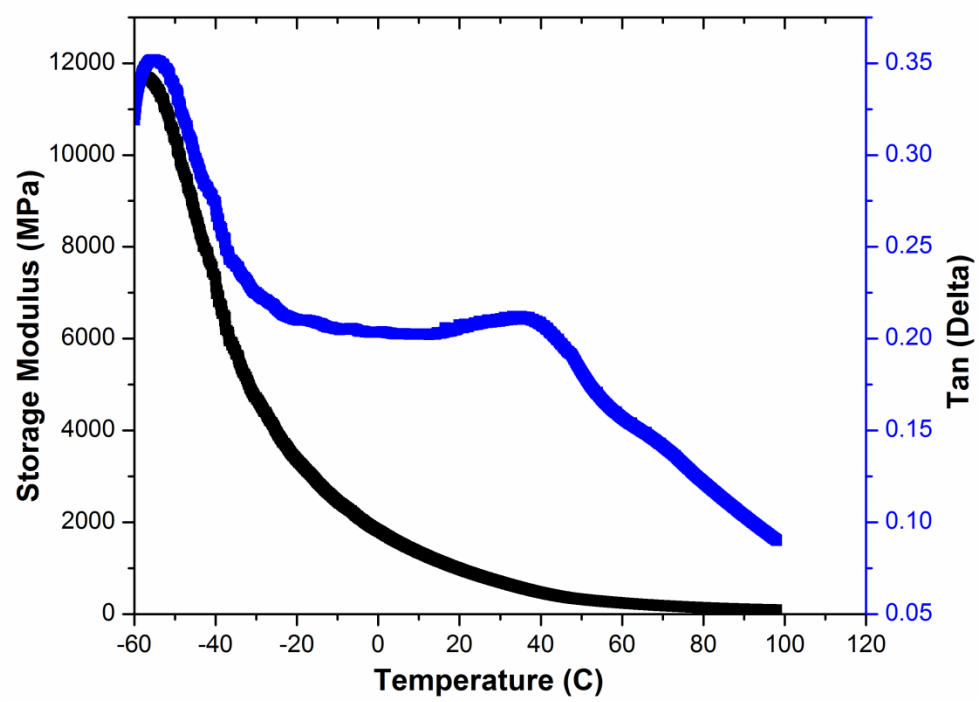

Figure 6.4.5.2 Dynamic mechanical analysis on a photopolymerized acrylate ceramic composite system.

6.5. Vinylether Ceramic Loaded Material System.

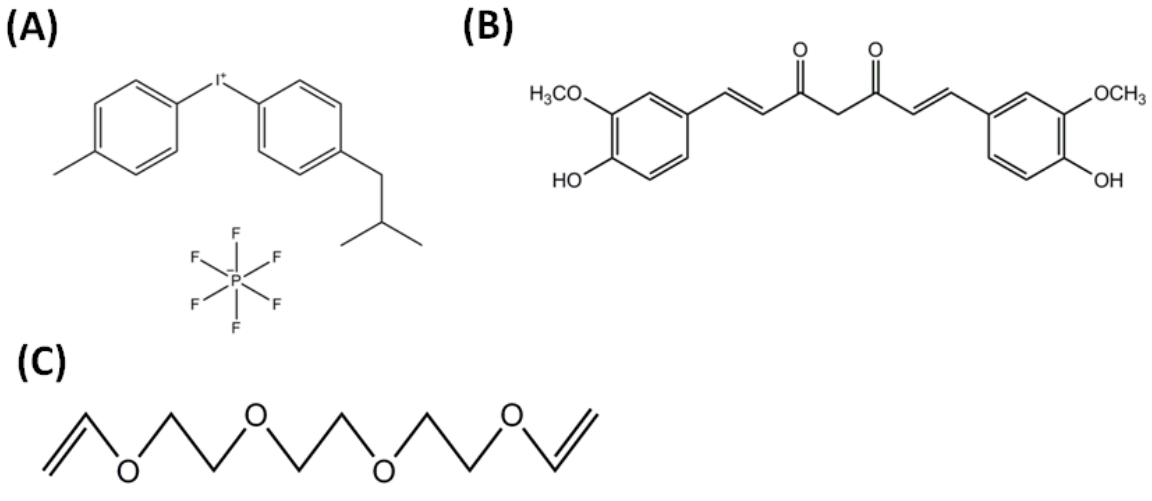

Figure 6.5.1. A vinylether ceramic composite material system consisting of (A) Irgacure 250 (B) curcumin (C) vinylether

Triethyleneglycol divinylether was purchased from Sigma Aldrich and used without further purification. The vinylether monomer is a colourless liquid with a viscosity of 9 mPas, density of 0.99 g/cm^3, and molecular weight of 202.25 g/mol. The extremely low viscosity of the vinylether monomer means that it can be used as the main resin for LAMP fabrication. The vinylether monomer is used together with an Irgacure 250 cationic photoinitiator and a curcumin photosensitizer.

The cationic photopolymerization mechanism of the vinylether monomer is shown in scheme 6.5.2. After UV exposure, an exciplex is formed between the excited state curcumin and Irgacure 250 photoinitiator.

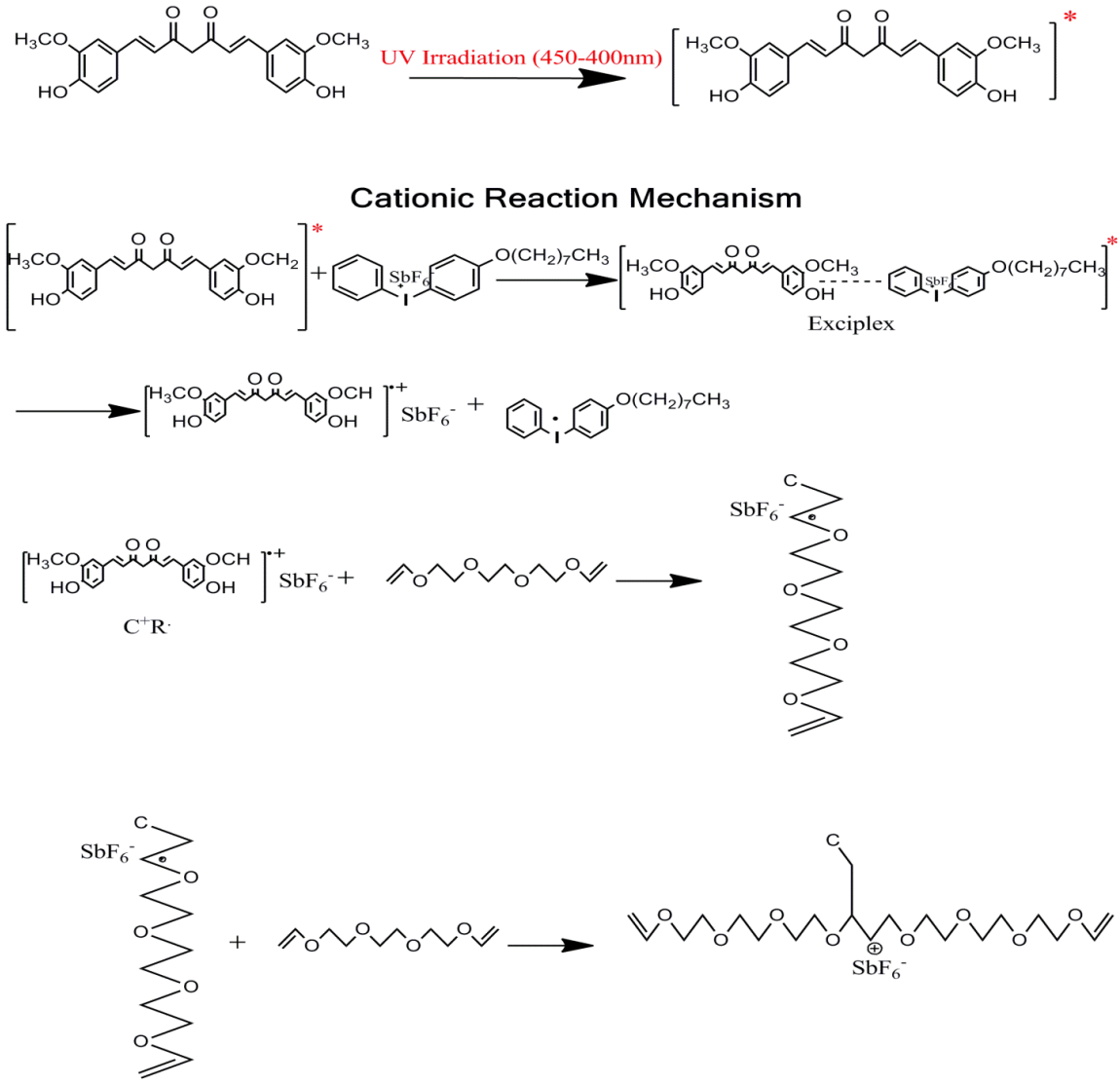

Scheme 6.5.2. Cationic photopolymerization mechanism of a vinylether monomer

Upon breakdown of the excited state complex, a reactive carbocation is formed that catalyses the polymerization of the vinylether monomer system.

6.5.1. Cure depth measurements

The graphs in figure 6.5.1.1A and B show the working curves for a vinylether material system containing varying concentrations of a cationic photoinitiator. In figure 6.5.1.1A, reducing the concentration of the cationic photoinitiator from 5 to 3 wt.%, in the

vinylether ceramic loaded material system, results in a rise in the depth of penetration (D_p). The same result is obtained when the photoinitiator concentration is reduced from 2 to 0.5 wt.% as shown in figure 6.5.1.1B.

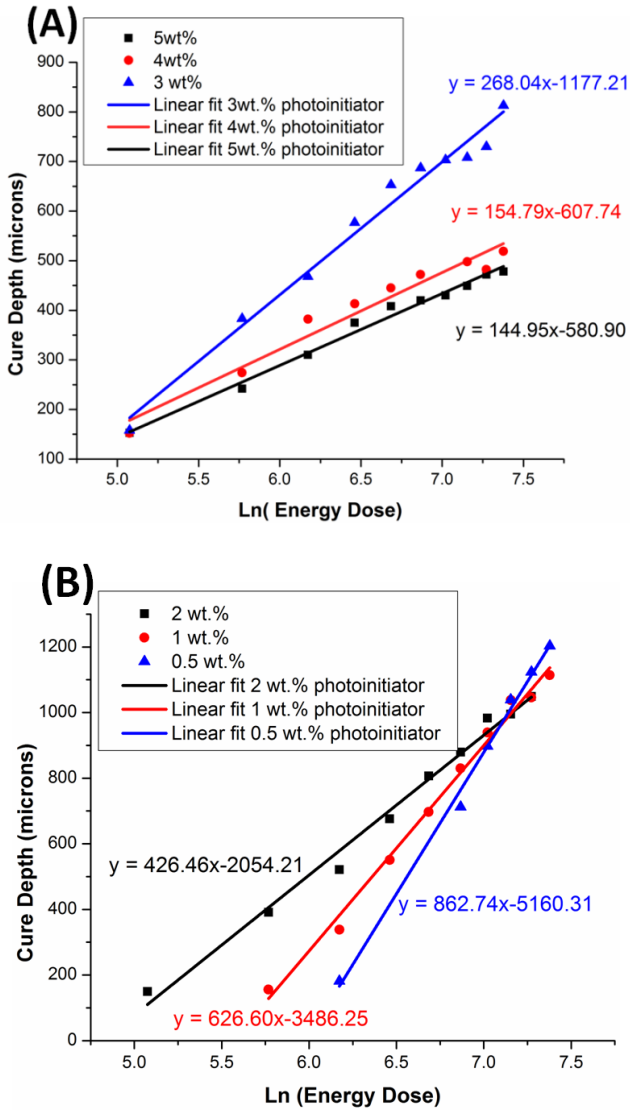

Figure 6.5.1.1. Graphs showing the plot of cure depth in microns versus natural logarithm of energy dose for (A) 5 wt.%, 4 wt.%, 3 wt.% and (B) 2 wt.%, 1 wt.%, 0.5 wt.% concentrations of photoinitiator in a vinylether material system.

However, with reducing photoinitiator concentration, the critical energy E_c increases. A vinylether material system for LAMP fabrication should have the lowest possible value

for E_c and the highest possible value for D_p parameters for high through-put fabrication purposes. Figure 6.5.1.2 shows a graph of E_c and D_p versus weight concentration of the cationic photoinitiator. At a cationic concentration of ~2 wt% the critical energy E_c and the depth of penetration D_p intersect on the graph. This weight concentration of photoinitiator appears to be optimal for the LAMP fabrication process.

The composition of the resulting vinylether material system designed for LAMP is shown in table 6.5.1.3.

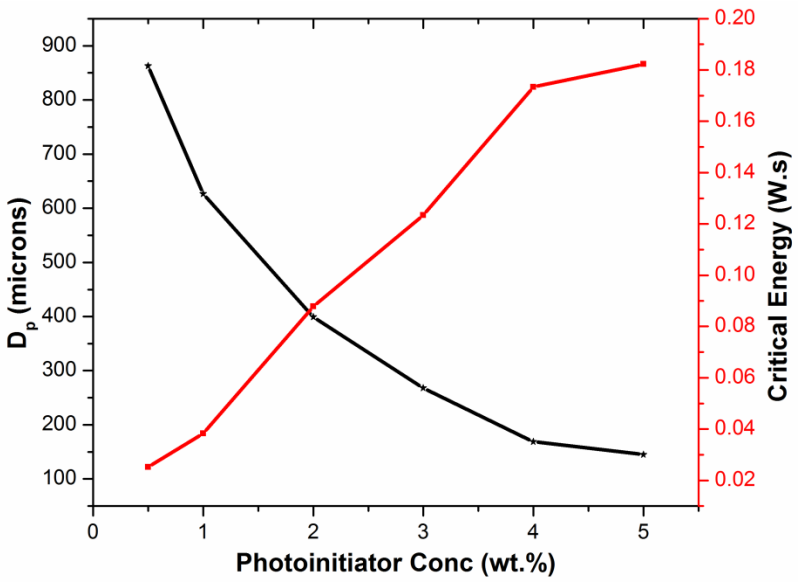

Figure 6.5.1.2. Graph showing the plots of Dp and Ec versus wt.% conc of photoinitiator

Table 6.5.1.3. Table showing the composition of vinylether ceramic loaded material system designed for LAMP.

Material	Composition
Fused Silica	55g to 100g of vinylether monomer
Dispersant	8.24g to 100g of fused silica
Irgacure 250	2g to 100g vinylether monomer
Curcumin	3g to 100g Irgacure 250

6.5.2. Degree of Conversion Measurements

Figure 6.5.2.1 shows the FTIR spectrum of a vinylether material system. The small intensity peak observed at 1700 cm^{-1} is from the carbonyl groups present in the photosensitizer molecule, while the peaks at 1650 cm^{-1} and 1450 cm^{-1} are from the carbon-carbon double bond group. The high intensity peak around 1100 cm^{-1} comes from the ester group. The ester peak remains constant during the whole photopolymerization process and is utilized as a reference peak for measuring the degree of conversion.

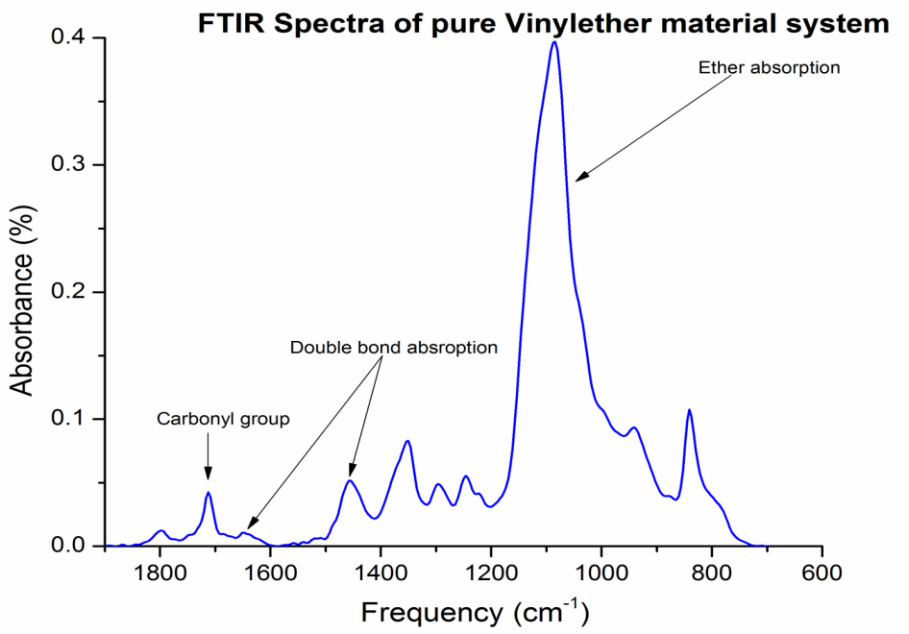

Figure 6.5.2.1. FTIR spectra of a vinylether ceramic composite system.

The degree of conversion for the vinylether ceramic loaded material system was determined using the formula below.

$$\alpha(t)_{vinylether} = \frac{\left[\frac{Area\ 1620 + Area1420}{Area\ 1100}\right]_0 - \left[\frac{Area\ 1620 + Area1420}{Area1100}\right]_t}{\left[\frac{Area\ 1620 + Area1420}{Area\ 1100}\right]_0} \times 100$$

Where $\alpha(t)_{vinylether}$ is the degree of conversion of the vinylether material system. Area 1620, area 1420, and area 1100 represent the intergration of the areas under the respective peaks in the FTIR spectra. Based on the ratios of the areas obtained from the FTIR spectra, the degree of conversion of the vinylether material system can be calculated. Figure 6.5.2.2 shows the degree of conversion measurements for a vinylether ceramic loaded material system.

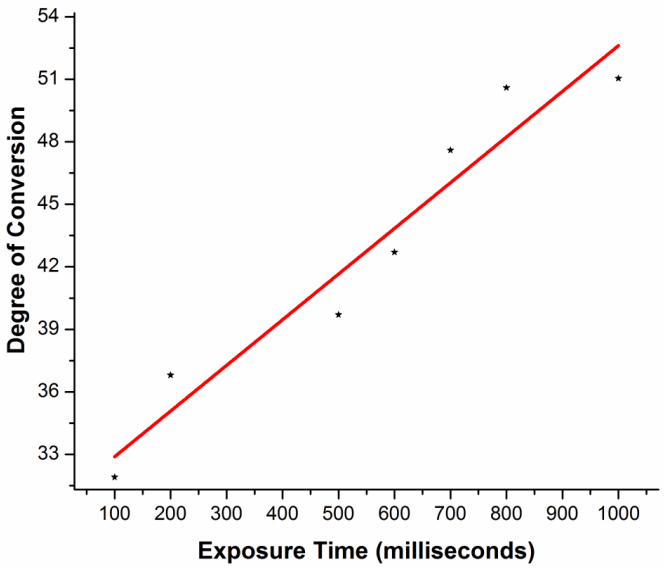

Figure 6.5.2.2. Graph showing the degree of conversion versus exposure time for a vinylether ceramic composite material system.

In comparison to the degree of conversion of an acrylate and acrylate-monomer ceramic system, the vinylether material system appears to show a very fast rate of polymerization at low exposure doses. The degree of polymerization of a vinylether material system appears to be 3× the degree of conversion of an acrylate material system when exposed to light for 100 milliseconds. However with increasing exposure doses, an acrylate ceramic composite achieves a higher degree of conversion than a vinylether ceramic loaded material system.

6.5.3. Thermo gravimetric analysis

Thermal decomposition information for the vinylether material system was obtained from a TA instruments Q500 TGA apparatus equipped with nitrogen and air flow gases. The temperature ramp rate was chosen as 5 $^{o}Cmin^{-1}$, and the thermal decomposition was carried out under nitrogen gas.

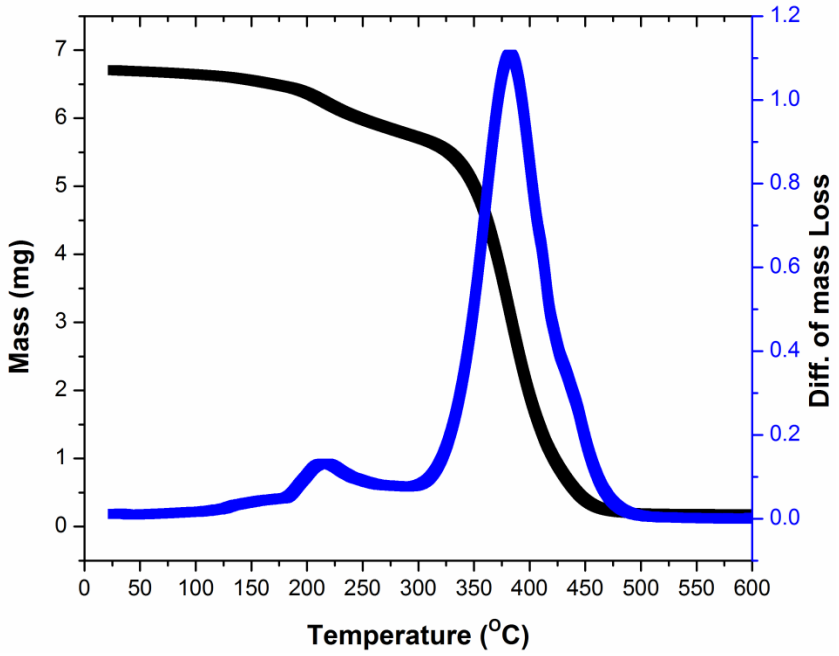

Figure 6.5.3.1. Graph showing the mass-loss versus temperature rise for photopolymerized vinylether material system.

From the TGA date in figure 6.5.4.1, the photopolymerized vinylether material system has a maximum rate of decomposition around 375ºC. Decomposition behaviors of the vinylether and acrylate material systems appear similar (as can be seen in figures 6.5.3.1 and 6.4.3.1A).

6.5.4. Viscosity Measurements

Figure 6.5.4 shows how the viscosity of a ceramic loaded vinylether material system varies with temperature. With decreasing temperature the viscosity of the vinylether material system is found to increase non-linearly. The viscosity of the vinylether ceramic loaded material system, however, is less compared to the viscosity of epoxy-acrylate ceramic loaded material systems.

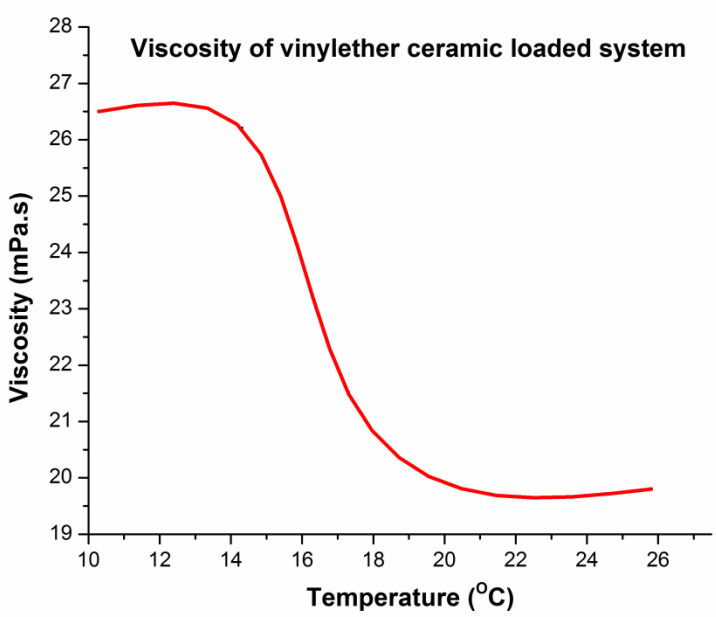

Figure 6.5.4. Graph showing the variation of viscosity (mPa.s) with temperature (ºC) for a vinylether ceramic loaded material system.

6.5.5. Dynamic mechanical thermal analysis

Dynamic mechanical thermal analysis (DMA) was obtained using a TA instruments Q200 dynamic mechanical thermal analyser. Tensile measurements were done using a multiple frequency sweep at a frequency of 1Hz and a strain of 0.1%. Temperature for all measurements was varied from -60 ºC to 100 ºC.

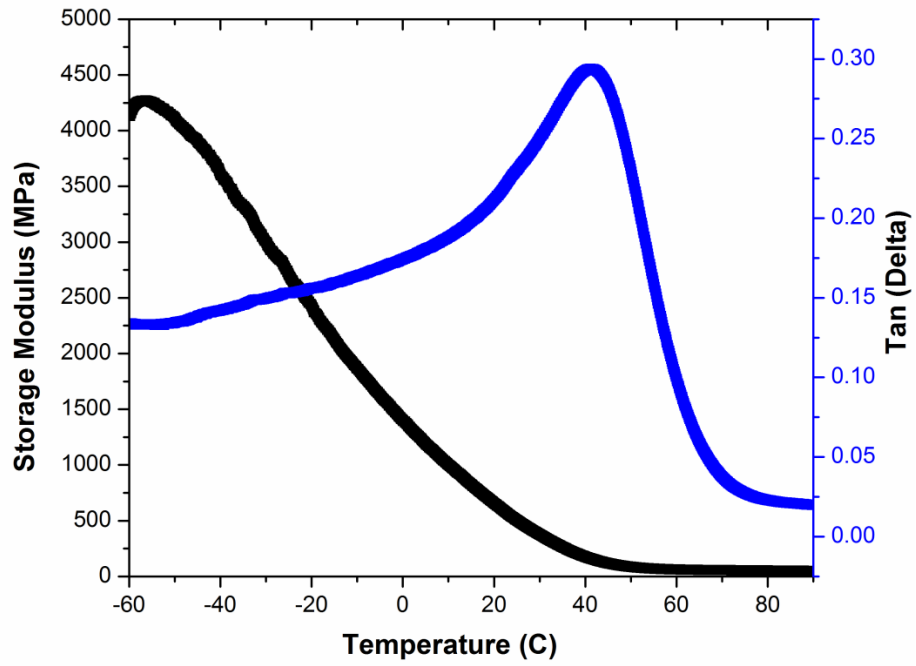

Figure 6.5.5 Dynamic mechanical analysis on a photopolymerized vinylether ceramic composite system.

Figure 6.5.5 shows a plot of storage modulus and tan (δ) as a function of temperature. The storage modulus for the vinylether ceramic loaded sample can be seen to decrease from 4.25 $\times 10^9$ Pa at the glassy state to ~0.5 $\times$ 10^6 Pa at the rubbery state. There is a sharp peak in the loss tan curve indicating a glass transition temperature at 40 ºC for the vinylether ceramic loaded material system.

6.6. Vinylether-acrylate ceramic loaded material system.

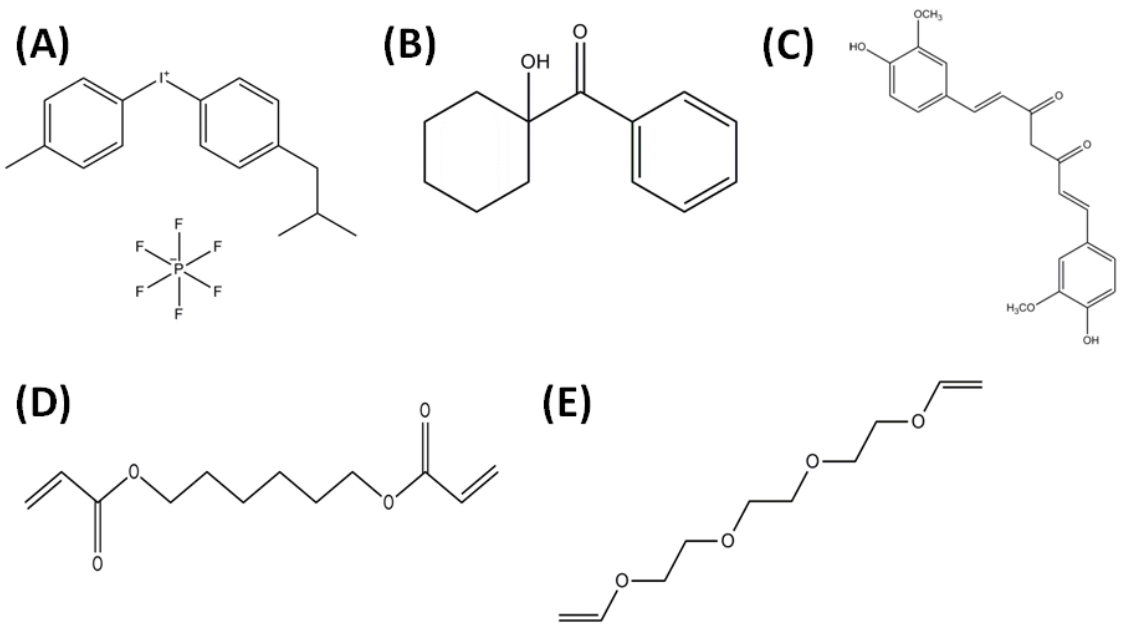

Figure 6.6.1. A vinylether-acrylate material system consisting of (A) Irgacure 250 (B) curcumin (C) hexanediol diacrylate and (D) vinylether.

A material system consisting of an acrylate and a vinylether monomers will undergo photocuring via the cationic photopolymerization mechanism, shown in scheme 6.5.2, and via the radical photopolymerization mechanism, shown in scheme 6.4.5.

6.6.1. Cure depth measurements

The graphs in 6.6.1.1A and B show the working curving for a vinylether-acrylate material system. In figure 6.6.1.1A increasing the weight concentration of vinylether from 10 to 40 wt.% results in a sharp reduction in both D_p and E_c. Further increase in the concentration of vinylether from 50-70 wt.% has no significant effect on the D_p and E_c values as shown in figure 6.6.1.1B.

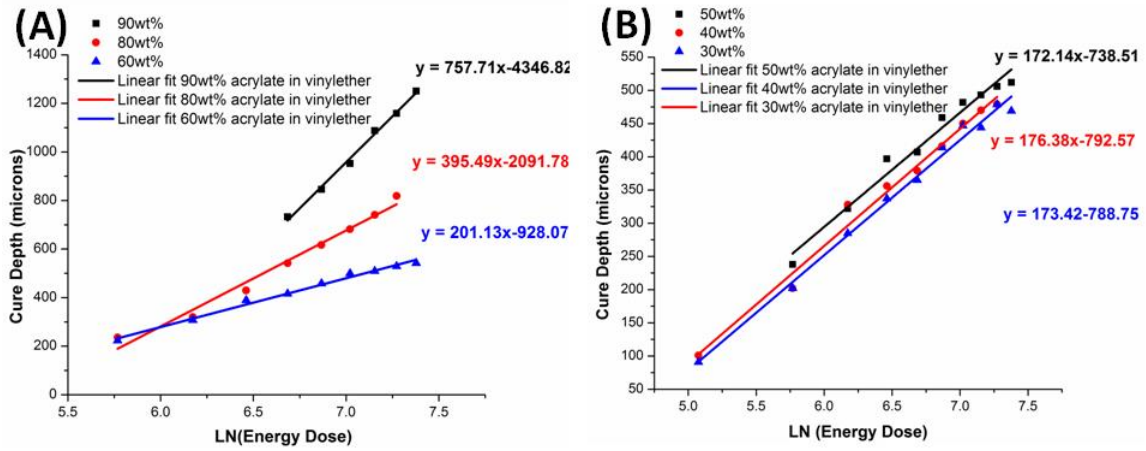

Figure 6.6.1.1. Graphs showing the plot of cure depth in microns versus natural logarithm of energy dose for (A) 90 wt.%, 80 wt.%, 60 wt.% and (B) 50 wt.%, 40 wt.%, 30 wt.% concentrations of acrylate in a vinylether material system.

Figure 6.6.1.2 is a graph showing the variation of D_p and E_c values for various concentrations of acrylate in a vinylether ceramic composite system.

From the figure 6.6.1.2, the E_c and D_p values increase with increasing weight concentration of acrylate in the vinylether material system. This implies that a vinylether material system requires lower energy dose for cure initiation compared to an acrylate material system. However, the depth of cure from a vinylether material system is generally lower than the depth of cure from an acrylate material system. The graph in figure 6.6.1.2. shows two points of intersection of the E_c and D_p curves. An approximate region between the intersection where D_p is greater than E_c was chosen for further investigation of the curing characteristics and decomposition properties.

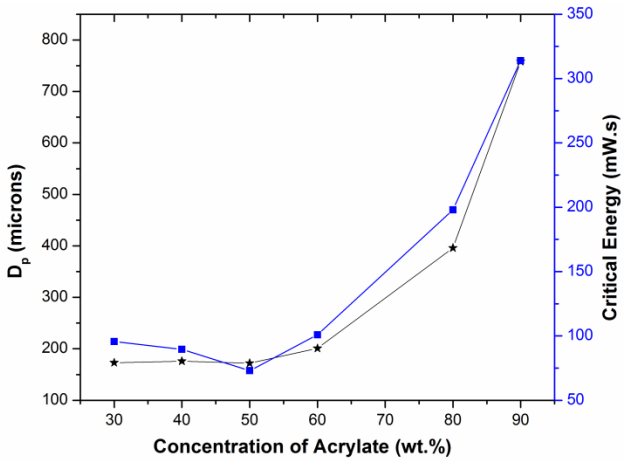

Figure 6.6.1.2. Graph showing the plots of Dp and Ec versus wt.% concentration of acrylate in a vinylether material system.

The composition of the resulting vinylether-acrylate material system designed for LAMP is shown in table 6.6.1.3.

Table 6.6.1.3. Table showing the composition of vinylether-acrylate ceramic loaded material system designed for LAMP.

Material	Composition
Fused Silica	55g to 100g of vinylether: acrylate (50:50)
Dispersant	8.24g to 100g of fused silica
Irgacure 250	2g to 100g vinylether monomer
Curcumin	3g to 100g Irgacure 250
Irgacure 184	6g to 100g HDDA

6.6.2. Degree of Conversion Measurements

Figure 6.6.2.1 shows the FTIR spectrum of a vinylether-acrylate ceramic loaded material system. The peak observed around 1700 cm^{-1} is from the carbonyl group present in the HDDA monomer and also present in the curcumin photosensitizer. The peaks centered at 1650 cm^{-1}, 1450 cm^{-1} come from the carbon-carbon double bonds present in both the HDDA and vinylether monomers. The peak around 1200 cm^{-1} is from the ester group present in the vinylether and HDDA monomers.

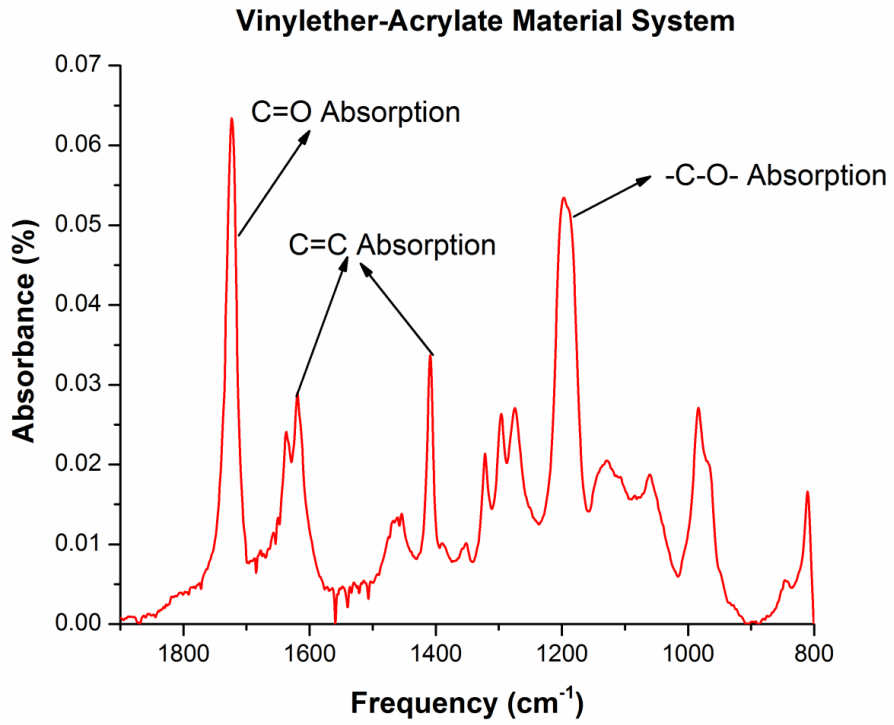

Figure 6.6.2.1. FTIR spectrum of a vinylether-acrylate ceramic composite system.

The degree of conversion was measured using the same formula as that used to measure the degree of conversion in the epoxy-acrylate material system, with the peak centered around 1700 cm^{-1} serving as the reference peak. Figure 6.6.2.2 shows the degree of conversion measurements for a vinylether –acrylate ceramic loaded material system.

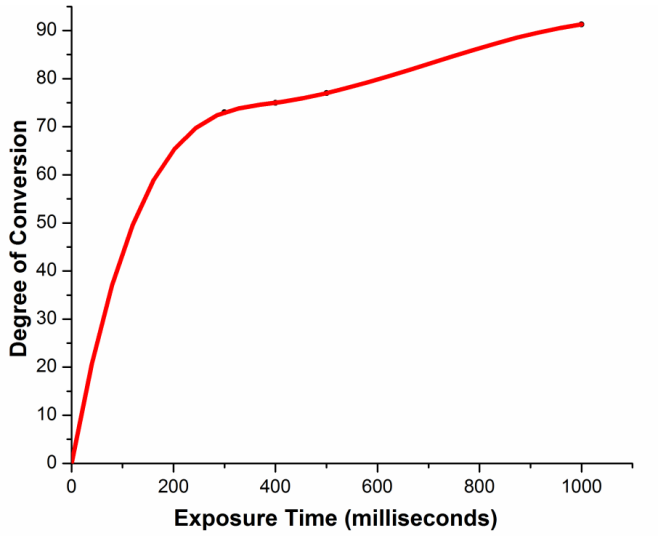

Figure 6.6.2.2. Graph showing the degree of conversion versus exposure time for a vinylether-acrylate ceramic composite material system.

From the degree of conversion data, a vinylether-acrylate ceramic-loaded material system is seen to demonstrate the combined characteristics of a vinylether and an acrylate material system. These characteristics, relating to degree of conversion, includes very fast polymerization kinetics under UV exposure for short period of time, and a high degree of conversion at UV exposure for large time periods.

6.6.3 Thermo gravimetric analysis

Thermal decomposition information for the vinylether material system was obtained from a TA instrument's Q500 TGA apparatus equipped with nitrogen and air flow gases. The temperature ramp rate was chosen as 5 $^{o}Cmin^{-1}$, and the thermal decomposition was carried out under nitrogen gas. From the TGA data in figure 6.6.3.1, the vinylether-acrylate material system has two overlapping peak decomposition periods.

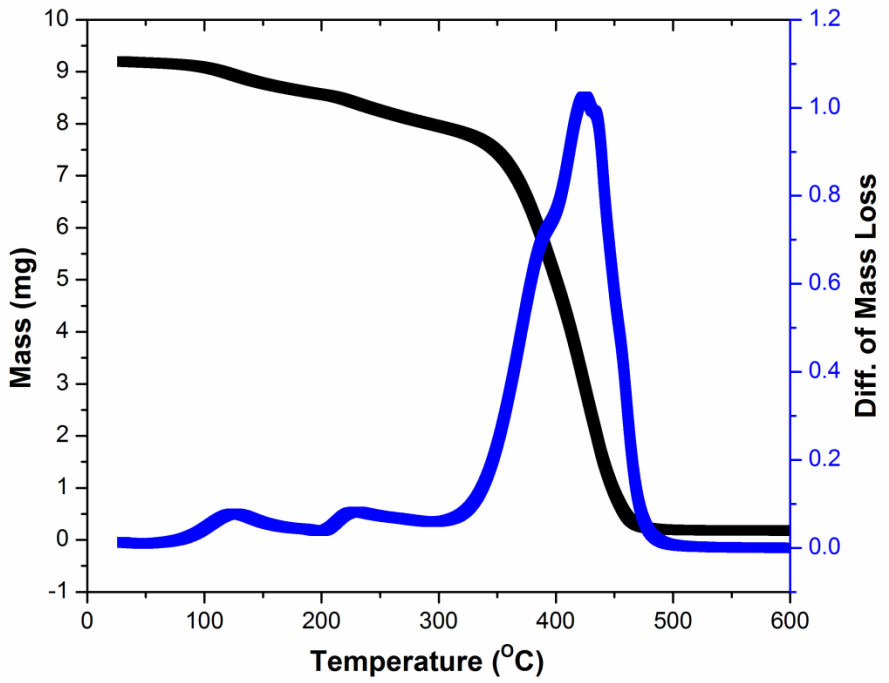

Figure 6.6.3.1. Graph showing the mass-loss versus temperature rise for photopolymerized vinylether-acrylate material system.

The two peaks at ~390 and 420 ºC correspond to the peak decomposition temperatures for the vinylether and acrylate monomers respectively.

6.6.4. Dynamic mechanical thermal analysis

Dynamic mechanical thermal analysis (DMA) was obtained using a TA instruments Q200 dynamic mechanical thermal analyser. Tensile measurements were done using a multiple frequency sweep at a frequency of 1Hz and a strain of 0.1%. Temperature for all measurements was varied from -60 ºC to 100 ºC.

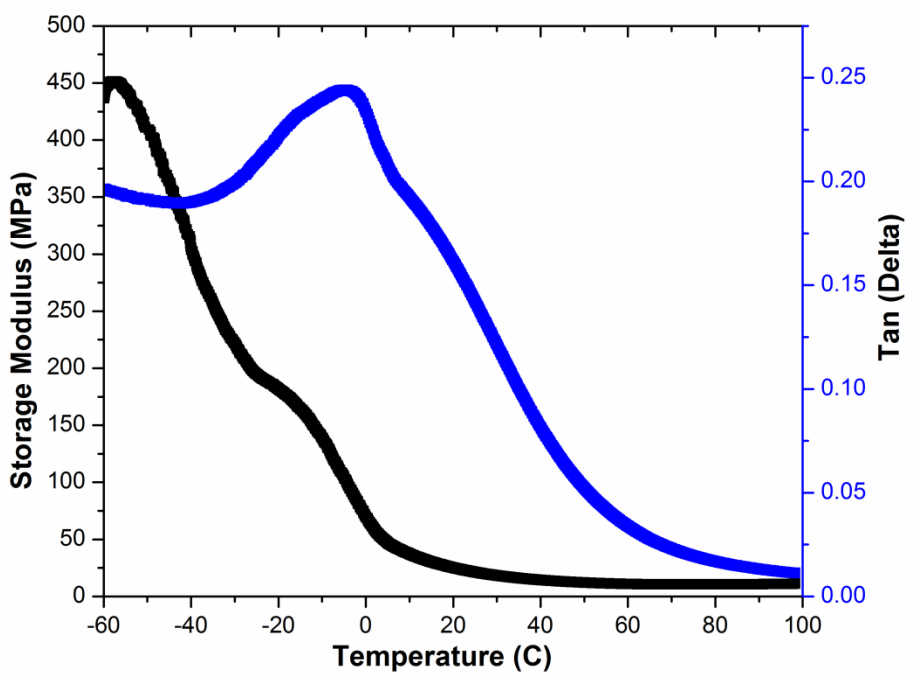

Figure 6.6.4 Dynamic mechanical analysis on a photopolymerized vinylether-acrylate ceramic composite system.

Figure 6.6.4 shows a plot of storage modulus and tan (δ) as a function of temperature. The storage modulus for the vinylether-acrylate ceramic loaded sample can be seen to decrease from 4.5 $\times 10^9$ Pa at the glassy state to ~0.5 $\times$ 10^6 Pa at the rubbery state. There appears to be two convoluted peaks in the plot of tan (δ) as a function of temperature, indicating 2 glass transition temperatures. The Broadness of the peak further indicates structural heterogeneity of the photopolymerized vinylether-acrylate ceramic composite system.

6.7. Conclusion

In this chapter we have successfully designed new material systems based on acrylate, epoxy and vinylether monomers for the LAMP technology. The material systems

designed included epoxy-acrylate, vinylether, and vinylether-acrylate material systems. We further investigated the curing characteristics of the material systems using FTIR and cure depth measuring techniques. The curing kinetics from the FTIR data indicates that the cationic photopolymerization mechanism from a pure vinylether material system gives a faster cure than that from an acrylate material system. The epoxy material system gives the lowest cure rate of all the three pure material systems investigated. The curing characteristics measured from cure depth analysis however show that a pure acrylate material system gives a greater cure depth and print through than the vinylether or epoxy material system. The thermal decomposition characteristics of the novel material systems were investigated using a TGA. From the TGA data obtained, an epoxy material appears to decompose at a lower temperature compared to the vinylether and acrylate material system. Analysis of the DMA date indicates that hybrid composite material systems with either a vinylether-acrylate, epoxy-acrylate show more structural heterogeneity that can be explored during the LAMP fabrication process.

CHAPTER 7

CONCLUSIONS AND FUTURE WORK

This chapter presents a summary of the research presented in this dissertation and recommendations for future work.

7.1 Summary of the Dissertation

The objective of this dissertation was to design new photomodifiable material systems for use in advanced state-of-the art manufacturing processe utilizing laser and broadband UV light sources. New soft material systems that were investigated and shown to have potential for texturing of silicon and silicon oxide ceramic materials are block copolymers, vinylether, epoxy and acrylate systems.

Chapter 3 discussed in detail the motivation for designing resists based on diblock copolymers. The limitations of conventional photoresists as well as the advantages of switching to a block copolymer type resist were discussed. The concept of block copolymer laser interference ablation was introduced as a viable means for the generation of features with ~30nm resolution. The technique was applied to two commercially available diblock copolymers: PS-b-P4VP and PS-b-PEO. The block copolymers showed feature density improvement over commercially available resists as well as potential for functionalization with other metallic materials.

Chapter 4 discussed a direct application of laser interference ablation of PS-b-P4VP block copolymer for the generation of functional metallic and ceramic features on various substrates including Si and SiO_2. Metal-loading of the laser patterned block copolymers was used to generate hierarchical arrays of metallic gold and platinum as

well as ceramic iron oxide and palladium oxide nanoarrays. Feature density of as-fabricated features was demonstrated together with experimental validation of theoretical results.

In Chapter 5, patterning of silicon oxide and silicon substrates was demonstrated as one of the application of the patterned arrays of metallic and ceramic features. The fabrication of blue-light emitting (photoluminescent) silicon oxide nanowires was demonstrated with discussion on the apparent ferromagnetic effect of the resulting features. Super hydrophobic effect of the as-generated nanoscale features on silicon oxide was also demonstrated. Fabricated features on silicon were also presented with potential applications discussed.

Chapter 6 presented data on the design of novel material systems that incorporate radical and cationic photopolymerization mechanisms, designed for LAMP fabrication. The material systems investigated were acrylate-epoxy, vinylether and vinylether-acrylate ceramic loaded material systems. The degree of cure and cure depth of the material systems as a function of exposure time to UV light was also investigated. The thermal degradation properties as well as mechanical properties of these novel material systems were also investigated using TGA and DMA equipments.

7.2. Contributions

The contributions of this dissertation can be divided into the following categories:

1. Development of a new technique combining laser interference ablation and block copolymers, as photoresist, for the generation of functional hierarchical nanofeatures on silicon and silicon oxide substrate

2. Design, characterization and development of new negative tone photoresist for visible light UV (450nm) curing of silica micro-composite for use in LAMP fabrication.

7.2.1. Hierarchical Silicon and Silicon Oxide Nanoarchitectures

This dissertation has demonstrated a novel inexpensive approach to the fabrication of functional hierarchical features on silicon and silicon oxide substrates with potential use in a broad range of applications. This technique can potentially be used for the fabrication of hierarchical arrays of various kinds of metals and ceramic materials on different substrates. The various combinations of nano-scaled metallic and ceramic materials that can be fabricated, and the different types of supporting substrates that these nanofeatures can be fabricated upon is enormous. The only limitation while using this novel technique is the researcher's imagination.

Continuous miniaturization of electronic devices as well as future advancements in electronics and computing devices is hinged upon the ability to inexpensively and accurately fabricate nanoscale features with resolutions in the ten's of nanometers range. Current lithography techniques including photoresists and photomasks technologies have been pushed to the maximum achievable limits in terms of resolution capability. The inexpensive fabrication of features, with nanoscale resolution, for future electronic, computing, and other devices can only be achieved via the development of new photoresists, and the design of new lithographic techniques. Block copolymers are viable candidates as new photoresists for low-cost fabrication of nanosclaed features on substrates. By combining block copolymer phase separation with laser interference

ablation, a novel lithographic technique is formed that eliminates the need for photomasks, and can generate nano-resolvable, hierarchical, features of various geometrical designs on various substrates.

In chapter 3, PS-b-P4VP and PS-b-PEO block copolymers were demonstrated to be potential materials for use as positive tone photoresist in the laser interference ablation technique. The laser interference patterning of both block copolymers was used to generate hierarchical line, square, hexagonal and triangular arrays on silicon and silicon oxide substrates. The primary chemical ordering of the hierarchical features was found to correlate with the inter-domain spacing of the block copolymer, while the secondary physical ordering was found to correlate with the periodicity of the laser interference ablation set-up.

In chapter 4, the primary chemical ordering from the laser-ablated PS-b-P4VP block copolymer was transformed into a physical ordering via the metal-loading of the P4VP component. Successful fabrication of sub-50nm hierarchical arrays of gold, platinum, palladium and iron was demonstrated.

In chapter 5, we demonstrated the use of the metal and ceramic arrays formed, in the fabrication of dense nanoforest array of silicon oxide nanowires. This represented the first reported fabrication of vertically aligned, high-aspect-ratio silicon oxide features without the use of catalysts and high temperature vapor-liquid-solid processes. We further demonstrated the ability to fabricate patterned arrays of silicon oxide nanowires by using the hierarchical features of iron-oxide as nanomasks. Sub-micron features were fabricated on Si<100> substrates using block copolymers as uni-functional positive tone

photoresists, while inverted hierarchical multi-scaled features were fabricated on silicon using PS-b-P4VP block copolymers as a di-functional photoresist with dual-scale ordering resolution. Potential application of the features fabricated in optoelectronic and electromechanical devices was investigated and established.

7.2.2. Negative Tone Photoresist: Vinylether-epoxy, Vinylether-acylate, and Vinylether Silica Composite for LAMP Fabrication

Photopolymerization is a technique that can be used for additive manufacturing involving the layer-by-layer fabrication of complex structures and geometries using photomodifiable resins and composites. Large area maskless photopolymerization (LAMP) is a form of additive manufacturing that uses the layer-by-layer manufacturing approach to fabricate complex geometries. In the LAMP fabrication process, a digital micromirror device (DMD) rasters light patterns from a bitmap file onto a photomodifiable composite resin for layer-by-layer fabrication of 3D geometries with resolution down to ~17μm. A problem limiting industrial large-scale application of LAMP is the absence of a data-base of material systems that can be referred to for the fabrication of different geometries, and for various applications. Currently, although several photomodifiable monomeric and oligomeric material systems exist, this systesm have yet to be modified and designed for use in stereolithography in general and LAMP in particular.

In chapter 6, material systems based on vinylether-acrylate, vinylether and epoxy-acrylate ceramic composite for use in the LAMP fabrication of complex geometries were developed. The material systems were analyzed using a TGA to

demonstrate their ease of removal during a binder burnout procedure. The vinylether, epoxy-acrylate and vinylether acrylate systems all showed good decomposition curves with the epoxy material system having the least temperature at maximum mass loss. Vinylether photopolymerized material system also showed maximum mass loss at 390 ºC while the acrylate material system showed a maximum mass loss at 400 ºC. Composite systems showed two main peaks for the mass-loss for either component of the resin. The cure characteristics of these novel material systems including cure depth measurements and degree of conversion measurements were performed to show how the material systems behave during photoexposure. All material systems designed showed good photocuring characteristics with the vinylether material system curing faster at low exposure doses and the acrylate material system curing deeper at higher exposure doses. The acrylate material system displayed deeper cure than vinylether and other hubrid systems investigated in this dissertation.

The dynamic mechanical analysis of the material systems showed indicates that the hybrid material systems designed have a broad glass transition temperature indicating structural heterogeneity of the photopolymerized resins.

7.3 Future Work

Several recommendations for future work can be made based on the research work that has been demonstrated in this thesis.

First, the hybrid approach combining laser interference ablation and block copolymer phase separation can potentially be used for the fabrication of patterned, vertically-oriented, arrays of silicon and germanium nanowires on silicon <111>

substrates for solar applications. There have been numerous reports on the fabrication of single crystal silicon and germanium nanowires using the vapor-liquid-solid (VLS) technique.[80-143] Gold is the main catalyst used to promote growth of the silicon and germanium nanowires under high temperature, in the presence of precursor gases [170-172]. The ability to fabricate patterned array of gold nanoparticles onto various substrate independent of substrate morphology, chemical composition or orientation can be utilized to generate hierarchical, patterned arrays of silicon, germanium, silicon oxide and other types of nanowires.

Scheme 7.3.1 shows line, square patterned array of single crystal, multicrystalline, or amorphous nanowires that can potentially be fabricated using the novel technique demonstrated in this thesis.

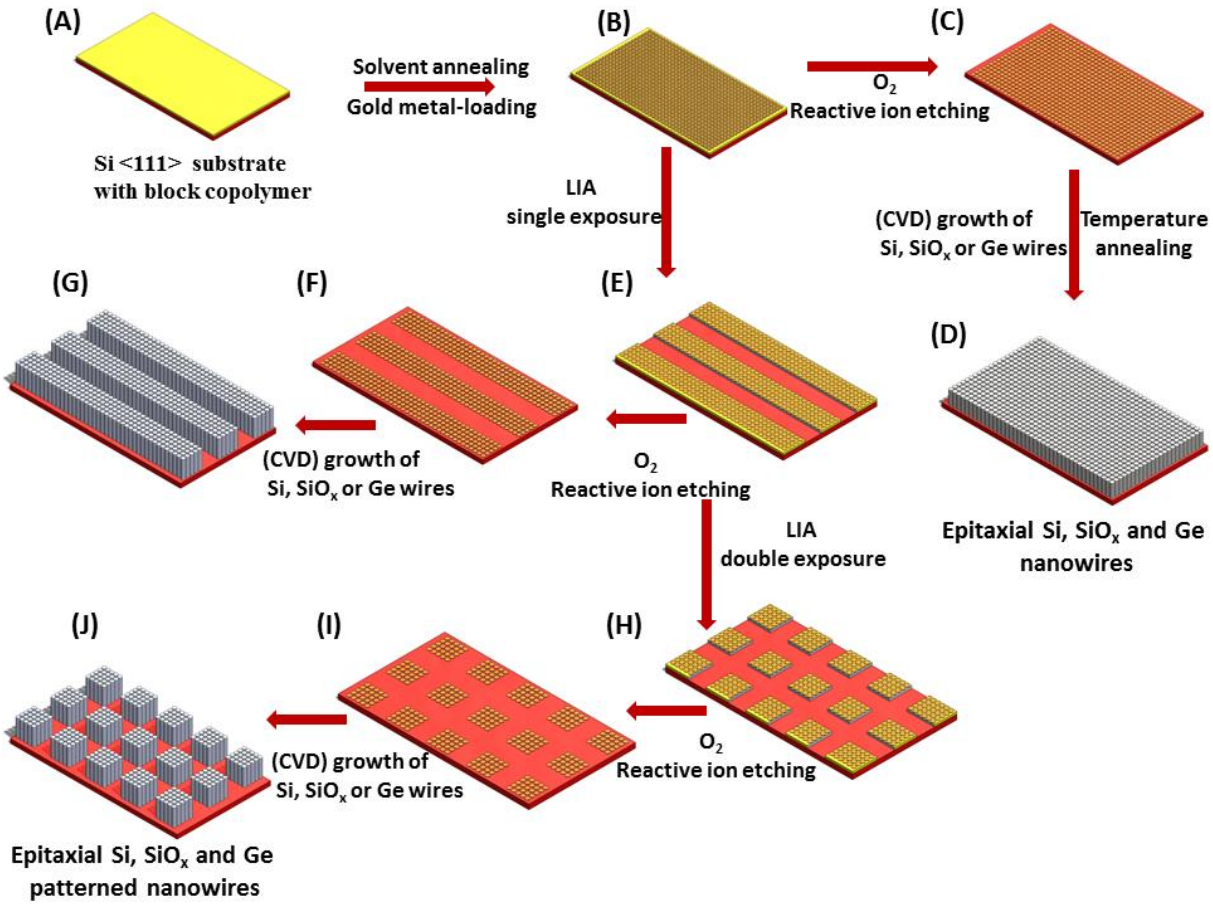

Scheme 7.3.1 Figure showing the steps to be followed for the chemical vapor deposition (CVD) epitaxial growth of patterned arrays of (D) hexagonal packed (G) linear (J) and square Si, SiOx, Ge nanowires.

Several issues will have to be addressed for the effective use of the as-generated nano gold features in the VLS catalyzed growth of nanowires. One of the issues that need to be addressed will be presence of organic impurities on the substrate. Most reports on the catalyzed growth of nanowires require conformal contact between the catalyst material and the single crystal substrate [143]. In the hybrid process demonstrated in this thesis, there is the possibility for some P4VP materials to exist between the gold

nanofeatures and the substrate. Non-conformal contact between the catalyst and the substrate may result in non-aligned catalyzed growth of the nanowires. The polymer layer may also contaminate the VLS chamber. A possible solution will be to increase the duration of annealing and pre-chamber bake time of the patterned gold nanofeatures. By increasing the annealing time, all the organic contaminants on the substrate can be removed, and crystallinity can be induced in the patterned array of gold nanoparticles.

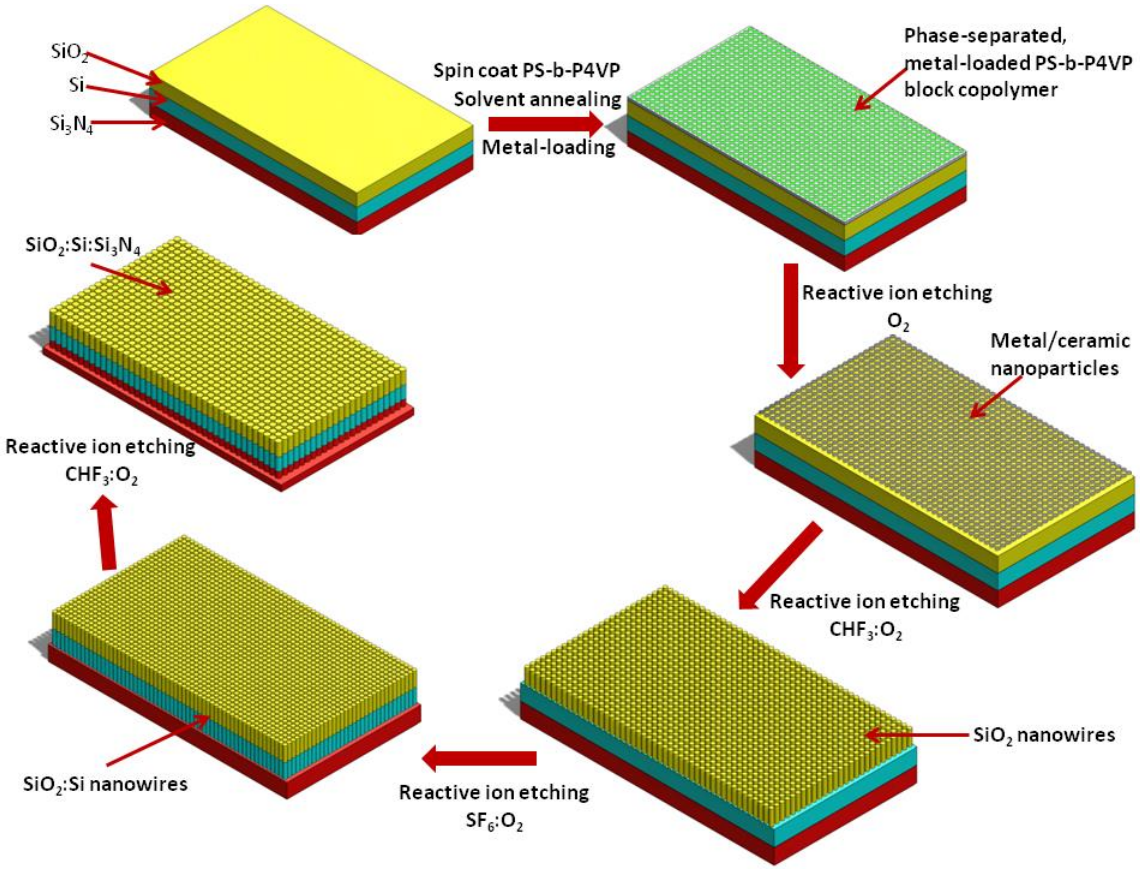

Scheme 7.3.2. Proposed scheme for the fabrication of vertically oriented, multilayered nanowires using LIA and block copolymer phase separation.

Second, the hybrid technique can also be used for the fabrication of 3D vertically oriented, heterogeneous nanowires as shown in scheme 7.3.2. The heterogeneous nanowires can be fabricated from multilayered substrates. The multilayered substrates can be fabricated in-house using chemical vapor deposition (CVD), atomic layer deposition (ALD) techniques or bought custom-made from silicon wafers inc. etc. The multilayered substrate is then exposed to similar processing parameters demonstrated in this thesis to obtain hierarchical metallic or ceramic nanofeatures. The substrate can then be etched in plasma RIE using different gas combinations to obtain vertical heterogeneous nanowires. Heterogeneous nanowires with SiO_2-Si-Si_3N_4, InP-SiO_2-Si, GaAs-SiO_2-Si, SiO_2-Si-GaAs segments can be fabricated using the hierarchical features as masks as shown in scheme 7.3.2.

Third, although this dissertation demonstrates the potential use of vinylether, vinylether-acrylate, vinylether-epoxy, epoxy-acrylate material systems for LAMP fabrication, there are several other resins that can serve as good candidates for use in the LAMP fabrication process. Examples of materials that can be investigated for use in LAMP fabrication are urethane acrylates, polyester acrylates, epoxyacrylates, polymethacrylates etc.

These material systems can be optimized specifically for LAMP or designed for application in other additive manufacturing technologies. Designing new material systems based on these material systems will further extend the data-base of materials for stereolithography and other additive manufacturing technologies.

Furthermore, the material systems that have demonstrated potential use for LAMP manufacturing have to be used for the eventual fabrication of real geometries. For the fabrication of ceramic loaded composite parts experiments have to be done to determine the real-time curing characteristics of these novel material systems during the fabrication of multilayer parts. In addition to this, the impact of photoabsorbers on the curing characteristics of these novel material systems have to investigated for better control of both the cure depth and scattering in ceramic loaded material systems.

After the fabrication of 3D geometries using epoxy-acrylate, vinylether, vinylether-acrylate ceramic loaded material systems, the geometries have to be subjected to a binder burnout step. During these step, the impact of varying temperature ramp rates on the geometry of the final ceramic part have to be investigated. The surface property, porosity, compliance as well as degree of crystallinity of the final ceramic part is determined in part by the curing characteristics of the polymeric sacrificial material, thus the need to engineer these novel material systems is of utmost importance to LAMP and potentially other additive manufacturing techniques.

APPENDIX A

SUPPLEMENTARY DATA FOR CHAPTER 3

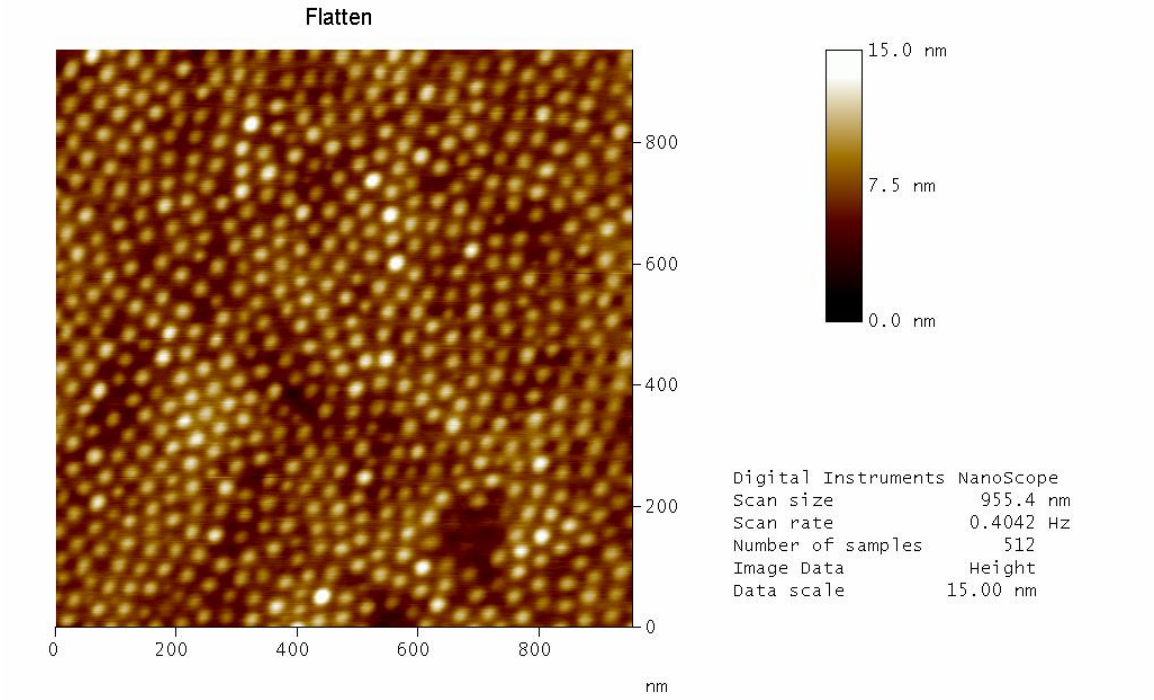

Figure A.1. AFM phase contrast image for a phase-separated PS-b-P4VP block copolymer.

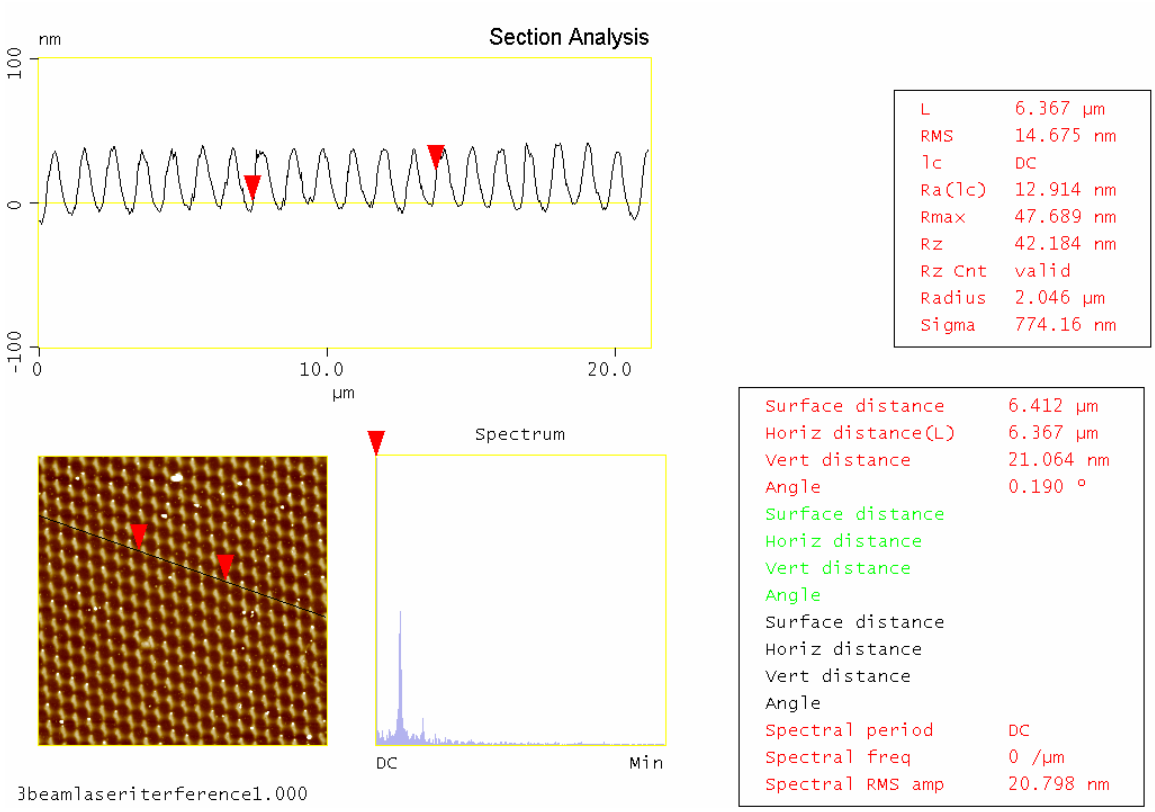

Figure A.2 AFM topographical contrast image of laser patterned PS-b-P4VP block copolymer showing the cross-sectional analysis.

APPENDIX B

SUPPLEMENTARY DATA FOR CHAPTER 4

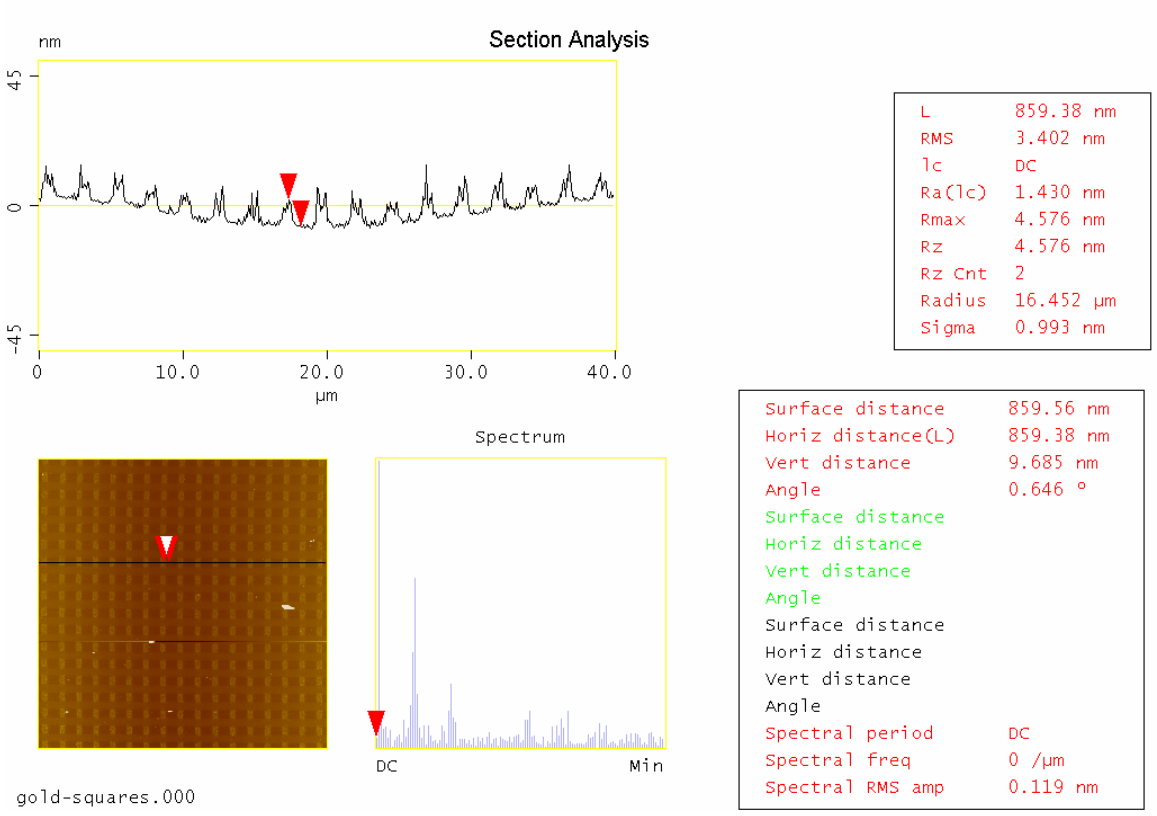

Figure B.1 AFM topographical contrast image of gold square arrays on a silicon substrate showing the cross-sectional analysis.

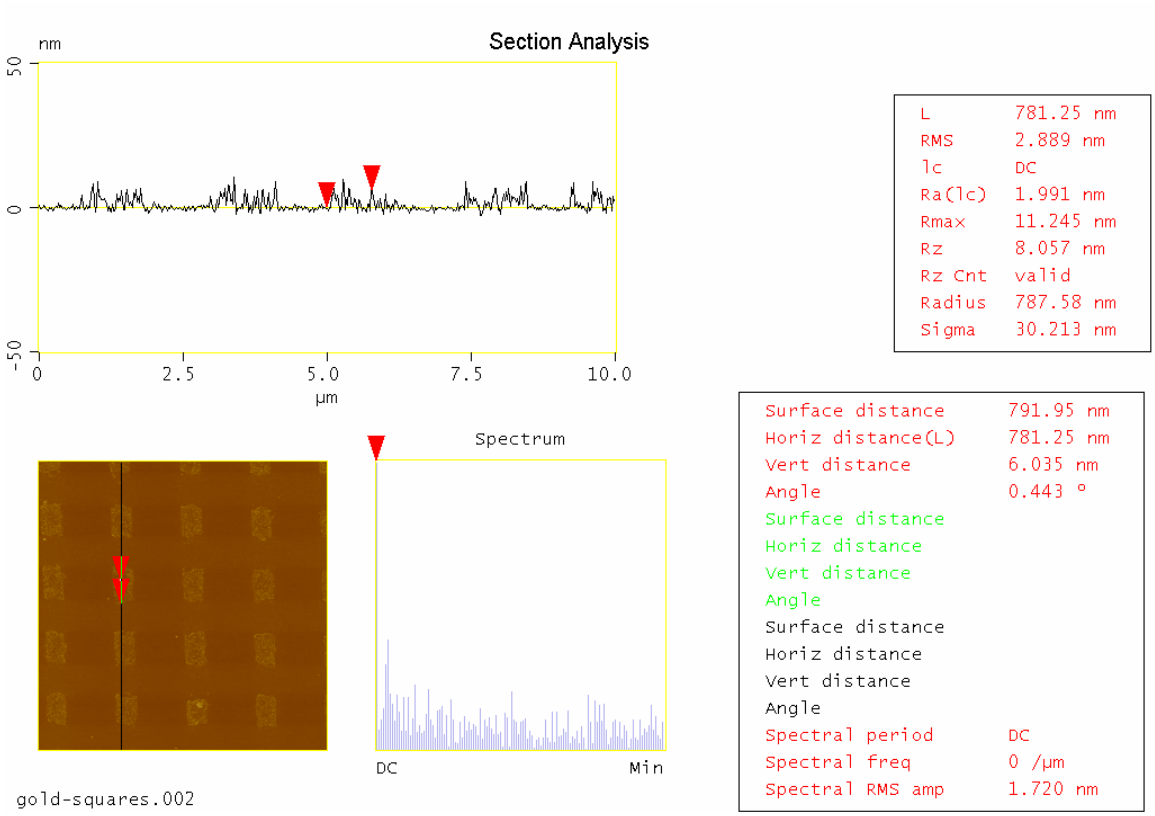

Figure B.2 A high resolution AFM topographical contrast image of gold square arrays on a silicon substrate showing the cross sectional analysis.

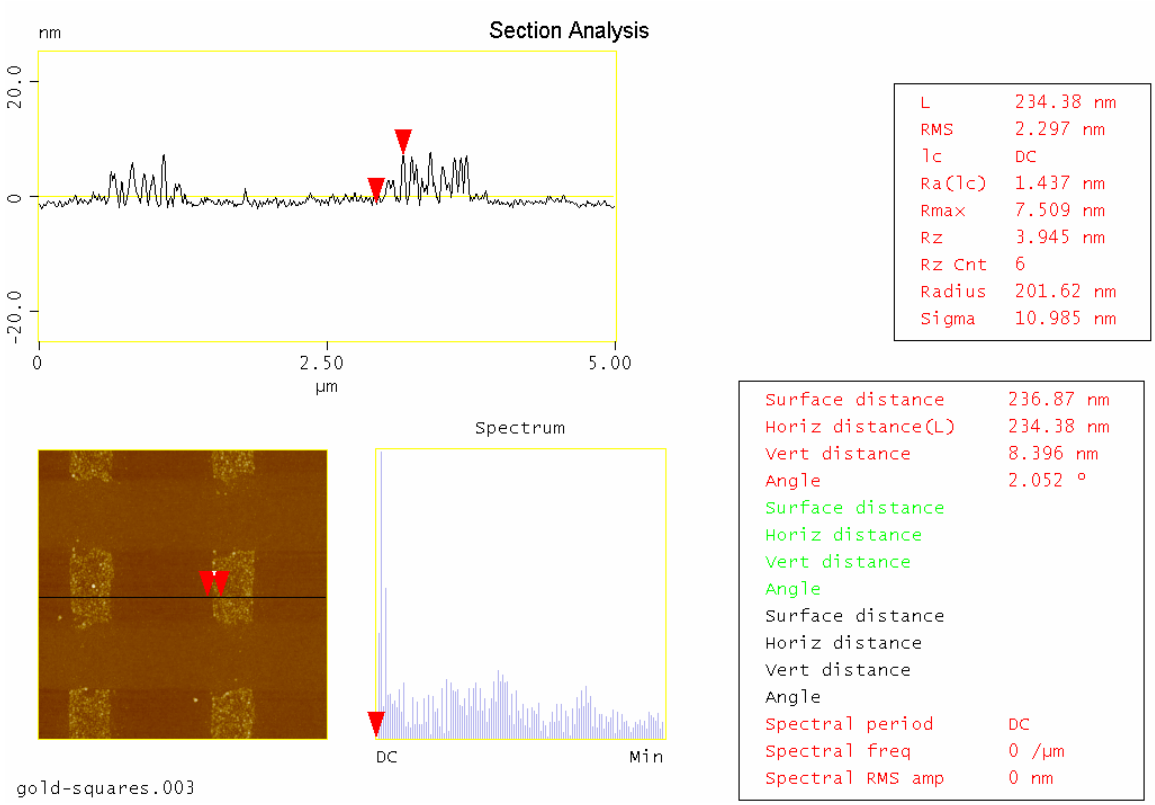

Figure B.3 A high resolution AFM topographical contrast image of gold square arrays on a silicon substrate showing the cross sectional analysis.

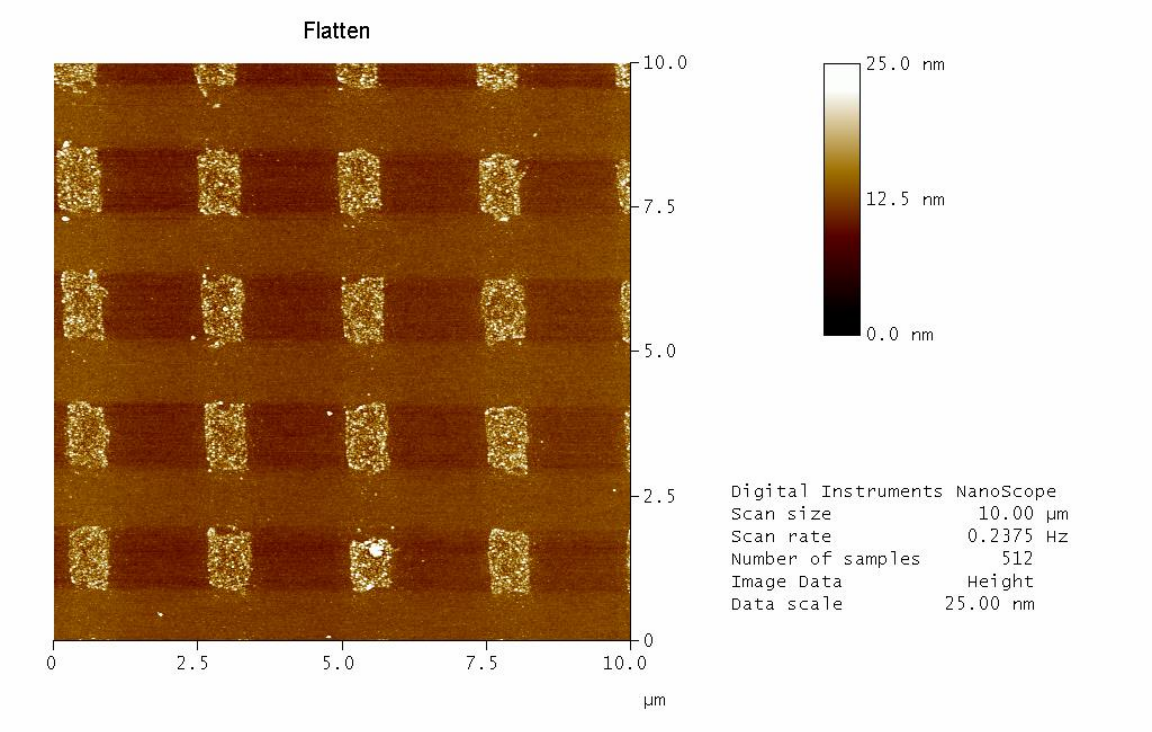

Figure B.4. A high resolution AFM topographical contrast image of gold square arrays on a silicon substrate.

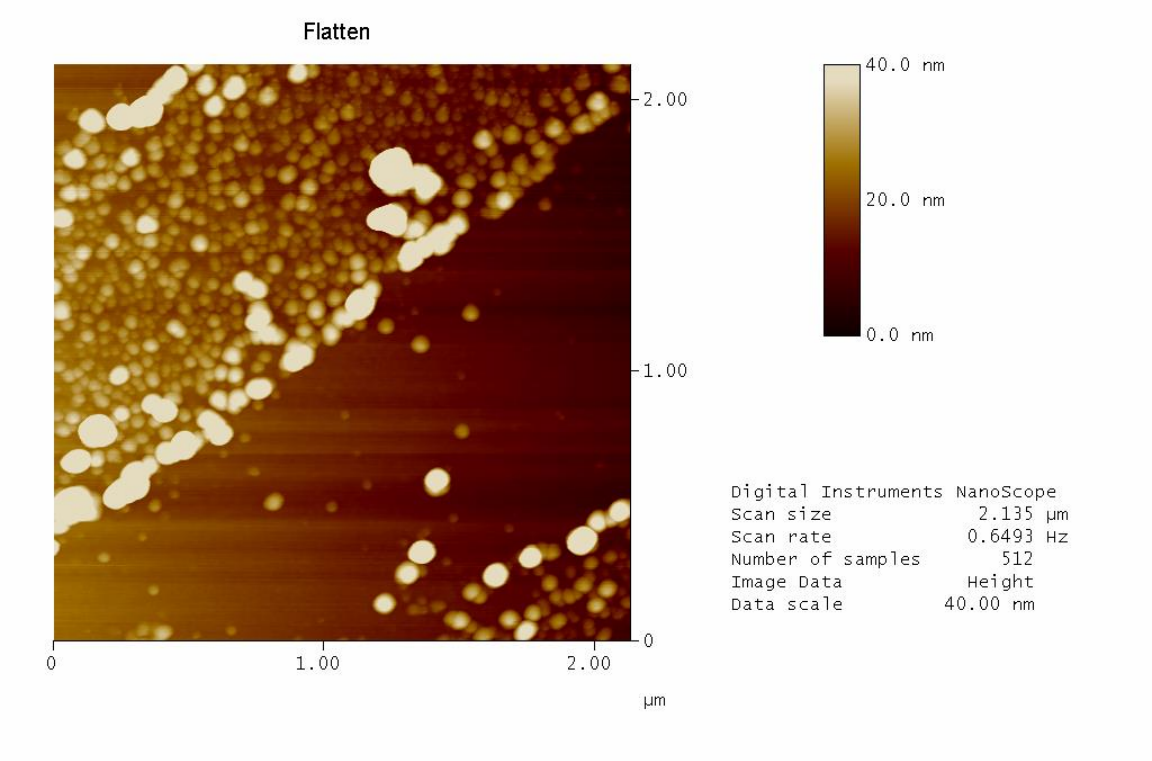

Figure B.5 A high resolution AFM topographical contrast image of gold line arrays on a silicon substrate.

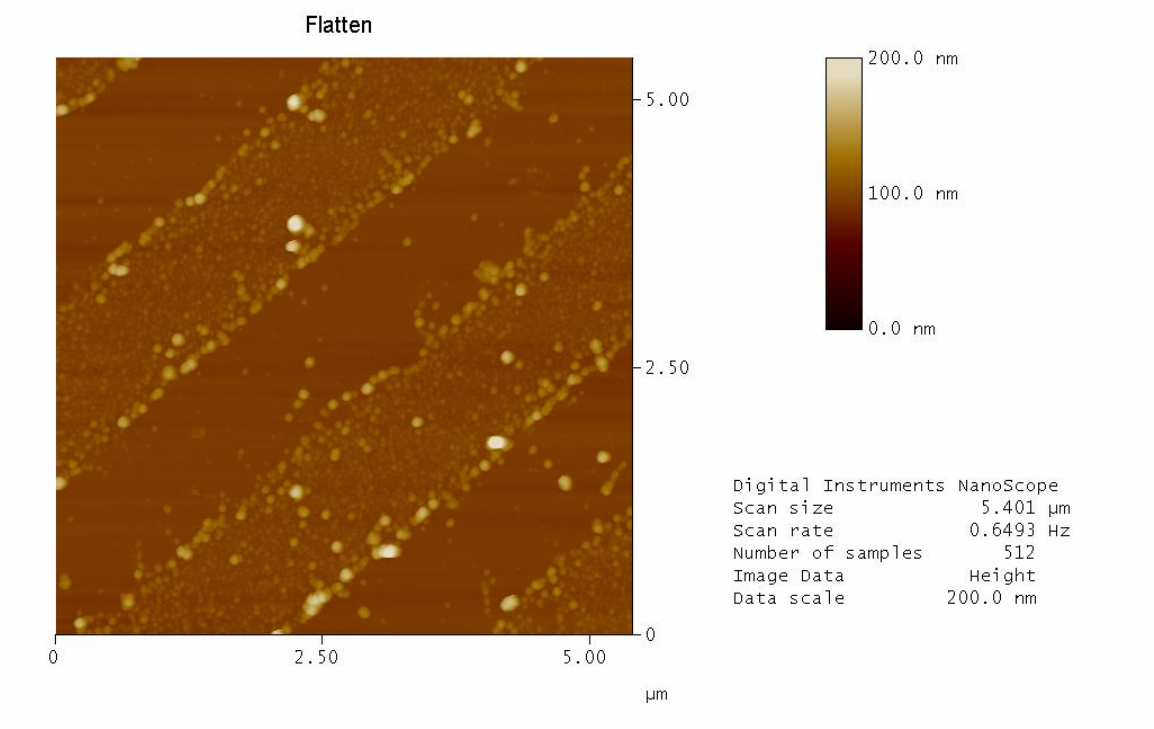

Figure B.6 A high resolution AFM topographical contrast image of gold line arrays on a silicon substrate, showing individual nanodots.

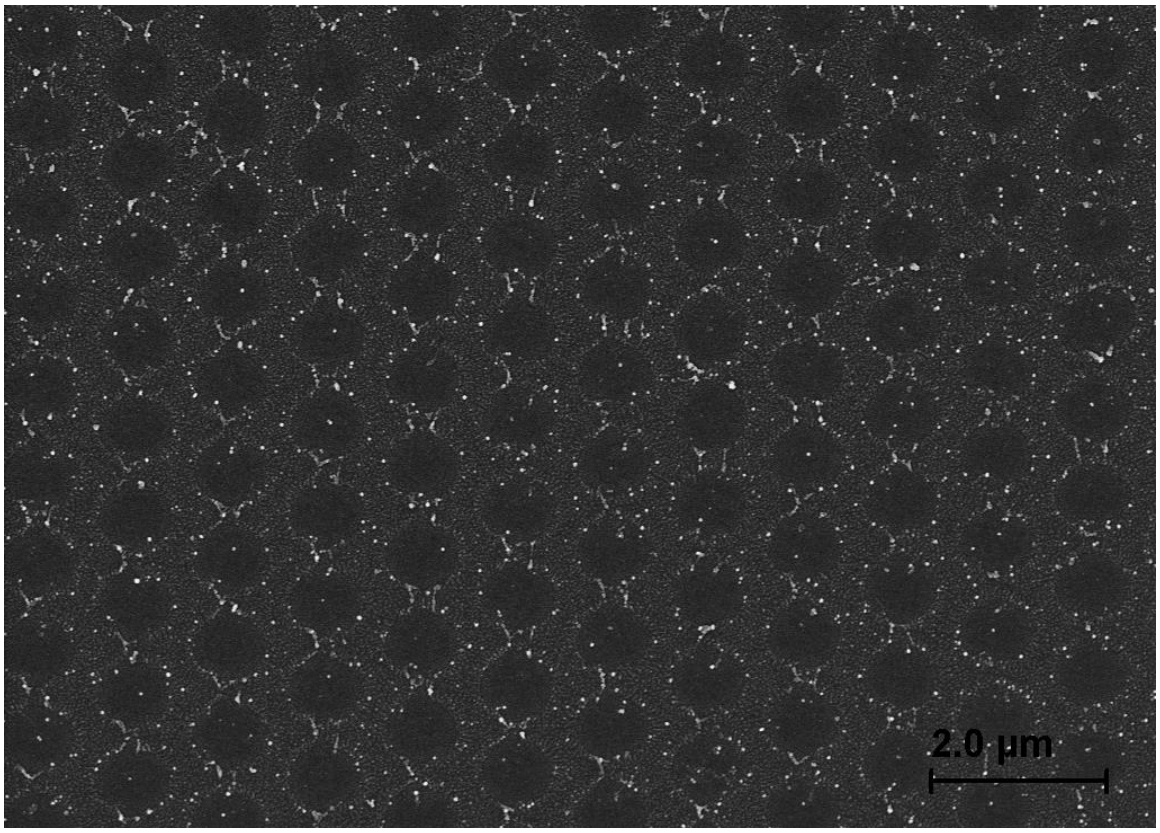

Figure B.7 SEM image of hexagonal patterned arrays of gold nanoparticles on a silicon oxide substrate.

APPENDIX C

SUPPLEMENTARY DATA FOR CHAPTER 5

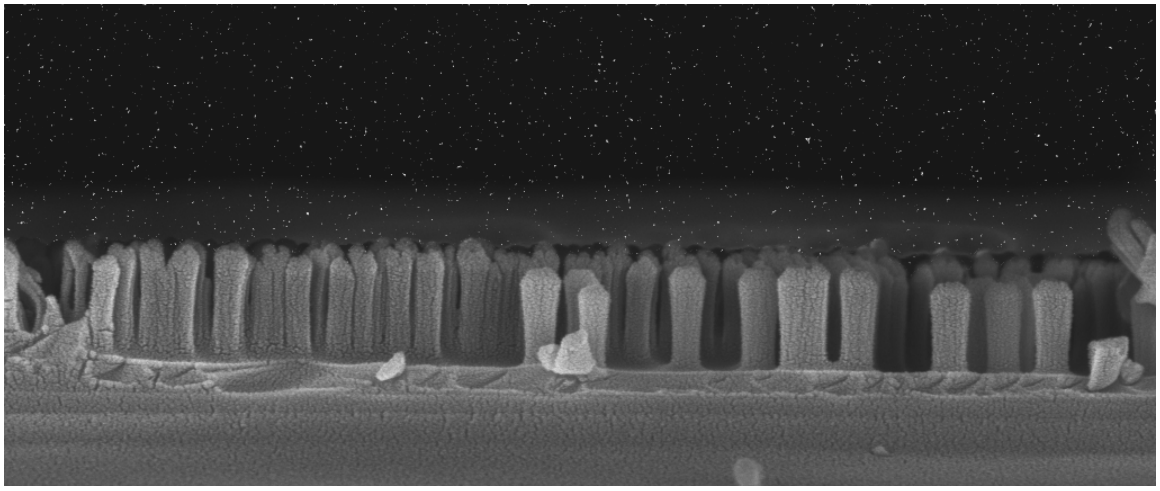

Figure C.1. SEM cross sectional image of silicon oxide nanowire arrays.

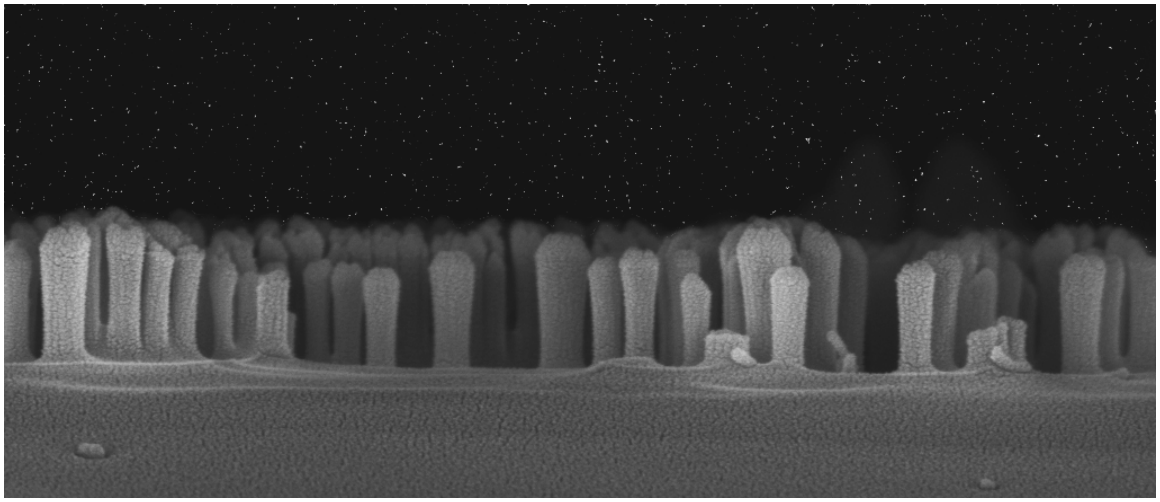

Figure C.2. SEM cross sectional image of silicon oxide nanowire arrays.

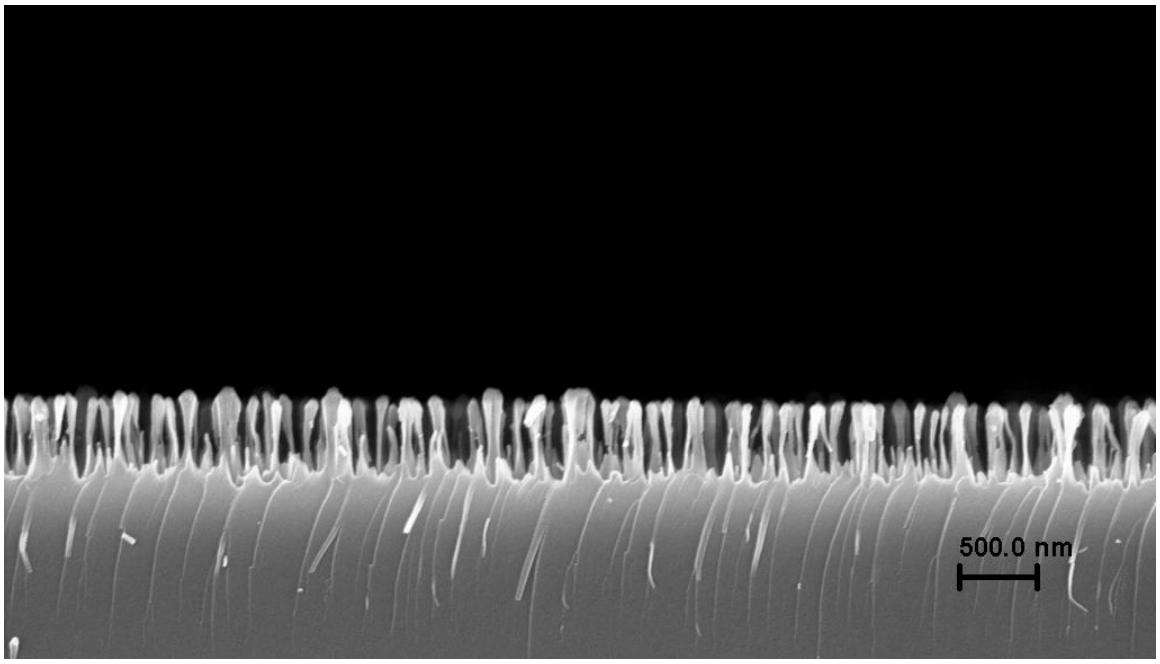

Figure C.3. SEM cross-sectional image of silicon oxide nanowire arrays.

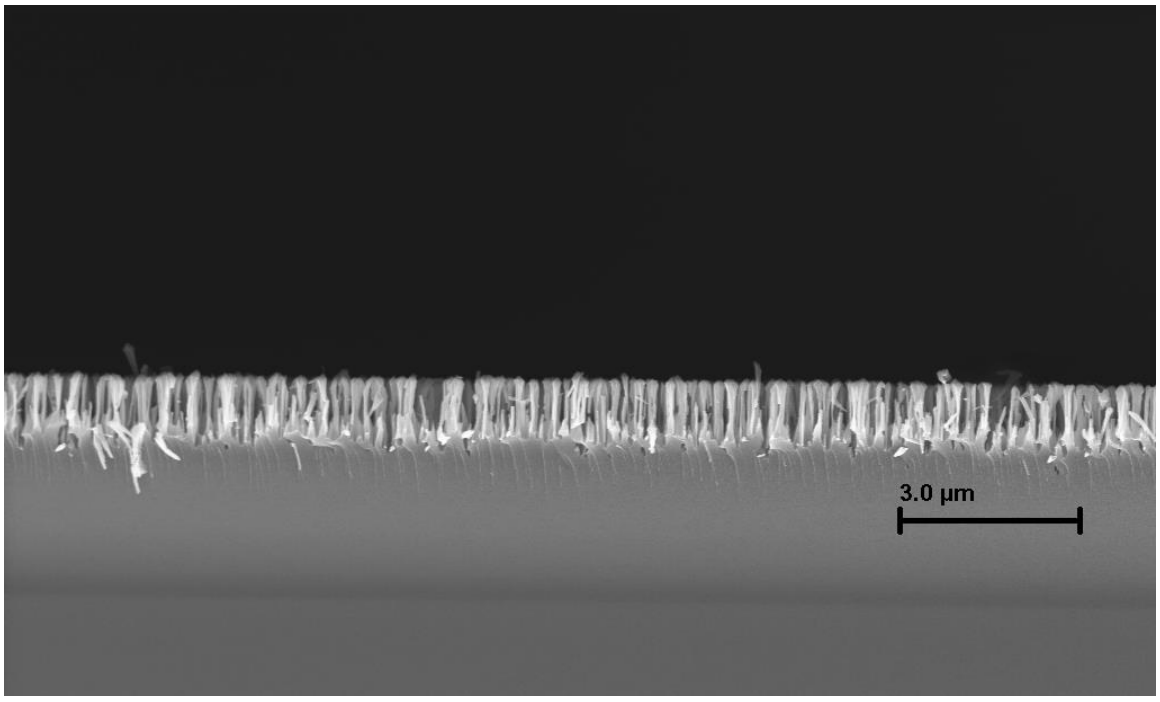

Figure C.4. Large area SEM cross-sectional image of high aspect ratio silicon oxide nanowire arrays.

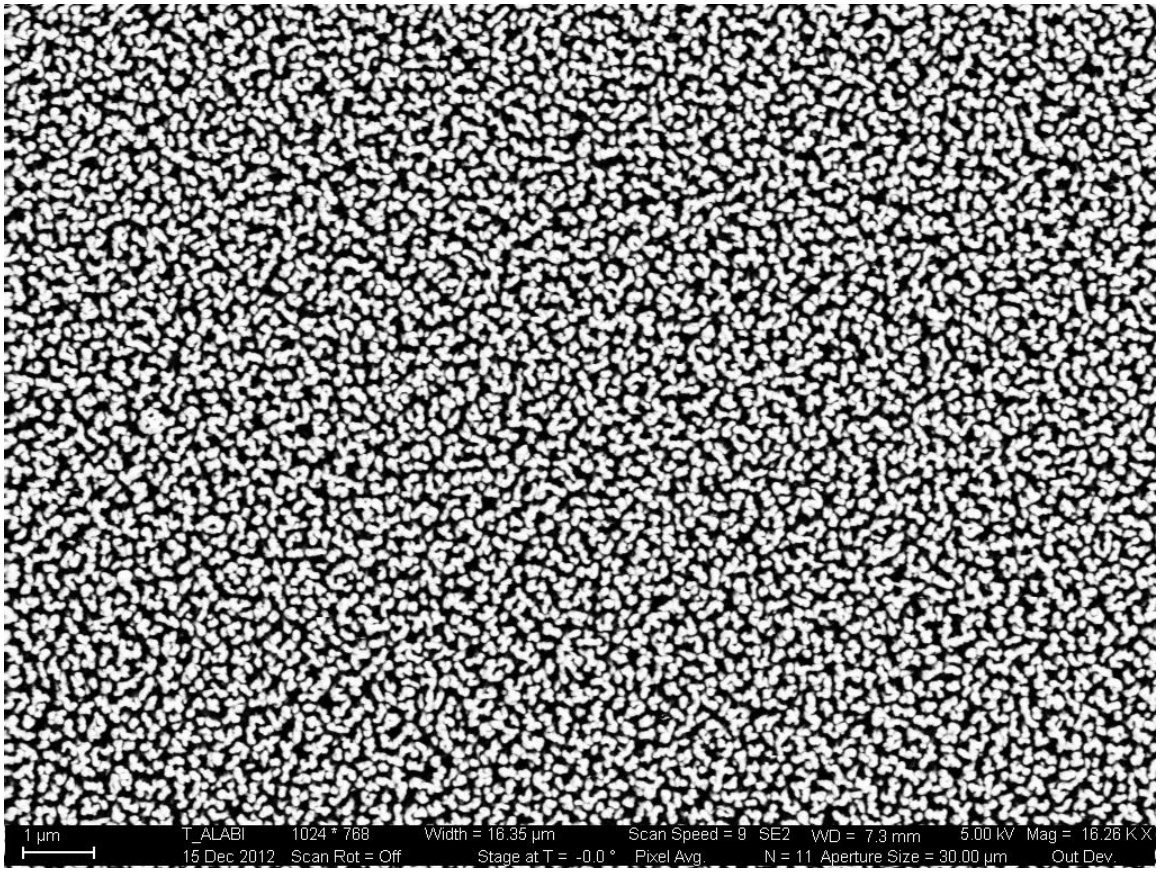

Figure C.5. Top-down view of silicon oxide nanowire arrays.

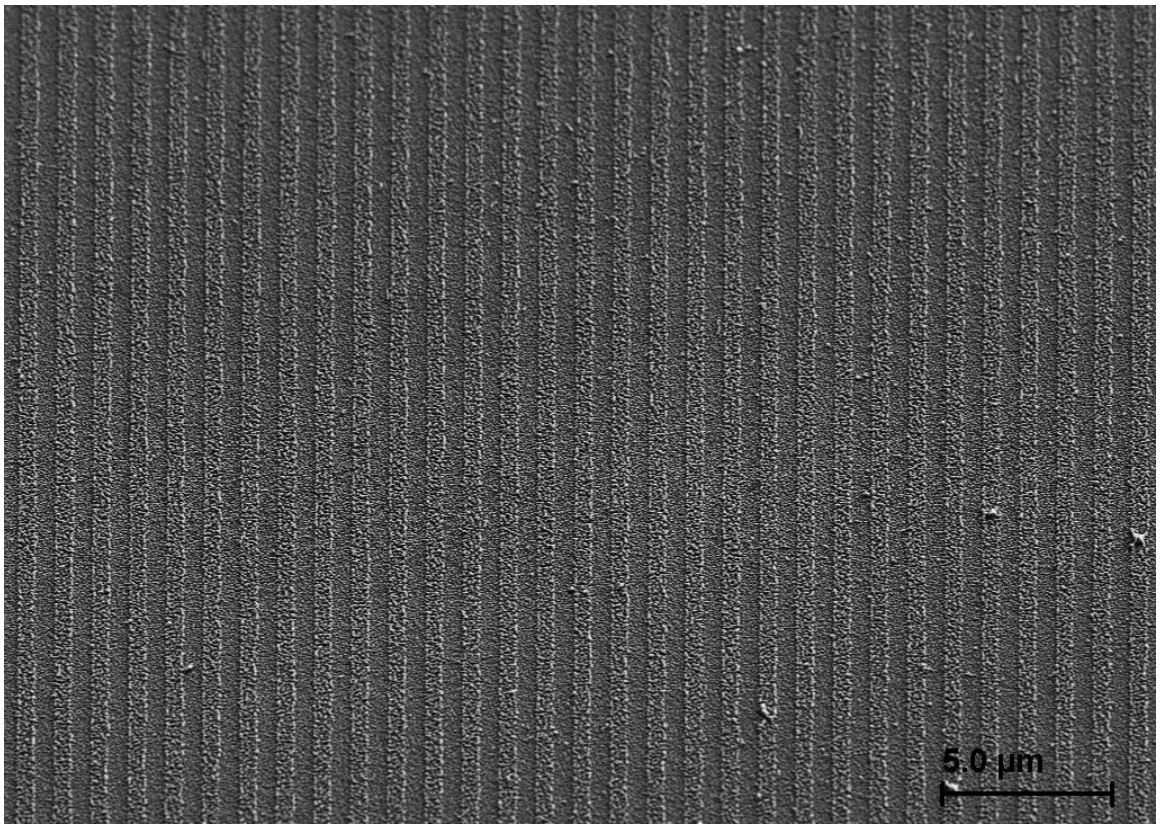

Figure C.6. Top-down view of patterned line arrays of silicon oxide nanowires.

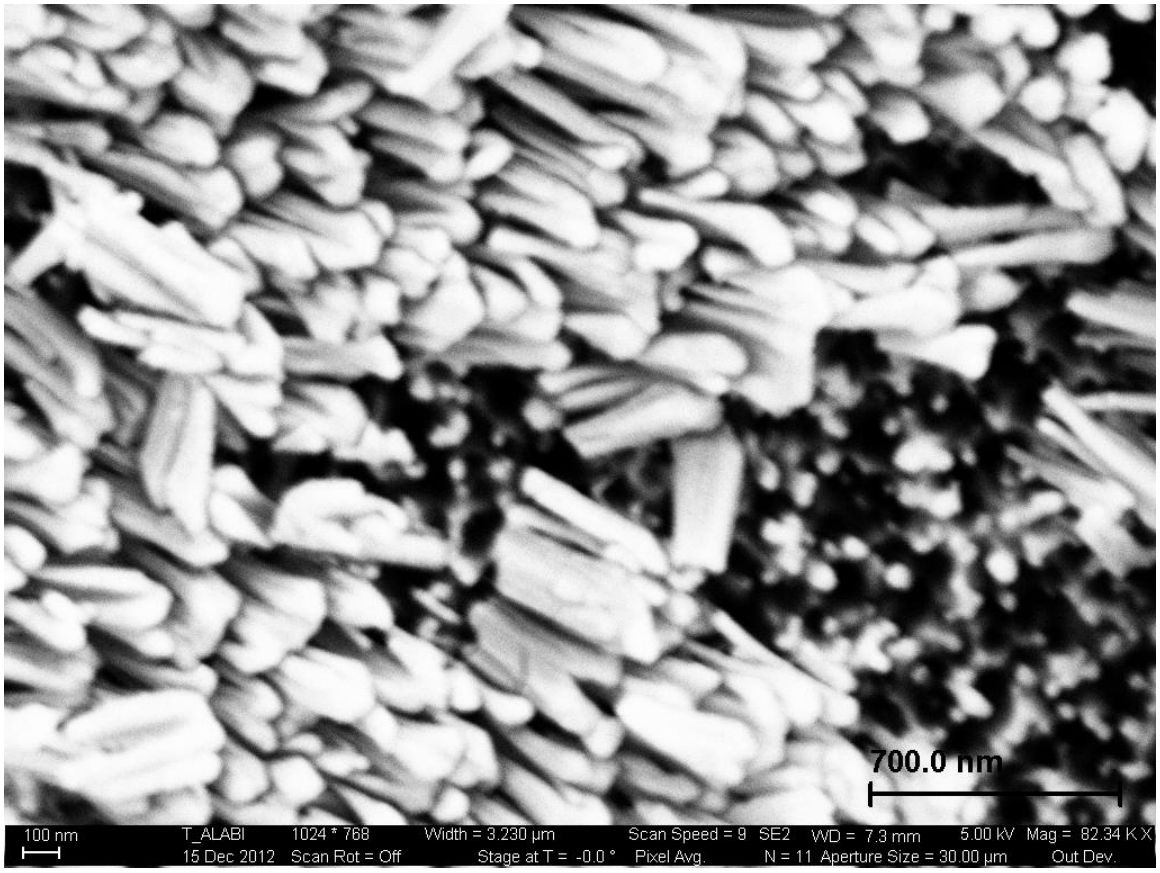

Figure C.7. SEM top-down view of silicon oxide nanowires lying down.

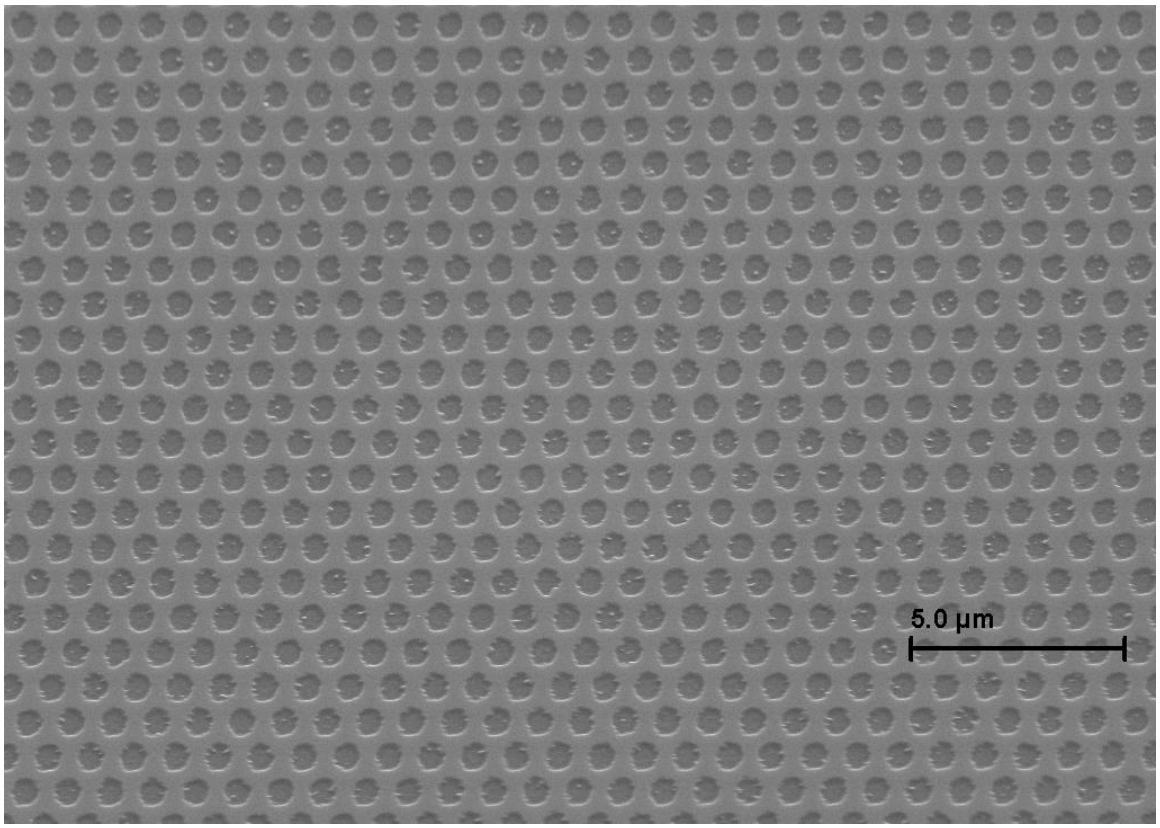

Figure C.8 SEM image of hexagonal-packed arrays of holes formed on silicon <100>.

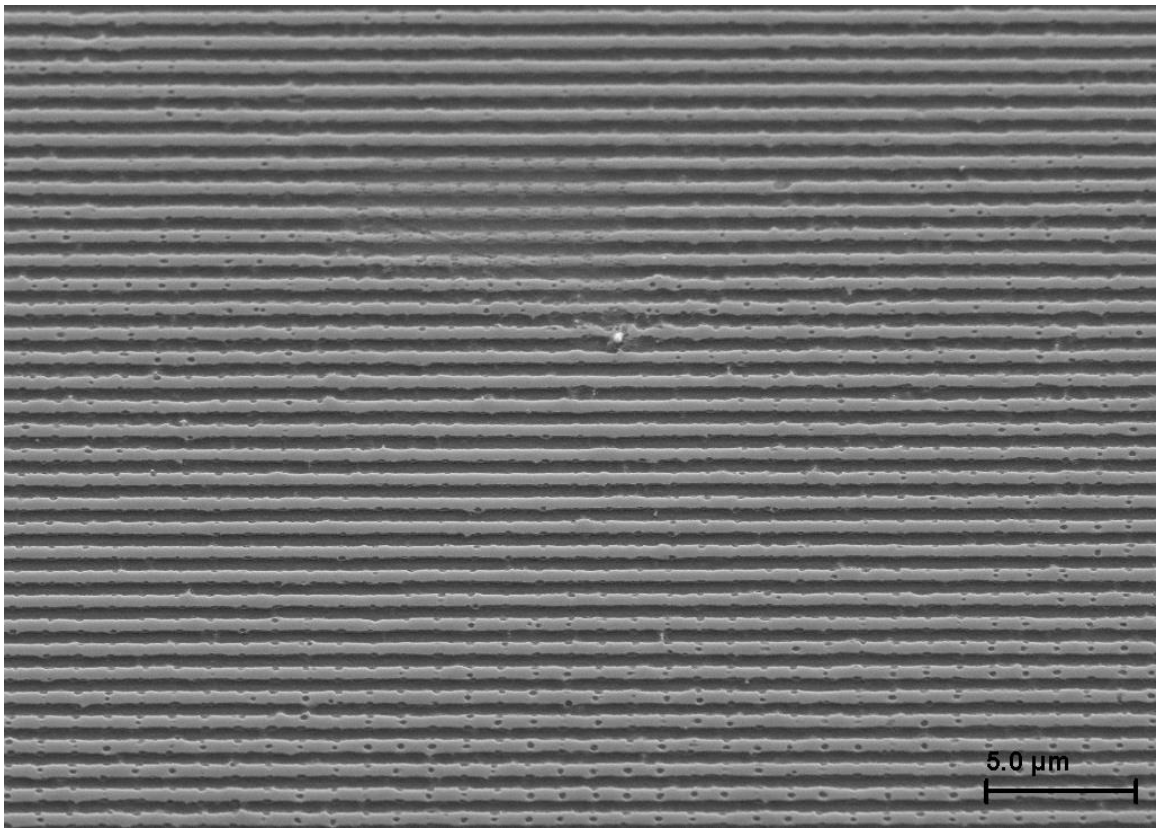

Figure C.9 SEM image of line arrays formed on silicon <100>.

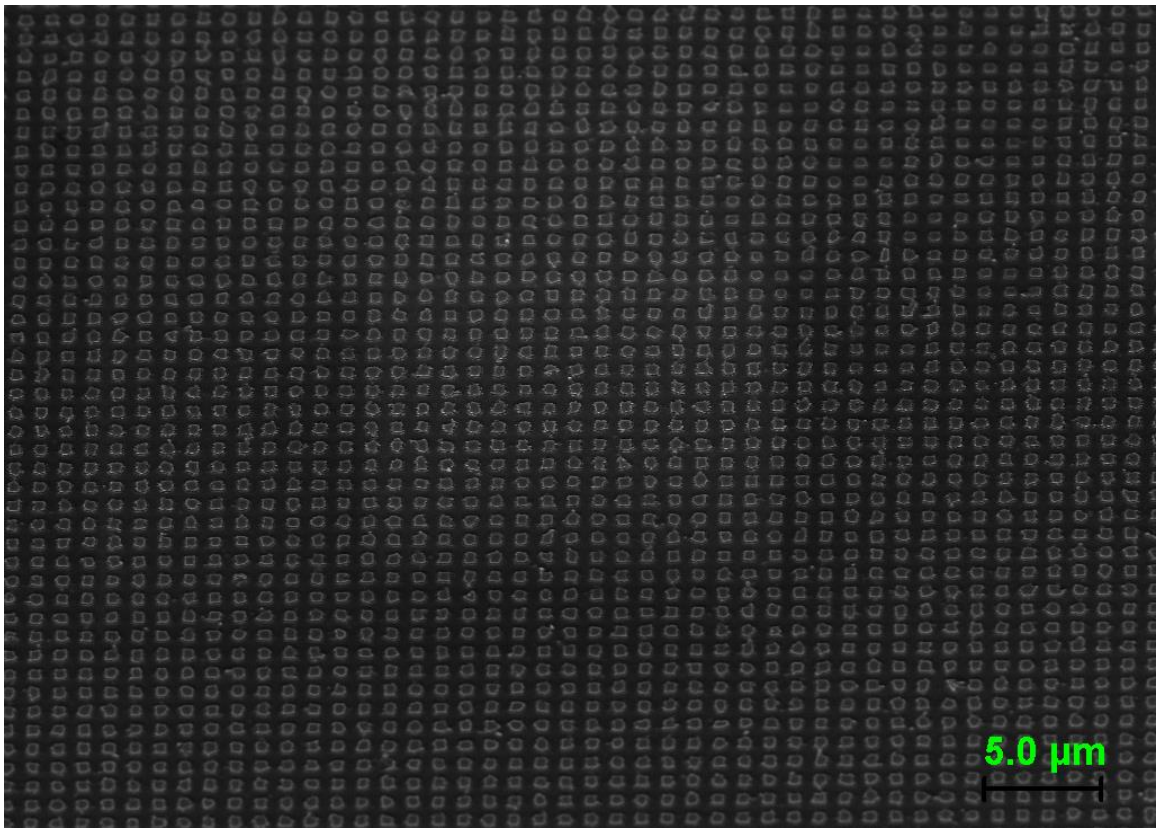

Figure C.10 SEM image of square arrays formed on silicon <100>.

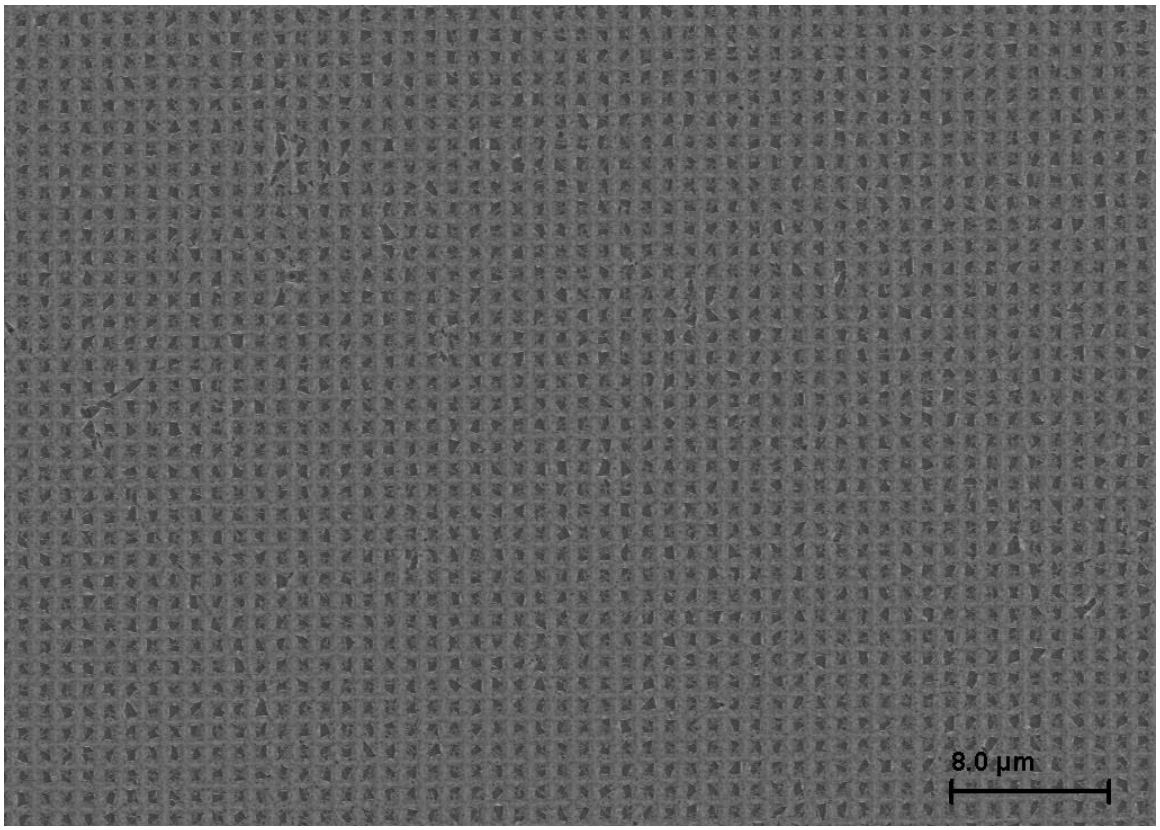

Figure C.11 Large area SEM image of square hole arrays formed from gold catalyzed reactive ion etching of silicon <100>.

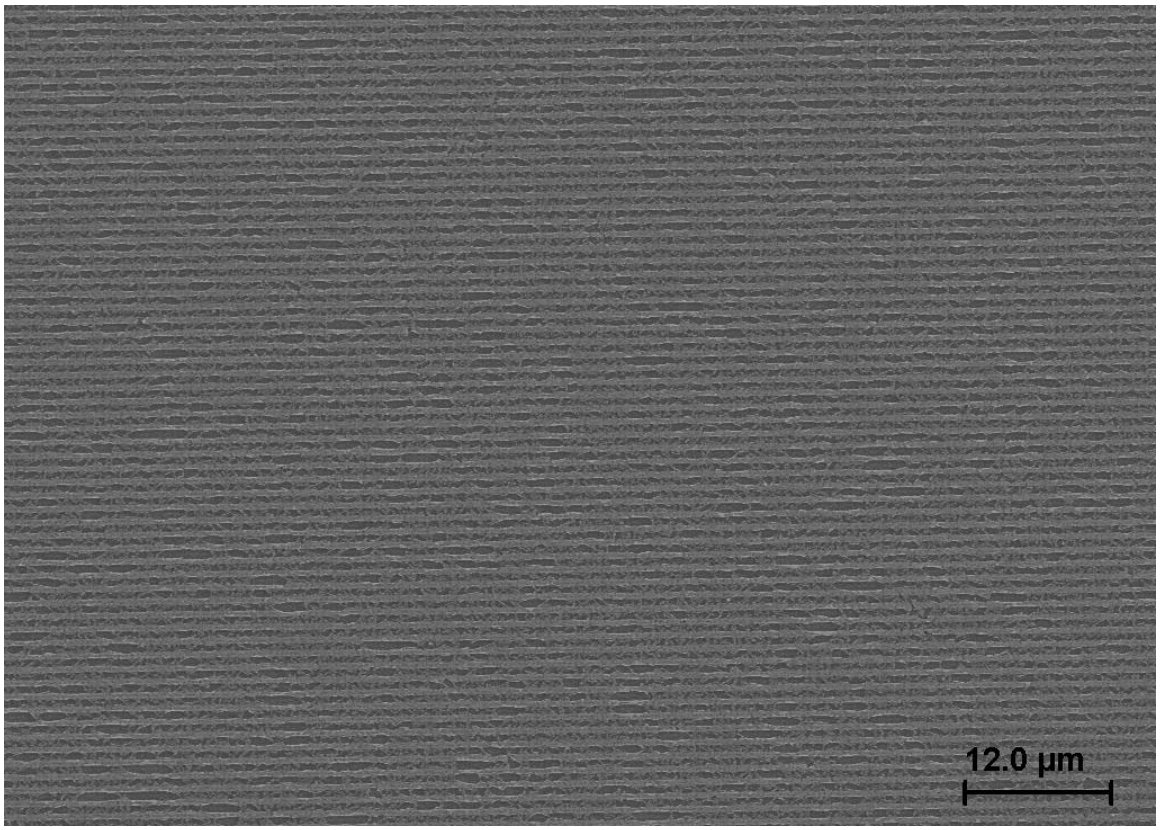

Figure C.12 Large area SEM image of line troughs formed from gold catalyzed reactive ion etching of silicon <100>.

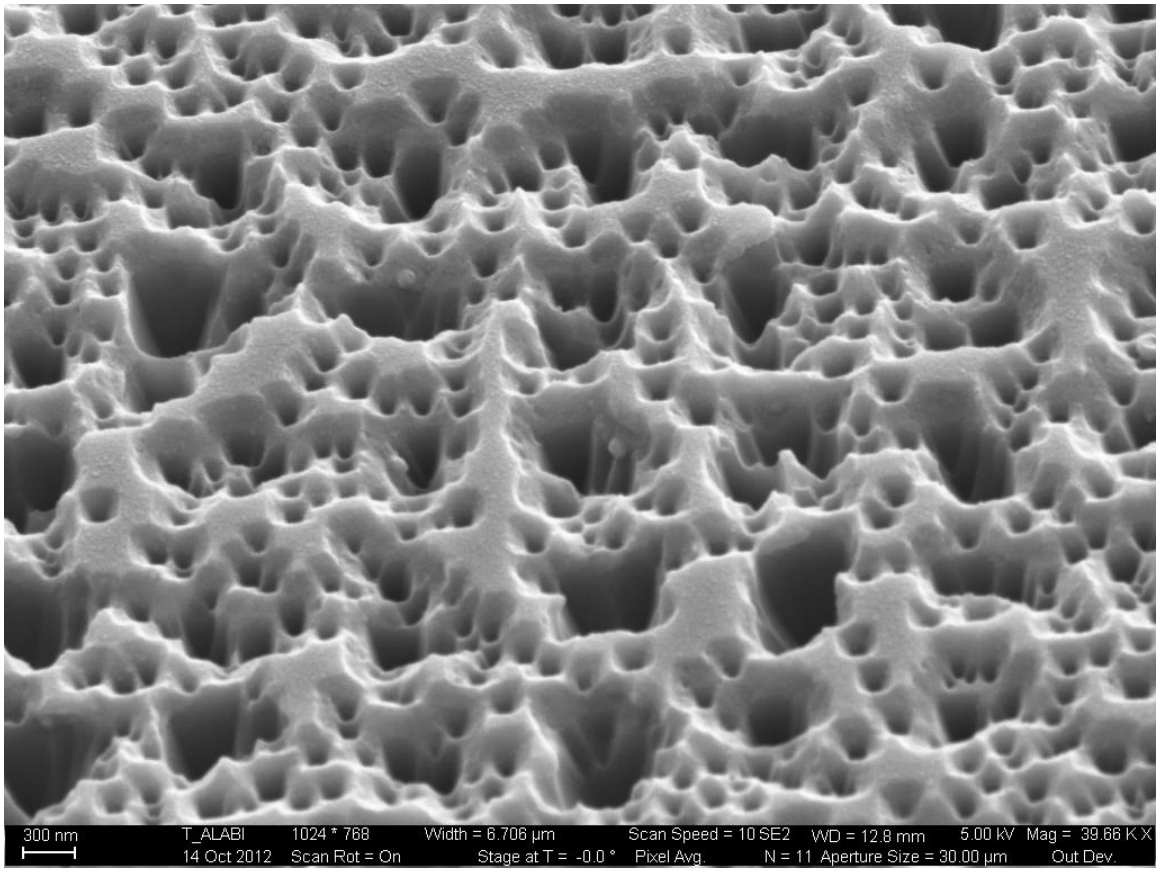

Figure C.13 SEM image of square holes formed from prolonged gold catalyzed etch on silicon <100>.

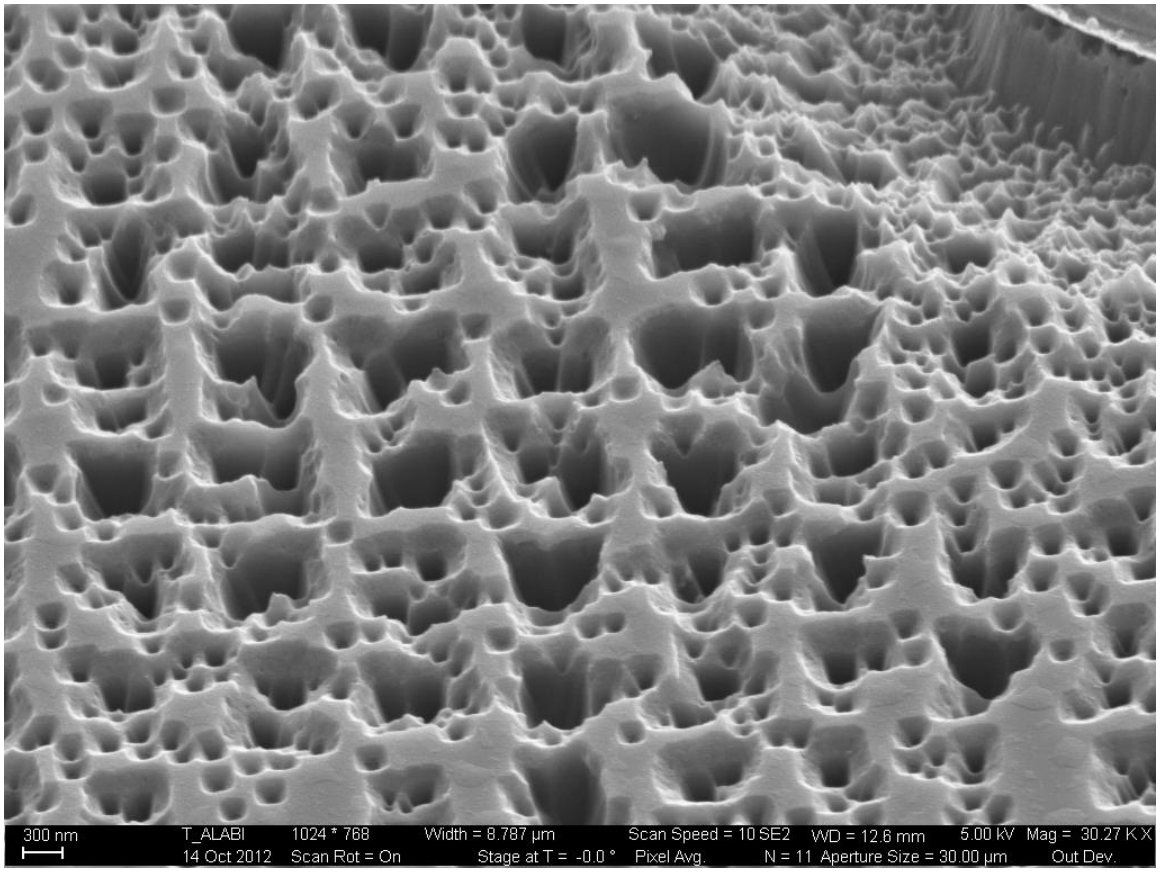

Figure C.14 Large area SEM image of square holes formed from prolonged gold catalyzed etch on silicon <100>.

APPENDIX D

SUPPLEMENTARY DATA FOR CHAPTER 6

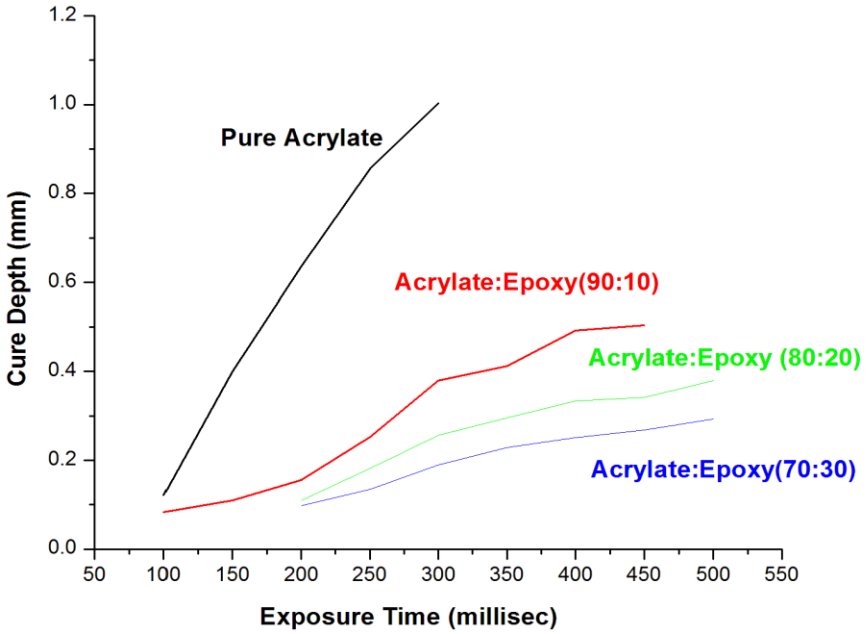

Figure D.1 Graph showing the plot of cure depth versus exposure time for a pure acrylate, (90:10) acrylate:epoxy, (80:20) acrylate:epoxy, and (70:30) acrylate:epoxy material system.

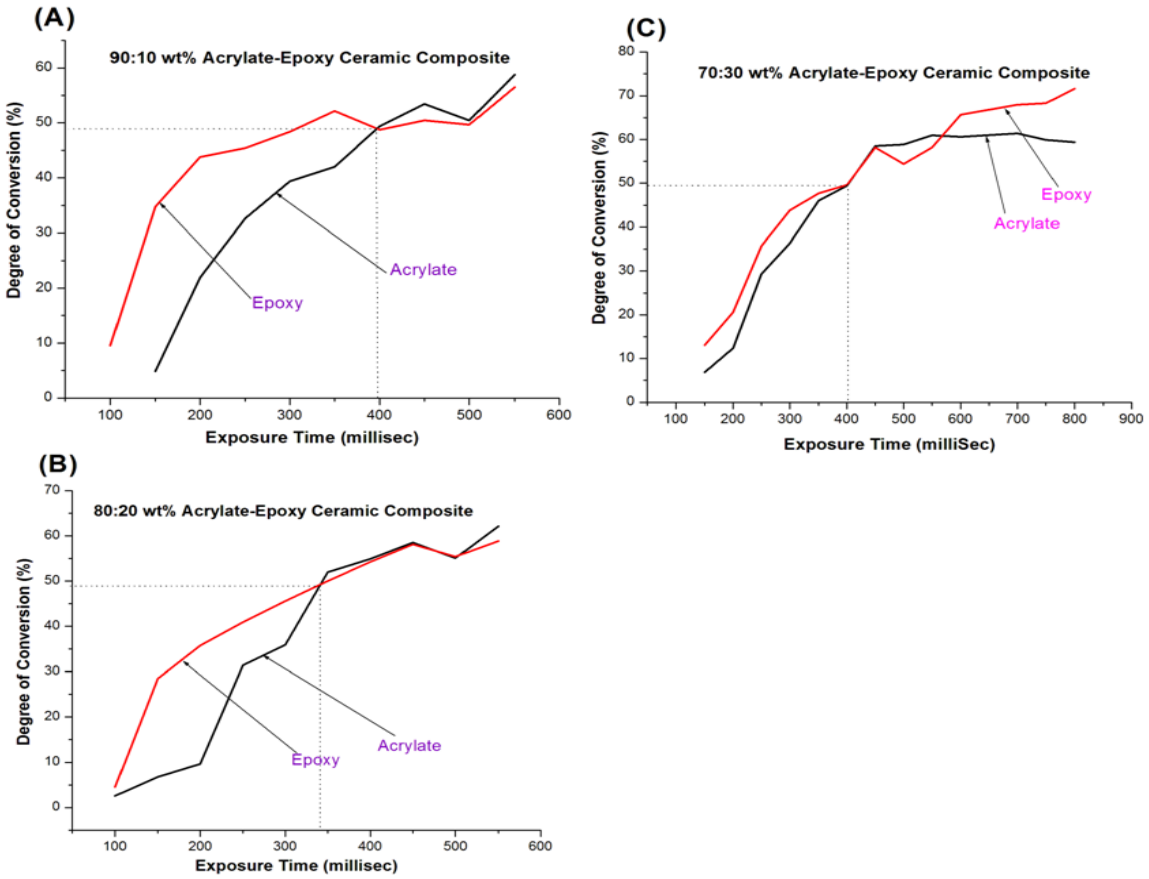

Figure D.2 Graphs showing the plot of degree of conversion versus exposure time for (A) 90:10 wt.% acrylate:epoxy, (B) 80:20 wt.% acrylate:epoxy, and (C) 70:30 wt.% acrylate:epoxy ceramic loaded material system.

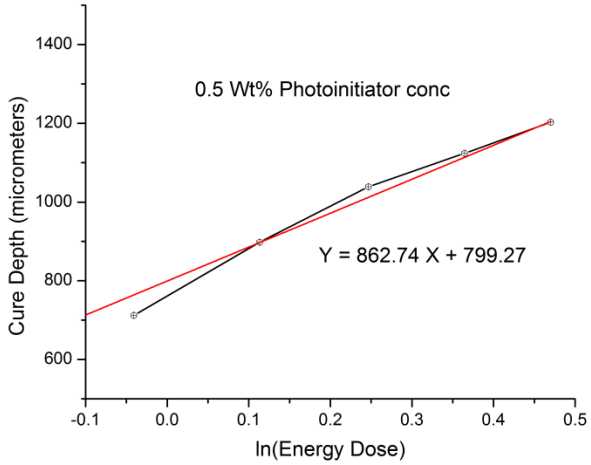

Figure D.3 Graph showing the working curve for a vinylether material system containing 0.5 wt.% photoinitiator.

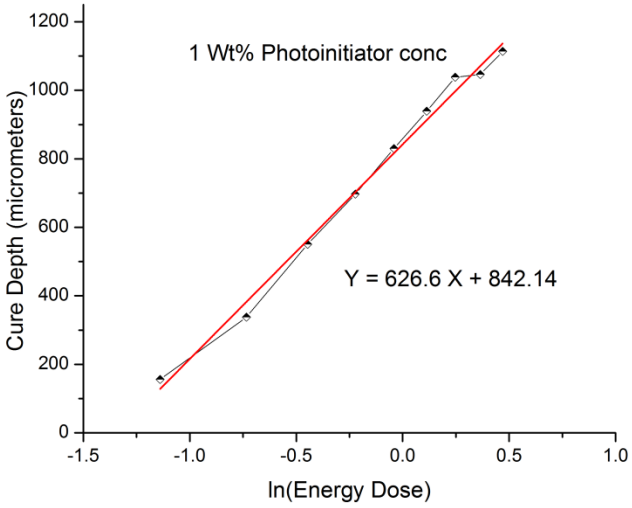

Figure D.4 Graph showing the working curve for a vinylether material system containing 1 wt.% photoinitiator.

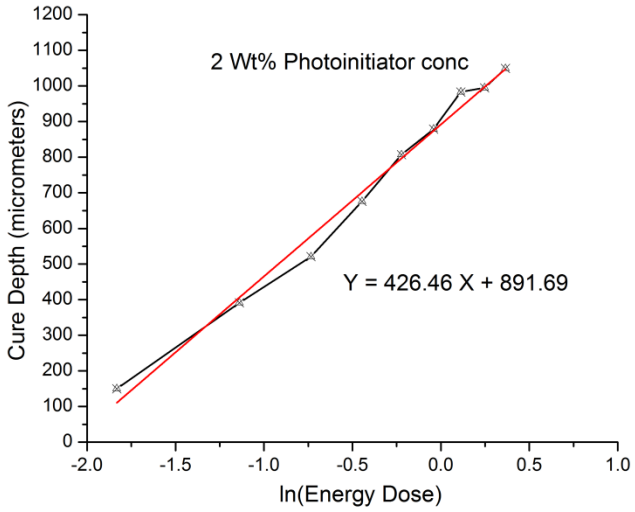

Figure D.5 Graph showing the working curve for a vinylether material system containing 2 wt.% photoinitiator.

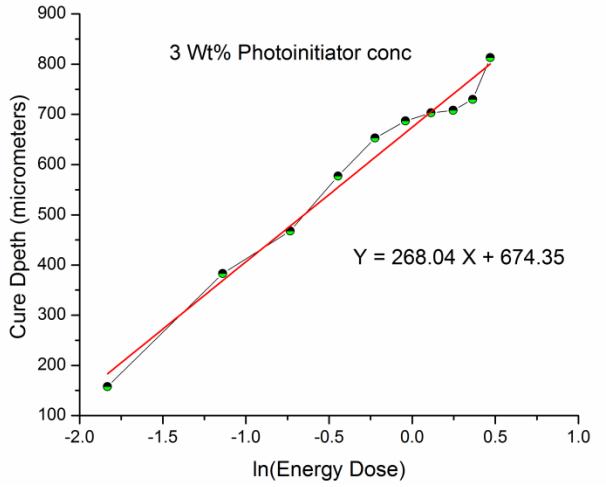

Figure D.6 Graph showing the working curve for a vinylether material system containing 3 wt.% photoinitiator.

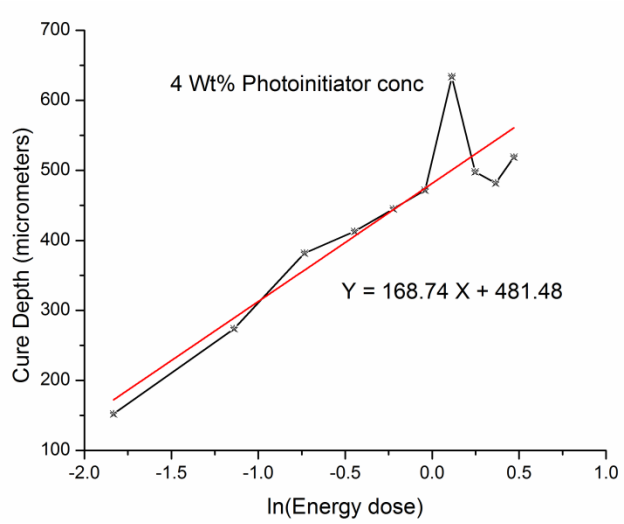

Figure D.7 Graph showing the working curve for a vinylether material system containing 4 wt.% photoinitator.

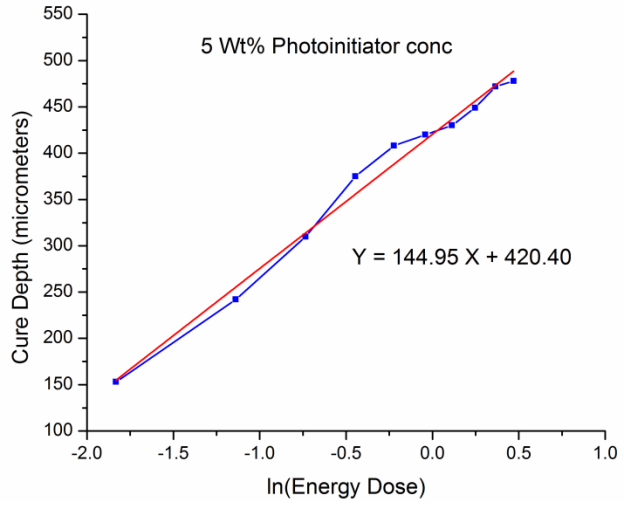

Figure D.8 Graph showing the working curve for a vinylether material system containing 5 wt.% photoinitiator.

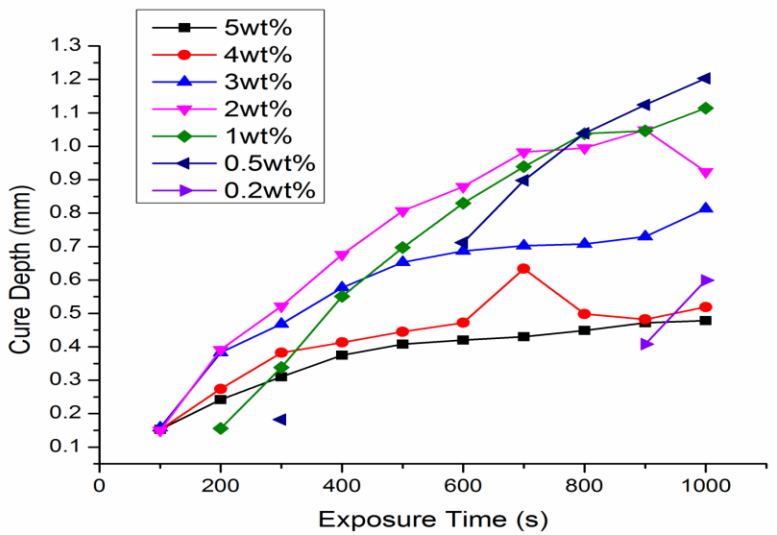

Figure D.9 Graph showing a plot of cure depth versus exposure time for varying concentrations of photoinitiator in a vinylether material system.

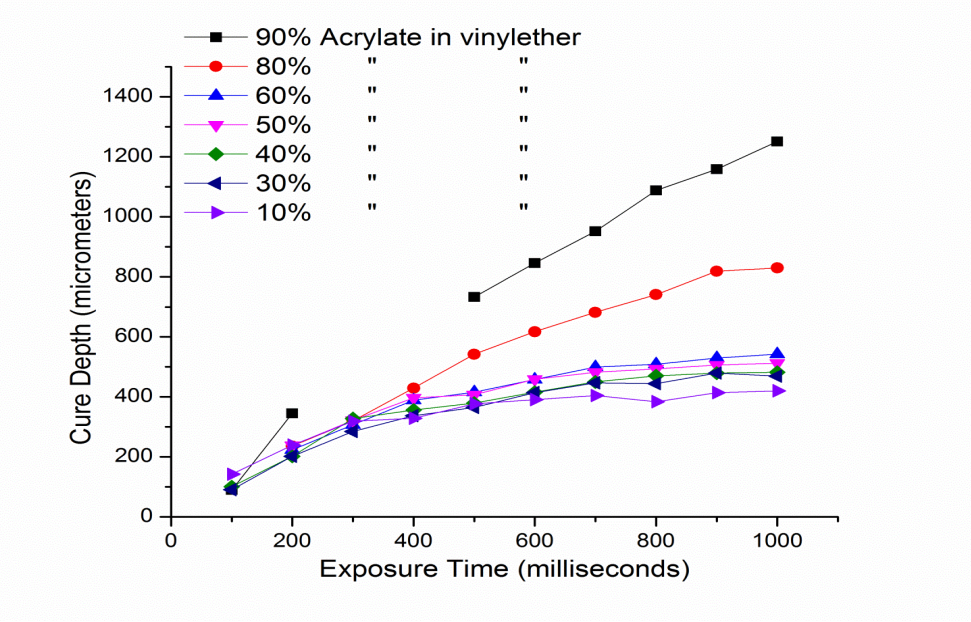

Figure D.10 Graph showing a plot of cure depth versus exposure time for varying concentrations of photoinitiator in a vinylether material system.

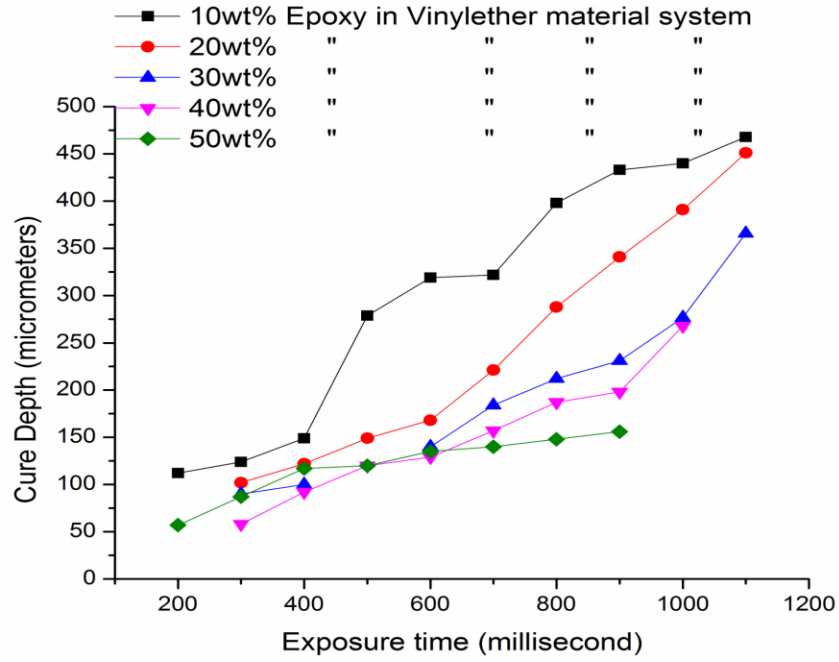

Figure D.11 Graph showing a plot of cure depth versus exposure time for varying concentrations of epoxy in a vinylether material system.

REFERENCES

[1] Arshady R. Desk reference of Functional Polymers: Synthesis and Applications. 1996.

[2] Lazzari M, López-Quintela M. Block Copolymers as a Tool for Nanomaterial Fabrication. Advanced Materials. 2003;15:1583-94.

[3] Park C, Yoon J, Thomas EL. Enabling nanotechnology with self assembled block copolymer patterns. Polymer. 2003;44:6725-60.

[4] Kim JK, Yang SY, Lee Y, Kim Y. Functional nanomaterials based on block copolymer self-assembly. Progress in Polymer Science. 2010;35:1325-49.

[5] Bang J, Jeong U, Ryu DY, Russell TP, Hawker CJ. Block Copolymer Nanolithography: Translation of Molecular Level Control to Nanoscale Patterns. Advanced Materials. 2009;21:4769-92.

[6] Hamley IW. Ordering in thin films of block copolymers: Fundamentals to potential applications. Progress in Polymer Science. 2009;34:1161-210.

[7] Park M, Harrison C, Chaikin PM, Register RA, Adamson DH. Block Copolymer Lithography: Periodic Arrays of ~1011 Holes in 1 Square Centimeter. Science. 1997;276:1401-4.

[8] Cheng JY, Ross CA, Chan VZH, Thomas EL, Lammertink RGH, Vancso GJ. Formation of a Cobalt Magnetic Dot Array via Block Copolymer Lithography. Advanced Materials. 2001;13:1174-8.

[9] Cheng JY, Ross CA, Thomas EL, Smith HI, Vancso GJ. Fabrication of nanostructures with long-range order using block copolymer lithography. Applied Physics Letters. 2002;81:3657-9.

[10] Lammertink RGH, Hempenius MA, van den Enk JE, Chan VZH, Thomas EL, Vancso GJ. Nanostructured Thin Films of Organic–Organometallic Block Copolymers: One-Step Lithography with Poly(ferrocenylsilanes) by Reactive Ion Etching. Advanced Materials. 2000;12:98-103.

[11] Chang S-W, Chuang VP, Boles ST, Ross CA, Thompson CV. Densely Packed Arrays of Ultra-High-Aspect-Ratio Silicon Nanowires Fabricated using Block-Copolymer Lithography and Metal-Assisted Etching. Advanced Functional Materials. 2009;19:2495-500.

[12] Jung YS, Ross CA. Orientation-Controlled Self-Assembled Nanolithography Using a Polystyrene−Polydimethylsiloxane Block Copolymer. Nano Letters. 2007;7:2046-50.

[13] Son JG, Chang J-B, Berggren KK, Ross CA. Assembly of Sub-10-nm Block Copolymer Patterns with Mixed Morphology and Period Using Electron Irradiation and Solvent Annealing. Nano Letters. 2011;11:5079-84.

[14] Son JG, Gwyther J, Chang J-B, Berggren KK, Manners I, Ross CA. Highly Ordered Square Arrays from a Templated ABC Triblock Terpolymer. Nano Letters. 2011;11:2849-55.

[15] Roman G, et al. Block copolymer micelle nanolithography. Nanotechnology. 2003;14:1153.

[16] Kang GB, Kim SI, Kim YT, Park JH. Fabrication of metal nano dot dry etching mask using block copolymer thin film. Current Applied Physics. 2009;9:S82-S4.

[17] Shin DO, Lee DH, Moon H-S, Jeong S-J, Kim JY, Mun JH, et al. Sub-Nanometer Level Size Tuning of a Monodisperse Nanoparticle Array Via Block Copolymer Lithography. Advanced Functional Materials. 2010:n/a-n/a.

[18] Ruiz R, Kang H, Detcheverry FA, Dobisz E, Kercher DS, Albrecht TR, et al. Density Multiplication and Improved Lithography by Directed Block Copolymer Assembly. Science. 2008;321:936-9.

[19] Shin K, Leach KA, Goldbach JT, Kim DH, Jho JY, Tuominen M, et al. A Simple Route to Metal Nanodots and Nanoporous Metal Films. Nano Letters. 2002;2:933-6.

[20] Thurn-Albrecht T, Schotter J, Kästle GA, Emley N, Shibauchi T, Krusin-Elbaum L, et al. Ultrahigh-Density Nanowire Arrays Grown in Self-Assembled Diblock Copolymer Templates. Science. 2000;290:2126-9.

[21] Kim DH, Kim SH, Lavery K, Russell TP. Inorganic Nanodots from Thin Films of Block Copolymers. Nano Letters. 2004;4:1841-4.

[22] Park M, Chaikin PM, Register RA, Adamson DH. Large area dense nanoscale patterning of arbitrary surfaces. Applied Physics Letters. 2001;79:257-9.

[23] Calvert P, Crockett R. Chemical Solid Free-Form Fabrication: Making Shapes without Molds. Chemistry of Materials. 1997;9:650-63.

[24] Yagci Y, Jockusch S, Turro NJ. Photoinitiated Polymerization: Advances, Challenges, and Opportunities. Macromolecules. 2010;43:6245-60.

[25] Haertling CL, Yoshikawa S, Newnham RE. Thick Film Patterned Ceramics Using UV-Curable Pastes. Journal of the American Ceramic Society. 1990;73:3339-44.

[26] Griffith ML, Halloran JW. Freeform Fabrication of Ceramics via Stereolithography. Journal of the American Ceramic Society. 1996;79:2601-8.

[27] Ikuta K, Hirowatari K. Real three dimensional micro fabrication using stereo lithography and metal molding. Micro Electro Mechanical Systems, 1993, MEMS '93, Proceedings An Investigation of Micro Structures, Sensors, Actuators, Machines and Systems IEEE1993. p. 42-7.

[28] Hinczewski C, Corbel S, Chartier T. Ceramic suspensions suitable for stereolithography. Journal of the European Ceramic Society. 1998;18:583-90.

[29] Wu KC, Halloran JW. Photopolymerization monitoring of ceramic stereolithography resins by FTIR methods. Journal of Materials Science. 2005;40:71-6.

[30] Badev A, Abouliatim Y, Chartier T, Lecamp L, Lebaudy P, Chaput C, et al. Photopolymerization kinetics of a polyether acrylate in the presence of ceramic fillers used in stereolithography. Journal of Photochemistry and Photobiology A: Chemistry. 2011;222:117-22.

[31] Tomeckova V, Halloran JW. Predictive models for the photopolymerization of ceramic suspensions. Journal of the European Ceramic Society. 2010;30:2833-40.

[32] Halloran JW, Tomeckova V, Gentry S, Das S, Cilino P, Yuan D, et al. Photopolymerization of powder suspensions for shaping ceramics. Journal of the European Ceramic Society. 2011;31:2613-9.

[33] Lasagni AF, Hendricks JL, Shaw CM, Yuan D, Martin DC, Das S. Direct laser interference patterning of poly(3,4-ethylene dioxythiophene)-poly(styrene sulfonate) (PEDOT-PSS) thin films. Applied Surface Science. 2009;255:9186-92.

[34] Fang H, Yuan D, Guo R, Zhang S, Han RPS, Das S, et al. Fabrication of Patterned Polymer Nanowire Arrays. ACS Nano. 2010;5:1476-82.

[35] Lasagni A, Yuan D, Das S. Rapid fabrication of pentaerythritol triacrylate periodic structures on large areas by laser interference patterning with nanosecond pulses. Journal of Applied Physics. 2009;105:023101-7.

[36] Rui G, Dajun Y, Suman D. Large-area microlens arrays fabricated on flexible polycarbonate sheets via single-step laser interference ablation. Journal of Micromechanics and Microengineering. 2011;21:015010.

[37] Yuan D, Guo R, Wei Y, Wu W, Ding Y, Wang ZL, et al. Heteroepitaxial Patterned Growth of Vertically Aligned and Periodically Distributed ZnO Nanowires on GaN Using Laser Interference Ablation. Advanced Functional Materials. 2010;20:3484-9.

[38] Wei Y, Wu W, Guo R, Yuan D, Das S, Wang ZL. Wafer-Scale High-Throughput Ordered Growth of Vertically Aligned ZnO Nanowire Arrays. Nano Letters. 2010;10:3414-9.

[39] Nikos Hadjichristidis SP, and George Floudas. Block Copoymers: Synthetic Strategies, Physical Properties, and Applications. Hoboken, New Jersey: John Wiley & Sons,Inc.; 2003. p. 419.

[40] Alabi TR, Yuan D, Das S. Photopatterneable Block Co-Polymers for Laser Interference Lithography. MRS Online Proceedings Library. 2012;1412:null-null.

[41] Alabi TR, Yuan D, Das S. Hierarchical Metallic and Ceramic Nanostructures Produced via a Hybrid Approach Combining Laser Interference Ablation and Block Co-Polymer Phase Separation. MRS Online Proceedings Library. 2012;1412:null-null.

[42] Corbin N, Prud'Homme J. Multiblock copolymers of styrene and isoprene. I. Synthesis and characterization. Journal of Polymer Science: Polymer Chemistry Edition. 1976;14:1645-59.

[43] Quirk RP, Lee B. Anionic synthesis of polystyrene and polybutadiene heteroarm star polymers. Makromolekulare Chemie Macromolecular Symposia. 1992;53:201-10.

[44] Varshney SK, Hautekeer JP, Fayt R, Jerome R, Teyssie P. Anionic polymerization of (meth)acrylic monomers. 4. Effect of lithium salts as ligands on the "living" polymerization of methyl methacrylate using monofunctional initiators. Macromolecules. 1990;23:2618-22.

[45] Matsushita Y, Nakao Y, Saguchi R, Choshi H, Nagasawa M. Studies of Styrene and 2-Vinylpyridine Block Copolymers; Preparation and Characterization. Polymer Journal. 1986;18:493-9.

[46] Grosius P, Gallot Y, Skoulios A. BLOCK COPOLYMERS FROM 2-VINYLPYRIDINE AND 4-VINYLPYRIDINES - SYNTHESIS, CHARACTERISATION AND STUDY OF MESOMORPHOUS PHASES. Makromolekulare Chemie. 1970;136:191-&.

[47] Barker MC, Vincent B. The preparation and characterisation of polystyrene/poly/ethylene oxide) AB block copolymers. Colloids and Surfaces. 1984;8:289-95.

[48] Ni Y, Rulkens R, Manners I. Transition Metal-Based Polymers with Controlled Architectures: Well-Defined Poly(ferrocenylsilane) Homopolymers and Multiblock Copolymers via the Living Anionic Ring-Opening Polymerization of Silicon-Bridged [1]Ferrocenophanes. Journal of the American Chemical Society. 1996;118:4102-14.

[49] Bellas V, Iatrou H, Hadjichristidis N. Controlled Anionic Polymerization of Hexamethylcyclotrisiloxane. Model Linear and Miktoarm Star Co- and Terpolymers of Dimethylsiloxane with Styrene and Isoprene. Macromolecules. 2000;33:6993-7.

[50] Lo GYS, Otterbacher EW, Gatzke AL, Tung LH. Studies on Dilithium Initiators. 3. Effect of Additives and Seeding. Macromolecules. 1994;27:2233-40.

[51] Tung LH, Lo GYS. Hydrocarbon-Soluble Di- and Multifunctional Organolithium Initiators. Macromolecules. 1994;27:1680-4.

[52] Matyjaszewski K. Cationic Polymerizations: Mechanisms, Synthesis & Applications: CRC; 1996.

[53] Kamigaito M, Sawamoto M, Higashimura T. Living cationic polymerization of isobutyl vinyl ether by protonic acid/zinc halide initiating systems: evidence for the halogen exchange with zinc halide in the growing species. Macromolecules. 1992;25:2587-91.

[54] Faust R, Weber C, Fiandanese V, Marchese G, Punzi A. One-step synthesis of dialkynyl-1,2-diones and their conversion to fused pyrazines bearing enediyne units. Tetrahedron. 1997;53:14655-70.

[55] Matyjaszewski K, Wang J-L, Grimaud T, Shipp DA. Controlled/"Living" Atom Transfer Radical Polymerization of Methyl Methacrylate Using Various Initiation Systems. Macromolecules. 1998;31:1527-34.

[56] Georges MK, Veregin RPN, Kazmaier PM, Hamer GK. Narrow molecular weight resins by a free-radical polymerization process. Macromolecules. 1993;26:2987-8.

[57] Chiefari J, Chong YK, Ercole F, Krstina J, Jeffery J, Le TPT, et al. Living Free-Radical Polymerization by Reversible Addition−Fragmentation Chain Transfer: The RAFT Process. Macromolecules. 1998;31:5559-62.

[58] Wayland BB, Poszmik G, Mukerjee SL, Fryd M. Living Radical Polymerization of Acrylates by Organocobalt Porphyrin Complexes. Journal of the American Chemical Society. 1994;116:7943-4.

[59] Hawker CJ, Piotti ME. Nitroxide-mediated Free Radical Polymerization. In: Buschow KHJ, Robert WC, Merton CF, Bernard I, Edward JK, Subhash M, et al., editors. Encyclopedia of Materials: Science and Technology. Oxford: Elsevier; 2001. p. 6164-77.

[60] Hawker CJ, Bosman AW, Harth E. New Polymer Synthesis by Nitroxide Mediated Living Radical Polymerizations. Chemical Reviews. 2001;101:3661-88.

[61] Cho CG, Feit BA, Webster OW. Initiation of vinyl ether polymerization by trimethylsilyl triflate, dimethyl sulfide, and adventitious water. Macromolecules. 1992;25:2081-5.

[62] Webster OW. The use of group transfer polymerization for the control of polymethacrylate molecular structure. Makromolekulare Chemie Macromolecular Symposia. 1990;33:133-43.

[63] Sogah DY, Hertler WR, Webster OW, Cohen GM. Group transfer polymerization - polymerization of acrylic monomers. Macromolecules. 1987;20:1473-88.

[64] Webster OW, Hertler WR, Sogah DY, Farnham WB, RajanBabu TV. Group-transfer polymerization. 1. A new concept for addition polymerization with organosilicon initiators. Journal of the American Chemical Society. 1983;105:5706-8.

[65] Hertler WR, Sogah DY, Boettcher FP. Group-transfer polymerization on a polymeric support. Macromolecules. 1990;23:1264-8.

[66] Teraoka I. Polymer Solutions: An Introduction to Physical Properties. In: Teraoka I, editor.: John Wiley & Sons, Inc.; 2002.

[67] Brunsveld L, Folmer BJB, Meijer EW, Sijbesma RP. Supramolecular Polymers. Chemical Reviews. 2001;101:4071-98.

[68] Thomas MMaEL. Periodic Materials and Interference Lithography for Photonics, phononics and Mechanics. Wiley-VCH; 2009.

[69] Zheng B, Wu Y, Yang P, Liu J. Synthesis of Ultra-Long and Highly Oriented Silicon Oxide Nanowires from Liquid Alloys. Advanced Materials. 2002;14:122-4.

[70] Ni H, Li X, Gao H. Elastic modulus of amorphous SiO[sub 2] nanowires. Applied Physics Letters. 2006;88:043108-3.

[71] Bauer LA, Birenbaum NS, Meyer GJ. Biological applications of high aspect ratio nanoparticles. Journal of Materials Chemistry. 2004;14:517-26.

[72] Sirringhaus H, Kawase T, Friend RH, Shimoda T, Inbasekaran M, Wu W, et al. High-Resolution Inkjet Printing of All-Polymer Transistor Circuits. Science. 2000;290:2123-6.

[73] Savas TA, Farhoud M, Smith HI, Hwang M, Ross CA. Properties of large-area nanomagnet arrays with 100 nm period made by interferometric lithography. Journal of Applied Physics. 1999;85:6160-2.

[74] Acar MH, Matyjaszewski K. Block copolymers by transformation of living anionic polymerization into controlled/“living” atom transfer radical polymerization. Macromolecular Chemistry and Physics. 1999;200:1094-100.

[75] Liu K, Feng Q, Yang Y, Zhang G, Ou L, Lu Y. Preparation and characterization of amorphous silica nanowires from natural chrysotile. Journal of Non-Crystalline Solids. 2007;353:1534-9.

[76] Uchino T, Kurumoto N, Sagawa N. Structure and formation mechanism of blue-light-emitting centers in silicon and silica-based nanostructured materials. Physical Review B. 2006;73:233203.

[77] Hu J, Odom TW, Lieber CM. Chemistry and Physics in One Dimension: Synthesis and Properties of Nanowires and Nanotubes. Accounts of Chemical Research. 1999;32:435-45.

[78] Gupta AK, Gupta M. Synthesis and surface engineering of iron oxide nanoparticles for biomedical applications. Biomaterials. 2005;26:3995-4021.

[79] Whitesides GM, Ostuni E, Takayama S, Jiang X, Ingber DE. SOFT LITHOGRAPHY IN BIOLOGY AND BIOCHEMISTRY. Annual Review of Biomedical Engineering. 2001;3:335-73.

[80] Jiang Z, Xie T, Yuan XY, Geng BY, Wu GS, Wang GZ, et al. Catalytic synthesis and photoluminescence of silicon oxide nanowires and nanotubes. Applied Physics A: Materials Science & Processing. 2005;81:477-9.

[81] Baker GA, Moore DS. Progress in plasmonic engineering of surface-enhanced Raman-scattering substrates toward ultra-trace analysis. Analytical and Bioanalytical Chemistry. 2005;382:1751-70.

[82] Zheng M, Yu M, Liu Y, Skomski R, Liou SH, Sellmyer DJ, et al. Magnetic nanodot arrays produced by direct laser interference lithography. Applied Physics Letters. 2001;79:2606-8.

[83] Henri J, Han G, Meint de B, Miko E, Jan F. A survey on the reactive ion etching of silicon in microtechnology. Journal of Micromechanics and Microengineering. 1996;6:14.

[84] Liu ZH, Pan CT, Chao CH, Ou ZY, Li CC, Liu CY. Influence of twice-deposited etching mask layers on verticality of nanostructures. Thin Solid Films. 2012;520:6757-64.

[85] McDonald JC, Duffy DC, Anderson JR, Chiu DT, Wu H, Schueller OJA, et al. Fabrication of microfluidic systems in poly(dimethylsiloxane). ELECTROPHORESIS. 2000;21:27-40.

[86] Tseng AA, Kuan C, Chen CD, Ma KJ. Electron beam lithography in nanoscale fabrication: recent development. Electronics Packaging Manufacturing, IEEE Transactions on. 2003;26:141-9.

[87] Vieu C, Carcenac F, Pépin A, Chen Y, Mejias M, Lebib A, et al. Electron beam lithography: resolution limits and applications. Applied Surface Science. 2000;164:111-7.

[88] Kwon Y, Faust R. Synthesis of Polyisobutylene-Based Block Copolymers with Precisely Controlled Architecture by Living Cationic Polymerization
New Synthetic Methods. Springer Berlin / Heidelberg; 2004. p. 247-55.

[89] Piner RD, Zhu J, Xu F, Hong S, Mirkin CA. "Dip-Pen" Nanolithography. Science. 1999;283:661-3.

[90] Xie XN, Chung HJ, Sow CH, Wee ATS. Nanoscale materials patterning and engineering by atomic force microscopy nanolithography. Materials Science and Engineering: R: Reports. 2006;54:1-48.

[91] Mullenborn M, Birkelund K, Grey F, Madsen S. Laser direct writing of oxide structures on hydrogen-passivated silicon surfaces. Applied Physics Letters. 1996;69:3013-5.

[92] Stubenrauch M, Fischer M, Kremin C, Stoebenau S, Albrecht A, Nagel O. Black silicon—new functionalities in microsystems. Journal of Micromechanics and Microengineering. 2006;16:S82.

[93] Leibler L. Theory of Microphase Separation in Block Copolymers. Macromolecules. 1980;13:1602-17.

[94] Phillip WA, Hillmyer MA, Cussler EL. Cylinder Orientation Mechanism in Block Copolymer Thin Films Upon Solvent Evaporation. Macromolecules. 2010;43:7763-70.

[95] Kloninger C, Rehahn M. Bicontinuous Gyroidic Morphologies in Ferrocenyldimethylsilane-b-Methyl Methacrylate Diblock Copolymer Blends. Macromolecules. 2004;37:8319-24.

[96] Matsen MW, Whitmore MD. Accurate diblock copolymer phase boundaries at strong segregations. The Journal of Chemical Physics. 1996;105:9698-701.

[97] Green PF, Limary R. Block copolymer thin films: pattern formation and phase behavior. Advances in Colloid and Interface Science. 2001;94:53-81.

[98] Allen KD, Sawin HH. The Plasma Etching of Polysilicon with CF 3Cl / Argon Discharges: II . Modeling of Ion Bombardment Energy Distributions. Journal of The Electrochemical Society. 1986;133:2326-31.

[99] Yoo J, Yu G, Yi J. Large-area multicrystalline silicon solar cell fabrication using reactive ion etching (RIE). Solar Energy Materials and Solar Cells. 2011;95:2-6.

[100] Lyding JW, Shen TC, Hubacek JS, Tucker JR, Abeln GC. Nanoscale patterning and oxidation of H-passivated Si(100)-2 x 1 surfaces with an ultrahigh vacuum scanning tunneling microscope. Applied Physics Letters. 1994;64:2010-2.

[101] Day HC, Allee DR. Selective area oxidation of silicon with a scanning force microscope. Applied Physics Letters. 1993;62:2691.

[102] Perez-Murano F, Abadal G, Barniol N, Aymerich X, Servat J, Gorostiza P, et al. Nanometer-scale oxidation of Si(100) surfaces by tapping mode atomic force microscopy. Journal of Applied Physics. 1995;78:6797-801.

[103] Hilton AM, Jacobson KW, Lynch BP, Simpson GJ. Enhanced local oxidation of silicon using a conducting atomic force microscope in water. Journal of Vacuum Science & Technology B: Microelectronics and Nanometer Structures. 2008;26:47-51.

[104] Kuo CW, Shiu JY, Cho YH, Chen P. Fabrication of Large-Area Periodic Nanopillar Arrays for Nanoimprint Lithography Using Polymer Colloid Masks. Advanced Materials. 2003;15:1065-8.

[105] Legtenberg R, Jansen H, de Boer M, Elwenspoek M. Anisotropic Reactive Ion Etching of Silicon Using SF 6 / O 2 / CHF 3 Gas Mixtures. Journal of The Electrochemical Society. 1995;142:2020-8.

[106] Kelly KL, Coronado E, Zhao LL, Schatz GC. The Optical Properties of Metal Nanoparticles: The Influence of Size, Shape, and Dielectric Environment. The Journal of Physical Chemistry B. 2002;107:668-77.

[107] Vallée F. Optical Properties of Metallic Nanoparticles. In: Bréchignac C, Houdy P, Lahmani M, editors. Nanomaterials and Nanochemistry: Springer Berlin Heidelberg; 2007. p. 197-227.

[108] Huang HH, Yan FQ, Kek YM, Chew CH, Xu GQ, Ji W, et al. Synthesis, Characterization, and Nonlinear Optical Properties of Copper Nanoparticles. Langmuir. 1997;13:172-5.

[109] Daniel M-C, Astruc D. Gold Nanoparticles: Assembly, Supramolecular Chemistry, Quantum-Size-Related Properties, and Applications toward Biology, Catalysis, and Nanotechnology. Chemical Reviews. 2003;104:293-346.

[110] Jiang Q, Zhang S, Zhao M. Size-dependent melting point of noble metals. Materials Chemistry and Physics. 2003;82:225-7.

[111] Bachels T, Güntherodt H-J, Schäfer R. Melting of Isolated Tin Nanoparticles. Physical Review Letters. 2000;85:1250.

[112] Lu A-H, Salabas EL, Schüth F. Magnetic Nanoparticles: Synthesis, Protection, Functionalization, and Application. Angewandte Chemie International Edition. 2007;46:1222-44.

[113] Voit J. Rep Prog Phys. 1994;57:977.

[114] Ohde H, Wai CM, Kim H, Kim J, Ohde M. Hydrogenation of Olefins in Supercritical CO2 Catalyzed by Palladium Nanoparticles in a Water-in-CO2 Microemulsion. Journal of the American Chemical Society. 2002;124:4540-1.

[115] Xia Y, Yang P, Sun Y, Wu Y, Mayers B, Gates B, et al. One-Dimensional Nanostructures: Synthesis, Characterization, and Applications. Advanced Materials. 2003;15:353-89.

[116] Gates BD, Xu Q, Stewart M, Ryan D, Willson CG, Whitesides GM. New Approaches to Nanofabrication: Molding, Printing, and Other Techniques. Chemical Reviews. 2005;105:1171-96.

[117] Lee K-B, Park S-J, Mirkin CA, Smith JC, Mrksich M. Protein Nanoarrays Generated By Dip-Pen Nanolithography. Science. 2002;295:1702-5.

[118] Rangelow IW. Reactive ion etching for high aspect ratio silicon micromachining. Surface and Coatings Technology. 1997;97:140-50.

[119] Fedynyshyn TH, Grynkewich GW, Dumas RH. Mask Dependent Etch Rates III. Journal of The Electrochemical Society. 1988;135:268-9.

[120] Lasagni AF, Yuan D, Das S. Layer-by-Layer Interference Lithography of Three-dimensional Microstructures in SU-8. Advanced Engineering Materials. 2009;11:408-11.

[121] van Rijn CJM. Laser interference as a lithographic nanopatterning tool. Journal of Microlithography, Microfabrication, and Microsystems. 2006;5:011012-6.

[122] Lasagni AF, Yuan D, Shao P, Das S. Periodic Micropatterning of Polyethylene Glycol Diacrylate Hydrogel by Laser Interference Lithography Using Nano- and Femtosecond Pulsed Lasers. Advanced Engineering Materials. 2009;11:B20-B4.

[123] Hamley IW. Nanostructure fabrication using block copolymers. Nanotechnology. 2003;14:R39.

[124] Fabre B, Herrier C. Automated sub-100 nm local anodic oxidation (LAO)-directed nanopatterning of organic monolayer-modified silicon surfaces. RSC Advances. 2012;2:168-75.

[125] Eppler AS, Rupprechter G, Guczi L, Somorjai GA. Model Catalysts Fabricated Using Electron Beam Lithography and Pulsed Laser Deposition. The Journal of Physical Chemistry B. 1997;101:9973-7.

[126] Baek I. Electron beam lithography patterning of sub-10?nm line using hydrogen silsesquioxane for nanoscale device applications. J Vac Sci Technol B. 2005;23:3120.

[127] Brus L. Luminescence of Silicon Materials: Chains, Sheets, Nanocrystals, Nanowires, Microcrystals, and Porous Silicon. The Journal of Physical Chemistry. 1994;98:3575-81.

[128] Baughman RH, Zakhidov AA, de Heer WA. Carbon Nanotubes--the Route Toward Applications. Science. 2002;297:787-92.

[129] Al'tshuler BL, Lee PA. Disordered Electronic Systems. Physics Today. 1988;41:36-44.

[130] Kind H, Yan H, Messer B, Law M, Yang P. Nanowire Ultraviolet Photodetectors and Optical Switches. Advanced Materials. 2002;14:158-60.

[131] Huang MH, Mao S, Feick H, Yan H, Wu Y, Kind H, et al. Room-Temperature Ultraviolet Nanowire Nanolasers. Science. 2001;292:1897-9.

[132] Song T, Lee S-T, Sun B. Silicon nanowires for photovoltaic applications: The progress and challenge. Nano Energy. 2012;1:654-73.

[133] Law M, Greene LE, Johnson JC, Saykally R, Yang P. Nanowire dye-sensitized solar cells. Nature Materials. 2005;4:455-9.

[134] Atashbar MZ, Banerji D, Singamaneni S. Room-temperature hydrogen sensor based on palladium nanowires. Sensors Journal, IEEE. 2005;5:792-7.

[135] Vayssieres L. Growth of Arrayed Nanorods and Nanowires of ZnO from Aqueous Solutions. Advanced Materials. 2003;15:464-6.

[136] Wei M, Konishi Y, Zhou H, Sugihara H, Arakawa H. A simple method to synthesize nanowires titanium dioxide from layered titanate particles. Chemical Physics Letters. 2004;400:231-4.

[137] Liu B, Boercker JE, Aydil ES. Oriented single crystalline titanium dioxide nanowires. Nanotechnology. 2008;19:505604.

[138] Boercker JE, Enache-Pommer E, Aydil ES. Growth mechanism of titanium dioxide nanowires for dye-sensitized solar cells. Nanotechnology. 2008;19:095604.

[139] Offermans P, Tong HD, van Rijn CJM, Merken P, Brongersma SH, Crego-Calama M. Ultralow-power hydrogen sensing with single palladium nanowires. Applied Physics Letters. 2009;94:223110-3.

[140] Kodambaka S, Hannon JB, Tromp RM, Ross FM. Control of Si Nanowire Growth by Oxygen. Nano Letters. 2006;6:1292-6.

[141] Cui Y, Lauhon LJ, Gudiksen MS, Wang J, Lieber CM. Diameter-controlled synthesis of single-crystal silicon nanowires. Applied Physics Letters. 2001;78:2214-6.

[142] Th S, Pietsch M, Andrä G, Falk F, Ose E, Christiansen S. Silicon nanowire-based solar cells. Nanotechnology. 2008;19:295203.

[143] Woodruff JH, Ratchford JB, Goldthorpe IA, McIntyre PC, Chidsey. Vertically Oriented Germanium Nanowires Grown from Gold Colloids on Silicon Substrates and Subsequent Gold Removal. Nano Letters. 2007;7:1637-42.

[144] Adhikari H, Marshall AF, Chidsey CED, McIntyre PC. Germanium Nanowire Epitaxy: Shape and Orientation Control. Nano Letters. 2006;6:318-23.

[145] Kim B-S, Koo T-W, Lee J-H, Kim DS, Jung YC, Hwang SW, et al. Catalyst-free Growth of Single-Crystal Silicon and Germanium Nanowires. Nano Letters. 2009;9:864-9.

[146] Hu PA, Liu YQ, Wang XB. Synthesis of highly aligned silicon oxide nanowires and their novel patterns. Applied Physics A: Materials Science & Processing. 2003;77:743.

[147] Wang F, Malac M, Egerton RF, Meldrum A, Li P, Freeman MR, et al. Controlled Growth of Silicon Oxide Nanowires from a Patterned Reagent. The Journal of Physical Chemistry C. 2007;111:1865-7.

[148] Kong J, Franklin NR, Zhou C, Chapline MG, Peng S, Cho K, et al. Nanotube Molecular Wires as Chemical Sensors. Science. 2000;287:622-5.

[149] Wang J, Gudiksen MS, Duan X, Cui Y, Lieber CM. Highly Polarized Photoluminescence and Photodetection from Single Indium Phosphide Nanowires. Science. 2001;293:1455-7.

[150] Duan X, Huang Y, Cui Y, Wang J, Lieber CM. Indium phosphide nanowires as building blocks for nanoscale electronic and optoelectronic devices. Nature. 2001;409:66-9.

[151] Duan X, Lieber CM. General Synthesis of Compound Semiconductor Nanowires. Advanced Materials. 2000;12:298-302.

[152] Li XX, Tang YH, Lin LW, Li JL. Blue light emission in mesoporous SiOx nano-structure. Microporous and Mesoporous Materials. 2008;111:591-5.

[153] Chen P, Xie S, Ren N, Zhang Y, Dong A, Chen Y, et al. Iron-Assisted Vapor-Phase Hydrothermal Method: A Low-Temperature Approach To Synthesize Blue Light Emissive SiOx Nanowires with Single-Crystal Structure of P21212. Journal of the American Chemical Society. 2006;128:1470-1.

[154] Fedynyshyn TH, Grynkewich GW, Ma TP. Mask Dependent Etch Rates II. Journal of The Electrochemical Society. 1987;134:2580-5.

[155] Fedynyshyn TH, Grynkewich GW, Hook TB, Liu MD, Ma TP. The Effect of Aluminum vs. Photoresist Masking on the Etching Rates of Silicon and Silicon Dioxide in CF_4 / O_2 Plasmas. Journal of The Electrochemical Society. 1987;134:206-9.

[156] Fedynyshyn TH, Grynkewich GW, Chen BA, Ma TP. The Effect of Metal Masks on the Plasma Etch Rate of Silicon. Journal of The Electrochemical Society. 1989;136:1799-804.

[157] Calvert P. Freeforming of polymers. Current Opinion in Solid State and Materials Science. 1998;3:585-8.

[158] Wu BM, Borland SW, Giordano RA, Cima LG, Sachs EM, Cima MJ. Solid free-form fabrication of drug delivery devices. Journal of Controlled Release. 1996;40:77-87.

[159] Conrad M. Experimental Investigations and Theoretical Modelling of Large Area Maskless Photopolymerization with Grayscale Exposure: Georgia Institute of Technology; 2011.

[160] Zhang X, Jiang XN, Sun C. Micro-stereolithography of polymeric and ceramic microstructures. Sensors and Actuators A: Physical. 1999;77:149-56.

[161] Kiran K. Characterization of curing kinetics and polymerization shrinkage in ceramic-loaded photocurable resins for large area maskless photopolymerization (LAMP) 2009.

[162] Wu KC, Seefeldt KF, Solomon MJ, Halloran JW. Prediction of ceramic stereolithography resin sensitivity from theory and measurement of diffusive photon transport. Journal of Applied Physics. 2005;98:024902-10.

[163] Griffith ML, Halloran JW. Scattering of ultraviolet radiation in turbid suspensions. Journal of Applied Physics. 1997;81:2538-46.

[164] Chartier T, Badev A, Abouliatim Y, Lebaudy P, Lecamp L. Stereolithography process: Influence of the rheology of silica suspensions and of the medium on polymerization kinetics – Cured depth and width. Journal of the European Ceramic Society. 2012;32:1625-34.

[165] Wang D, Carrera L, Abadie MJM. Photopolymerization of glycidyl acrylate and glycidyl methacrylate investigated by differential photocalorimetry and FT-I.R. European Polymer Journal. 1993;29:1379-86.

[166] Crivello JV, Varlemann U. The synthesis and study of the photoinitiated cationic polymerization of novel cycloaliphatic epoxides. Journal of Polymer Science Part A: Polymer Chemistry. 1995;33:2463-71.

[167] Crivello JV, Bulut U. Curcumin: A naturally occurring long-wavelength photosensitizer for diaryliodonium salts. Journal of Polymer Science Part A: Polymer Chemistry. 2005;43:5217-31.

[168] Crivello JV. Radical-Promoted Visible Light Photoinitiated Cationic Polymerization of Epoxides. Journal of Macromolecular Science, Part A: Pure and Applied Chemistry. 2009;46:474 - 83.

[169] Decker C, Nguyen Thi Viet T, Decker D, Weber-Koehl E. UV-radiation curing of acrylate/epoxide systems. Polymer. 2001;42:5531-41.

[170] Kodambaka S, Tersoff J, Reuter MC, Ross FM. Diameter-Independent Kinetics in the Vapor-Liquid-Solid Growth of Si Nanowires. Physical Review Letters. 2006;96:096105.

[171] Wagner RS, Ellis WC. VAPOR-LIQUID-SOLID MECHANISM OF SINGLE CRYSTAL GROWTH. Applied Physics Letters. 1964;4:89-90.

[172] Wang D, Dai H. Low-Temperature Synthesis of Single-Crystal Germanium Nanowires by Chemical Vapor Deposition. Angewandte Chemie. 2002;114:4977-80.

VITA

Taiwo R. Alabi

Taiwo was born in Lagos, Nigeria. He attended Lagos State Model College Meiran where he obtained his high school leaving certificate and was given the best science student award. He was later awarded a Bilateral Educational Agreement Scholarship award to study Chemical Engineering and Biotechnology at The Mendeleyeev University of Chemical Technology, Moscow, Russia. He proceeded to Russia and completed his Bachelor's Degree in 2008 with the highest honors and a 5.0/5.0 CGPA. Taiwo later proceeded to Bowling Green State University in Bowling Green Ohio for a year graduate study program in the Photochemistry and photophysics department. He started his PhD research at Georgia Tech in 2009, he is pursuing a doctoral degree in Polymer and Fiber Engineering with minors in both Materials Science and Chemistry, and a CGPA of 3.62 with over 51 credit hours worth of graduate classes. He has won **MRS scholarship travel award**, **TMS student Best paper award**, **Best poster presentation award** amongst other awards. He is a fluent speaker of Russian, Yoruba dialect and French. He enjoys reading, playing football, basketball, volleyball, wallyball, chess, flagfootball.